Dual Perspectives on Polymer Modifications – Synergies between Inverse Vulcanization and Flow Chemistry

Zur Erlangung des akademischen Grades eines

DOKTORS DER NATURWISSENSCHAFTEN

(Dr. rer. nat.)

von der KIT-Fakultät für Chemie und Biowissenschaften
des Karlsruher Instituts für Technologie (KIT)

genehmigte

DISSERTATION

von

M.Sc. Alexander Paul Grimm

aus Karlsruhe

1. Referent: Prof. Dr. Patrick Théato
2. Referent: Prof. Dr. Peter W. Roesky
Tag der mündlichen Prüfung: 05.05.2025

für Harald, Eva und Anna

Declaration of Authorship

Die vorliegende Arbeit wurde im Zeitraum von Februar 2022 bis März 2025 am Institut für Technische Chemie und Polymerchemie (ITCP) und dem Institut für Biologische Grenzflächen 3 (IBG-3) am Karlsruher Institut für Technologie (KIT) unter der wissenschaftlichen Betreuung von Prof. Dr. Patrick Théato angefertigt.

Hiermit erkläre ich, dass die vorliegende Arbeit im Rahmen der Betreuung durch Prof. Dr. Patrick Théato selbstständig verfasst und keine anderen als die angegebenen Quellen und Hilfsmittel verwendet wurden. Inhaltlich oder wörtlich übernommene Stellen wurden als solche gekennzeichnet, sowie wurde die Satzung des Karlsruher Instituts für Technologie (KIT) zur Sicherung guter wissenschaftlicher Praxis beachtet. Des Weiteren erkläre ich, dass ich mich derzeit in keinem laufenden Promotionsverfahren befinde, und auch keine vorausgegangenen Promotionsversuche unternommen habe. Die elektronische Version der Arbeit stimmt mit der schriftlichen Version überein und die Primärdaten sind gemäß Abs. A (6) der Regeln zur Sicherung guter wissenschaftlicher Praxis des KIT beim Institut abgegeben und archiviert.

Karlsruhe, den 14.05.2025

_____

Alexander Paul Grimm

Kurzfassung

Elementarer Schwefel, ein Abfallprodukt der industriellen Öl- und Gasraffination, wird derzeit in einem globalen Überschuss von 12 Megatonnen pro Jahr produziert. Infolgedessen wird Schwefel in oberirdischen Depots gelagert, wo er langsam in den Boden gelangt, und keine entsprechende praktische Nutzung findet. 2013 wurde eine chemische Methode entwickelt, die es ermöglicht, langlebige und formstabile polymere Materialien mit einem Schwefelgehalt von bis zu 90 Gew.-% herzustellen. Diese Technik, bekannt als inverse Vulkanisation, hat die Polymerwissenschaft durch die einfache und direkte Umwandlung von kostengünstigem elementarem Schwefel in Hochleistungspolymere revolutioniert. Aufgrund der harschen Reaktionsbedingungen ist mittels konventioneller inverser Vulkanisation jedoch nur begrenzte Kontrolle über Polymerstrukturen und -eigenschaften möglich. Zusätzlich ist die Anzahl polymerisierbarer Comonomere beschränkt. Daher sind chemische Ansätze erforderlich, um invers vulkanisierte Polymere gezielt hinsichtlich ihrer Polymerstrukturen und Materialeigenschaften zu kontrollieren und modifizieren.

Die in dieser Arbeit verfolgte Strategie beruht auf der Post-Polymerisationsmodifikation (PPM) von hochschwefelhaltigen polymeren anstelle der direkten Anpassung der Polymerisation selbst. Basierend auf der PPM aktiver Ester, einer etablierten Strategie der konventionellen kohlenstoffbasierten Polymerchemie, wurden Polymerstrukturen durch Amidierung dieser Ester gezielt modifiziert, um die Eigenschaften eines reaktiven Ausgangspolymers für spezifische Anwendungen anzupassen.

Pentafluorophenyl acrylat (PFPA) und dessen vollständig *cis*-hydriertes Analogon all-*cis*-2,3,4,5,6-Pentafluorcyclohexyl acrylat (PFCHA) wurden mit elementarem Schwefel umgesetzt. Während PFPA den harschen Reaktionsbedingungen nicht standhielt, wurde PFCHA in Gegenwart von Triethoxyvinylsilane zu einem stabilen Schwefel-Copolymer mit einem Schwefelgehalt von 61 Gew.-% umgesetzt. Dieses Copolymer war nicht amidierbar, konnte jedoch erfolgreich als Kathodenmaterial in Li-S-Akkumulatoren eingesetzt werden, wobei es sich positiv auf die Kapazitätserhaltung und die Unterdrückung der Selbstentladung auswirkte.

Als Alternative zu PFPA wurde die inverse Vulkanisation von Norbornenyl-pentafluorophenylester (NB-PFPE) untersucht, und das resultierende Polymer durch Amidierung mit vier verschiedenen primären Aminen unter milden Bedingungen

modifiziert. Die Modifikation erfolgte mit *α*-Amino-*ω*-methoxy-polyethylenglykol, Aminopropyltrimethoxysilan, Allylamin und Ferrocenylmethylamin. Die resultierenden Materialien ließen sich auf verschiedene Art praktisch anwenden, darunter nanoskalige, schwefelhaltige Polyethylenglykolpartikel in wässrigen Umgebungen. Zudem ermöglichte die PPM mit Aminopropyltrimethoxysilan und Allylamin die jeweilige Herstellung von quervernetzten Quecksilber Adsorbenzien, Schwefelbeschichtungen und hochschwefelhaltigen Netzwerken mit gezielt einstellbaren thermischen Eigenschaften. Darüber hinaus konnte durch den Einbau von Ferrocen-Gruppen elektrochemische Aktivität in das Material integriert werden. Die große Auswahl an kommerziell erhältlichen Aminen für die PPM von Aktivestern unterstreicht die Vielseitigkeit von Poly(S-*r*-NB-PFPE) als Ausgangsmaterial für spezialisierte schwefelbasierte Materialien.

Mit dem Aufkommen der computergestützten Strömungschemie in den letzten Jahren hat die Polymerchemie eine starke Entwicklung in Richtung autonomer Reaktionsführung und schneller Datenerfassung mit minimalem Benutzereingriff erfahren. Allerdings ist die Untersuchung funktioneller Monomere und ihre entsprechende PPM in diesem Kontext bislang in der chemischen Forschung unterrepräsentiert, was die Möglichkeiten zur Synthese komplexer Polymerstrukturen einschränkt. Daher wurde die RAFT-Polymerisation von PFPA und Pentafluorostyrol (PFSty) sowie deren PPM im kontinuierlichen Durchfluss untersucht. Die Polymerisation von PFPA wurde auf einer automatisierten Reaktorplattform autonom optimiert, und die Ergebnisse wurden in einem unabhängigen Flussreaktor reproduziert und bestätigt. Die PPM von Poly(PFPA) durch Amidierung konnte durch präzise Dosierung von zwei Paaren aus primären Aminen im kontinuierlichen Durchfluss exakt gesteuert werden, wobei das Modifikationsverhältnis mit einer Genauigkeit von über 90 % mittels ^{19}F- oder ^{1}H-NMR vorhergesagt werden konnte. Die RAFT-Polymerisation von PFSty wurde hingegen durch transientes *Timesweeping* kinetisch untersucht, wodurch die schnelle Bestimmung der kinetischen Propagationsraten der Polymerisation möglich war. Poly(PFSty) wurde gleichzeitig über eine *para*-Fluor-Thiol Reaktion mit zwei verschiedenen fluorierten Thiolen modifiziert. Durch Kontrolle der Flussraten der jeweiligen Edukt Ströme konnte das Modifikationsverhältnis mit einer Präzision von über 80 % eingestellt werden, wie durch ^{19}F-NMR-Spektroskopie bestätigt wurde.

Schließlich wurden die beiden oben genannten Hauptprojekte kombiniert, um die Synergie zwischen inverser Vulkanisation und Strömungschemie anhand der PPM von Poly(S-*r*-NB-PFPE) im kontinuierlichen Durchfluss zu demonstrieren. Wie durch ^{1}H-NMR-Spektroskopie nachgewiesen, konnte Poly(S-*r*-NB-PFPE) unter milden Bedingungen mit zwei Paaren primärer Amine und einer Genauigkeit von über 95 % modifiziert werden, was eine bislang unerreichte Kontrolle über invers Vulkanisierte hochschwefelhaltige Polymere darstellt.

Zusammenfassend befasst sich diese Arbeit mit dem Konzept der PPM zur gezielten Kontrolle kohlenstoff- und schwefel-basierter Polymere und demonstriert die erfolgreiche Amidierung reaktiver Ester in Poly(S-*r*-NB-PFPE) für verschiedene Anwendungen, darunter Quecksilberadsorption, Schwefelbeschichtungen und elektrochemisch aktive Materialien. Darüber hinaus wurden neuartige strömungschemische Techniken verwendet, um die RAFT-Polymerisation aktiver Monomere zu untersuchen und optimieren und eine präzise Einstellung von Polymermodifikationen mit hoher Genauigkeit zu ermöglichen. Die Kombination aus inverser Vulkanisation und Strömungschemie stellt einen neuartigen Ansatz beispiellosen Kontrolle über hochschwefelhaltige Polymere dar und erweitert deren potenziellen Einsatz für spezialisierte Anwendungen.

Abstract

Elemental sulfur, a waste product from industrial oil and gas refining is currently produced with a global surplus of 12 Mt per year. Consequently, sulfur is stored in overground deposits where it slowly leaks into the earth and is of no according practical use. In 2013, a chemical technique has been invented which is capable to create long-lasting and shape-retaining polymeric materials with sulfur contents up to 90 wt%. This technique, called inverse vulcanization, has since revolutionized polymer material science by its facile and straightforward conversion of cheap elemental sulfur into high performance polymers. However, due to the harsh reaction conditions, only poor control over polymer structures and properties is achieved by conventional inverse vulcanization and the number of polymerizable comonomers is limited. Therefore, chemical approaches are necessary in order to exert control over polymer structures and material properties made by inverse vulcanization.

The strategy employed in this thesis relies on post-polymerization modification (PPM) of high-sulfur content polymers rather than altering the polymerization itself. Based on the PPM of active esters, a well-established strategy in conventional carbon-based polymer chemistry, polymer structures are altered *via* amidation of these active esters in order to tune the properties of a reactive parent polymer towards various applications.

Pentafluorophenyl acrylate (PFPA) and its all-*cis*-hydrogenated counterpart all-*cis*-2,3,4,5,6-pentafluorocyclohexyl acrylate (PFCHA) were reacted with elemental sulfur and while PFPA was found to not withstand the harsh reaction conditions, PFCHA was able to form a stable sulfur copolymer with triethoxyvinylsilane and a final sulfur content of 61 wt%. This copolymer did not undergo amidation but was successfully employed as cathode material in Li-S batteries where it beneficially influenced the batteries capacity retention and suppressed self-discharge.

As an alternative to PFPA, norbornenyl-pentafluorophenyl ester (NB-PFPE) was subjected to inverse vulcanization and the resulting polymer was modified by amidation using four different primary amines under mild conditions. Modification with *α*-amino-*ω*-methoxy polyethylene glycol, aminopropyl trimethoxy silane, allylamine, and ferrocenyl methylamine. The resulting materials had diverse applications, including nanoscale sulfur-containing poly(ethylene glycol) particles in aqueous environments.

Additionally, PPM with aminopropyl trimethoxy silane and allylamine enabled the creation of cross-linked mercury adsorbents, sulfur surface coatings, and high-sulfur-content networks with predictable thermal properties, respectively. In addition, electrochemical activity could be introduced into the material by incorporation of ferrocene groups. The wide range of commercially available amines for PPM highlights the versatility of poly(S-*r*-NB-PFPE) as a precursor polymer for specialized sulfur-based materials.

With the emergence of computer-assisted flow-based chemistry in recent years, polymer chemistry has experienced a dramatic upswing in autonomous reaction design and rapid data acquisition with low user intervention. However, the investigation of functional monomers and PPM used in this context remains underrepresented to this day which limits the chemical possibilities of researchers for creating of complex polymer structures. Thus, the RAFT polymerization of PFPA and pentafluorostyrene (PFSty) and their respective PPM was investigated in continuous flow. The polymerization of PFPA was autonomously optimized in an automated reactor platform and the results were recreated and validated in an independent different flow reactor. PPM of poly(PFPA) via amidation could be precisely controlled by exact dosing of two pairs of primary amines in continuous flow and the ratio of modification could be predicted with over 90 % accuracy using ^{19}F NMR or ^{1}H NMR, respectively. The RAFT polymerization of PFSty on the other hand was kinetically investigated by transient timesweeping which allowed rapid determination of kinetic propagation rates of the polymerization. Poly(PFSty) was modified via *para*-fluoro-thiol reaction with two different fluorinated thiols at the same time. By controlling the flow rates of the respective reactant stream, the ratio of modification could be tuned with a precision of over 80 % using mixing and dosing in continuous flow and ^{19}F NMR spectroscopy.

Consequently, the two major projects mentioned above were combined in order to demonstrate the synergy between inverse vulcanization and flow chemistry through PPM of poly(S-*r*-NB-PFPE) in continuous flow. As shown by ^{1}H NMR spectroscopy, poly(S-*r*-NB-PFPE) could be modified with two pairs of primary amines under mild conditions and with accuracies of over 95 % which represents unprecedented control over high sulfur content polymers made by inverse vulcanization.

In summary, this thesis explores the concept of PPM to fine-tune carbon- and sulfur-based polymers, demonstrating the successful amidation of reactive esters in poly(S-

r-NB-PFPE) for diverse applications, including mercury adsorption, sulfur coatings, and electrochemically active materials. Additionally, this work utilized novel flow chemistry techniques, in order to optimize the RAFT polymerization of active monomers and enabling precise control over polymer modifications with high accuracy. The combination of inverse vulcanization and flow chemistry presents a novel approach to achieving unprecedented control over high sulfur-content polymers, expanding their potential for specialized applications.

Table of Contents

List of Figures

List of Schemes

List of Tables

List of Appendices

List of Abbreviations

Å	Angstrom (10^{-10} m)
a.t.	ambient temperature
AA	allylamine
ADMET	acyclic diene metathesis
AI	artificial intelligence
AIBN	azobisisobutyronitrile
Amino-mPEG	*α*-amino-*ω*-methoxy polyethylene glycol
AOA	acetone oxime acrylate
APTMS	aminopropyl trimethoxy silane
et al.	*et alii* (and others)
ATR FT-IR	attenuated total reflection Fourier-transform infrared
ATRP	atom transfer radical polymerization
BA	benzylamine
BAAm	benzyl acrylamide
BDE	bond-dissociation energy
br	broad (IR)
cat.	catalyst
CBCDMPC	2-cyano-2-butyl-4-chloro-3,5-dimethyl-1H-pyrazole-1-carbodithioate
CDCTPA	4-cyano-4-[[(dodecylthio) carbonothioyl]thio] pentanoic acid
CHA	cyclohexyl acrylate
CHIP	chalcogenide hybrid inorganic/organic polymer
CLMOO	closed-loop multi-objective optimization
CPDT	cyanopropyl dodecyl trithiocarbonate
CRP	controlled radical polymerization
CSIRO	Commonwealth Scientific and Industrial Research Organisation
CuAAC	copper(I)-catalyzed alkyne-azide cycloaddition
CV	cyclic voltammetry
CV-AAS	cold-vapor atom absorption spectroscopy
Δ	thermal energy

Đ	dispersity
d	days
DBU	1,8-diazabicyclo[5.4.0]undec-7-ene
DCC	*N*,*N'*-dicyclohexylcarbodiimide
DCM	dichloromethane
DCP	dynamic covalent polymerization
DCPD	dicyclopentadiene
DI	deionized
DIB	diisopropenyl benzene
D_{Li^+}	diffusion coefficient of lithium ions
DLS	dynamic light scattering
DMAc	*N,N*-dimethylacetamide
DMAP	4-dimethylaminopyridine
DME	1,2-dimethoxyethane
DMF	*N,N*-dimethylformamide
DMSO	dimethyl sulfoxide
DOL	1,3-dioxolane
DoPAT	2-(dodecylthiocarbonothioylthio) propanoic acid
DSC	differential scanning calorimetry
DVB	divinylbenzene
E. coli	*Escherichia coli*
e.g.	*exempli gratia* (for example)
EA	elemental analysis
EIS	electrochemical impedance spectroscopy
eq	equivalents
etc.	*et cetera* (and so forth)
EtOAc	ethyl acetate
EtOH	ethanol
FBA	4-fluorobenzyl amine
FBAm	4-fluorobenzyl amide
FBM	4-fluorobenzyl mercaptan
FcMA	ferrocenyl methyl amine
FRP	free radical polymerization
GCPL	galvanostatic cycling with potential limitation

HFIPA	hexafluoro isopropyl acrylate
h	hours
HPLC	high-performance liquid chromatography
HR-MS	high-resolution mass spectrometry
hν	photon energy
i.e.	*id est* (meaning)
IR	infrared
IUPAC	International Union of Pure and Applied Chemistry
IV	inverse vulcanization
k_{act}	rate constant of activation
K_d	distribution coefficient
k_{deact}	rate constant of deactivation
k_{prop}	rate constant of the polymer propagation
LED	light-emitting diode
LHC	Latin hypercube
Li-S	lithium-sulfur
LSB	lithium-sulfur battery
m	medium (IR) / multiplet (NMR)
MeOH	methanol
MIA	1-methyl imidazole
ML	machine learning
M_n	number average molecular weight
M_p	peak molecular weight
MRI	magnetic resonance imaging
Mt	megatons (10^9 kg)
M_w	weight average molecular weight
NASA	National Aeronautics and Space Administration
NB	norbornenyl
NBMA	norbornenyl methyl amine
NBMAAm	norbornenyl methyl acrylamide
NB-PFPE	norbornenyl-pentafluorophenyl ester
net	*network*
NHS	*N*-hydroxysuccinimide
NHSA	*N*-hydroxysuccinimide acrylate

NMP (polymerization)	nitroxide-mediated polymerization
NMP (solvent)	*N*-metyhl-2-pyrrolidone
NMR	nuclear magnetic resonance
ORMOCHALC	organically modified chalcogenides
p	conversion
PAS	polyarylsulfone
PEDOT	poly(3,4-ethylenedioxythiophene)
PEEK	polyether ether ketone
PEG	poly(ethylene glycol)
PES	polyethersulfone
PFA	perfluoro alkoxy alkane polymer
PFCHA	all-*cis*-2,3,4,5,6-pantafluorocyclohexyl acrylate
PFP	pentafluorophenol
PFPA	pentafluorophenyl acrylate
PFPMA	pentafluorophenyl methacrylate
PFSty	pentafluorostyrene
PFT	*para*-fluoro-thiol
PISA	polymerization-induced self-assembly
PLED	polymer light emitting diodes
PMMA	poly(methyl methacrylate)
PNPMA	*para*-nitrophenyl methacrylate
PPM	post-polymerization modification
ppm	parts per million
PPNCl	bis(triphenylphosphoranylidene) ammonium chloride
PS	polystyrene
PSS	poly(styrene sulfonic acid)
Q_e	uptake capacity
r	*random*
RAFT	reversible addition-fragmentation chain-transfer
RDRP	reversible-deactivation radical polymerization
Red.	reduction
RI	refractive index
RLH	robotic liquid handler

rpm	rounds per minute
s	strong (IR) / singlet (NMR)
SAA	salicylic acid acrylate
SD	standard deviation
SEC	size exclusion chromatography
SEM	scanning electron microscopy
S_nAr	nucleophilic aromatic substitution
SUMI	single-unit monomer insertion
$T_{5\%}$	decomposition temperature at 5 % weight loss
$T_{95\%}$	decomposition temperature at 95 % weight loss
TCPA	trichlorophenyl acrylate
TEA	triethylamine
TEM	transmission electron microscopy
TEVS	triethoxyvinylsilane
TFBA	3,4,5-trifluorobenzylamine
TFBAAm	3,4,5-trifluorobenzyl acrylamide
TFBM	4-(trifluoromethyl)benzyl mercaptan
TFMBA	4-(trifluoromethyl)benzylamine
TFMBAAm	4-(trifluoromethyl)benzyl acrylamide
TFMBAm	4-(trifluoromethyl)benzylamide
T_b	boiling temperature
T_g	glass transition temperature
TGA	thermogravimetric analysis
THF	tetrahydrofuran
T_m	melting temperature
ToF-SIMS	time-of-flight secondary ion mass spectrometry
t_r	residence time
TSEMO	Thompson sampling efficient multi-objective optimization
TT	transient timesweep
TTMA	thiazolidine-2-thione methacrylate
UK	United Kingdom
USA	United States of America
vs	very strong (IR)
vw	very weak (IR)

w	weak (IR)
X	electronegativity (Pauling)
Z_{im}	imaginary component of the impedance
$Zn(DTC)_2$	zinc diethyldithiocarbamate
Z_{re}	real component of the impedance

1 Introduction

The ever-growing production of fossil fuels that primarily drive our modern society to this date has led to the accumulation of 80 Mt of elemental sulfur by desulfurization of natural oil and gas in 2024.[1,2] Despite its abundance and associated low-cost, the use of elemental sulfur for industry applications is mainly limited to the production of sulfuric acid,[3] alongside minor demands in cosmetic,[4] fertilizer,[5] and rubber industry.[6] The imbalance between production and consumption of elemental sulfur gave rise to a phenomenon termed ‘excess sulfur problem’ necessitating stockpiling of elemental sulfur in overground deposits.[7,8] In 2013, CHUNG and coworkers pioneered a synthetic strategy, called ‘inverse vulcanization’ (IV), to make use of elemental sulfur as feedstock for polymeric materials with unique properties which can consist of up to 90 wt% of pure elemental sulfur.[8] Therein, elemental sulfur is classically mixed with an unsaturated organic comonomer, often referred to as ‘cross-linker’, and heated above the melting temperature of sulfur of 120 °C to facilitate the copolymerization of polysulfides with the organic cross-linker (for detailed information about the inverse vulcanization process refer to **Chapter 2.2** Inverse vulcanization). Owing to the high sulfur content of IV materials, various characteristic applications have been identified which are ongoing fields of research. Most prominently, IV materials have been proven to be efficient cathode materials in lithium-sulfur batteries (LSBs),[8,9] heavy metal adsorbents for wastewater remediation,[10–12] healable materials,[13–15] infrared (IR) lenses,[16] and other more niche applications.[17–19]

Despite the versatile applicability, low cost, and straightforward synthesis associated with IV materials, major challenges and questions remain in order to elevate IV from laboratory-scale research to a broader industry-scale research and development level. Notably, the ability to reliably characterize polymers derived from IV is a major challenge owing to the limited applicability of established polymer analysis methods such as size exclusion chromatography (SEC) or nuclear magnetic resonance (NMR) spectroscopy caused by the lack of analysis standards, poor solubility of materials, and a fundamental lack of understanding of the rection mechanism and resulting polymer structure.[20,21,22] Although several publications claim IV to be a step towards a greener and more sustainable polymer landscape owing to the waste-like nature of elemental sulfur as essential feedstock, a full life cycle assessment from production of base materials to end-of-life recycling of IV materials remains elusive.[23] Unlike the

extensively developed polymer chemistry of carbon-based monomers, managing key parameters of inverse vulcanized polymers, such as molar mass, solubility, and thermomechanical properties, remains challenging and is highly sensitive to reaction conditions and choice of cross-linker.[24] Furthermore, the application of inverse vulcanized polymers is constrained by the limited availability of functional comonomers suitable for the polymerization itself. Achieving control over the properties and structure of these polymers remains difficult for current research, largely due to the dynamic behavior of sulfur-sulfur bonds and the high temperatures required for inverse vulcanization reactions.[25]

One strategy for producing functional inverse vulcanized polymers or customizing their properties for specific applications is the post-polymerization modification (PPM) of reactive precursors. Early works in this area demonstrated methods such as nucleophilic substitution of pendant groups,[26] photochemical[27] and FRIEDEL-CRAFTS cross-linking,[28] dynamic covalent polymerization (DCP),[29,30] and silane polycondensation.[24,31] While these advancements have broadened the scope of IV and improved control over material properties, the creation of a versatile and fundamental synthetic platform for systematic and efficient PPM remains challenging.

However, with the development of automated laboratory management and machine learning (ML), data-driven polymer and material science have experienced a dramatic upswing and a paradigm shift from batch to flow-based reaction and laboratory management in recent years.[32,33] Where conventional batch chemistry conducted in a round bottom flask falls short, flow chemistry excels: reactions under high pressure, access to short-lived species, superior mass and heat transfer, scalability, reproducibility, increased safety, precision, real time feedback for optimization, and rich data sets are key advantages of flow over batch chemistry.[34] Notably, the integration of inline analysis with computer-assisted feedback and optimization algorithms is one of the major advancements in the chemical field in recent years.[35] However, flow polymer chemistry is still mostly limited to non-functional monomers such as acrylates,[36,37–39] acrylamides,[40,41] and styrene.[42] Investigation of complex functional building blocks for modifiable, advanced polymers remains underrepresented in the field of flow chemistry while the promising method of IV has, as of 2024, not been employed in a flow chemistry context. To fill this gap, the identification and development of platform polymers that are able to efficiently undergo PPM in continuous flow is vital. Consequently, this thesis will offer insights into how the

approach of PPM can combine the fields of IV and flow polymer chemistry to introduce control over the properties of IV materials on one hand and advance the complexity of carbon-based flow polymer chemistry on the other.

2 Theoretical Background

The current chapter provides a brief introduction into the polymerization and PPM techniques used in this thesis. Polymerization methods are focused on IV and reversible addition-fragmentation chain-transfer (RAFT) polymerization while PPM techniques via active ester substitution and *para*-fluoro-thiol reaction are discussed in detail. Finally, a brief introduction and general considerations about relevant flow polymer chemistry techniques is provided.

2.1 The Element Sulfur

Sulfur, with the chemical symbol S and atomic number 16, is a nonmetal element belonging to Group 16 (the chalcogens) of the periodic table. It is a vital element for life and has been recognized since antiquity, often associated with gunpowder, fire and brimstone due to its distinctive yellow color and pungent smell when burned.[43,44] Sulfur's unique properties and versatile chemistry make it essential in various natural and industrial processes.[45]

2.1.1 Abundance and Production

Sulfur is one of the most abundant elements in the Earth's crust, atmosphere, and biosphere. It ranks as the 10th most abundant element in the universe and the 16th most abundant in the Earth's crust, comprising approximately 0.035 wt%.[46] Sulfur occurs in several forms in nature. It is most commonly found as sulfide minerals such as pyrite (FeS_2), galena (PbS), sphalerite (ZnS), and sulfate minerals such as gypsum ($CaSO_4 \cdot 2H_2O$) and baryte ($BaSO_4$). Elemental sulfur is also present in volcanic regions, where it sublimates from volcanic gases which causes the characteristic yellow coloration of the Jupiter moon Io and the Grand Prism Lake in the Yellowstone National Park (refer to **Figure 1**). In the atmosphere, sulfur exists primarily as sulfur dioxide (SO_2), a byproduct of volcanic activity and anthropogenic emissions.[47] In biological systems, sulfur is an essential element, playing a critical role in amino acids (such as cysteine and methionine), vitamins (like thiamine and biotin), and cofactors. It is also a key component of sulfur-containing proteins and enzymes that facilitate numerous biochemical processes.[43,48]

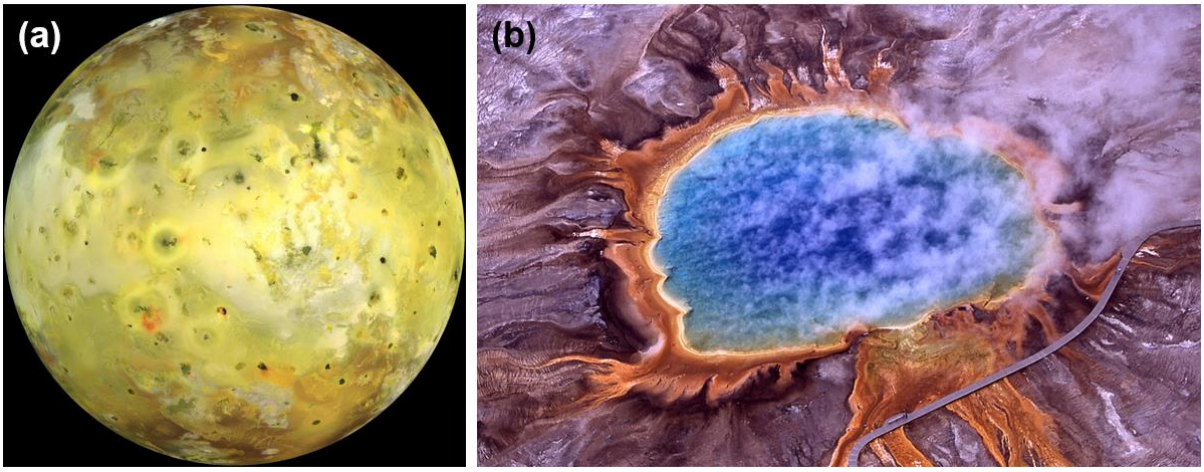

Figure 1. (a) Photograph of Jupiter's moon Io taken by the Galileo spacecraft from the National Aeronautics and Space Administration (NASA) in 1999. Image from NASA (public domain). (b) The Grand Prismatic Spring located in Yellowstone National Park (USA) in 2011. Image from the National Park Service (public domain). The yellow coloration is caused by naturally occurring sulfur and sulfite species.

Up until the early 19th century, the prominent source of sulfur was located on the island of Sicily where it was extracted from volcanic soil.[49] With the industrialization in the mid-19th century came an increasing demand for sulfur along with methods for cheaper extraction, rendering the Sicilian source non-practical.[50] Today, the global production of sulfur primarily involves the recovery of sulfur from fossil fuels and natural gas. The majority of elemental sulfur is derived from the purification of natural gas and crude oil, where sulfur compounds are removed to prevent the formation of harmful emissions during combustion. This process, known as the CLAUS-process, converts hydrogen sulfide (H_2S) into elemental sulfur. In a two-step process, H_2S is first oxidized with O_2 to SO_2 and H_2O. This mixture is then catalytically converted to sulfur and water in a subsequent reaction (refer to **Scheme 1**). The CLAUS-process is highly efficient and yields elemental sulfur with very high purity of around 99.5 %.[47]

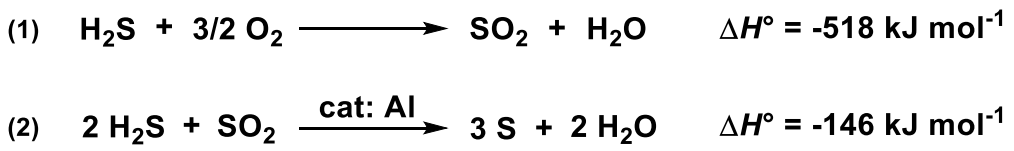

Scheme 1. Chemical equations of the two-step CLAUS-process for sulfur production. In the first step, sulfur is oxidized with oxygen to SO_2 which is then reduced to elemental sulfur under presence of a catalyst, here aluminum.

Another significant source of sulfur is the mining of sulfide minerals, such as pyrite, by the FRASCH-process. Heated water is pumped into a deposit of sulfur-containing

minerals, where it melts the sulfur which separates from mineral impurities. Air is injected to the molten sulfur which foams and is propelled to the surface due to its lower density (refer to **Figure 2**).[47] The FRASCH-process has declined in popularity due to environmental concerns and the abundance of sulfur recovered from industrial processes.[51]

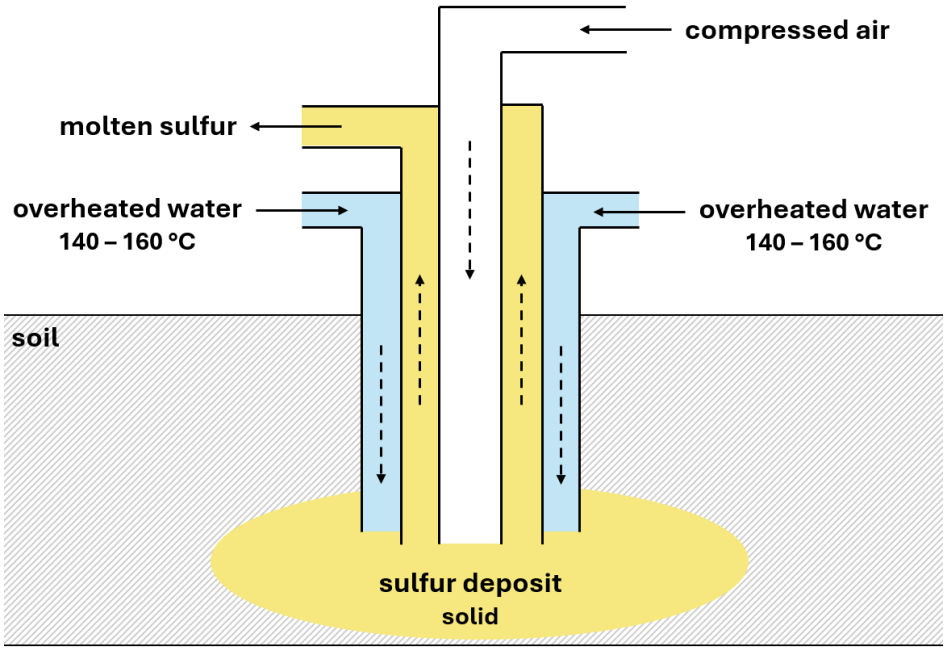

Figure 2. Schematic visualization of the Frasch-process for geological extraction of sulfur with water and compressed air. Figure redrawn from literature.[51]

Secondary sources of sulfur include the recovery from industrial waste streams and flue gases, where sulfur compounds are captured to reduce air pollution and repurposed for industrial use.[52]

The production of sulfur is critical for several industries, particularly in the manufacture of sulfuric acid (H_2SO_4), one of the most widely used industrial chemicals. Approximately 85 % of produced sulfur are further processed to H_2SO_4.[53] Sulfuric acid is essential in the production of phosphoric acid (H_3PO_4), fertilizers, petroleum refining, mineral processing, and chemical synthesis.[2] Consequently, the demand for sulfur is closely tied to agricultural and industrial activity. However, as of 2024, the global annual production of sulfur has exceeded 80 Mt and after approximately 85 % of those being processed to H_2SO_4, the world is faced with an overproduction of approximately 12 Mt each year.[2] This has led to a phenomenon termed ‘excess sulfur problem’ and the creation of overground sulfur stockpiles, causing environmental and health concerns

by acidic drainage[54] but also motivate researchers to put further use to this abundant resource (refer to **Figure 3**).[17,22,23,50,55,56]

Figure 3. Overground sulfur stockpile located in Vancouver, Canada. Image recreated from literature.[8] Copyright 2013, Nature Publishing Group.

2.1.2 The Chemistry of Sulfur

In its elemental form, sulfur commonly exists as cyclic, covalently bound S_8 molecules, which form a warped ring structure with yellow orthorhombic crystal structure (α-S). At 96 °C, sulfur transforms from an orthorhombic to a monoclinic crystal structure, called β-S. The natural melting temperature (T_m) of sulfur is around 120 °C, where it forms a yellow melt comprised of eight-membered rings with low viscosity (λ-S). Keeping the sulfur melt above its melting point leads to the formation of non-eight-membered sulfur rings (π-S) alongside linear polysulfides (μ-S). It is at 159 °C where the viscosity of a sulfur melt increases with temperature, due to the formation of highly viscous long chain polysulfides. The color changes from yellow, over orange, to deep brown with increasing temperature and viscosity. Boiling of sulfur occurs at the boiling temperature (T_b) of 445 °C with the gas phase being comprised of S_2 – S_8 molecules. S_1 atoms dominate the gas phase above 2200 °C (refer to **Scheme 2**).[53,57]

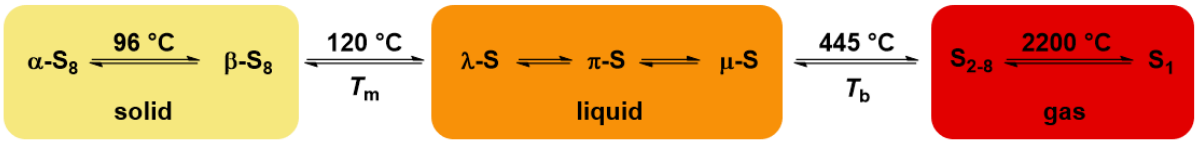

Scheme 2. States of sulfur allotropes in solid, liquid, and gaseous phase.

Given the complex composition of gaseous sulfur, the phase diagram of elemental sulfur is still a topic of debate in the scientific community.[58] Sulfur is known for its rich and diverse chemistry, which stems from its ability to exist in multiple oxidation states ranging from -2 to +6. Due to similar covalent radii and electronegativity (*X*), the chemical reactivity of sulfur is more comparable to that of selenium (Se) and tellurium (Te) than that of oxygen (O) (refer to **Table 1**).[59]

Table 1. Covalence radii, electronegativities, valence electron configuration, and abundance in the Earth's crust of oxygen, sulfur, selenium, and tellurium, respectively.[46]

Element symbol	O	S	Se	Te
Covalence radius / Å	0.64	1.04	1.18	1.37
X (PAULING)	3.44	2.58	2.55	2.10
Valence electron configuration	[He]2$s^2$2p^4	[Ne]3$s^2$3p^4	[Ar]3d^{10}4$s^2$4p^4	[Kr]4d^{10}5$s^2$5p^4
Abundance / wt%	46.1	$3.5 \cdot 10^{-2}$	$5.0 \cdot 10^{-6}$	$1.0 \cdot 10^{-7}$

For sulfur atoms, to obtain the most stable noble gas configuration of argon [Ne]3$s^2$3p^6, they are required an oxidation state of -2, explaining the tendency of sulfur to form inorganic salts such as Li_2S, ZnS, PdS, and HgS or bivalent organic compounds such as thioethers, thioesters, and disulfides. However, sulfur is known to adopt every oxidation state from -II to +VI with the most common being -2, +4, and +6, caused by the high stability of the resulting electron configurations of [Ne]3$s^2$3p^6/[Ar], [Ne]3s^2, and [He]2$s^2$2p^6/[Ne], respectively.[57] Elemental sulfur is relatively stable under standard conditions but reacts readily with oxygen, producing sulfur dioxide (SO_2), a precursor to sulfuric acid.[54] Sulfur exhibits high reactivity with metals, forming metal sulfides, which are important ores for extracting metals such as iron, copper, and zinc, but also reacts with nonmetals like hydrogen to form hydrogen sulfide (H_2S), a toxic gas with the characteristic odor of rotten eggs.[47] In the presence of halogens, sulfur forms compounds such as sulfur dichloride (SCl_2) and sulfur hexafluoride (SF_6),[57] the latter

being a potent greenhouse gas widely used as an electrical insulator.[60] In aqueous environments, sulfur compounds play an important role in the form of sulfuric oxygen anions such as sulfites (SO_3^{2-}), sulfates (SO_4^{2-}), thiosulfates ($S_2O_3^{2-}$), and tetrathionates ($S_4O_6^{2-}$) in chemical and biological systems.[47,61] Sulfites are reducing agents and utilized as preservatives in the food and beverage industry, while sulfates are stable and commonly found in natural water systems.[62]

The reactivity of sulfur enables its use in various industrial applications, from vulcanizing rubber and manufacturing dyes to producing pesticides and pharmaceuticals. Its chemical versatility ensures that sulfur remains a cornerstone of modern chemistry and industry.[44]

2.1.3 Sulfur in polymers

Beyond its elemental form and traditional uses, sulfur has found significant applications in polymer chemistry, where it contributes to the synthesis and properties of diverse polymeric materials. This sections briefly introduces the role of sulfur in carbon-based polymer chemistry with the limitation to polymeric structures with sulfur in the backbone, rather than in the pendant chain. This section is subdivided into polysulfides, thioethers and their oxides, thiophenes, and thiocarbonyls (refer to **Figure 4**).

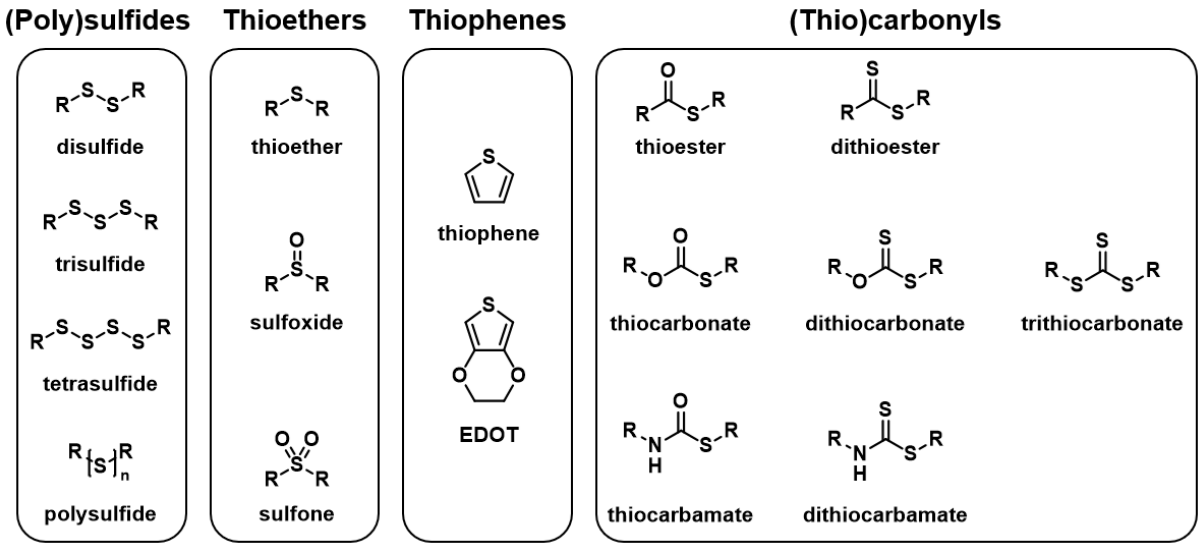

Figure 4. Chemical motifs of organic sulfur-containing functional groups categorized into (poly)sulfides, thioethers, thiophenes, and (thio)carbonyls.

2.1.3.1 (Poly)sulfides

Polysulfides are a class of polymers characterized by the presence of sulfur-sulfur (S-S) bonds in their backbone with the general chemical formula R-S_n-R (R = alkyl or aryl rest, R ≠ H, n ≥ 3).[63] Disulfides can be readily synthesized via oxidation of thiols (1) or their condensation with for example sulfenic acids (2) (refer to **Scheme 3**). Higher order oligosulfides are available through the reaction of disulfur dichloride (S_2Cl_2) with metal sulfides (3) or thiols (4). Polysulfides with higher sulfur ranks can be synthesized directly from elemental sulfur by insertion of S_8 into disulfide bonds (5) or by reaction with sodium sulfide (Na_2S) (6).[44,57,64]

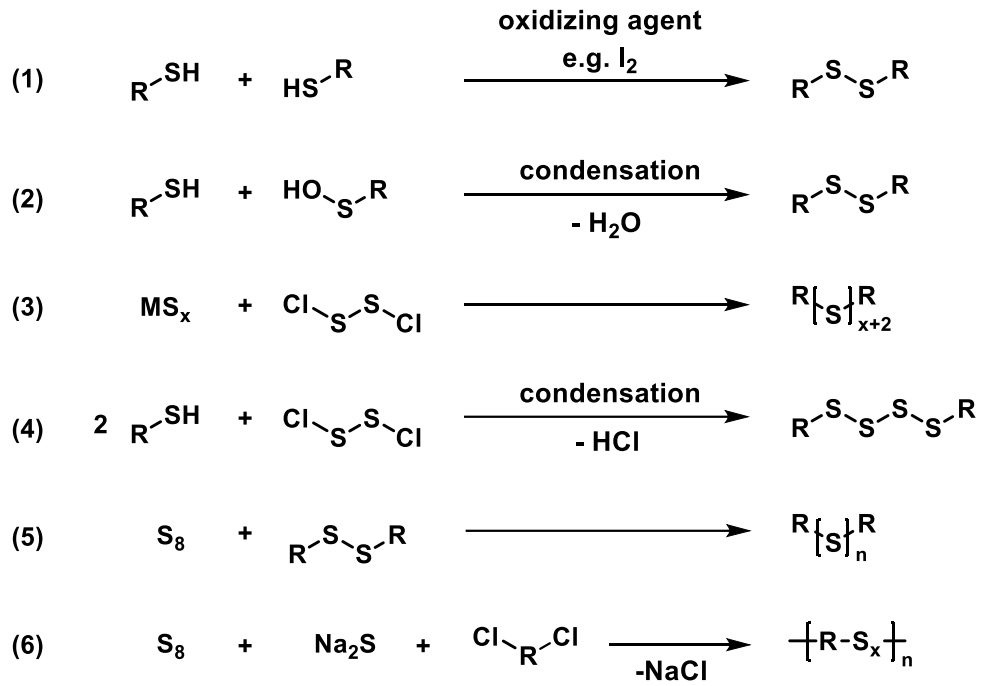

Scheme 3. Exemplary reactions schemes for various synthesis routes of organic sulfides and polysulfides. R = organic rest.

Polysulfides exhibit unique properties such as flexibility, chemical resistance, and impermeability to gases, making them valuable in various applications.[65] One of the most prominent uses of polysulfides is in sealants and adhesives, particularly in the aerospace and construction industries.[66] Their excellent resistance to fuels, oils, and weathering ensures durability in demanding environments. Additionally, polysulfides are employed in the manufacture of rubber materials and as additives to enhance the performance of other polymers.[67] From a chemical perspective, the low binding energy of S-S bonds imparts self-healing properties to polysulfides. When mechanically damaged, the S-S bonds can undergo reversible cleavage and reformation, enabling the material to restore its structural integrity. This attribute has

spurred research into polysulfides for advanced applications, including smart coatings, and self-healing materials.[68]

2.1.3.2 Thioethers

Thioethers, also known as sulfides in organic chemistry, are organic compounds containing a sulfur atom bonded to two carbon atoms (C-S-C). In polymer chemistry, thioethers serve as key structural units that impart unique chemical and physical properties to the resulting materials. Thioether-based polymers are synthesized via various methods, including the polycondensation of dithiols with dihalides or the thiol-ene click reaction.[69]

Thioether-containing polymers are notable for their enhanced thermal and oxidative stability compared to their oxygen analogs, ethers.[70] Thioether polymers find use in high-performance applications such as flame-retardant materials.[71]

The chemical versatility of thioethers also allows for functionalization, most notably conversion into sulfoxides and sulfones *via* selective oxidation with *tert*-butyl hydroxy peroxide (*t*-BuOOH) or hydrogen peroxide (H_2O_2), enabling the design of polymers with tailored properties for specific applications.[72] Compared to thioether-containing polymers, polysulfoxides are permeable to polar compounds[73] and can be used as polymeric oxidizing agents,[74] compatibilizers,[75] and stationary phases in high-performance liquid chromatography (HPLC) columns.[76] Polysulfones were commercialized in the late 1960s and early 1970s as aromatic resins containing sulfone and ether linkages in an aromatic polymer backbone, such as polyethersulfone (PES) and polyarylsulfone (PAS) (refer to **Figure 5**).[77] They were synthesized by FRIEDEL-CRAFTS electrophilic aromatic substitution or nucleophilic aromatic substitution of activated aromatic dihalides and show good resistance towards creep and stress cracking, good thermoplastic properties, low water absorption, and a high glass transition temperature (T_g) in the range of 200 °C.[78] Due to the presence of deactivating sulfone groups in the backbone, polysulfones exhibit high resistance to oxidation and thermal exposure.[79] In recent years, polysulfones have gained increased interest as application in proton exchange membranes.[80]

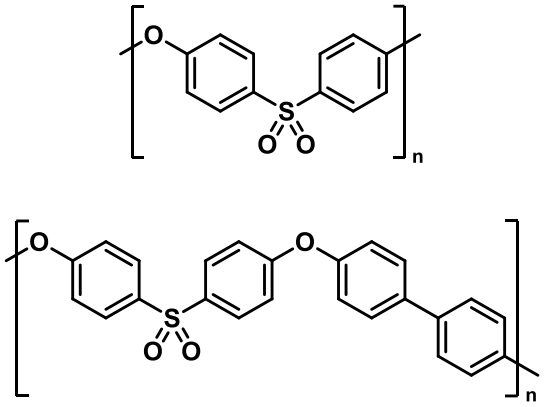

Figure 5. Chemical structures of PES (top) and PAS (bottom).

2.1.3.3 Thiophenes

Thiophenes are heterocyclic compounds containing a sulfur atom within a five-membered aromatic ring. These structures are of significant interest in polymer chemistry due to their conjugated nature, which imparts electronic conductivity and optical properties.[81] Polythiophenes are synthesized through polymerization methods such as oxidative coupling,[82] GRIGNARD metathesis,[83] and electrochemical polymerization.[84] These materials exhibit unique properties, including flexibility, lightweight, and tunable electronic conductivity, making them ideal for use in organic solar cells and light-emitting diodes (LEDs).[85,86]

The incorporation of functional groups into the thiophene ring enables further control over the electronic properties of polythiophenes. For instance, alkyl or alkoxy substituents can enhance solubility and processability, while electron-withdrawing groups can modulate the bandgap for specific electronic applications.[87] One major advancement of applicability of conductive polymers came with the invention of poly(3,4-ethylenedioxythiophene) (PEDOT) in 1989 by the BAYER AG.[88] While the oxidation of asymmetrically substituted thiophene derivatives yields polymers with irregular head-to-tail, head-to-head, and tail-to-tail connection, this issue does not need to be considered when polymerizing symmetric compounds.[86] PEDOT does not undergo undesired *α*,*β*- and *β*,*β*-coupling withing the polymer backbone and was found to form very stable, transparent, and thin films with outstanding conductivity (ca. 300 S cm^{-1}). Doping PEDOT with poly(styrene sulfonic acid) (PSS), circumvents the poor solubility of pure PEDOT, making PEDOT:PSS the single most successful conductive polymer that is commercially available in aqueous dispersion and is widely used in polymer light emitting diodes (PLEDs),[89] sensors,[90] solid electrolytes in

energy storage systems,[91] and other fields where organic conductors play a vital role (refer to **Figure 6**).[92]

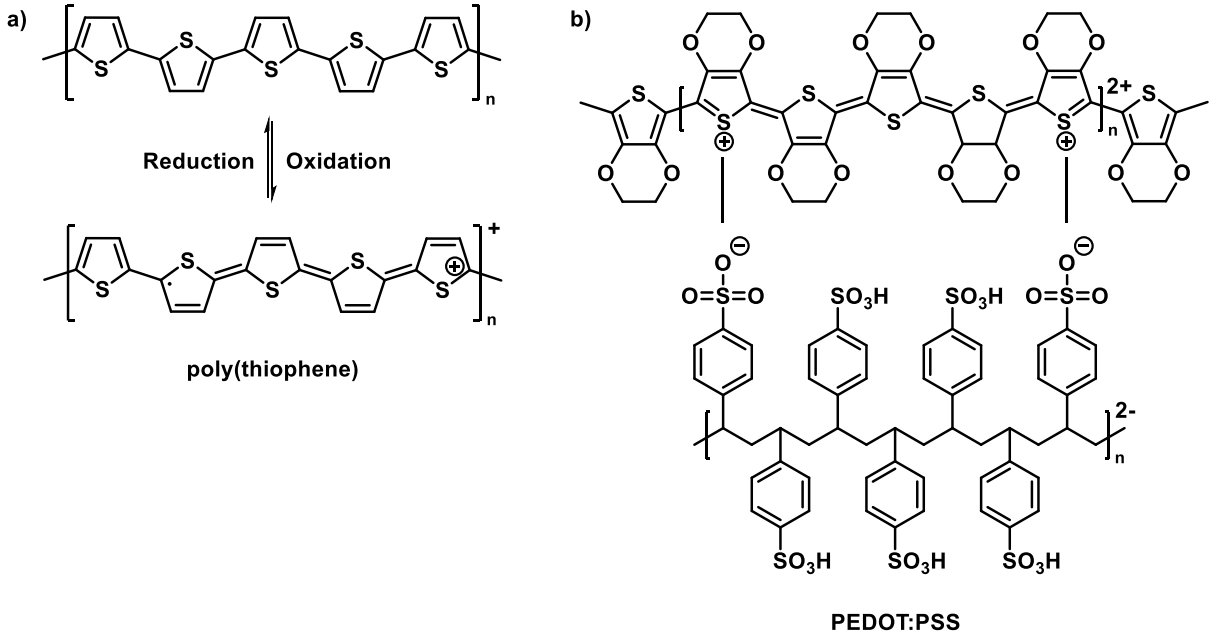

Figure 6. Proposed oxidized and reduced molecular structures of poly(thiophene) (a) and PEDOT:PSS (b). In PEDOT:PSS the coordination with sulfonic acid groups prevents interpolymer complexation and provides solubility. Redrawn after reference. [93]

2.1.3.4 (Thio)carbonyls

In the field of thiocarbonyls, three groups are of special interest: (i) thioesters, (ii) thiocarbonates, (iii) and thiocarbamates. All these polymer classes can be subdivided into mono-, di-, and trithio (only carbonate) derivatives, depending on the amount of oxygen atoms substituted with sulfur. It needs to be noted that the naming of thiocarbonyl compounds is ambiguous in regard of position of the sulfur-substituted oxygen atom in a given structure. For polymonothioesters, the term polythionoester is used to indicate the double bound sulfur atom in the thiocarbonyl group,[94] however, according to the IUPAC Goldbook both RC(=O)SH and RC(=S)OH are monothiocarboxylic acids with no differentiation between thioacid or thionoacid.[95] Generally, in organic chemistry thiocarbonyls are molecules containing a carbon-sulfur double bond (C=S), analogous to carbonyls (C=O). However, due to clarity considerations, the general group of sulfur substituted carbonyl compounds is summarized as thiocarbonyls in this chapter, regardless of the position of sulfur atom. Generally, polythioesters are synthesized via ionic ring-opening polymerization of

thiolactones/thionolactones,[96] or enzymatic polymerization routes (refer to **Scheme 4**).[97]

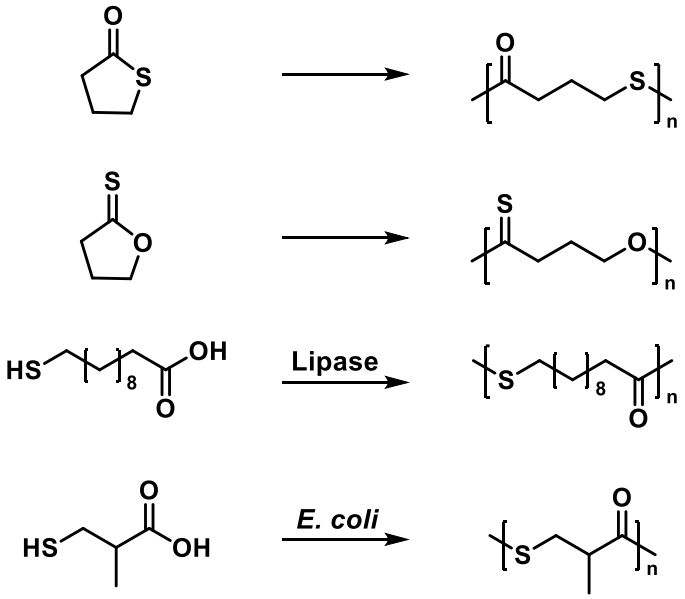

Scheme 4. Exemplary reactions schemes for various synthesis routes of polythiolesters and polythionoeters from thiolactones, thionolactones, and thiocarboxylic acids, respectively.

Polythiocarbonates are the sulfur analogues of polycarbonates and include mono-, di-, and trithiocarbonates. There are various strategies to synthesize polythiocarbonates, depending on the desired degree of sulfuration and position of sulfur atoms (refer to **Scheme 5**). In general, two main routes have been established to effectively create polythiocarbonates. Firstly, they can be synthesized via polycondensation of diols or dithiols with thiophosgene or phosgene, respectively (1 and 2).[98] The second method is the anionic ring-opening polymerization of ethylene oxide or ethylene sulfide derivatives in combination with carbon disulfide (CS_2) or carbonyl sulfide (COS), respectively (3).[99] However, the formation of cyclic low molecular mass byproducts is a common issue occurring during the polymerization of ethylene sulfide with CS_2 which can in turn be overcome depending of the choice of catalyst.[100] Poly(propylene trithiocarbonate) (4) with its exceptionally high sulfur content of around 64 wt% is, to this day, the polymer with the highest sulfur content at a well-defined repeating unit. Due to the high sulfur content, the refractive index of poly(propylene trithiocarbonate) is very high at 1.78 at 633 nm, imparting possible applications in optical lenses.[100]

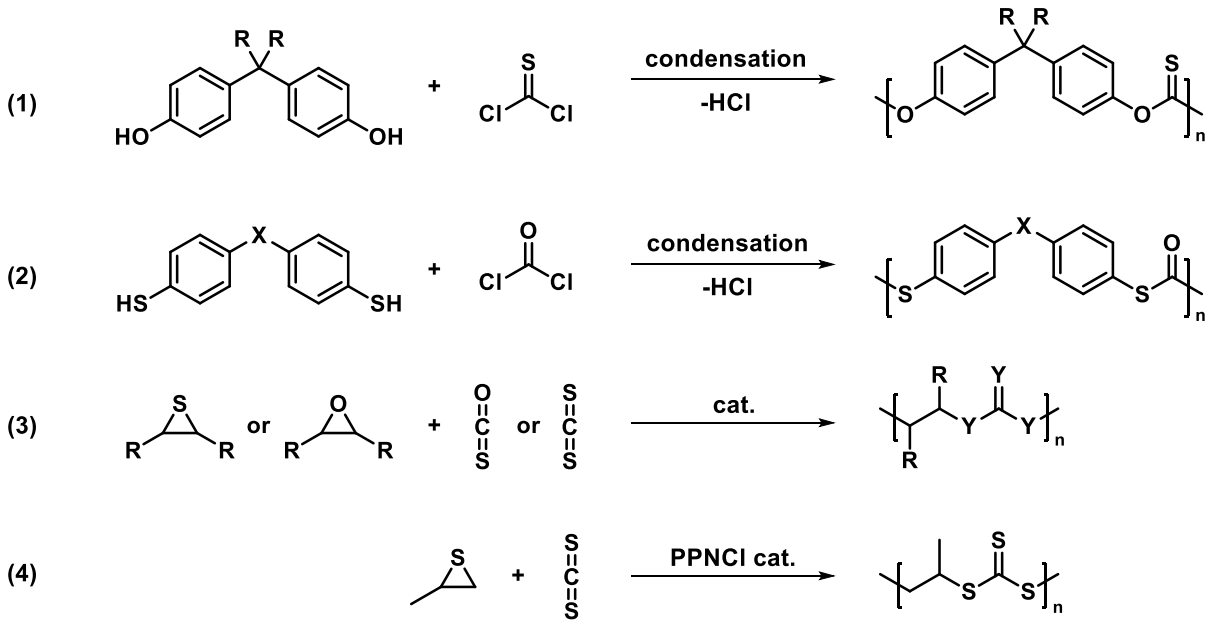

Scheme 5. Exemplary reactions schemes for various synthesis routes of polythiocarbonates with one, two, or three sulfur substituents. R = organic rest; X = CH_2, O, or S; Y = O or S; PPNCl = bis(triphenylphosphoranylidene) ammonium chloride.

Polymers with R_2N-C(=O)-O-R motifs in their backbone are called polycarbamates or polyurethanes. Analogous to thioesters and thiocarbonates, substitution of oxygen with sulfur gives a substance class known as thiocarbamates. Similar to thioesters, the position of sulfur atoms allows distinction between thiolcarbamates (R_2N-C(=O)-S-R), thionocarbamates (R_2N-C(=S)-O-R), and dithiocarbamates (R_2N-C(=S)-S-R).[101] Polythiocarbamates are typically synthesized via polyaddition between diisocyanates or diisothiocyanates with diols or thiols, depending on the desired degree of sulfuration and position of sulfur atom (refer to **Scheme 6**).[102] Polyaddition of diisocyanates with dithiols yields polythiolcarbamates (1)[103] while usage of diisothiocyanates with diols results in the formation of polythionocarbamates (2).[104] Polydithiocarbamates can be obtained via polyaddition of diisothiocyanates with dithiols (3).[102]

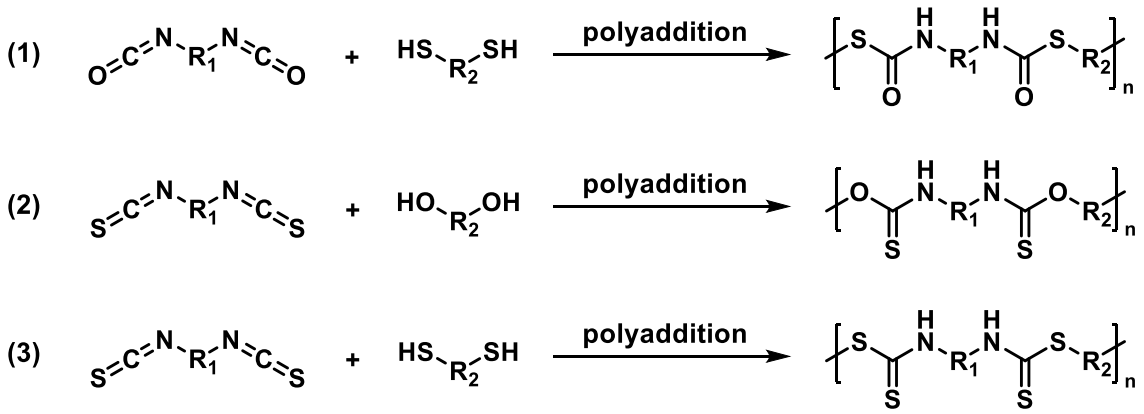

Scheme 6. Exemplary reaction schemes for the synthesis of polythiolcarbamates (1), polythionocarbamates (2), and polydithiocarbamates (3) *via* polyaddition.

To this day, thiocarbonyl-based polymers have not been commercialized on an industry scale and their relevance is mostly limited to academic research compared to their immensely distributed oxygen-containing counterparts of polyesters, polycarbonates, and polycarbamates/polyurethanes. However, with the rising interest in recyclable polymer materials, sulfur derivatives of these polymers may increase in popularity due to their inherent degradability and sustainability.[94,105]

2.2 Inverse vulcanization

The name vulcanization goes back to the vulcanization of rubber, invented by CHARLES GOODYEAR in 1839.[106] Therein, unsaturated polymers such as polyisoprene or polybutadiene were cross-linked with sulfur to form rubber. Initially, this method was, and is to this day, prominently used to fabricate and repair tires by cross-linking rubber with sulfur bridges between unsaturated polymer backbones.[107] The sulfur content in vulcanized rubber is then around 1 – 3 wt%.[108] The concept of inverse vulcanization (IV) was invented in 2013 by CHUNG and coworkers and refers to the inverse concept of conventional vulcanization.[8] Instead of cross-linking large amounts of organic polymers with small amounts of sulfur (1 – 3 wt%), the opposite approach is taken where molten sulfur is copolymerized with alkenes at temperatures typically between 120 – 185 °C. As introduced in **Chapters 2.1.1** Abundance and Production and **2.1.2** The Chemistry of Sulfur, sulfur is a highly abundant waste product of oil and gas desulfuration that can form polymeric sulfur chains above its melting temperature. However, pure polymeric sulfur is a metastable configuration which depolymerizes and forms low molecular sulfur rings upon cooling, rendering pure polymeric sulfur with little use as material.[57] In IV, the depolymerization of polysulfides is hindered by cross-

linking sulfur chains with unsaturated organic comonomers, also referred to as cross-linkers, which allows fabrication of materials with up to 90 wt% of sulfur permanently bound in the polymer (refer to **Scheme 7**).[8] IVs are characterized by their synthetic simplicity, scalability, and low cost. In their simplest form, sulfur and cross-linkers are mixed and heated to temperatures between 120 – 185 °C for minutes to hours, depending on the temperatures. The polymeric products are directly collected from the reaction vessel without further purification. Kilogram scale reactions are realized without issues.[109]

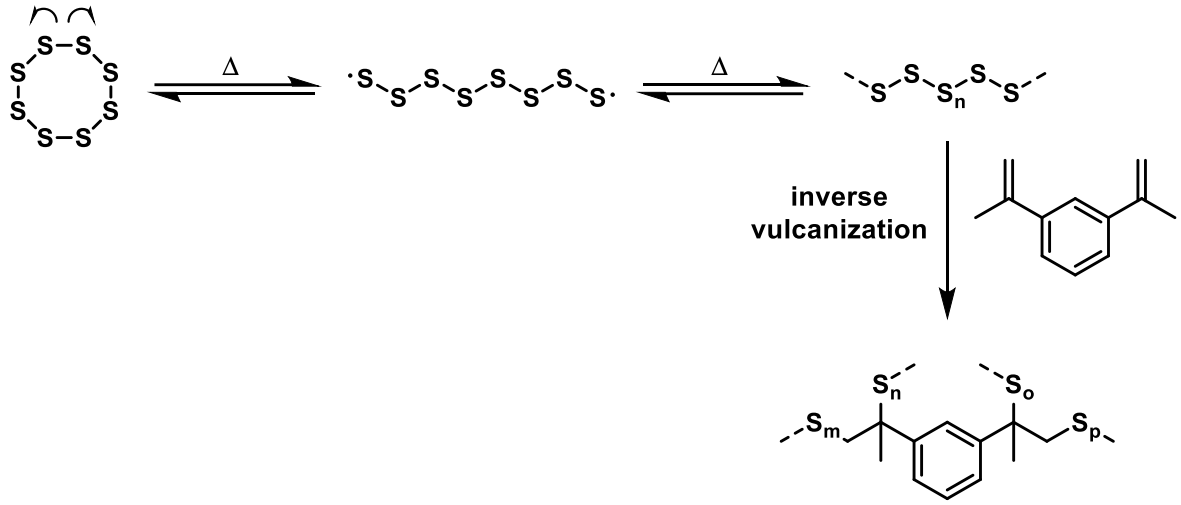

Scheme 7. General reaction scheme for the inverse vulcanization of diisopropenyl benzene. Brackets of repeating units are omitted for clarity and sulfur chains are abbreviated by dashed lines.

Given IV is a new scientific field, no conclusive nomenclature for inverse vulcanized polymers has been agreed on to this day. Popular terms found in literature include 'organically modified chalcogenides (ORMOCHALCs)',[110] 'chalcogenide hybrid inorganic/organic polymer (CHIP)',[111] 'polysulfides',[112] and 'inverse vulcanized polymer'.[113] In this thesis the term 'inverse vulcanized polymer (IV polymer)' will be used. Originally, available cross-linkers for IV were limited to organic compounds with reactive C=C double bonds that also exhibit high boiling points. To ensure efficient and predictable reactions, the boiling points of reactants need to be below the reaction temperature, which caused early works to focus on divinylbenzene (DVB),[114] diisopropenyl benzene (DIB),[8] oleyl amine,[115] fatty acids,[11] and natural dienes as cross-linkers.[116] However, in the last decade since its first description, IV has experienced an upswing in academic research interest leading to many reviews and some key advancements in the field, some of which are highlighted in the

following.[12,17,19,23,117,118] The first notable milestone of IV was the investigation of catalytic pathways by the group of HASELL in 2019.[56] They found that transition metal organyls, specifically zinc diethyldithiocarbamate, act as efficient accelerator of IV. Formation of toxic H_2S gas during the reaction could be reduced alongside with reaction times and temperatures. The proposed organo-metal catalysts may function as phase transfer agent, circumventing the poor miscibility of sulfur with some organic cross-linkers. Thereby, the reaction is accelerated, and the range of applicable cross-linkers is extended from non-polar alkenes to acrylates, acetals, and siloxanes. It needs to be noted, that the term 'catalyst' is formally incorrect for the role of the respective reactant since it is not retrievable after the reaction and remains bound in the material.[56,119] Hence, 'accelerator' would be a more fitting term rather than 'catalyst'. Nevertheless, the term 'catalytic IV' has been established in literature following its first introduction. In 2022, the concept of photoinduced IV was introduced by Jia *et al.*[120] By utilizing UV light rather than temperature to drive the IV, the reaction temperature could be lowered to ambient temperature which allowed the polymerization of gaseous cross-linkers in an IV context for the first time. Reaction times and H_2S formation were lowered and high molecular weight polymers with almost 100 % atom economy were obtained by this method.[120] Another strategy for IV at ambient temperature was reported by the group of HASELL in 2022 with the concept of mechanochemical IV. Therein, the chemical reaction is driven by the mechanical energy of a ball mill which allowed the efficient IV of low-boiling cross-linkers such as isoprene and dimethyl butadiene.[121] With climate change and environmental impact of our modern society being one of the key challenges of this time, the question of sustainability and degradability of polymers has occupied researchers in recent years and these considerations extended to IV polymers.[23,122] In 2024, DENG and coworkers reported the synthesis of high sulfur content materials with tunable properties via IV by reacting elemental sulfur with cyclic thioctic acid derivatives without additives at 120 – 130 °C. Importantly, these materials were degradable in alkali aqueous solutions, representing an important step towards sustainability of IV polymers and sulfur valorization.[123] IV polymers have shown to exhibit some unique properties which are derived from their high sulfur content in the form of polysulfide chains. In contrast to well-established polyolefins and vulcanized rubber with carbon backbones and stable C-C bonds, IV polymers are largely comprised of a dynamic S-S bond network due to the low bond dissociation enthalpy (BDE) of polysulfides (refer to **Figure 7**). In S_8, the

BDE is 138 kJ mol^{-1} while in polystyrene it is significantly higher with around 330 kJ mol^{-1}.[124] Exploitation of this dynamic sulfur network and the high sulfur content has led to the application of IV polymers as healable or recyclable materials,[13,125,126] Li-S battery cathodes,[8,127,128] heavy metal adsorbents,[10–12,25,118,119,129,130,131] adhesives,[15,132] IR optics,[16,133] anti-microbial surfaces,[134] metal and particle templates,[125,135] thermal insulators,[136] flame retardants,[29] and fertilizers.[137]

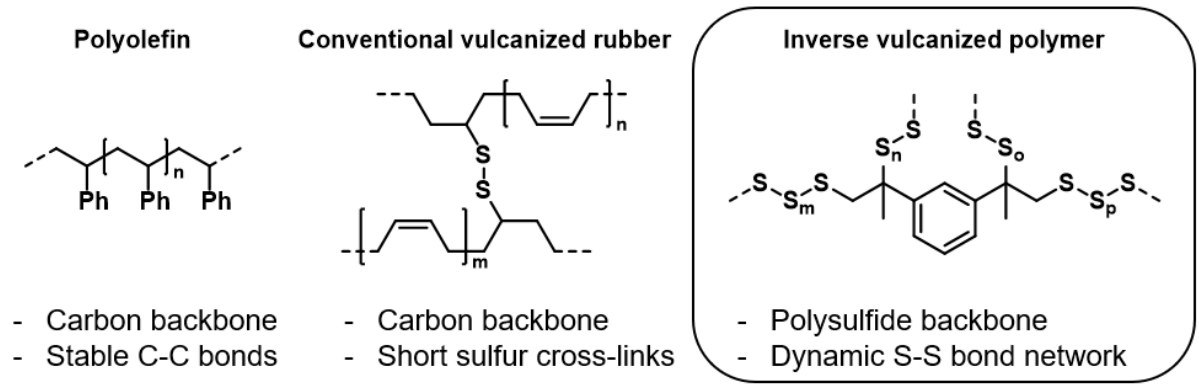

Figure 7. Visualized comparison between conventional polyolefins, vulcanized rubber, and IV polymers. Here polystyrene, vulcanized polybutadiene, and inverse vulcanized poly(sulfur-*random*-DIB) are chosen for visualization purposes, respectively. Brackets of repeating units are omitted for clarity and sulfur chains are abbreviated by dashed lines. Redrawn from reference.[19]

Despite the rapid development and major advancements in recent years, IV still suffers from major drawbacks compared to established carbon-based polymer chemistry. Most notably, the poor understanding of the exact reaction mechanism makes predictions on the precise polymer structure difficult, which in turn slows down material development down to trial-and-error approaches. To this day, only the IV mechanisms and resulting molecular structures of DIB and styrene explicitly have been studied.[20,138] Due to the poor solubility associated with cross-linked polymers in general and high sulfur content polymers specifically, analysis of IV polymers is often limited to solid-state spectroscopy or bulk analyses, limiting the available molecular information about a given material.[22] However, one of the key issues researchers face with IV is the lack of control fundamental polymer parameters, such as molecular mass and its distribution, solubility, (micro)phase separation, and sulfur rank. Initially, material properties of IV polymers were solely tuned by the amount of sulfur and the cross-linker employed during the polymerization, however, this proved non-satisfactory in order to predict material properties and reaction pathways.[139,140] Due to the dynamic nature of polysulfides, modification of materials via DCP has shown to be a feasible

method to alter polymer structures and properties by integrating additional alkenes into the polymer composition (refer to **Scheme 8**).[29,111] High control over molecular weight and mechanical strength was recently demonstrated by SCHEIGER and coworkers by controlled polycondensation in precisely defined compositions of alkoxysilane-containing IV polymers.[24] However, caused by the harsh reaction conditions of classic IV compared to conventional carbon-based polymerization techniques, the number of functional groups able to withstand these conditions is limited and defined PPM strategies for controlled straightforward modification towards desired predefined material properties largely remain elusive.[25]

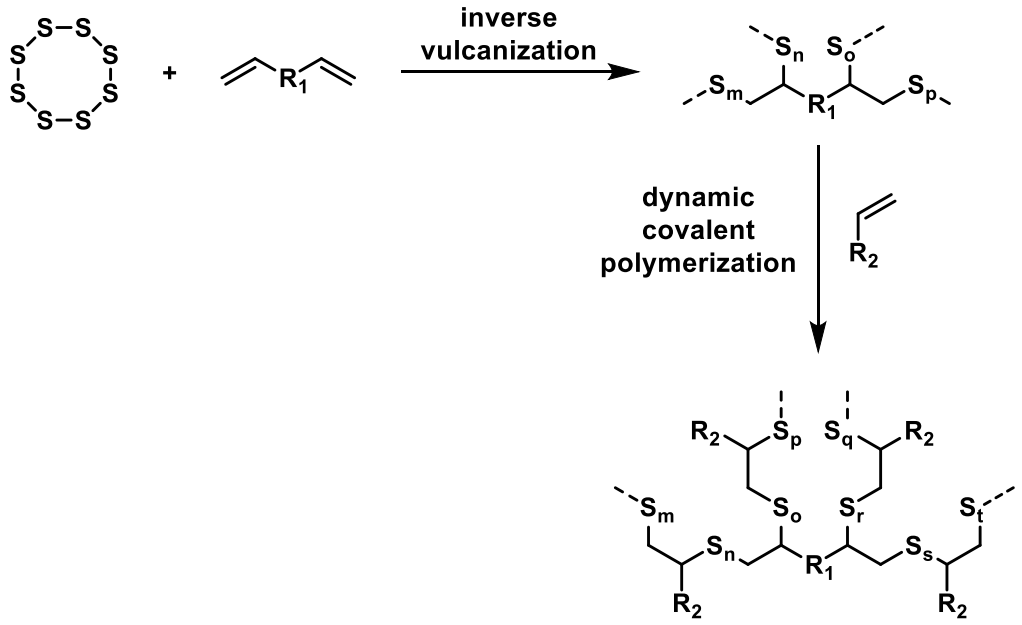

Scheme 8. General reaction scheme of a dynamic covalent polymerization for modification of an inverse vulcanized polymer. R_1, R_2 = organic rest. Brackets of repeating units are omitted for clarity and sulfur chains are abbreviated by dashed lines.

2.3 Reversible-Deactivation Radical Polymerization

Aside from the recent development IV in 2013, there are numerous established controlled techniques to create the vast amount of synthetic polymers that drive our modern society today. Polymerization strategies can be categorized by their underlying growing mechanism into chain and step polymerizations, which in turn can be subdivided further (refer to **Figure 8**). It needs to be noted that a categorization of IV is difficult, given the lack of understanding about the exact polymerization pathway. IV shows characteristics of both a free radical polymerization (FRP) and a step growth polyaddition.[20,141] Therefore, IV is omitted in **Figure 8**. Radical polymerization

accounts for over 50 % of all synthetic polymer production globally which can be explained by the straightforward polymerization conditions, low demand for high-purity reagents, and high tolerance to monomers and functional groups.[142] In conventional FRP reactions, high molecular weight polymers and monomer conversions are obtained in relatively short time, making FRP a feasible method for large scale material synthesis. However, FRP suffers from the lack of control it offers over molecular weight, dispersity (*Đ*), and polymer architecture in contrast to ionic polymerization methods where termination reactions are absent due to ionic repulsion of active chain ends.[143] In FRP, termination reactions such as backbiting, disproportionation, recombination, and radical transfer occur significantly which leads to uneven chain growth of macromolecules and therefore broad distribution of molecular weights.[144] Reversible-deactivation radical polymerization (RDRP) (often referred to as controlled radical polymerization (CRP)) has revolutionized the field of radical polymer chemistry by enabling precise control over molecular weight, composition, and architecture.[145] In RDRPs, radical termination and undesired side reactions are suppressed by one of two ways. In the first concept an equilibrium between active and inactive polymer species is established which is dominant on the dormant site, thereby decreasing the number of free radicals able to undergo termination. This principle is applied in nitroxide-mediated polymerization (NMP) and atom transfer radical polymerization (ATRP). In the second concept continuous radical transfer over all growing polymer chains is guaranteed with constant low radical concentration in presence of an excess transfer agent, which leads to an even growth of macromolecules. This is the underlying principle of reversible addition-fragmentation chain-transfer (RAFT) polymerization.[146] Unlike conventional free-radical polymerization, due to the generation of macromolecules with defined end-groups and functionalities all of these RDRP techniques provide access to well-defined polymers with low dispersity and complex structures, such as block, graft, and star-shaped polymers.[147] These advancements have broad implications for materials science, biomedicine, and nanotechnology, where tailored polymer properties are essential.[148] However, in RDRPs the termination reactions are only suppressed and never eliminated since transfer or termination by recombination and disproportionation of radicals will eventually occur and are not hindered by electronic repulsion, like they are in ionic polymerizations.[149] Thus, the only truly living polymerization is the anionic polymerization.[150] However, given the outstanding control that RDRPs offer, which is

often satisfactory for the desired applications, the term ‘quasi-living’ polymerizations has prevailed in literature.[151] In the following, NMP, ATRP, and RAFT polymerization are introduced in more detail.

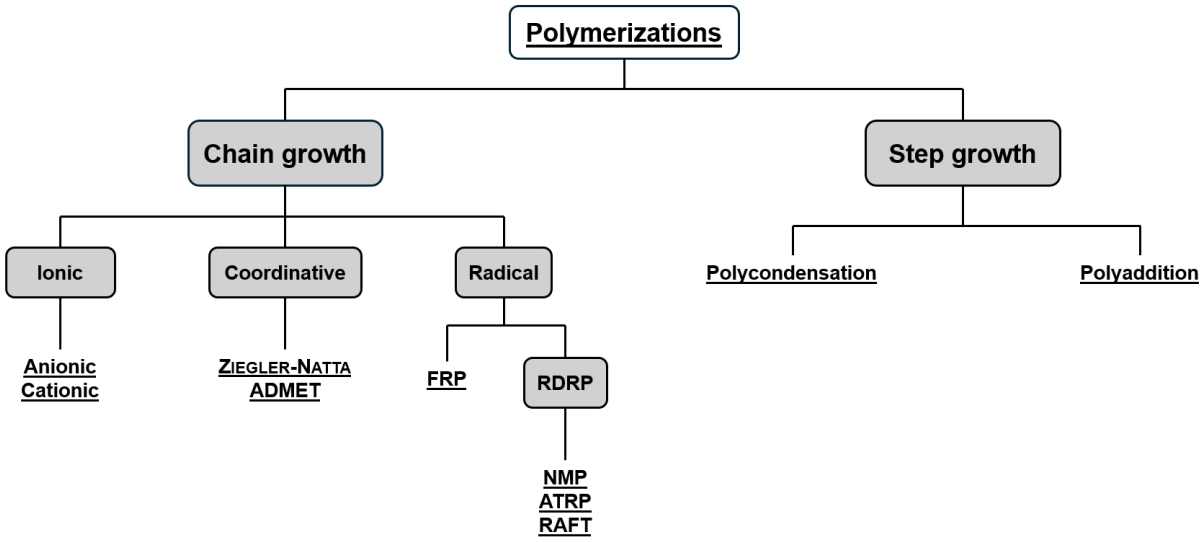

Figure 8. Categorization of polymerization techniques depending on the growing mechanism of the macromolecules. Chain growth polymerizations are further subdivided depending on the nature of propagating species during the chain growth.

2.3.1 Nitroxide-mediated Polymerization

Nitroxide-mediated polymerization (NMP) was first published via patent in 1984 by researchers at the Commonwealth Scientific and Industrial Research Organization (CSIRO) in Australia and represents the first instance of RDRP methods.[152] Nitroxides are organic compounds with $\cdot O\text{-}NR_2$ binding motifs which can exist in form of stable radicals at room temperature. The IUPAC prefers the term aminoxyls, since the term nitroxide implies the existence of nitro groups.[153] However, in order to keep the historical context, the term nitroxide is used throughout this chapter. Due to the persistent radical effect, they are unable to initiate polymerizations on their own but rely on the reaction with carbon radicals to form labile alkoxyamines which represent the dormant species in the chain growth equilibrium. Thermal homolytic cleavage of the C-O bond causes the creation of active species, which then take part in the radical chain growth with suitable monomers. In principle, two initiation methods are used for NMP. First, an external initiator can be employed as carbon radical source which then react with the nitroxide (refer to **Scheme 9a**). The second method is the use of thermolabile alkoxyamines which dissociate into a nitroxide and the propagating

species (refer to **Scheme 9b**). Since the ratio between radical and nitroxide should ideally be 1:1 to ensure control over the polymerization the latter is more commonly used. NMPs are typically slow compared to ATRP and RAFT polymerizations due to the stability of the alkoxyamine bond which necessitates high reaction temperatures. However, well-defined polymer structures with low dispersities are achievable without the need for additional reactants such as metals or transfer agents, which sets NMP apart from the other two RDRP methods introduced in the following section.[154]

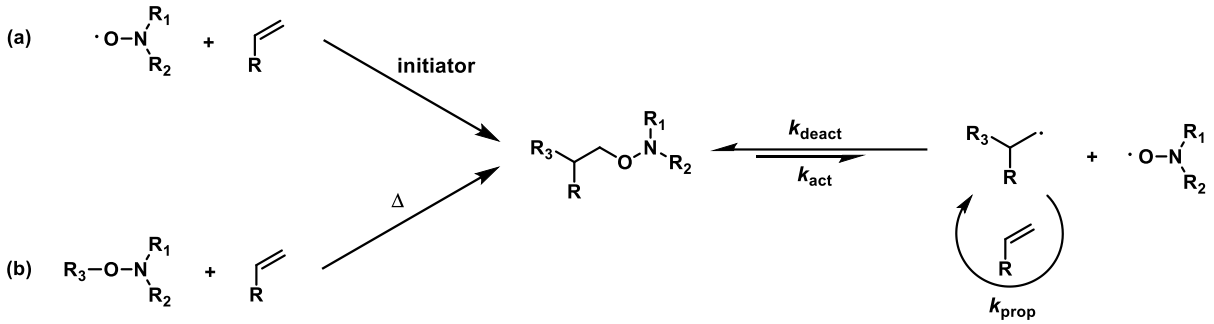

Scheme 9. General reaction mechanism of a NMP polymerization. Path (a) utilizes an external initiator while path (b) employs a thermolabile alkoxyamine species for initiation and mediating species. R, R_1, R_2 and R_3 = organic rest; k_{prop} = rate constant of propagation; k_{deact} and k_{act} = rate constants of capture and release of the active species, respectively.

2.3.2 Atom Transfer Radical Polymerization

The principle of ATRP was independently discovered by the groups of SAWAMOTO and MATYJASZEWSKI in 1995 and is based on the oxidation and reduction of transition metals for radical formation.[155] A transition metal complex in a lower oxidation state (M^m/L) is employed in combination with an alkyl halide (R-X) as initiating system. A single electron transfer through halide complexation leads to the formation of a carbon radical, which can undergo propagation in presence of a suitable monomer (refer to **Scheme 10**). The reversible atom transfer from the metal complex to the propagating chain represents the main equilibrium in this reaction and controls the polymerization. When the ratio of deactivation is orders of magnitude higher than the rate of activation, the equilibrium is primarily on the side of the deactivated species, thereby resulting in a low radical concentration and thus suppressing termination reactions, which are typically bimolecular reactions. The most common transition metal used in ATRP is copper with its stable oxidation states Cu^{1+} and Cu^{2+}.[156] Due to the one-electron difference in stable oxidation states of many transition metals ATRPs have been

reported various metals such as Fe,[157] Ni,[158] Mo,[159] Ru,[160] Rh,[161] Pd,[162] and Re.[163]

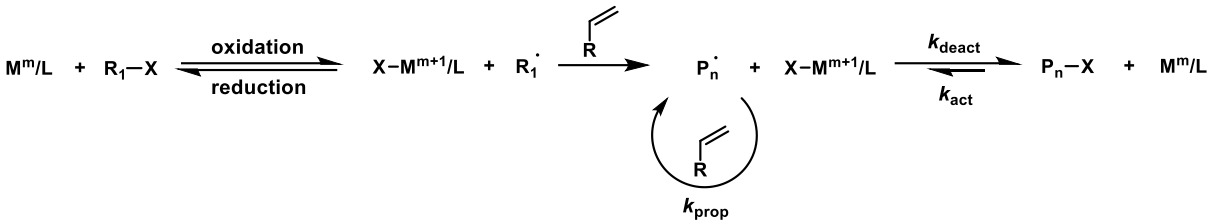

Scheme 10. General reaction mechanism of an ATRP polymerization. R, R_1 = organic rest; M^m = transition metal in oxidations state m; L = ligand; X = halide atom; k_{prop} = rate constant of propagation; k_{deact} and k_{act} = rate constants of capture and release of the active species, respectively.

ATRP-derived polymers inherently carry halide end groups, which facilitates efficient end group modification via nucleophilic substitution or block-building by subsequent polymerization with additional monomers.[164] However, the use of transition metals during the reaction generally leads to a high oxygen sensitivity and requires preferrable inert conditions as well as removal of toxic heavy metals from the product after polymerization.[165]

2.3.3 Reversible Addition-Fragmentation Chain-Transfer Polymerization

The last notable RDRP method is the RAFT polymerization and was also invented by researchers at the CSIRO in early 1998.[166] Opposite to NMP and ATRP, RAFT polymerization does not rely on control by equilibrating a reaction towards low radical concentration, but rather the constant transfer of radicals to many different macromolecules via chain transfer agents, referred to as RAFT-agents. This leads to a constant, higher radical concentration compared to NMP and ATRP, resulting in higher polymerization rates.[167] The key reactant here is the RAFT-agent which is often a specifically designed molecule featuring a reactive C=S double bond. Commonly used molecule classes for RAFT-agents are dithioesters, dithiocarbonates (xanthates), trithiocarbonates, and dithiocarbamates which contain a stabilizing group (Z) and a leaving group (R) (refer to **Figure 9**).[168]

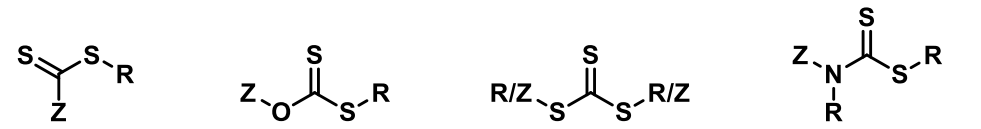

Figure 9. Chemical structures of commonly used RAFT-agents. R = initiating group; Z = stabilizing group.

R and Z groups must be carefully chosen to fit the desired polymerization. The Z group has to stabilize the forming intermediate radical just enough for it to be formed without creating a persistent radical species. Commonly used Z groups are alkyl and phenyl groups. The R group has to a chemical moiety which is able to reinitiate polymerization after its cleavage from the RAFT-agent.[168] In order to ensure uniform end groups in every macromolecule, the R radical should be the same as the initiating radical from the external initiator. Today, a wide range of RAFT-agents are commercially available, for a broad variety of common monomers.[169] The RAFT mechanism passes five main steps, which are summarized in **Scheme 11**. The reaction starts by initiation with an external initiator which releases a propagating radical either by thermal or photoinduced dissociation (1). The propagating chain then enters the pre-equilibrium with the RAFT-agent (2), creating the intermediate radical mentioned above. Here it is important to avoid retardation caused by non-suitable leaving groups. The R group then reinitiates chain propagation (3) before the main equilibrium is reached in which the active propagating radicals are reversibly transferred to all macromolecules (4). Alternating capture and release of growing chains results in an even distribution of active reaction time over all macromolecules, thereby leading to a low *Đ* and controlled polymerization. Analogue to all RDRP methods, termination (5) occurs via radical recombination or disproportionation.[170] RAFT polymerizations are one of the most commonly used RDRP methods owing to the high control over the polymerization of a variety of monomers with a suitable RAFT-agent. They are compatible with different reaction conditions and tolerant to most functional groups such as acids,[171] amides,[172] halogens,[173] and hydroxyl groups.[174] Additionally, RAFT polymerization does not require removal of toxic metals and is generally faster than NMP.[147] Complex polymer architectures are achievable and chain end modification is easily done via addition of monomer blocks or cleavage of the RAFT group, respectively.[175]

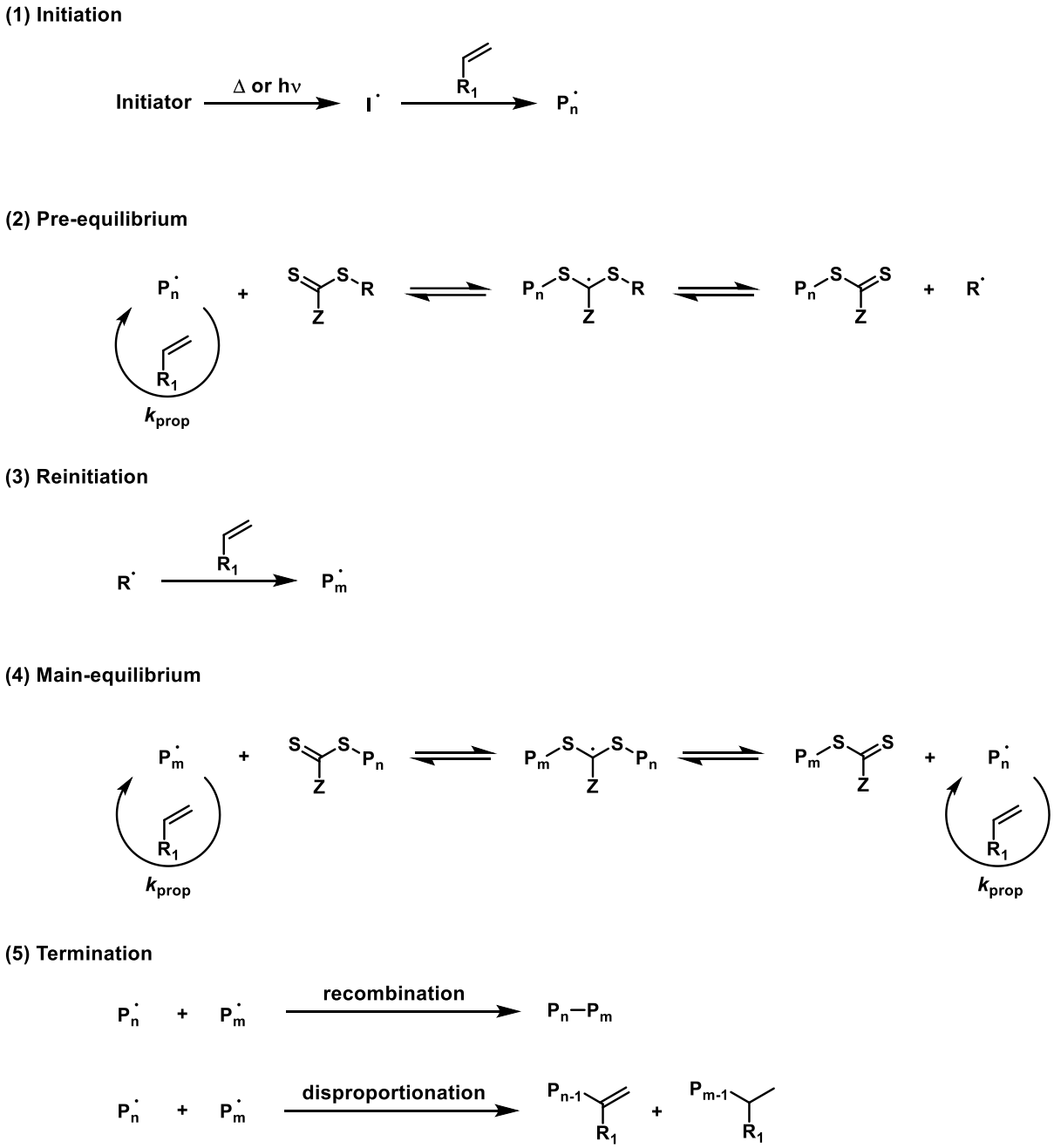

Scheme 11. General reactions mechanism of a RAFT polymerization with initiation (1), pre-equilibrium (2), reinitiation (3), main-equilibrium (4), and termination (5). R = initiation group, R_1 = organic rest, k_{prop} = rate constant of propagation.

In general, RDRPs are characterized by a linear relation between number average molecular weight (M_n) and monomer conversion, similar to living polymerizations.

2.4 Post-Polymerization Modification

The concept of modifying polymers is as old as the concept of polymerization itself and has been executed ever since. From the vulcanization of rubber in 1839,[107] over

cellulose modification with nitric acid in 1847,[176] to its acetylation with acetic acid in 1865,[177] PPM was conducted even before HERMANN STAUDINGER formally coined the term polymer and fought for its acceptance as scientific field in the 1930s.[178] When faced with the task of creating functional polymers, chemists are left with one of two choices: (i) either directly polymerize a functional monomer or (ii) modify an existing polymer to meet the desired requirements (refer to **Scheme 12**). PPM (also known as 'polymer analogous reaction') is a way to obtain a broad range of functional polymers, which monomers are often not polymerizable or accessible, through modification of available precursor polymers.[179]

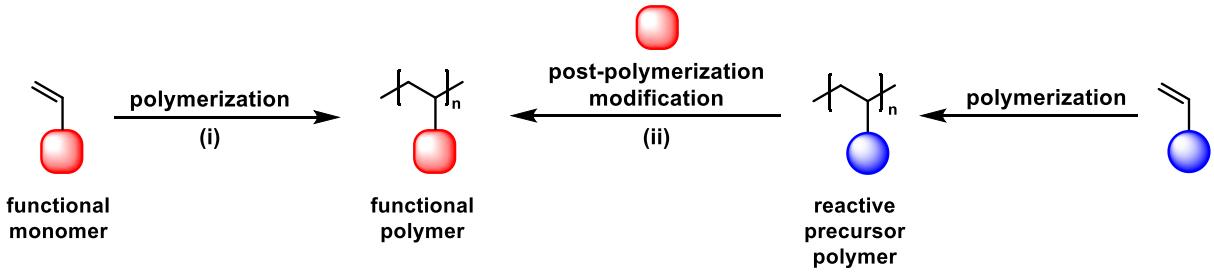

Scheme 12. Visual representation of the concept of PPM. When direct polymerization of a functional monomer is not an option, PPM of a reactive precursor polymer may represent a promising alternative for synthesis of functional polymers. Blue circle = reactive functional group; red square = desired, unreactive functional group.

Even though PPM has been around as long as polymers, its relevance and potential excelled with the emergence of RDRP methods, allowing precise synthesis of complex chemical structures and architectures. Ideally, PPM reactions are designed to be quantitative in conversion and chemo-selective without the occurrence of side reactions. Understandably, development of highly efficient and selective 'Click'-reactions such as copper(I)-catalyzed alkyne-azide cycloaddition (CuAAC), thiol-ene addition, and DIELS-ALDER addition represented a dramatic advancement of PPM. Today, the possibilities for PPM are almost limitless and span over the whole toolbox of organic chemistry.[180] Given the vast number of possible PPM reactions, the following sections will focus on active ester substitution and para-fluoro-thiol reaction as efficient PPM methods used in this thesis.

2.4.1 Active Ester Amidation

Active esters as precursors for functional polymers were first introduced by FERRUTI and RINGSDORF in 1972 and 1973, respectively.[181,182] In general, an active ester is an

ester derivative which is highly reactive toward nucleophiles, especially amines, due to electron-withdrawing substituents. This leads to a reduced electron density on the carbonyl carbon, making it susceptible to nucleophilic attack.[183] Polymers containing active esters either as pendant or end groups can react with amines under irreversible formation of the more stable respective amides (refer to **Scheme 13**).[184]

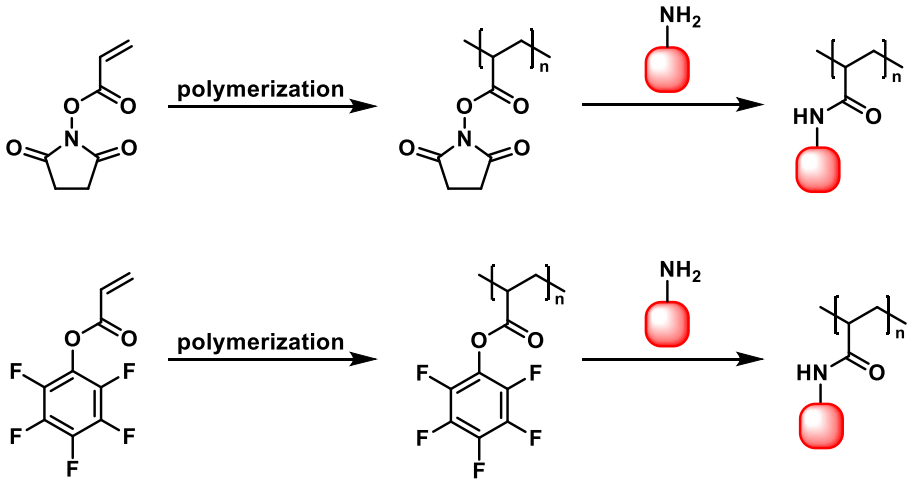

Scheme 13. PPM of active precursor polymers via amidation of active esters with primary amines. Top: NHS-based polymer system; bottom: PFPA-based polymer system; red square = desired, unreactive functional group.

Amidation of active esters represents one of the most useful PPM methods due to the mild reactions conditions while still yielding quantitative conversion without the use of metal catalysts. The most extensively studied chemical motifs used for active ester amidation are *N*-hydroxysuccinimide (NHS) and pentafluorophenyl (PFP) esters in combination with a wide range of polymerizable groups such as vinyls, alkynes, norbornenes, or ring-opening groups (refer to **Figure 10**).[185] Early works utilizing *N*-hydroxysuccinimide acrylate (NHSA) as active ester containing monomer found the reactive polymer to be quite resistant to hydrolysis while being easily modifiable with allylamine (AA), yielding a polymer not accessible by direct polymerization.[181] However, poly(NHSA) suffers from poor solubility in conventional organic solvents, which is often circumvented by copolymerization with other monomers.[185] This, however, increases the complexity of the process, since copolymerization parameters and different reactivities of monomers need to be considered when moving from homo- to copolymerization approaches.[186] In 2005, EBERHARD *et al.* reported the homopolymerization of pentafluorophenyl (meth)acrylate (PFP(M)A), leading to a

precursor polymer for efficient active ester amidation with increased resistance against hydrolysis and improved solubility in common organic solvents.[187]

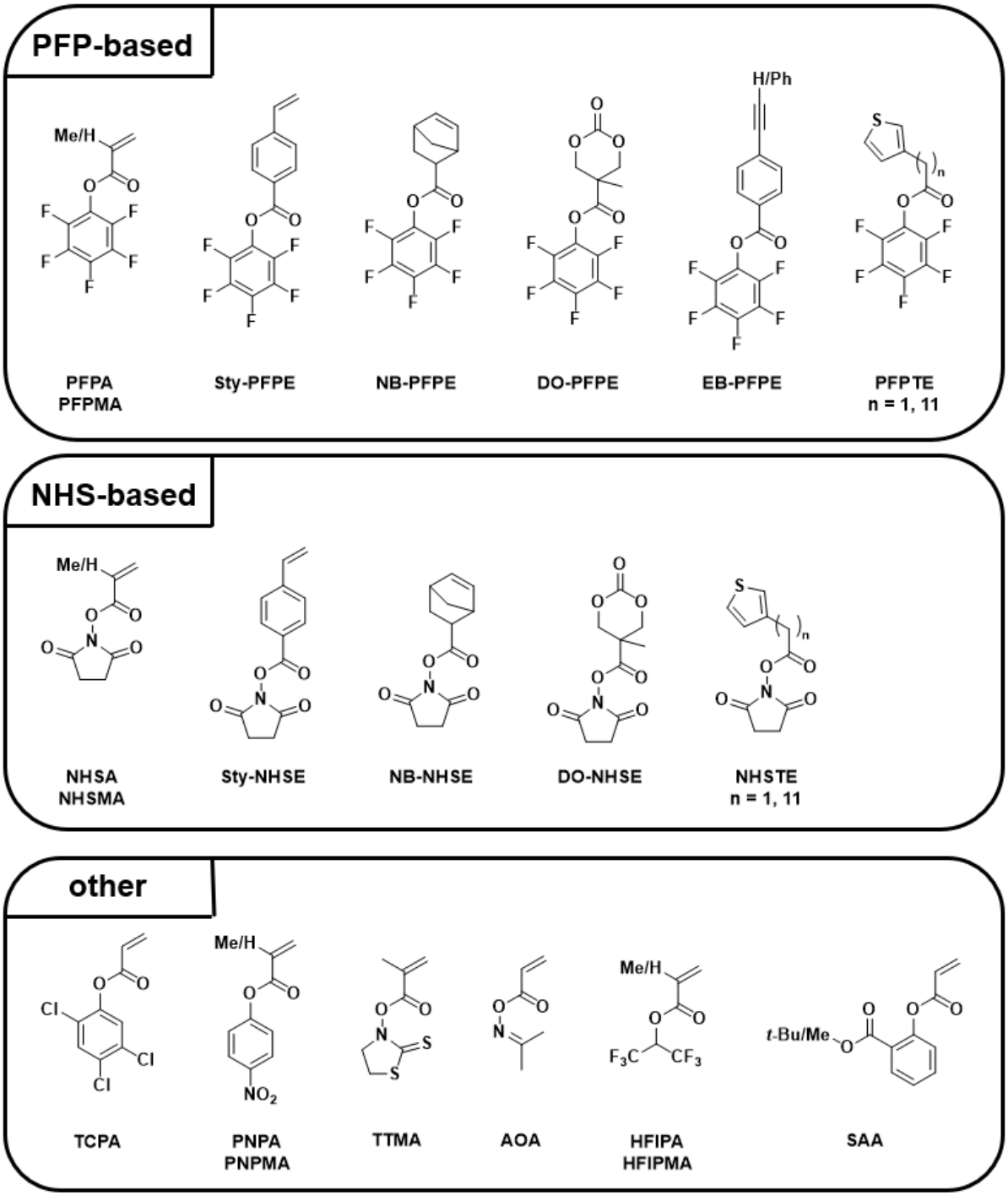

Figure 10. Active ester-containing monomers for PPM reported in literature. The most prominent groups of active esters are PFP- and NHS-based systems. Adapted from reference.[185]

Importantly, the efficiency of PPM is determined by the reactivity of the substituting nucleophile as well as the structure of the ester. Two main trends were reported for the two main active esters (NHS- and PFP-based). Firstly, compared to NHS-esters, the

amidation of PFP-esters proceeds faster and secondly the reactivity of amines decreases from aliphatic, primary amines to aliphatic, secondary amines and is lowest for aromatic amines.[185] Transesterification of PFP-esters with alcohols is also possible but requires increased temperature and the use of auxiliary bases such as 4-dimethylaminopyridine (DMAP) for satisfactory conversion.[188] Aside from NHS- and PFP-based systems, PPM of other active esters has been investigated, including reports of trichlorophenyl acrylate (TCPA),[189] *para*-nitrophenyl methacrylate (PNPMA),[190] cyclic thiazolidine-2-thione methacrylate (TTMA),[191] acetone oxime acrylate (AOA),[192] hexafluoro isopropyl acrylate (HFIPA),[193] and salicylic acid acrylate derivatives (SAA).[194] Due to mild, catalyst-free reaction conditions, high selectivity, and rapid conversion, the amidation of active esters has become one of the most important concepts for PPM and in combination with RDRP methods represents a highly versatile strategy towards highly complex functional polymers.[179]

2.4.2 *Para*-Fluoro-Thiol Reaction

Aromatic para-fluorine atoms are known to exhibit special reactivity towards aromatic nucleophilic substitution (S_nAr) by alcohol,[195] amine,[196] phosphite,[197] azide,[198] and thiol groups.[199] The quantitative conversion and high efficiency and selectivity at mild conditions have earned the *para*-fluoro-thiol (PFT) reaction a place in the realm of click reactions, even though it is less used than the more prominent CuAAC or thiol-ene click reactions.[200] Alternative terms found in literature are thio-*para* fluoro click reaction, thiol/*para* fluorine click reaction, *para*/fluoro thiol click reaction, and metal-free S_nAr *para* fluoro click reaction.[201] In general, a non-nucleophilic base (most commonly 1,8-diazabicyclo[5.4.0]undec-7-ene (DBU) or triethylamine (TEA)) is used to deprotonate the thiol, which then substitutes the para fluorine atom via nucleophilic attack (refer to **Scheme 14**).[202]

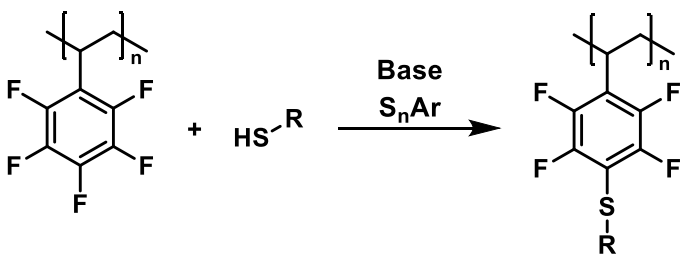

Scheme 14. General reaction scheme of the PFT reaction for PPM of poly(pentafluorostyrene). R = organic rest.

The PFT reaction typically works well in aprotic polar organic solvents such as *N,N*-dimethylacetamide (DMAc), *N,N*-dimethylformamide (DMF), or tetrahydrofuran (THF) while it hardly occurs in non-polar solvents such as toluene.[201,203] *Para*-fluoro substitution reactions can also be carried out in ethanol or basic water, owing to the higher selectivity towards thiolates than hydroxyls.[204] The reaction kinetics are relatively fast with full conversion after minutes to hours between ambient temperature (a.t.) and 70 °C. The progress of the reaction can conveniently be followed by ^{19}F NMR spectroscopy since *ortho*, *meta*, and *para* fluorine atoms exhibit distinctly separated nuclear resonances.[201] Importantly, the thiol substitution was found to be regioselective towards the *para* fluorine atom in pentafluorobenzyl compounds (R-CH_2-C_6F_5) while multiple substitution in *meta* and *para* positions can occur in PFPMA units.[205] Therefore, most studies utilizing PFT reactions use the commercially available PFSty as starting compound over PFPMA.[201] PFT reactions have been carried out to successfully modify polymers with primary, secondary, tertiary aliphatic, and aromatic thiols and the reactivity was found to decrease from aromatic over primary to tertiary thiols (aromatic, glycosidic > primary aliphatic > secondary aliphatic > tertiary aliphatic).[199] Today, thiols represent a versatile group of functional compounds which are often commercially available or readily synthesized, making the PFT reaction a powerful tool to create functional materials.[206]

2.5 Automated Synthesis and Characterization of Polymers in Continuous Flow

Historically, chemical reactions are conducted in a batch approach in confined reaction vessels such as round bottom flasks or pressurized containers, which allows assumption of an ideal batch reactor model to characterize reactions on a smaller scale. In recent years, the shift from batch to continuous flow reactors has gained significant interest in chemical research, due to a number of crucial advantages which include: improved heat transfer due to a high surface-to-volume ratio, higher safety, scalability, reproducibility, reactions under high pressure, and importantly, real-time feedback for optimization and rich data sets thanks to computation.[32] Whereas screening of multiple reaction conditions requires setting up multiple reaction vessels in traditional batch chemistry (refer to **Figure 11a**), a flow approach allows rapid screening of reaction conditions by simple control of pump flowrates. However, the use

of flow chemistry also comes with disadvantages and challenges. The handling of solid reaction compounds is an issue when working in continuous flow, albeit not impossible. Additionally, viscosity plays a more prominent role in flow than in batch and needs to be monitored in order to avoid blockages.[34] In batch chemistry, the reaction time is determined by the time from start to finish during that an external stimulus (heat or radiation) is applied to the reaction vessel. In flow chemistry, the reaction time is determined by the residence time (t_r [min]) that a given molecule experiences in the flow reactor from entrance to exit and which is defined as reactor volume (V [mL]) divided by flowrate (f [mL min^{-1}]):

$$t_r = \frac{V}{f}$$

As in batch chemistry, flow reactors can be designed for all kinds of chemical driving forces such as temperature, light, or sound.[207] In the field of liquid phase chemistry, a flow reactor can be as simple as a tube that is homogenously heated or irradiated. Commonly used materials for flow reactors are perfluoro alkoxy alkane polymers (PFA), polyether ether ketone (PEEK), and stainless steel due to their chemical inertness, temperature resistance, and affordability.[208] Tubular flow reactors are categorized depending on channel diameter into microfluidic (0.01 – 0.5 mm) and mesofluidic/minifluidic (0.5 – 5 mm).[209] One of the key advancements in flow chemistry is arguably derived from the rapid development of digitalization and artificial intelligence (AI) and ML in the last decades. In general, AI refers to a field of computer science devoted to the creation of computer systems that can perform tasks that typically require human intelligence such as problem-solving, reasoning, and decision-making.[210] ML on the other hand is a subset of AI that enables computer programs to improve their performance over time from learning data without being explicitly programmed. Trained ML algorithms can then identify patterns in data and make predictions based on that learning data.[210] Whereas seminal work on flow polymerization goes back to the 1953 when HICKS and MELVILLE reported the synthesis of poly(butylacrylate-*co*-styrene) and poly(acrylonitrile-*co*-styrene) block copolymers,[211] flow techniques have come a long ways. The use of modern AI-assisted synthesis has entered every field of automated chemistry including small organic molecules,[212] inorganic materials,[213] high-entropy alloys,[214] biomedical drugs,[215] and next-generation energy storage systems.[216] Today, every type of

polymerization has been conducted in flow utilizing real time reaction monitoring by online analysis to gain instant feedback on the reaction quality by the means of monomer conversion, molar mass dispersity, or other product parameters. Widespread distribution of control or monitoring software for chemical processes based on open source software packages such as LabView™, MATLAB™, or Python™ allows development of self-optimizing algorithms which can interpret measurement results from analytical devices which are installed directly inline or online a reaction stream and predict reaction parameters for improved product quality (refer to **Figure 11b**).[34]

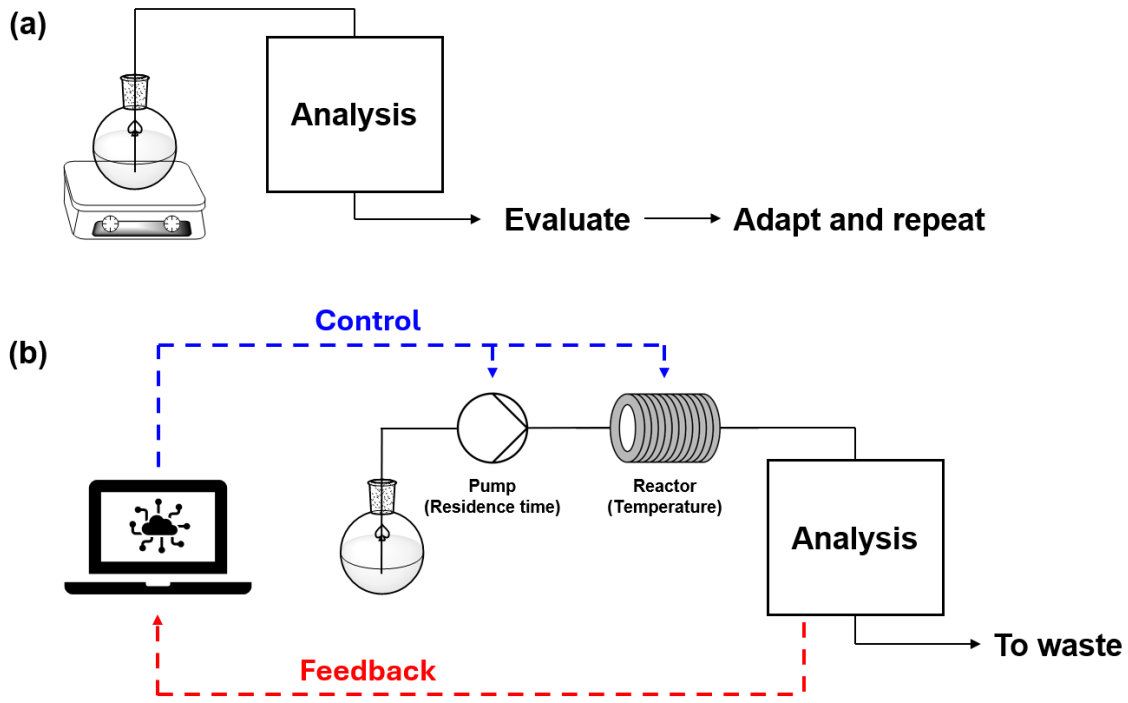

Figure 11. Comparative visualization of batch-based (a) and flow-based (b) chemical synthesis. Flow-based chemistry allows control over reaction parameters by real time feedback of analyses and automated control of the reactor setup.

By utilizing automated flow polymerization, development of novel specialized materials can be accelerated and optimized by increasing data density, reduce trial-and-error, and alleviate polymer chemistry in terms of sustainability and green chemistry. In the following sections the two main flow polymerization techniques used in this thesis are discussed.[35]

2.5.1 Closed-loop Multi Objective Optimization

Polymer chemistry, with its vast array of monomers, reaction conditions, and processing techniques, offers immense potential for creating materials with tailored properties. However, this complexity poses significant challenges in identifying optimal reaction pathways, particularly when multiple, often competing objectives must be satisfied. Closed-loop multi-objective optimization (CLMOO) has emerged as an approach to address these challenges, combining experimental and computational methodologies to accelerate polymer discovery and development.[217] In polymer chemistry, the desired quality factors of a polymerization such as monomer conversion, *Đ*, or particle size often conflict, necessitating trade-offs. For example, enhancing monomer conversion may compromise *Đ*, or decreasing particle size might reduce monomer conversion during the reaction. Traditional optimization approaches, relying on a trial-and-error basis or single-objective focus, struggle to efficiently navigate this complex objective space. CLMOO provides a systematic methodology to explore these trade-offs by simultaneously considering multiple performance metrics. It identifies a set of PARETO-optimal solutions, where no single objective can be improved without compromising another. This facilitates informed decision-making in material design and advances the development of polymers that meet specific desired properties. 'Closed-loop' refers to an iterative approach where experimental data is combined with computational modelling which can be summarized thusly:[218]

1. A set number of initial training experiments is conducted with randomly selected reaction parameters (*e.g.*, temperature, residence time, light intensity, *etc.*). Alternatively, previously obtained experimental data can be fed to the algorithm as base for optimization.
2. A predictive algorithm identifies promising reaction parameters that balance the competing objectives. The underlying statistic considerations behind different optimizing algorithms are complex and are out of scope of this thesis. However, a commonly used method is Bayesian optimization which is a way to optimize an unknown objective function and does not require prior knowledge to evaluate given data. It works by evaluating the initial data points to train a surrogate model which is a probabilistic model to approximate the true objective function.[219] A popular surrogate model is Gaussian process which can predict the objective function while respecting uncertainty. An acquisition function then predicts new experiments while balancing exploration (searching in less-known

areas) and exploitation (focusing on known regions likely to yield the best results).[220]

3. The surrogate model is updated and the cycle repeats until a maximum number of iterations is reached, or the optimization converges. The closed nature of this process ensures that each iteration refines the model and enhances the efficiency of the search for optimal solutions.[221] Different to traditional batch chemistry, where the composition of the reaction mixture changes over time in the reaction vessel, flow reactors need to reach a steady state where all exiting molecules experienced the same reaction conditions. Changing these conditions (*i.e.* flow rate or temperature) requires re-equilibrating of the reactor before samples are analyzed and interpretated.[208]

In a practical polymer-related example, the objectives to be optimized are conversion (preferably p = 1.0) and dispersity (also preferably $Đ$ = 1.0) which make up the objective space with a utopian point at p = 1.0 and $Đ$ = 1.0. The variable reaction parameters are temperature and residence time, and they represent the investigated parameter space. The quality of any given result of the optimization can be evaluated by its hypervolume which is the area in the objective space defined by the distance of the result from the reference point. In this example, a hypervolume of 1.0 would refer to the optimal utopian solution. Points closest to the utopian points make up the PARETO front and are all optimal solutions balancing the trade-off between competing objectives (refer to **Figure 12**).[222]

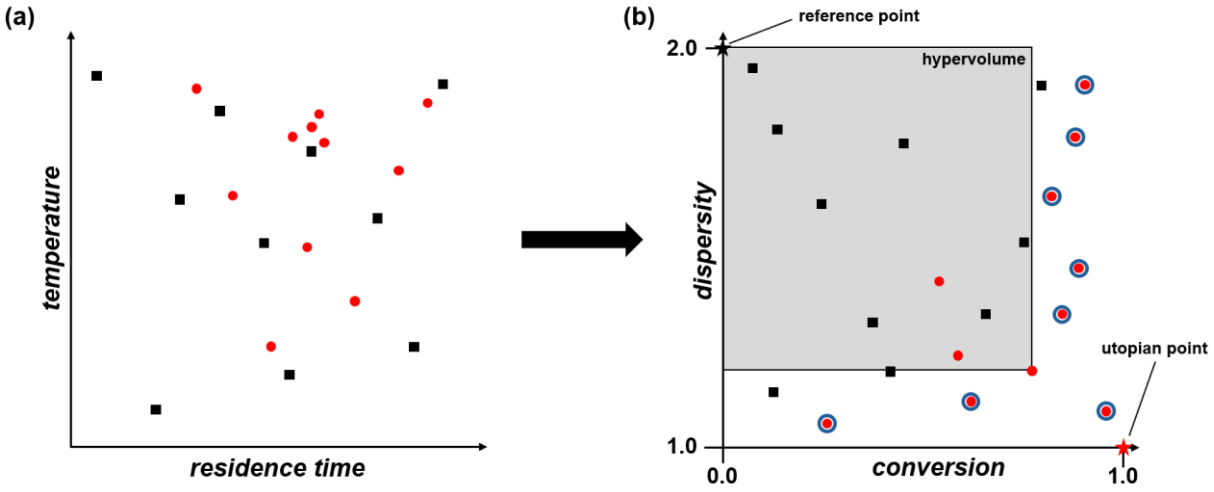

Figure 12. Exemplary parameter space (a) and objective space (b) of a CLMOO of dispersity and conversion by control of reaction temperature and residence time. Black data points: initial training experiments; Red data points: experiments proposed by the optimization algorithm; Blue: non-dominated solutions of the optimization problem (PARETO front).

2.5.2 Kinetic Screening *via* Transient Timesweeping

Different from CLMOO, where data points are acquired one after another with a stabilization period in between, transient timesweeping (TT) is a flow-based method to obtain large amounts of kinetic data about a chemical reaction in a shorter amount of time. Early work utilizing this method goes back to 2012 when MOZHAROV *et al.* investigated the kinetics of the KNOEVENAGEL condensation between ethyl cyanoacetate and benzaldehyde in continuous flow using an inline RAMAN spectrometer.[223] Since then, this concept has gained interest and found its way to polymer chemistry to obtain information about the kinetic parameters of polymerization reactions.[224] In general, TT makes use of the time it takes for an ideal plug flow reactor to equilibrate between two flow rates A and B after a sudden flow rate change (refer to **Figure 13**). At steady state, before a flow rate change, the residence time of each volume increment in the reactor depends on its position in the reactor and the increment exiting the reactor will have experienced a residence time corresponding to flow rate A. Instantly changing the flow rate leads to the current reactor volume to leave the reactor with a gradient of residence times corresponding to flow rates A and B.[37]

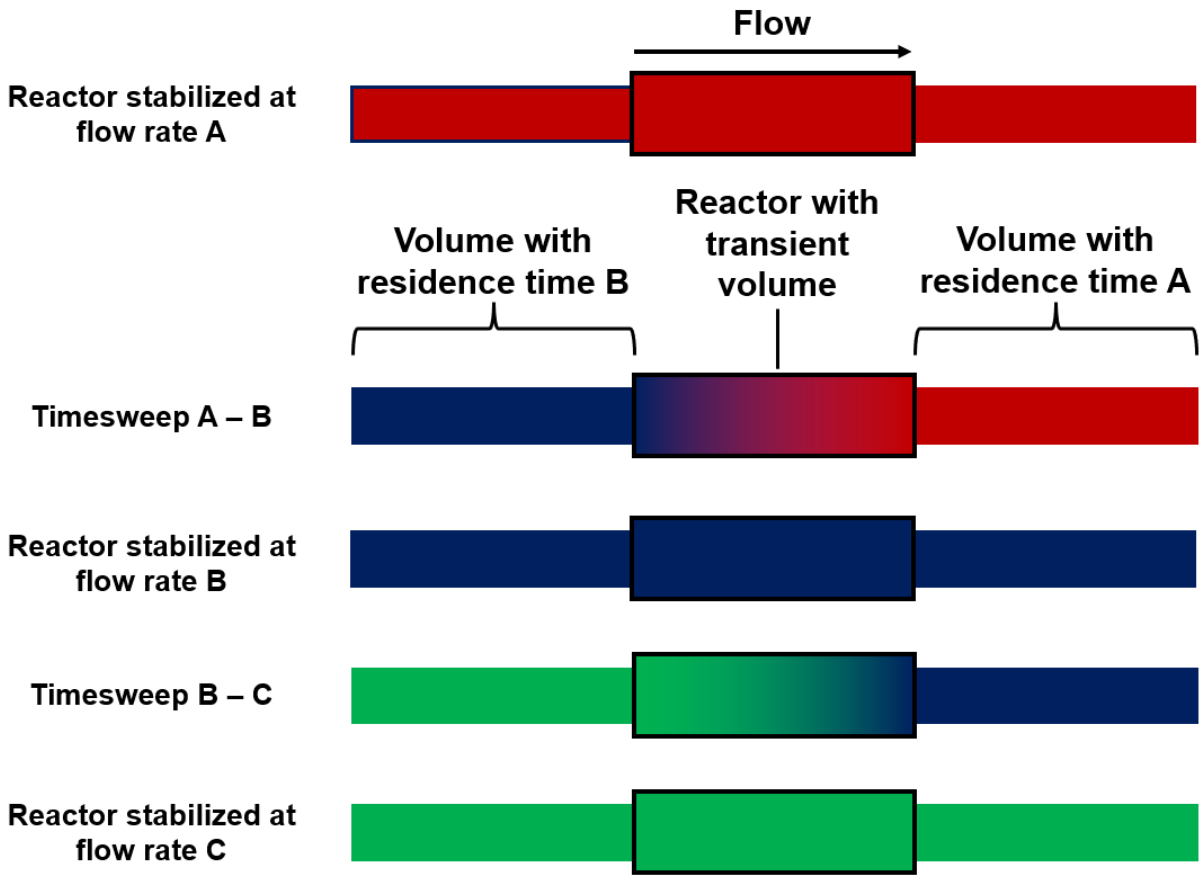

Figure 13. Visual representation of the concept of transient timesweeping between three flow rates A, B, and C. The reactor volumes which experienced transient residence times contain the kinetic information about the chemical reaction.

At known volumes between reactor and analysis device (dead volume), the time for data acquisition can be precisely timed for measurement. Analyzing this transient volume, in which every residence time between A and B is present, by inline and online analyses, such as NMR and SEC, allows direct acquisition of kinetic data from monomer conversion and development of changes in molecular weight, respectively. For controlled polymerizations at pseudo first-order kinetics, the rate of propagation can be derived from the slope of -ln(p) vs. t_r and yields important information about the control over polymerization.[225] It needs to be noted, that the total experiment time includes the TT segments as well as the time passed by waiting for dead volume to pass between time sweeps. Deleting the latter and adjusting the timescale gives the kinetic profile from the individual timesweeps (refer to **Figure 14**). In general, timesweeps can be performed from fast-to-slow or slow-to-fast flowrates but is usually advised to separate large residence time windows into smaller individual sweeps due

to non-ideal flow behavior and therefore inaccurate data acquisition at large flow rate changes.[37]

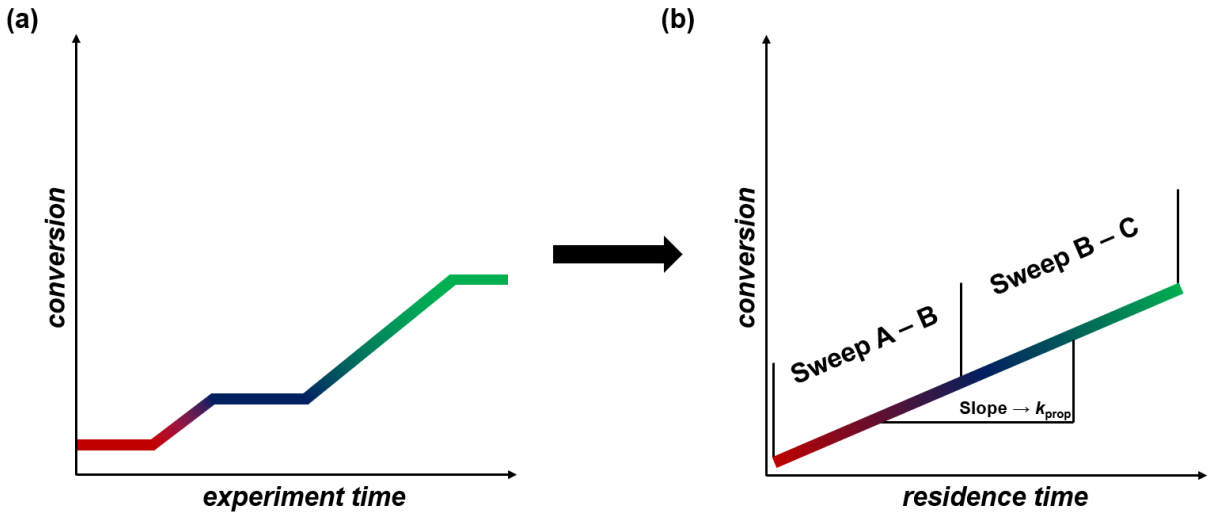

Figure 14. Exemplary plots of conversion and experiment time data obtained during a TT experiment (a). Removal of steady state data yields a conversion vs. residence time plot comprised of the individual timesweeps (b). The slope of this linear curve contains information about the propagation rate (k_{prop}) of the reaction.

3 Results and Discussion

The current chapter in this thesis summarizes the scientific work conducted during the doctorate. Experiments and results are discussed, divided into five main subchapters in logical order with each subchapter representing a conclusive project.

First, the IV of fluorinated acrylates is discussed as the direct transfer of a well-established monomer for carbon-based polymers to high sulfur content IV polymers. Investigation of two acrylate-based fluorinated cross-linkers was performed with the focus on applicability as functional IV polymers (**Chapter 3.1** Inverse Vulcanization of Fluorinated Acrylates).

Based on the results of **Chapter 3.1** Inverse Vulcanization of Fluorinated Acrylates, the subsequent section is about the development of a high-sulfur content polymer material by IV, which is able to undergo PPM by amidation of active esters with primary amines. The versatility of this norbornene-based precursor polymer is demonstrated by application in four different chemical contexts (**Chapter 3.2** Inverse Vulcanization of Norbornenyl-Pentafluorophenyl-Ester).

In order to advance the field of IV from batch to flow-based reaction management, the automated synthesis and modification of pentafluorophenyl acrylate in continuous flow is discussed in the third chapter. Development of a straightforward and versatile technique for PPM of active ester containing polymers in a flow reactor is demonstrated by utilization of ^{1}H and ^{19}F NMR techniques (**Chapter 3.3** Automated Synthesis and Post-polymerization Modification of Polypentafluorophenyl Acrylate in Continuous Flow).

Based on the results of **Chapter 3.3** Automated Synthesis and Post-polymerization Modification of Polypentafluorophenyl Acrylate in Continuous Flow, the developed methodology for control over modification of active ester containing polymers is extended towards post-polymerization modification via *para*-fluoro-thiol reaction of poly(PFSty). Investigation of kinetic parameters of the polymerization of PFSty with subsequent PPM is discussed, which demonstrates the power of flow-based reaction management for rapid data acquisition and control over polymer structures (**Chapter 3.4** High-throughput Polymerization and Post-polymerization Modification of Pentafluorostyrene in Continuous Flow).

The fifth and concluding section of this chapter represents the combination of **Chapters 3.2** Inverse Vulcanization of Norbornenyl-Pentafluorophenyl-Ester and **3.3** Automated Synthesis and Post-polymerization Modification of Polypentafluorophenyl

Acrylate in Continuous Flow. The developed norbornene-based sulfur precursor polymer was subjected to PPM in continuous flow which represents the first application of an IV polymer in a flow context (**Chapter 3.5** Post-polymerization Modification of poly(S-r-NB-PFPE) in Continuous Flow).

3.1 Inverse Vulcanization of Fluorinated Acrylates

The IV of two fluorinated acrylates, namely pentafluorophenyl acrylate (PFPA) and all-*cis*-2,3,4,5,6-pentafluorocyclohexyl acrylate, was conducted. The former monomer is known to yield polymers that can undergo amidation with amines due to the presence of an active ester which allows efficient PPM,[185] while the latter was hypothesized to have beneficial influences on the cycling performance of Li-S batteries due to a high dipolar moment caused by all-*cis* fluorination.[226] The synthesis, characterization, and applicability of high sulfur content polymers derived from these two cross-linkers is discussed in this chapter.

3.1.1 Pentafluorophenyl Acrylate

The synthesis of PFPA was conducted according to a procedure published in 2020 by ZERDAN *et al.*[227] In general, pentafluorophenol (PFP) was deprotonated with TEA in dichloromethane (DCM) under cooling. Acryloyl chloride was added to the reaction mixture and after stirring at a.t., PFPA was obtained after filtration and column chromatography with typical yields of 75 % – 85 %. The successful synthesis of PFPA was confirmed by ^{1}H, ^{13}C, ^{19}F NMR, and attenuated total reflection Fourier-transform infrared (ATR FT-IR) spectroscopy (refer to **Appendix 1**).

IV of PFPA was performed by reacting equal masses of PFPA with elemental sulfur at elevated temperatures with or without accelerator (refer to **Scheme 15**). In accordance with published literature the resulting polymer was entitled poly(sulfur-*random*-pentafluorophenyl acrylate) (poly(S-*r*-PFPA)) where '*random*' indicates the random distribution of cross-linkers in the resulting sulfur network. Without the addition of an accelerator, the reaction was conducted at 160 °C for 4 hours, which is in range of typical IVs reported in literature. Two accelerators were utilized to investigate their influence on the conversion of sulfur and reaction temperature. Zinc diethyldithiocarbamate ($Zn(DTC)_2$) is known to be an efficient accelerator for IV by promoting phase transfer between the sulfur and organic phase yielding more homogenous products with less H_2S formation.[56] With $Zn(DTC)_2$ the reaction was carried out at 150 °C for 1 hour. Alternatively, 1-methyl imidazole (MIA) has been used as accelerator because organic amines have been reported to accelerate IV by initiating the nucleophilic cleavage of sulfur rings, thus allowing to dramatically reduce

the reaction temperature.[228] With MIA the reaction was carried out at 120 °C for 1 hour. 5 wt% of each accelerator were employed for the respective experiments.

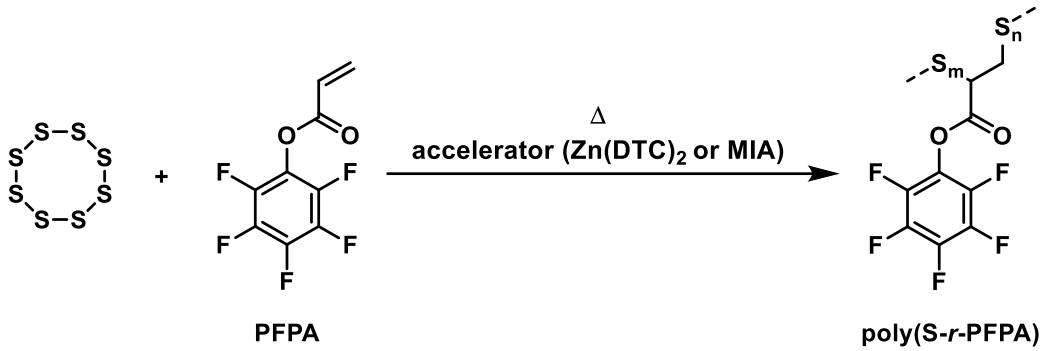

Scheme 15. Reaction scheme of the IV of PFPA yielding poly(S-*r*-PFPA). $Zn(DTC)_2$: zinc diethyldithiocarbamate; MIA: methyl imidazole. Brackets of repeating units are omitted for clarity and sulfur chains are abbreviated by dashed lines.

^{1}H NMR spectroscopy of poly(S-*r*-PFPA) with and without accelerator revealed quantitative conversion of C=C double bonds under all chosen reaction conditions as was confirmed by the disappearance of vinyl protons in the region of 6.0 – 7.0 ppm. However, the ^{19}F NMR spectra showed a shift of fluorine resonances attributed to PFPA *ortho*, *para*, and *meta* fluorine atoms from -153 ppm, -158 ppm, and -162 ppm, respectively, towards lower chemical shift (refer to **Figure 15**). The ratio of product fluorine atoms was found to be 2:2:1, which indicated a detachment of PFP species from the parent PFPA active ester during the IV by nucleophilic side reactions with thiyl radicals. Initiation with MIA may have led to the formation of nucleophilic sulfide anions, which could have reacted with active esters under formation of thiolesters.[229]

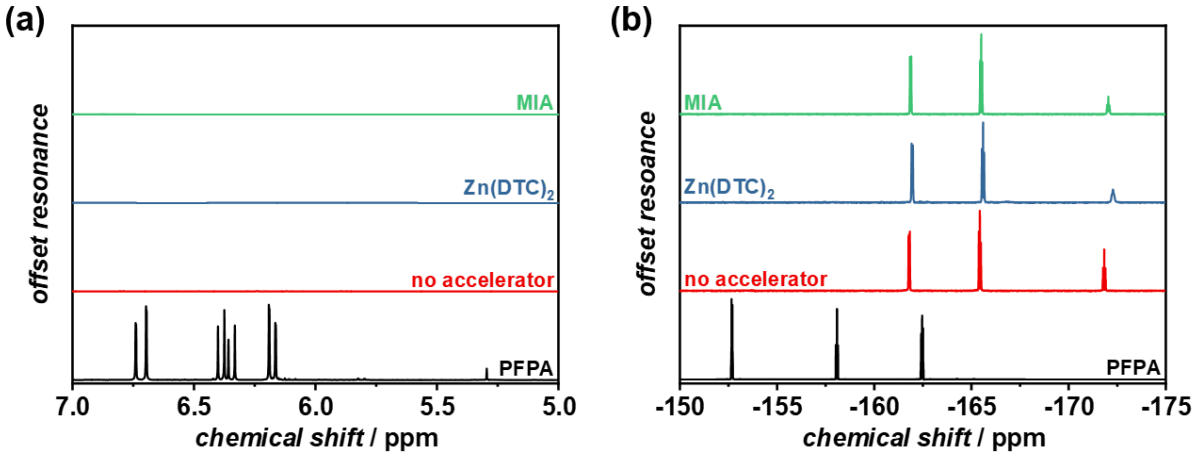

Figure 15. ^{1}H NMR spectra (a) and ^{19}F NMR spectra (b) of PFPA (black), poly(S-*r*-PFPA) without additional accelerator (red), poly(S-*r*-PFPA) with $Zn(DTC)_2$ (blue), and poly(S-*r*-PFPA) with MIA (green) as accelerator. Solvent: $CDCl_3$. ^{1}H NMR spectra are reduced to the region of C=C double bond protons.

The conversion of elemental sulfur was determined by differential scanning calorimetry (DSC), a main analysis method for the evaluation of IV. Sulfur exhibits a natural melting point of around 120 °C, depending on the exact composition of sulfur allotropes present in a sulfur sample. Thus, the absence of a melting in the area of 110 – 120 °C is an important indication for the complete consumption of crystalline sulfur. It needs to be noted that the absence of a sulfur melting peak in the DSC thermogram is not necessarily a confirmation for the absence of elemental sulfur itself. In 2022 the group of HASELL coined the term 'dark sulfur' that refers to sulfur released from an IV polymer over time, which then does not occur in DSC measurements as it does not crystallize in the polymer.[230] Evaluation of residual crystalline sulfur in IV polymers is based on the first heating ramp subjected to the equilibrated polymers since molten sulfur can undergo *in-situ* polymerization and allotrope change in the sample, thereby forming a metastable polymer during the measurement. Indeed, DSC measurements of poly(S-*r*-PFPA) revealed the presence of a sulfur melting peak between 110 and 120 °C, regardless of the presence of an accelerator (refer to **Figure 16**). One possible explanation for the presence of residual crystalline sulfur is the high polarity of acrylates, which is unfavorable for IV due to the low miscibility of molten sulfur.[56]

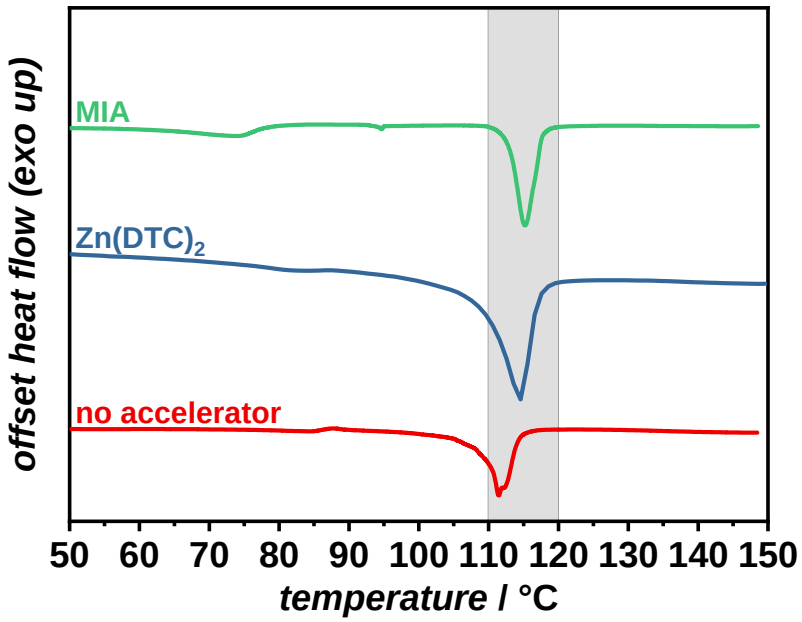

Figure 16. DSC thermograms of poly(S-*r*-PFPA) without accelerator (red), with $Zn(DTC)_2$ (blue), and with MIA (green) as accelerator. Highlighted: thermal range of sulfur melting. The first heating cycle is displayed. Heating rate: 10 K min^{-1}.

The unsatisfactory conversion of elemental sulfur and the decomposition of the PFP active ester groups during polymerization, showed that the IV of PFPA was not a suitable strategy for synthesizing active ester containing high sulfur content polymers and a different cross-linker system needed to be developed. This is further discussed in **Chapter 3.2** Inverse Vulcanization of Norbornenyl-Pentafluorophenyl-Ester.

3.1.2 All-cis-2,3,4,5,6-pentafluorocyclohexyl Acrylate

3.1.2.1 Disclaimer

The content of this chapter has been published in the European Polymer Journal from Elsevier (Amsterdam, Netherlands).[231] The complete authors list in the original order is Alexander P. Grimm, Dr. Bijian Deng, Dr. Shyamkumar V. Haridas, Dr. Dominik Voll, Dr. Christian W. Schmitt, Prof. Dr. Max von Delius, Dr. Frieder Scheiba, and Prof. Dr. Patrick Théato.

Alexander P. Grimm is the first author of the article. Parts of this chapter and the corresponding parts in the experimental section were adapted with permission from this publication written by the author (Alexander P. Grimm).

The author contributions were as follows: A. P. G.: conceptualization, methodology, validation, formal analysis, investigation, data curation, writing – original draft & review & editing, visualization; B. D.: validation, formal analysis, investigation, data curation, writing – review & editing; S. V. H.: validation, formal analysis, investigation, writing – review & editing; D.V. and C. W. S.: supervision, project administration, writing – review & editing; M. v. D., F. S., and P. T.: supervision, project administration, funding acquisition, writing – review & editing.

3.1.2.2 Results and discussion

Another interesting, fluorinated acrylate is all-*cis*-2,3,4,5,6-pantafluorocyclohexyl acrylate (PFCHA) which is the all-cis fluorinated derivative of cyclohexyl acrylate (CHA) and can be synthesized by a three-step synthesis route (refer to **Scheme 16**). First, pentafluoro anisole (1) was selectively all-*cis*-hydrogenated with pressurized hydrogen gas under presence of the rhodium catalyst [Rh(CAAC)(COD)Cl] (refer to **Appendix 2** for detailed complex structure).[226] The, so-called, 'JANUS-faced' (*i.e.* two-faced, from the two-faced roman god JANUS) all-*cis*-fluorinated methoxy derivative (2) was then deprotected to obtain all-*cis*-2,3,4,5,6-pentafluorocyclohexyl alcohol (3).[232] Analogous

to the synthesis of PFPA from PFP, the alcohol functional group was converted to an acrylate by reaction of **3** with acryloyl chloride in presence of a base, in this case 2,6-lutidine, yielding PFCHA.

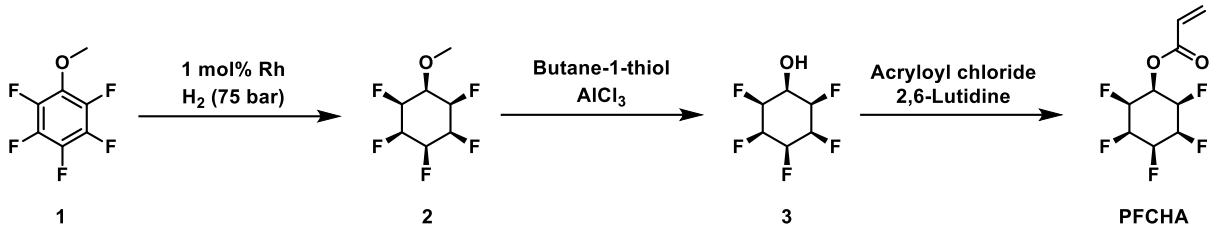

Scheme 16. Synthesis route of PFCHA from pentafluoro anisole via selective hydrogenation, deprotection, and acrylation. Rh = [Rh(CAAC)(COD)Cl].

The successful synthesis of PFCHA has been confirmed by ^{1}H NMR, ^{13}C NMR, and ^{19}F NMR spectroscopy as well as high-resolution mass spectrometry (HR-MS) (refer to **Appendix 3**). All-*cis*-fluorinated cyclohexyl derivatives are known to exhibit outstanding dipole moments (μ = 6.2 D for all-*cis*-1,2,3,4,5,6-hexafluorocyclohexane) which comes with some unique anion and cation binding interactions and aggregation.[233–235] One feature of particular interest is the capability of these JANUS-faced molecules to coordinate to anions due to their high dipole moment, thereby hindering their movement which has been confirmed for F^-, Cl^-, Br^-, I^-, and NO_3^- anions.[226] It was hypothesized that presence of JANUS-faced moieties in a high sulfur content polymer would have beneficial influence on the cycling behavior of Li-S battery cells. Despite the high energy density (theoretical capacity: 1672 mAh g^{-1}) and high specific energy (2567 Wh kg^{-1}) of Li-S batteries, these battery types suffer from a number of drawbacks, one of which is the so-called 'shuttle-effect'. The shuttle-effect refers to the diffusion of soluble intermediate lithium polysulfide and oligosulfides species which are formed during the redox mechanism of a Li-S cell. These poly- and oligosulfides can diffuse ('shuttle') to the Li anode where they form an insoluble passivating Li_2S layer (refer to **Figure 17**). This leads to a rapid capacity fading of Li-S cells and is one of the major issues Li-S based battery systems face to this day, despite the abundance and safety of sulfur as alternative feedstock for high-performance energy storage systems.[236]

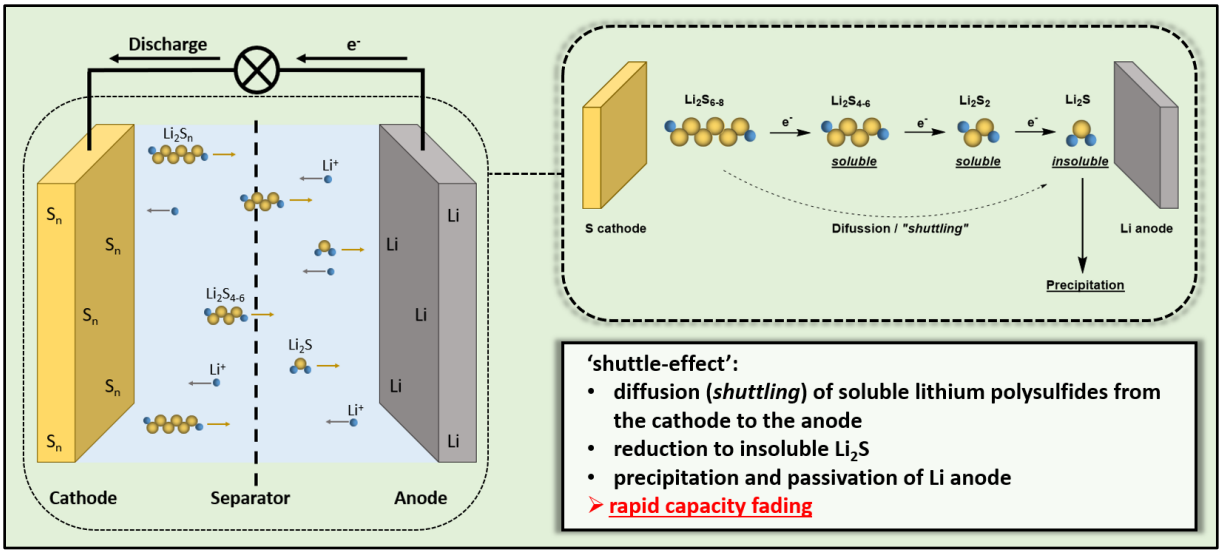

Figure 17. Schematic representation of a Li-S cell with polysulfide diffusion during discharge (left) and detailed visualization of the reduction of soluble poly and oligosulfides to insoluble Li_2S (right) which leads to capacity fading.

JANUS-faces motifs are hypothesized to coordinate sulfide anions, similar to the aforementioned halogen and nitrate anions which would allow the reduction of sulfide shuttling by reduction of diffusion. Therefore, a material was designed to fulfil 3 main criteria:

1. Sulfur content – Since the electrochemical capacity directly correlates with the amount of sulfur present in the cathode, the sulfur content of the cathode material needs to be as high as possible while not being too high to ensure complete stabilization of the sulfur network by the chosen cross-linkers.

2. Coordination sites – The number of Janus-faced cyclohexyl moieties needs to be high enough to allow a significant amount of sulfur to be coordinated while not compromising cathode capacity

3. Insolubility – Electrolytes used in Li-S batteries are typically based on liquid 1,3-dioxolane (DOL) and dimethoxyethan (DME). The cathode material therefore needs to be insoluble in these solvents to ensure spatial separation between cathode and anode.

Based on earlier works, insolubility of the material was derived from the hydrolysis and polycondensation of ethoxy silanes and triethoxyvinylsilane (TEVS) was employed as a termonomer during the IV of PFCHA. Thus, the IV of PFCHA was conducted with TEVS in *N*-metyhl-2-pyrrolidone (NMP) with weight ratios of 50 wt% sulfur, 25 wt% PFCHA and 25 wt% TEVS at 150 °C for 18 hours. The reaction temperature was limited by the boiling point of TEVS of 160 °C. The use of transition metal catalysts

was avoided due to the planned application in a battery cell and the associated influence of redox active compounds therein. After the polymerization, the reaction mixture was poured into H_2O to induce the hydrolysis of ethoxy groups of TEVS. Cross-linking via polycondensation was subsequently done by removal of water at 70 °C under reduced pressure. The obtained material was named poly(sulfur-all-*cis*-2,3,4,5,6-pentafluorocyclohexyl acrylate-triethoxyvinylsiloxane) (poly(S-PFCHA-TEVS)) (refer to **Scheme 17**). The respective non-fluorinated material, named poly(sulfur-cyclohexyl acrylate-triethoxyvinylsiloxane) (poly(S-CHA-TEVS)) was synthesized using cyclohexyl acrylate (CHA) instead of PFCHA as a comparative reference material for the proof-of-concept of the beneficial influence of all-*cis*-fluorinated moieties on electrochemical performance in Li-S cells.

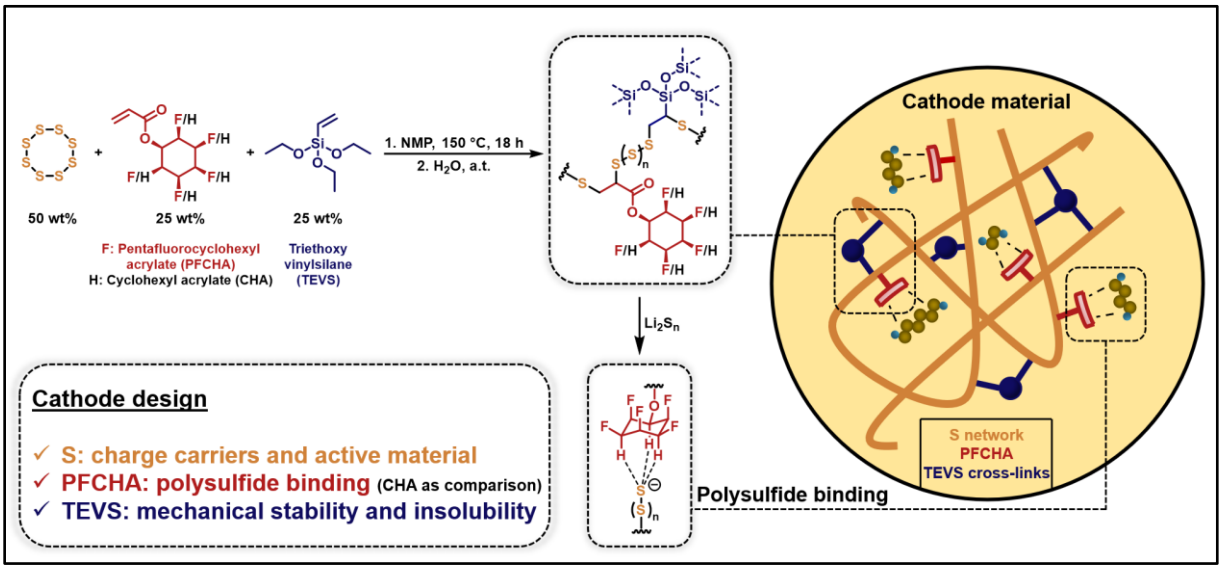

Scheme 17. Reaction scheme of the inverse vulcanization of both fluorinated (red) and non-fluorinated (black) cyclohexyl acrylate with triethoxyvinylsilane (left). Silane hydrolysis and condensation yields insoluble cathode materials with modulated polarity, which facilitates coordination of polysulfides and therefore hinders polysulfide shuttling in the cathode material (right).

DSC confirmed the full conversion of elemental sulfur into organic polysulfides was as the DSC traces showed no melting of crystalline sulfur in the range of 110 – 120 °C for both poly(S-PFCHA-TEVS) and poly(S-CHA-TEVS). Additionally, poly(S-CHA-TEVS) was found to have a glass transition at 25 °C which shifted to 5 °C in the second heat run. Poly(S-PFCHA-TEVS) did not show a glass transition in the investigated temperature range between -25 °C and 150 °C (refer to **Figure 18a**). However, increasing the heating rate from 10 K min^{-1} to 20 K min^{-1} allowed estimation of a T_g for poly(S-PFCHA-TEVS) of 138 °C (refer to **Figure 18b**). This is believed to be caused

by the strong interaction between the two JANUS faces of the fluorinated cyclohexyl rings, which influences thermal chain movement and therefore affects the T_g compared to the non-fluorinated material.[235] Increasing the sulfur content from 50 wt% to 60 wt% resulted in the presence of residual crystalline sulfur in poly(S_{60}-$PFCHA_{25}$-$TEVS_{15}$), thereby limiting the amount of sulfur to 50 wt% to ensure complete conversion of elemental sulfur during polymerization (refer to **Figure 18c**).

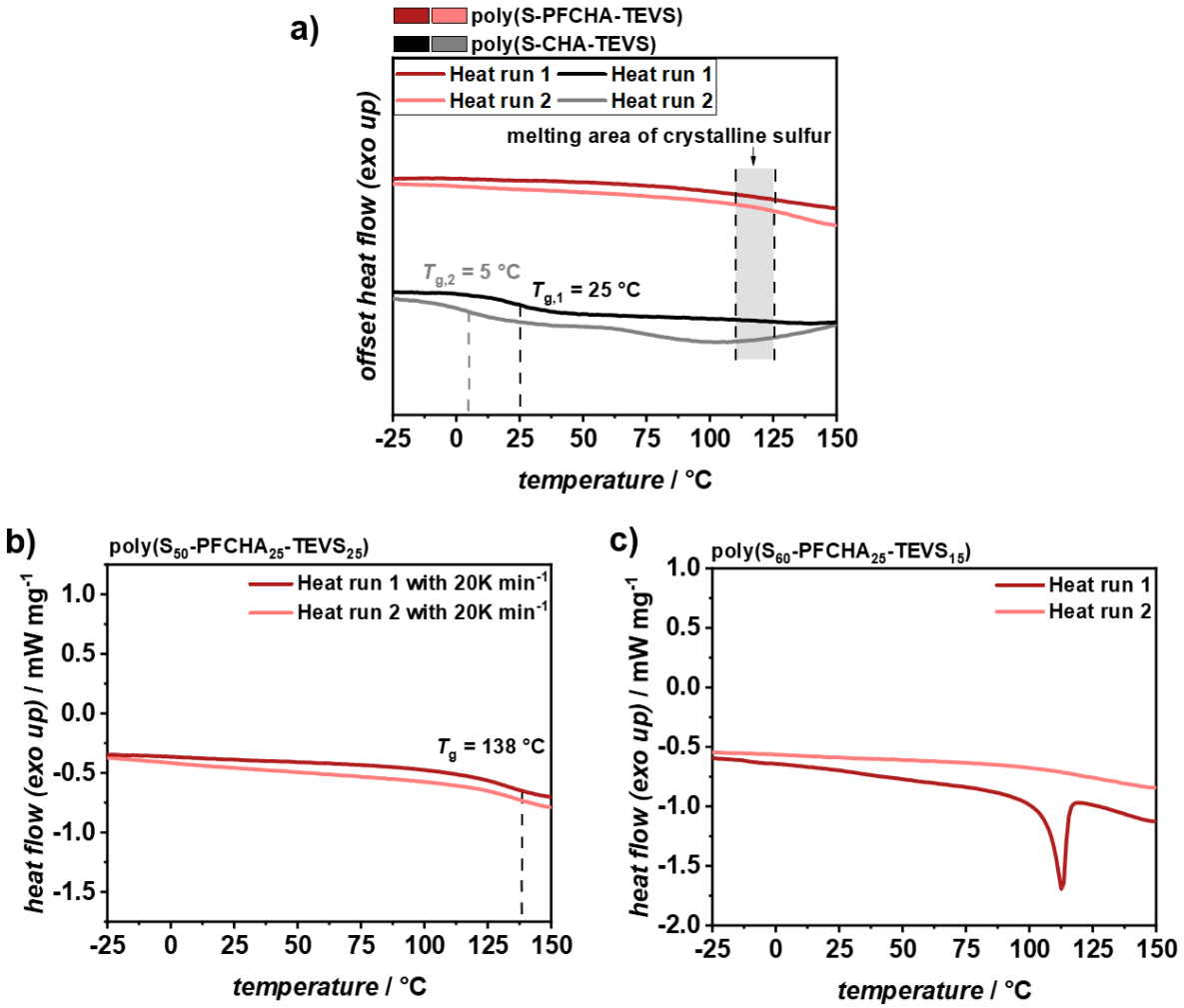

Figure 18. a) DSC thermograms of poly(S-PFCHA-TEVS) (red) and poly(S-CHA-TEVS) between -25 °C and 150 °C. Highlighted: thermal range of sulfur melting. T_g of poly(S-CHA-TEVS) shifted from 25 °C in the first to 5 °C in the second heat run. Heating rate: 10 K min^{-1}. b) DSC analysis of poly(S-PFCHA-TEVS) at a heating rate of 20 K min^{-1} allowed estimation of the T_g at 138 °C. c) IV of PFCHA and TEVS with 60 wt% S, 25 wt% PFCHA, and 15 wt% TEVS resulted in the presence of residual crystalline sulfur in the material which melted at 112 °C.

ATR FT-IR spectroscopy confirmed the presence of Si-O-Si networks by polycondensation of TEVS by a very strong and broad absorption band in the region of 1250 – 900 cm^{-1}.[237] Additionally, the absence of characteristic vinyl C-H and C=C bond vibrations at 3080 and 900 cm^{-1}, respectively, was indicative for the successful

conversion of comonomer double bonds during the IV under the chosen reaction conditions (refer to **Figure 19**). Elemental analysis (EA) of poly(S-CHA-TEVS) revealed a final sulfur content in the material of 61 wt%, which is in line with the theoretically expected sulfur content of 57 wt%, after elimination of ethanol due to polycondensation.

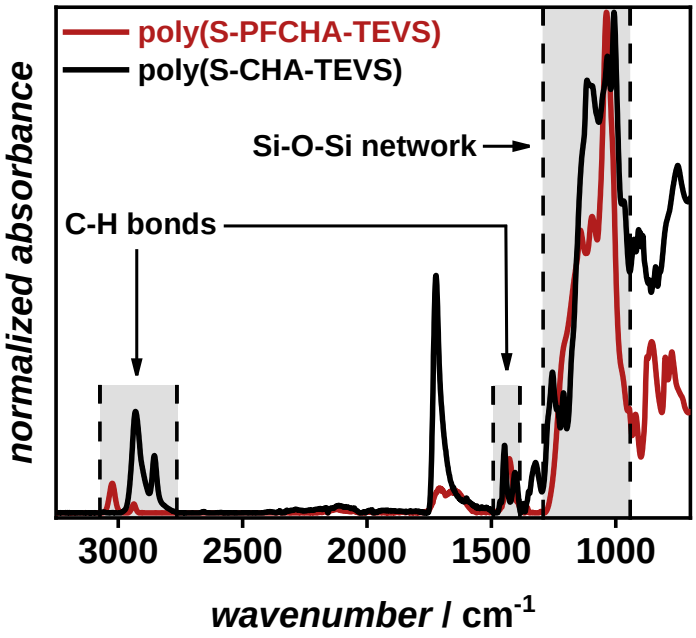

Figure 19. ATR FT-IR spectra of poly(S-PFCHA-TEVS) (red) and poly(S-CHA-TEVS) (black). Resolution: 2 cm^{-1}.

Both materials were found to be insoluble in a mixture of DME:DOL (1:1 v/v), which is representative of the liquid electrolyte used for cell fabrication (refer to **Figure 20a and b**). Reducing the TEVS content to 15 wt% resulted in a material that was still slightly soluble in DME/DOL (1:1 v/v) as was found by coloration of the solution (refer to **Figure 20c**). IV of PFCHA without TEVS (poly(S_{50}-$PFCHA_{50}$)) gave a material that was readily soluble in THF and NMP and was therefore not applicable as cathode material in liquid electrolyte-based batteries (refer to **Figure 20d and e**).

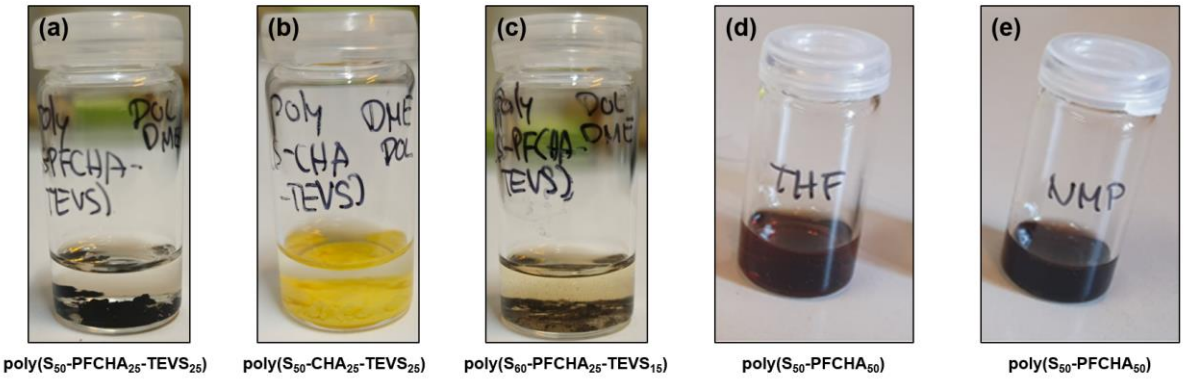

Figure 20. Photographs of insoluble poly(S-PFCHA-TEVS) (a) and poly(S-CHA-TEVS) (b) in a solution of DME/DOL (1:1 v/v). Poly(S_{60}-$PFCHA_{25}$-$TEVS_{15}$) exhibited slight solubility in DME/DOL (1:1 v/v) (c) and materials without TEVS were soluble in THF (d) and NMP (e).

Since elemental analysis of highly fluorinated materials poses a challenge to the sensitive analytical devices, thermogravimetric analysis (TGA) was conducted to further validate the sulfur contents of both materials. The thermograms of poly(S-PFCHA-TEVS) and poly(S-CHA-TEVS) show one pronounced thermal degradation occurring at approximately 180 °C, which accounts for a weight loss of around 60 wt% and can be associated with the decomposition of polysulfide species in the material and is in close agreement to the sulfur content determined by elemental analysis of poly(S-CHA-TEVS) (refer to **Figure 21**). The residual 34 wt% are attributed to undecomposed siloxanes which are known to exhibit outstanding thermal stability.[238]

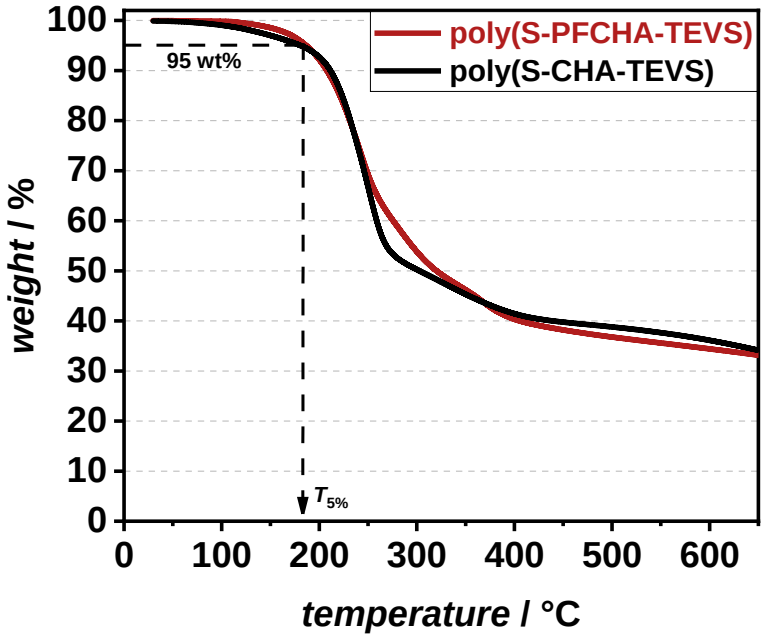

Figure 21. TGA profile of poly(S-PFCHA-TEVS) (red) and poly(S-CHA-TEVS) (black) from a.t. to 650 °C. Heating rate: 10 K min^{-1}. $T_{5\%}$ = 180 °C for both materials.

Li-S cells with poly(S-PFCHA-TEVS) or poly(S-CHA-TEVS) as cathode materials, respectively, and subjected to cyclic voltammetry (CV) to evaluate their electrochemical activity (for detailed cell fabrication process, refer to **Chapter 5.2.2** Fabrication of Li-S cells).

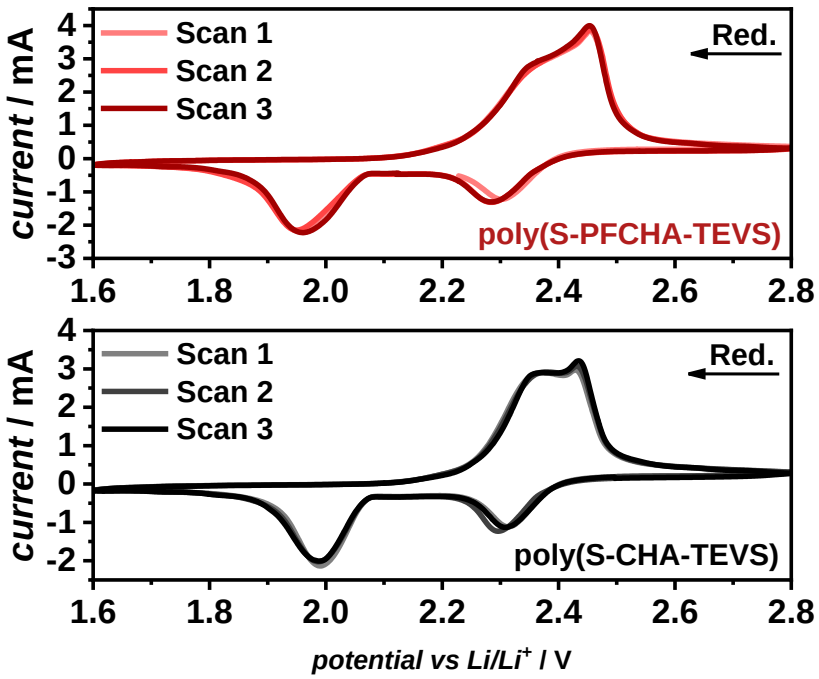

Figure 22. CV plots of poly(S-PFCHA-TEVS) (top) and poly(S-CHA-TEVS) (bottom) with three cycles each. Cathodic peaks up; Anodic peaks down. Scan rate: 0.2 mV s^{-1}.

During the initial cycle, two cathodic peaks were detected at 2.30 V and 1.95 V for poly(S-PFCHA-TEVS) and at 2.30 V and 1.99 V for poly(S-CHA-TEVS), demonstrating that the redox potential remained unaffected by changes in the acrylate structure. These peaks are characteristic of the sequential reduction of elemental sulfur into lower-rank polysulfide species occurring in liquid electrolyte Li–S batteries (refer to **Figure 22**).[239] The peak at 2.30 V corresponds to the reduction of polysulfide chains, forming high-order inorganic lithium polysulfides (Li_2S_x, where x = 6 – 8) and high-order organic polysulfides bonded to PFCHA and TEVS, respectively (C–S_x–Li, where x = 6 – 8). Further reduction at approximately 1.95 V and 1.97 V, respectively, led to the formation of low-order inorganic lithium polysulfides (Li_2S_x, where x = 1 – 3) and low-order organic polysulfides (C–S_x–Li, where x = 1 – 3).[128] On the reverse sweep, a split broad anodic peak with maxima at 2.36 V and 2.45 V for both materials indicated the oxidation of low-order inorganic and organic polysulfides back to their high-order

forms (refer to **Scheme 18**).[240] The slightly larger peak area in the cyclic voltammogram of poly(S-PFCHA-TEVS), particularly at the second oxidation and first reduction peaks, suggests enhanced polysulfide conversion facilitated by improved Li^+ ion mobility.[241] The consistent appearance of cathodic and anodic peaks over all three CV cycles highlighted the robust reversibility of the electrochemical reactions.

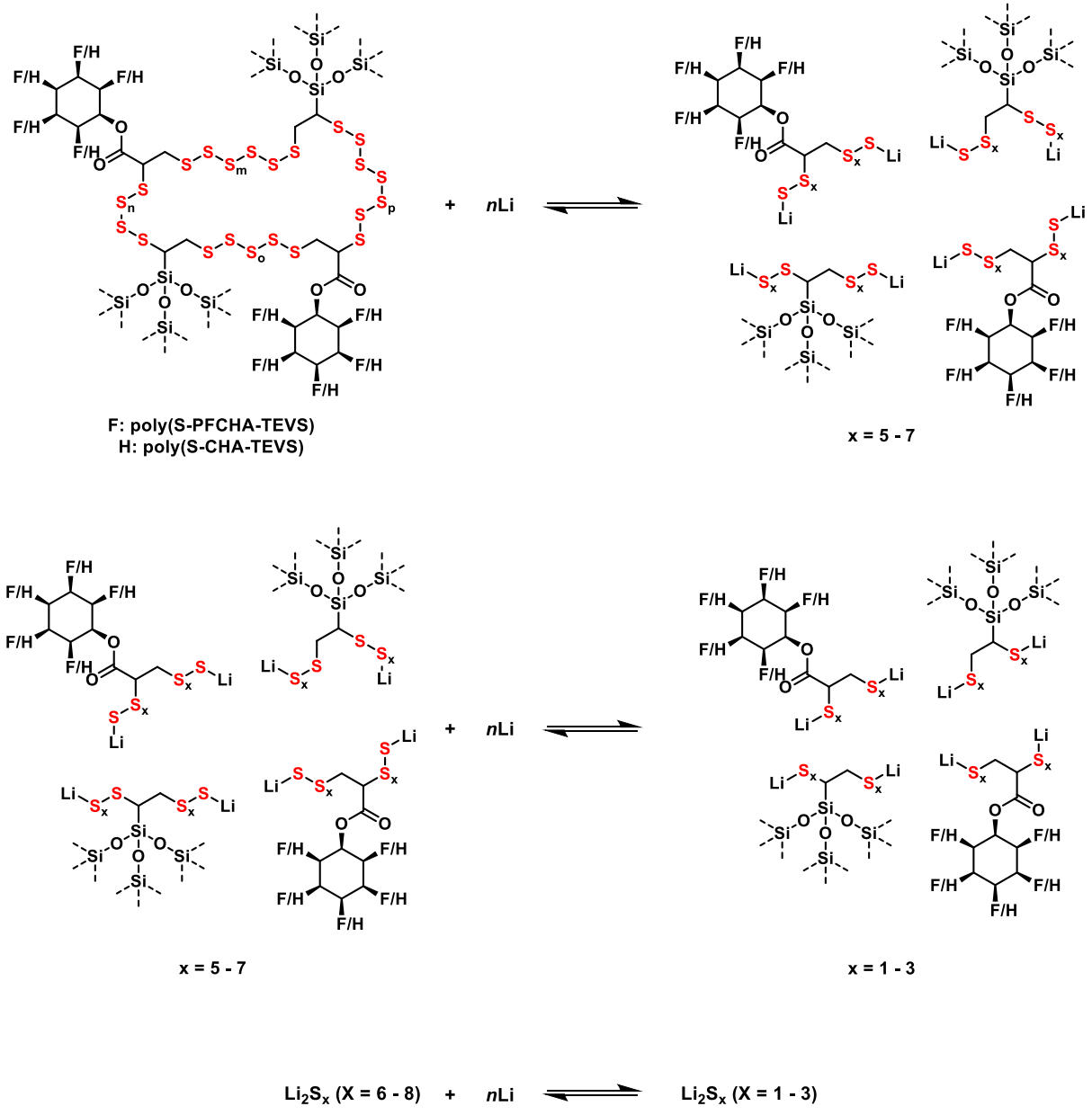

Scheme 18. Schematic visualization of the redox mechanism of poly(S-PFCHA-TEVS) and poly(S-CHA-TEVS) with lithium. Siloxane networks are abbreviated with dashed lines.

It is known that the fluorine face of all-cis fluorinated cyclohexyl derivatives can coordinate to alkali metal cations such as Na^+ and Li^+,[242] while the hydrogen face of all-*cis* fluorinated cyclohexyl derivatives has been found to bind anions such as

halogenides and nitrates (refer to **Figure 23**).[226,234] Thus, the proposed polysulfide coordination by the JANUS-faced PFCHA moieties was hypothesized to be expressed by an influence on electrolyte viscosity and therefore Li^+ ion diffusion during cycling. CV measurements of both poly(S-PFCHA-TEVS) and poly(S-CHA-TEVS) with varying sweep rates from 0.02 mV s^{-1} to 0.5 mV s^{-1} were conducted to elucidate the diffusion of Li^+ ions in the cells (refer to **Figure 24a**).

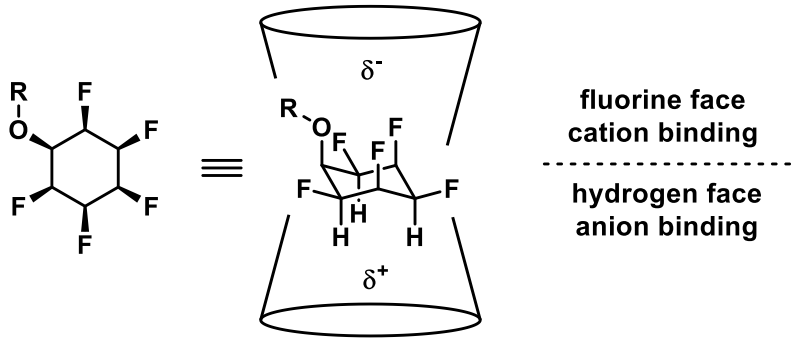

Figure 23. Structure of the JANUS-face aspect present in PFCHA. Two protons are omitted for clarity.

The anodic and cathodic peak currents showed an increase in current with the scan rate, which is consistent with the RANDLES-ŠEVČÍK equation (Eq. 1) which correlates CV peak currents with the square root of the respective scan rate in dependency of the apparent diffusion coefficient of lithium ions (D_{Li^+} [cm^2 s^{-1}]):

$$I_p = (2.69 \times 10^5) n^{1.5} A C_{Li} \sqrt{D_{Li^+} \nu} \qquad \text{(Eq. 1)}$$

I_p is the peak current of the individual redox peak [A], n is the number of charge carriers transferred during a redox step (here: n = 1), A is the electrode area [cm^2], C_{Li} is the concentration of lithium ions [mol L^{-1}], and v is the CV scan rate [V s^{-1}]. The peak currents were found to correlate linearly with the square root of the scan rate and the slope of the linear fit allowed calculation of D_{Li^+} (refer to **Figure 24b**).

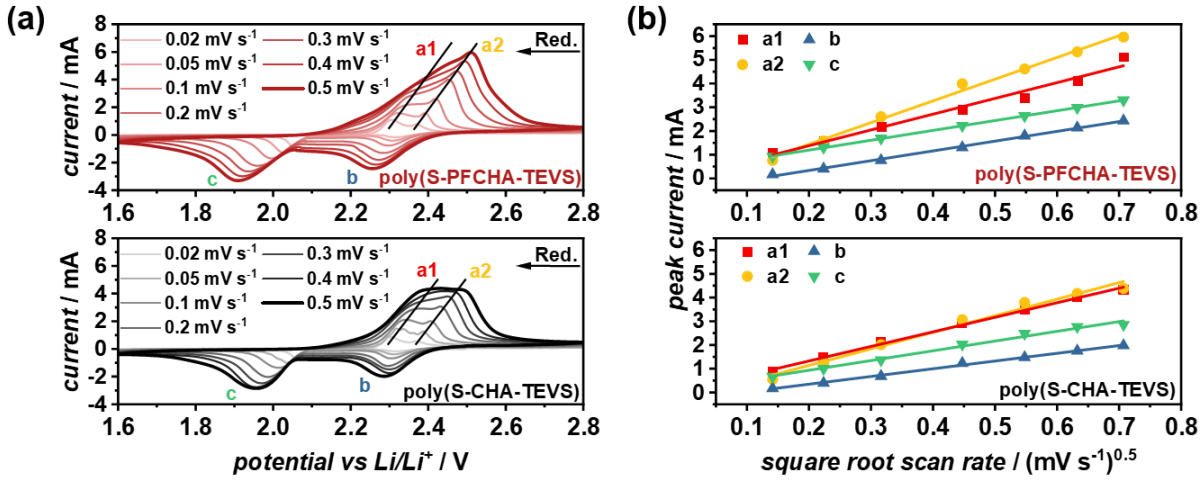

Figure 24. a) CV measurements of poly(S-PFCH-TEVS) (top) and poly(S-CHA-TEVS) (bottom) at different scan rates. b) Plots of peak current vs. the square root of the scan rate with linear fits for both materials.

The resulting D_{Li^+} values were calculated according to the RANDLES-ŠEVČÍK equation for each individual redox peak and are shown in **Figure 25**. It is apparent that D_{Li^+} was significantly higher in Li-S cells containing poly(S-PFCHA-TEVS) compared to poly(S-CHA-TEVS), which indirectly confirms the binding of polysulfides by PFCHA units through lower electrolyte viscosity due to reduced distribution of polysulfides in the electrolyte.

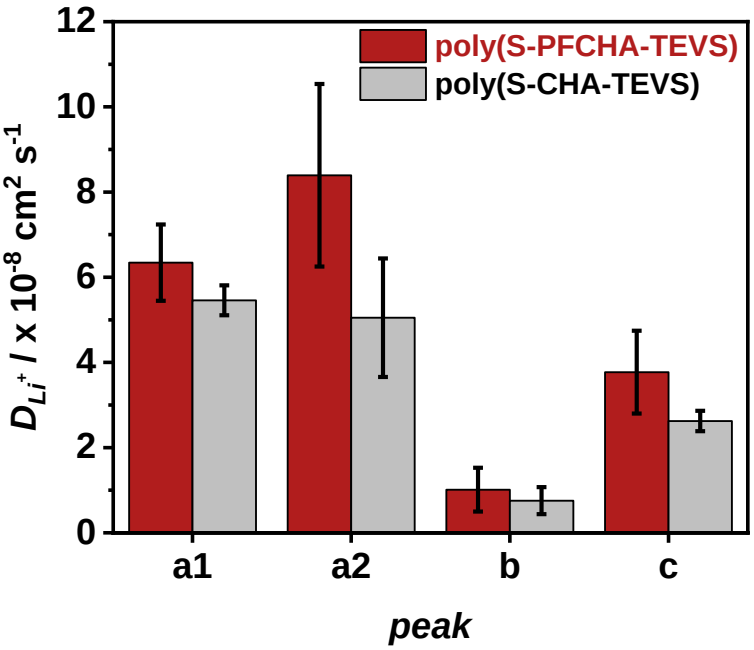

Figure 25. Lithium-ion diffusion coefficients of each redox peak identified during CV measurements of poly(S-PFCHA-TEVS) (red) and poly(S-CHA-TEVS) (gray). Error bars are derived from the uncertainty of the linear fits of the slopes used for the RANDLES-ŠEVČÍK calculation.

It needs to be noted that the exact structure of coordination between PFCHA and lithium polysulfides remains elusive to this day. It is unclear whether the lithium sulfide species dissociate in the presence of PFCHA to be coordinated separately through lithium cations and polysulfide anions (refer to **Figure 26a**) or if the lithium polysulfides are coordinated as a whole (refer to **Figure 26b**). Further studies are necessary to uncover the complex coordination conditions and structures present in Li-S cells during cycling.

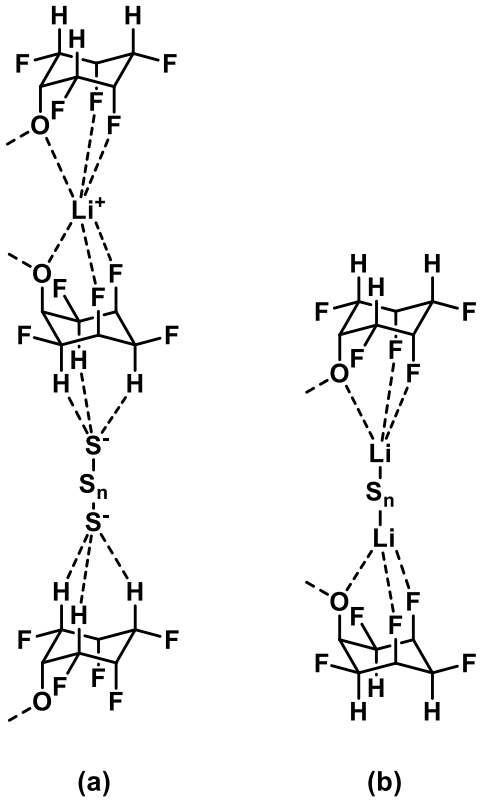

Figure 26. Possible structures of lithium polysulfides coordinated by PFCHA moieties: (a) dissociated into lithium cations and polysulfide anions and (b) associated as lithium polysulfide. Only the cyclohexyl rings of PFCHA are shown for clarity. Two protons are omitted per ring.

The electrochemical charge-discharge cycling performance of poly(S-PFCHA-TEVS) and poly(S-CHA-TEVS) against was evaluated through long-term cycling against lithium metal at 1 C and 0.5 C (refer to **Figure 27**). Notably, poly(S-CHA-TEVS) initially exhibited a capacity of approximately 550 mAh g^{-1}, which rapidly declined to around 280 mAh g^{-1} within the first 50 cycles (approximately 51 % retention). This initial capacity loss was attributed to the irreversible loss of soluble polysulfide species and the deposition of lithium sulfides and decomposed electrolyte components on the lithium metal anode. After 200 cycles, only 38 % of the initial capacity remained before

the cells failed. In contrast, poly(S-PFCHA-TEVS) did not experience this early capacity loss and instead, its capacity increased by approximately 12 %, rising from 550 mAh g^{-1} to 650 mAh g^{-1} over the first 100 cycles before gradually declining. By cycle number 200, the initial capacity of 550 mAh g^{-1} was reached and after 400 cycles, the cells failed, retaining only 150 mAh g^{-1}, which corresponds to approximately 27 % of the initial capacity.

Additional long-term cycling at 0.5 C revealed an expected overall increase in capacity for both poly(S-PFCHA-TEVS) and poly(S-CHA-TEVS) as cathode materials due to the rate-capacity effect. However, in contrast to PFCHA-containing cells, cells with CHA exhibited a sharp 29 % capacity loss within the first 10 cycles. After 500 cycles, CHA-based cells retained a capacity of 543 mAh g^{-1}, representing an overall capacity retention of 63 %. Meanwhile, poly(S-PFCHA-TEVS) cells cycled at 0.5 C displayed a less uniform capacity trend but maintained 96% of their initial capacity after 200 cycles before capacity fading began. After 500 cycles at 0.5 C, the cells retained 44 % of the initial capacity at 391 mAh g^{-1}. Although the underlying mechanism for the capacity increase during cycling and good capacity retention despite low Coulombic efficiency remains unclear, the integration of all-*cis*-fluorinated cyclohexyl groups into the cathode material over non-fluorinated counterparts appears to significantly enhance cycling performance.

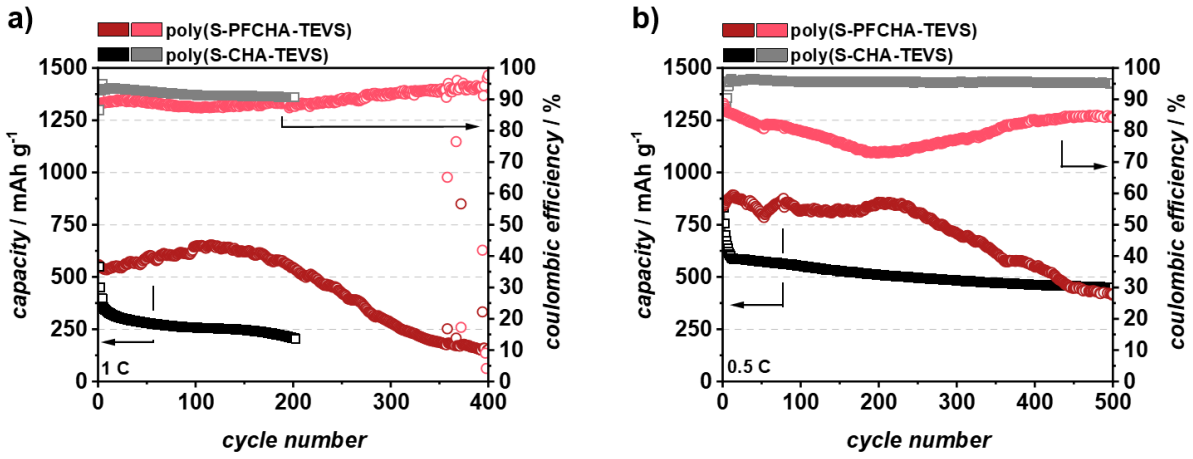

Figure 27. Long-term cycling of poly(S-PFCHA-TEVS) (red) and poly(S-CHA-TEVS) (black) against lithium at 1 C for 400 cycles (a) and at 0.5 C for 500 cycles (b).

To investigate charge transfer processes at the electrode/electrolyte interface, electrochemical impedance spectroscopy (EIS) was conducted on Li-S cells with poly(S-PFCHA-TEVS) and poly(S-CHA-TEVS) cathodes after 100 and 200 cycles

(refer to **Figure 28a**). Notably, cells containing poly(S-PFCHA-TEVS) as the cathode material exhibited no significant increase in impedance after an additional 100 cycles, aligning with their stable long-term cycling performance. CHA-containing cells on the other hand showed an increase in impedance between cycles 100 and 200, likely due to the formation of a passivating Li_2S/Li_2S_2 layer on their active mass surface.[243] Interestingly, PFCHA-based cells displayed an additional semicircle in the 1 Hz – 1 kHz range, which is hypothesized to result from charge transfer in adsorbed ions at the electrolyte/electrode interface.[244] The relative differences in the impedance spectra are visualized via normalized $-Z_{im}$ over the investigated frequency range. The additional semicircle can be clearly seen between 1 Hz and 1kHz (refer to **Figure 28b**).

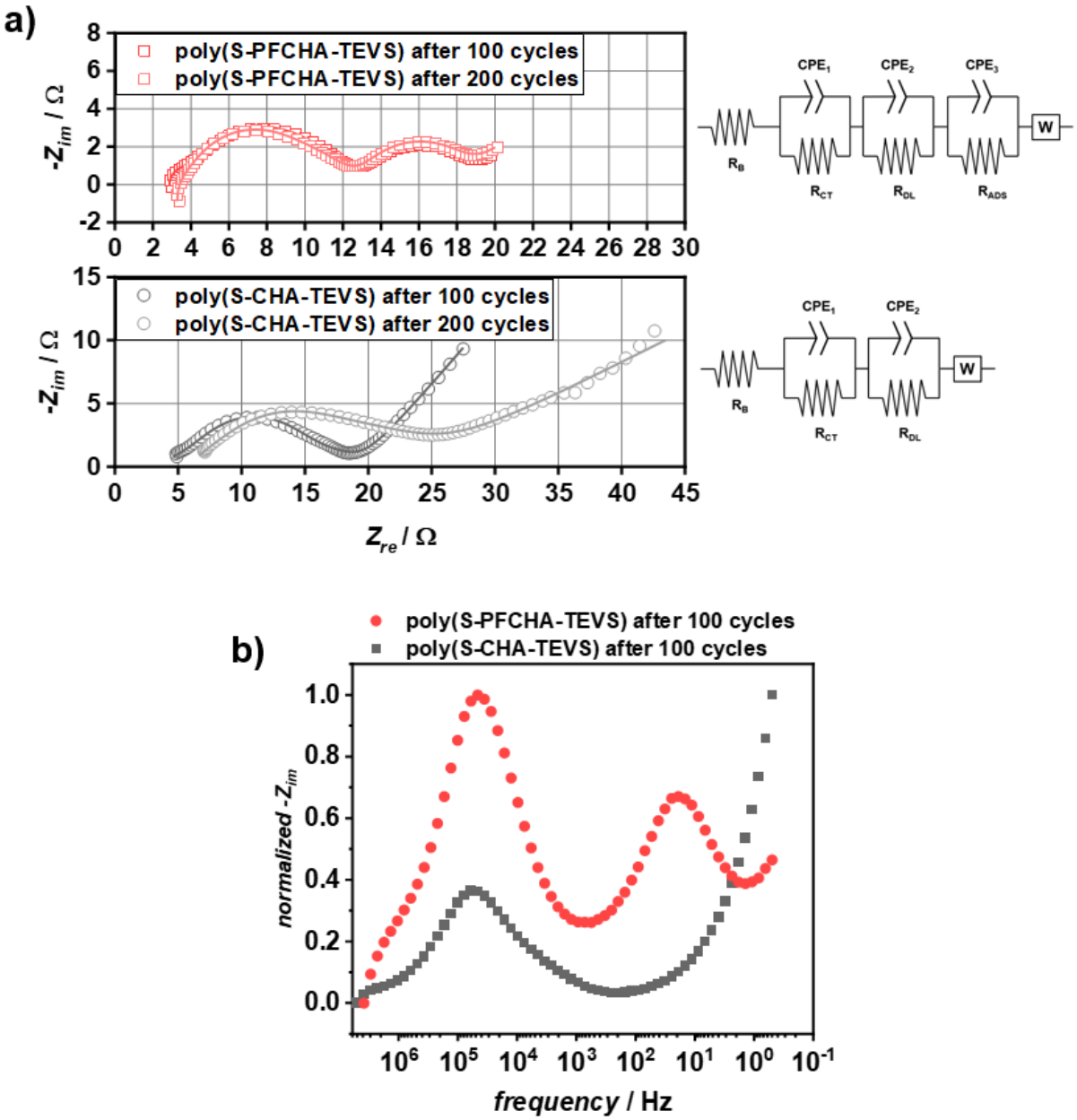

Figure 28. a) EIS spectra (left) of poly(S-PFCHA-TEVS) (red) and poly(S-CHA-TEVS) (gray) after 100 and 200 cycles, respectively and the equivalent circuits used for data fitting (right). R_{CT} = charge transfer resistance; R_{DL} = double layer resistance; R_{ADS} = adsorption resistance; W = Warburg resistance; CPE = constant phase element. b) Plot of normalized $-Z_{im}$ vs. frequency to visualize the different shapes of the EIS spectra.

Future research is necessary in order to explore whether this effect is specific to all-*cis*-fluorinated cyclohexane derivatives or if it can be generalized to other high-dielectric-permittivity compounds.[245] To assess the rate capabilities of both poly(S-PFCHA-TEVS) and poly(S-CHA-TEVS), galvanostatic cycling with potential limitation (GCPL) was conducted (refer to **Figure 29**). Both exhibited satisfactory capacity reversibility. Notably, poly(S-CHA-TEVS) effectively recovered from C-rates as high as 3 C back to its original capacities at 0.5 C (100 %), 0.2 C (97 %), and 0.1 C (88 %).

Conversely, while poly(S-PFCHA-TEVS)-containing cells displayed significantly higher capacities, they were less effective at regaining the original capacity after cycling at 3 C, after which only 92 % of the capacity at 0.5 C were achievable. Further reduction of C-rate to 0.2 C and 0.1 C showed a capacity retention of 90 % and 88 % of the respective capacities that were reached before cycling at 3 C.

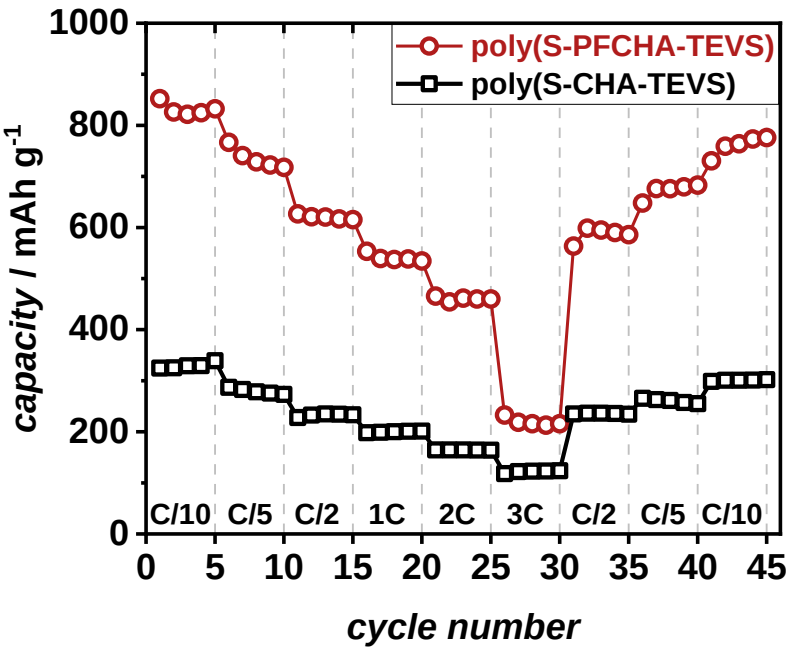

Figure 29. GCPL of poly(S-PFCHA-TEVS) (red) and poly(S-CHA-TEVS) (black) at different C-rates against lithium.

Charge-discharge profiles revealed that poly(S-PFCHA-TEVS) had a lower voltage difference between charge and discharge plateaus (Δ = 171 mV) compared to poly(S-CHA-TEVS) (Δ = 183 mV), indicating reduced electrochemical polarization (refer to **Figure 30**). This effect became more pronounced at higher C rates due to an accelerated conversion of soluble lithium polysulfides to insoluble Li_2S_2/Li_2S facilitated by poly(S-PFCHA-TEVS) compared to CHA-containing cells.[243]

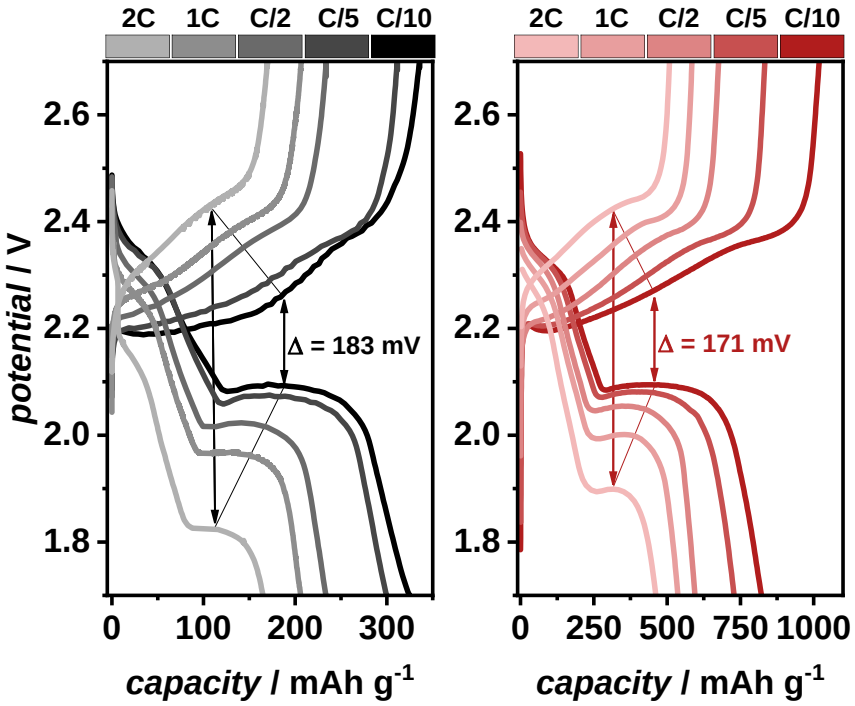

Figure 30. Charge-discharge profiles of poly(S-PFCHA-TEVS) (right) and poly(S-CHA-TEVS) (left) at different C-rates against lithium.

Self-discharge in Li-S batteries occurs when soluble polysulfides diffuse to the anode and react with lithium, forming insoluble and passivating Li_2S/Li_2S_2 on the active material. This process leads to a gradual decline in potential between the sulfur cathode and lithium anode. To investigate whether the incorporation of all-*cis*-fluorinated cyclohexyl groups inhibits polysulfide shuttling, the self-discharge behavior of Li-S cells using poly(S-PFCHA-TEVS) and poly(S-CHA-TEVS) as cathode materials was compared by monitoring open-circuit voltage over time.[245,246] Fresh cells were cycled at 0.2 C for two cycles before stopping the current flow, after which their open-circuit voltage was tracked for 21 days. Both cells exhibited an initial rapid voltage drop once the power was turned off and interestingly, the poly(S-CHA-TEVS) cell showed a continuous and gradual voltage decline over 14 days before stabilizing. In contrast, the poly(S-PFCHA-TEVS) cell displayed almost no further voltage decay after the initial drop, maintaining stability for 21 days and exhibiting minimal self-discharge (refer to **Figure 31**). Specifically, poly(S-PFCHA-TEVS) cells showed only a 20 mV decrease after 21 days, whereas poly(S-CHA-TEVS) cells lost 70 mV over the same period. This stable voltage retention suggests that the suppression of polysulfide diffusion through the electrolyte is primarily due to their coordination with the highly polar all-*cis*-cyclohexyl anchor points, effectively mitigating self-discharge.[226,247]

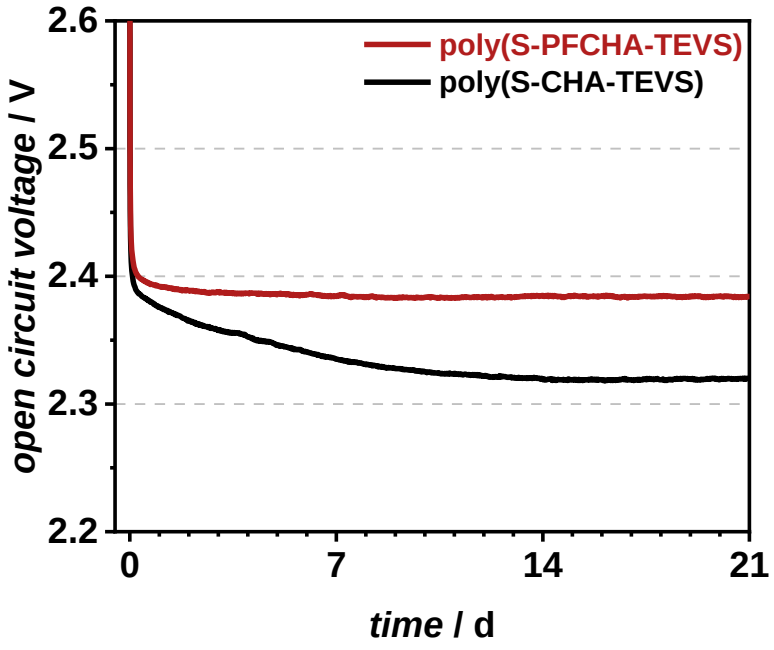

Figure 31. Self-discharge of Li-S cells with poly(S-PFCHA-TEVS) (red) and poly(S-CHA-TEVS) (black) as cathode material.

3.1.3 Summary

In summary, the IV of PFPA and PFCHA was investigated. PFPA was found to be unsuitable for IV due to the lability of the active ester functional group, which did not withstand the harsh IV polymerization conditions. PFCHA, however, was successfully incorporated into a high sulfur content material via IV and applied as cathode material in Li-S cells. The performance of the PFCHA-containing material was significantly improved compared to the non-fluorinated reference material, as confirmed by superior lithium-ion diffusion observed in CV analysis. Cycling experiments demonstrated excellent capacity retention, with 98 % remaining after 200 cycles at 1 C and 96 % after 200 cycles at 0.5 C before capacity fading began. In contrast, the reference material retained only 38 % and 61 % of its capacity after 200 cycles at 1 C and 0.5 C, respectively. Self-discharge studies revealed a voltage decay of just 20 mV over 21 days in PFCHA-containing Li-S cells, compared to 70 mV in the reference system. It is proposed that the presence of highly polar moieties in PFCHA inhibits sulfide shuttling, however, other factors, such as an overall increase in dielectric permittivity, cannot be ruled out. Further investigations are required to fully understand the structural characteristics and coordination behavior of polysulfides at JANUS-faced moieties in Li-

S batteries, which could expand the applicability of such compounds in modern energy storage systems.

Despite these open questions, the synthetic strategy presented here represents a highly promising approach for developing next-generation high-performance energy storage systems based on all-cis-fluorinated compounds.

3.2 Inverse Vulcanization of Norbornenyl-Pentafluorophenyl-Ester

3.2.1 Disclaimer

The content of this chapter (excluding **Chapter 3.2.7** PPM with Ferrocenyl Methylamine) has been published in Angewandte Chemie International Edition from Wiley-VCH GmbH (Weinheim, Germany).[25] The complete authors list in the original order is Alexander P. Grimm, Dr. Martina Plank, Andreas Stihl, Dr. Christian W. Schmitt, Dr. Dominik Voll, Prof. Dr. Felix H. Schacher, Prof. Dr. Jörg Lahann, and Prof. Dr. Patrick Théato.

Alexander P. Grimm is the first author of the article. Parts of this chapter and the corresponding parts in the experimental section were adapted with permission from this publication written by the author (Alexander P. Grimm).

The author contributions were as follows: A. P. G.: conceptualization, methodology, validation, formal analysis, investigation, data curation, writing – original draft & review & editing, visualization; M. P.: validation, formal analysis, investigation, data curation, writing – review & editing; A. S.: validation, formal analysis, investigation, writing – review & editing; C. W. S and D. V.: supervision, project administration, writing – review & editing; F. H. S., J. L., and P. T.: supervision, project administration, funding acquisition, writing – review & editing.

3.2.2 Strategy

Based on the results presented in **Chapter 3.1.1** Pentafluorophenyl Acrylate, an alternative to PFPA as cross-linker was necessary in order to facilitate efficient PPM of IV polymers via amidation of active esters. Motivated by previous results published by Scheiger *et al.*,[24] as well as the establishment of norbornene (NB) derivatives in IV, norbornenyl-pentafluorophenyl-ester (NB-PFPE) was chosen as potential cross-linker for IV. NB-PFPE was synthesized according to literature which was confirmed

by ^{1}H NMR, ^{19}F NMR, and ATR FT-IR spectroscopy (refer to **Appendix 4**).[248] In general, PFP was reacted with 5-norbornene-2-carboxylic acid in a STEGLICH-esterification with *N*,*N'*-dicyclohexylcarbodiimide (DCC) and 4- DMAP in DCM under cooling. NB-PFPE was obtained after filtration, washing, and column chromatography. NB-PFPE was subjected to IV yielding a material entitled poly(sulfur-*random*-norbornenyl-pentafluorophenyl ester) (poly(S-*r*-NB-PFPE)) which was reacted with different primary amines to tune the active precursor polymer towards different applications depending on the amine used for PPM. Precisely, *α*-amino-*ω*-methoxy polyethylene glycol (Amino-mPEG), allylamine (AA), aminopropyl trimethoxy silane (APTMS), and ferrocenyl methyl amine (FcMA) were used to modify poly(S-r-NB-PFPE) (refer to **Scheme 19**). Synthesis and characterization of poly(S-*r*-NB-PFPE) as well as its PPM are discussed in the following sections.

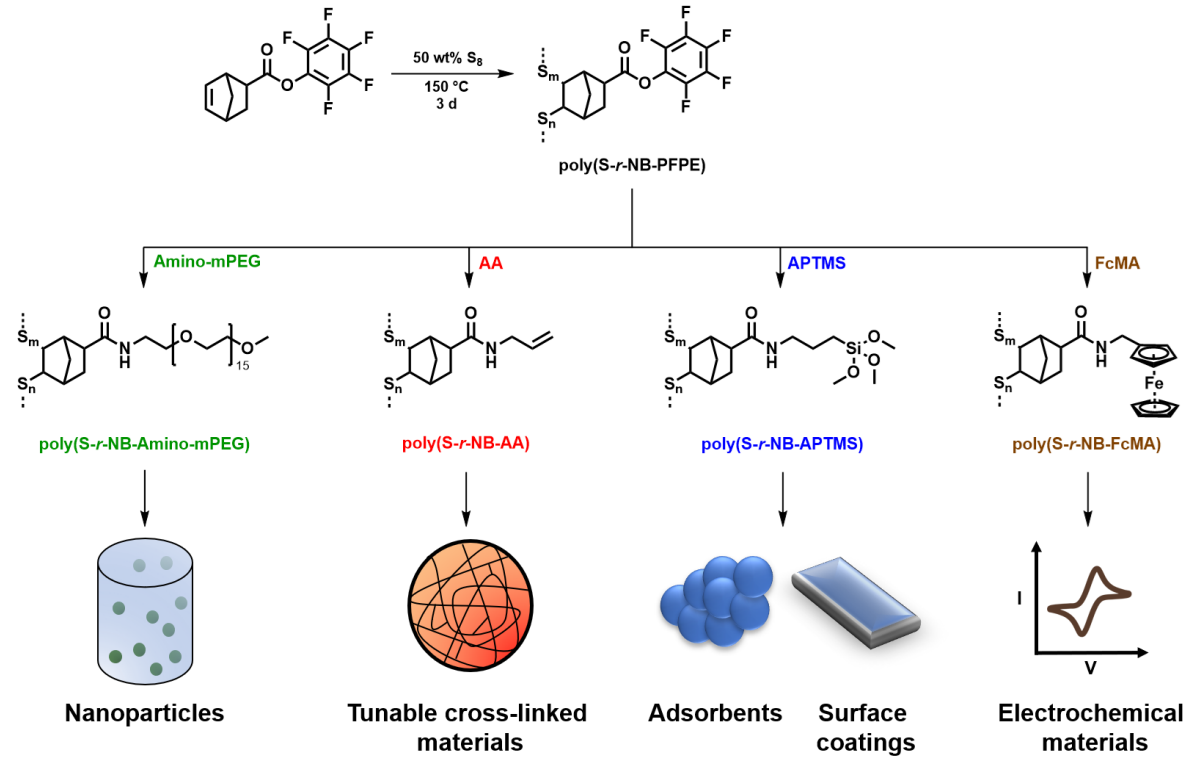

Scheme 19. Schematic visualization of the IV of NB-PFPE with subsequent amidation of the reactive PFP-ester for usage in a wide range of applications. Brackets of repeating units are omitted for clarity and sulfur chains are abbreviated by dashed lines.

3.2.3 Synthesis and Characterization

Poly(S-*r*-NB-PFPE) was synthesized by reacting equal masses of elemental sulfur and NB-PFPE at temperatures ranging from 150 °C to 170 °C for different durations to

determine the optimal reaction conditions (refer to **Figure 32a**). Complete conversion of norbornenyl C=C double bonds was found through ^{1}H NMR and ^{13}C NMR spectroscopy after only 4 h of reaction at 150 °C. The ^{1}H NMR spectrum of poly(S-*r*-NB-PFPE) exhibited no resonances between 6.5 ppm and 6 ppm, confirming the absence of norbornenyl C=C bonds, while the presence of aromatic C=C bonds was verified via ^{13}C NMR spectroscopy in the 137 – 143 ppm range (refer to **Figure 32b and c**).

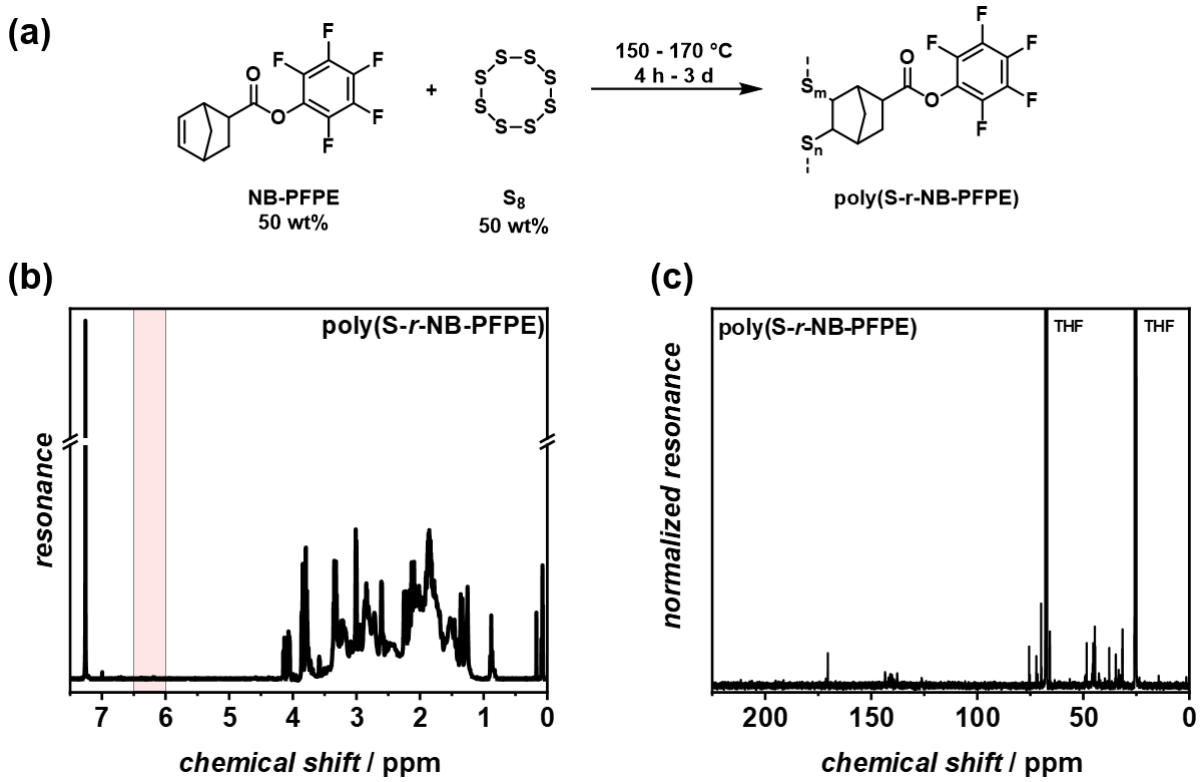

Figure 32. a) Reaction scheme of the IV of NB-PFPE with investigated reaction conditions. Brackets of repeating units are omitted for clarity and sulfur chains are abbreviated by dashed lines. ^{1}H NMR (b) and ^{13}C NMR (c) spectra of poly(S-*r*-NB-PFPE) in $CDCl_3$ and THF-d_8, respectively. The highlighted area in the ^{1}H NMR spectrum (6.0 - 6.5 ppm) shows the absence of C=C double bond proton resonances, confirming full C=C bond conversion.

However, DSC revealed that complete conversion of elemental sulfur required 3 d of reaction time, as indicated by the disappearance of the melting peak at 110 – 120 °C, which corresponds to residual elemental sulfur (refer to **Figure 33a**). Additionally, the T_g of poly(S-*r*-NB-PFPE) increased with longer reaction times, rising from -2 °C after 4 h to 32 °C after 3 days. This trend suggests that extended reaction times lead to greater sulfur incorporation and higher molecular weight, resulting in enhanced material stability. Increasing the reaction temperature to 160 or 170 °C did not

significantly accelerate sulfur conversion, as full conversion still required 3 d, regardless of temperature (refer to **Figure 33b and c**).

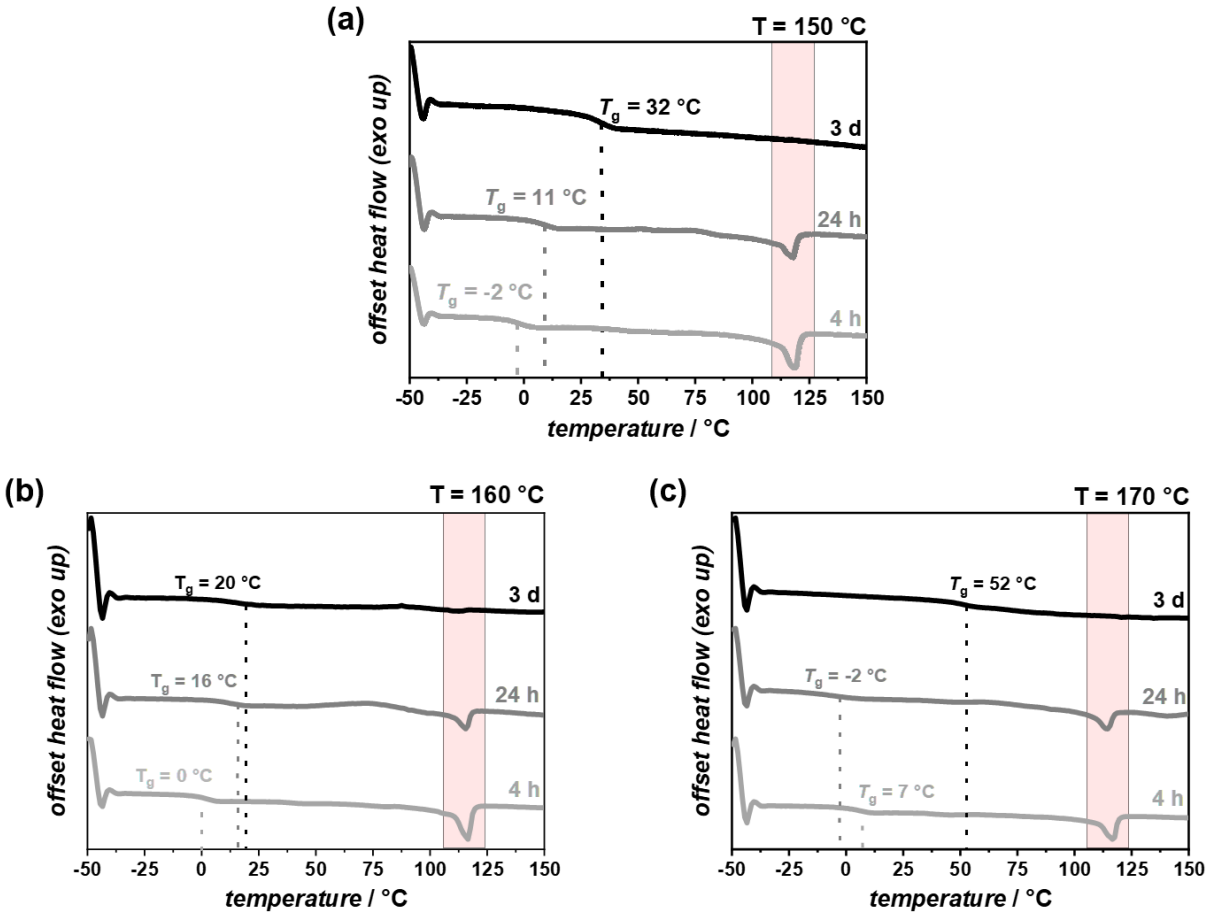

Figure 33. DSC thermograms of poly(S-*r*-NB-PFPE) synthesized at 150 °C (a), 160 °C (b), and 170 °C (c) for 4 h (light gray), 24 h (gray), and 3 d (black), respectively. 3 days of reaction time were necessary for full sulfur conversion, regardless of the reaction temperature. Heating rate: 10 K min^{-1}. Only the first heat run is shown.

The impact of reaction temperature and time on molecular weight and the stability of the active PFP-ester was further assessed. SEC was used to analyze the molecular weight evolution of poly(S-*r*-NB-PFPE) over time and at different temperatures. After 4 h, SEC traces indicated the presence of oligomers, with a consistent molecular weight distribution across all reaction conditions (refer to **Figure 34a**). However, it needs to be noted that molecular weights determined by SEC need to be viewed with caution as no standard materials for SEC calibration exist to this day and the interaction of polysulfides with column materials is not yet known. M_n values in the regions of hundreds to thousands of g mol^{-1} are common in literature and may not precisely represent the actual molecular weight of IV polymers.[22] After 24 hours, a slight broadening of the molecular weight distributions was observed at 150, 160, and

170 °C. After 3 d of reaction time, the molecular weight distribution became more pronounced at 170 °C, with significantly higher molecular weights compared to lower-temperature reactions. This was attributed to additional cross-linking, likely caused by the substitution of aromatic PFP-rings by nucleophilic sulfur species (refer to **Figure 34b and c**).[229] A full display of M_n, M_w, and $Đ$ of poly(S-*r*-NB-PFPE) after different reaction conditions can be found in the appendix (refer to **Appendix 5**).

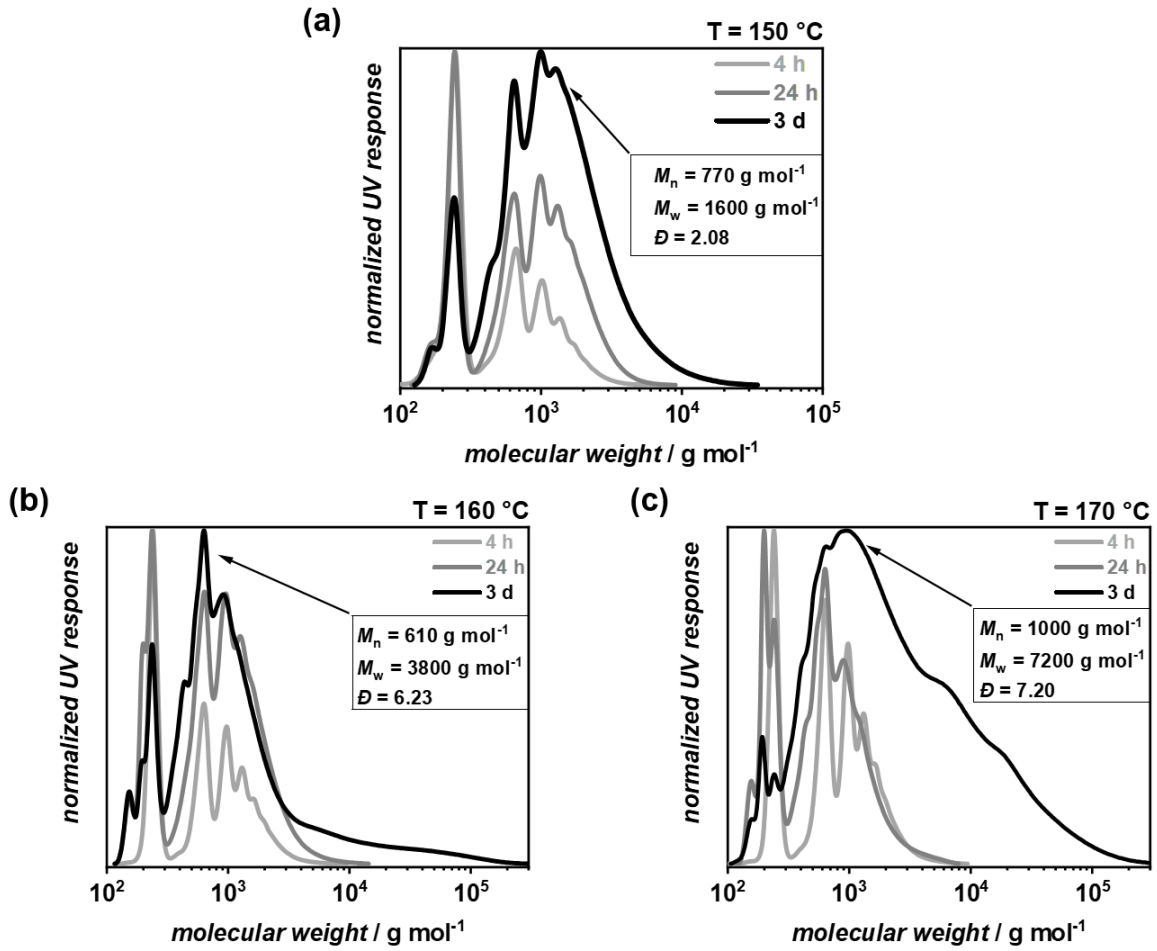

Figure 34. SEC traces of poly(S-*r*-NB-PFPE) synthesized at 150 °C (a), 160 °C (b), and 170 °C (c) for 4 h (light gray), 24 h (gray), and 3 d (black), respectively. The increased molecular weight at higher reaction temperatures is believed to derive from additional cross-linking via substitution of the aromatic pentafluorophenyl ring by sulfur.[229] M_n, M_w, and $Đ$ are shown for the samples with 3 d of reaction time, respectively. Solvent: THF; calibration: PS.

As the reaction temperature increased from 150 °C to 170 °C, the formation of PFP as a by-product, became more prominent, as detected by ^{19}F NMR spectroscopy (refer to **Figure 35**). This suggests that elevated temperatures promote undesired aromatic side reactions, likely due to the nucleophilic nature of radical S· species generated during inverse vulcanization. Consequently, maintaining the reaction temperature at or

below 150 °C is crucial to prevent nucleophilic substitution or radical abstraction of aromatic fluorine atoms, as well as to avoid the thermal degradation of NB-PFPE as was observed during the IV of PFPA (refer to **Chapter 3.1.1** Pentafluorophenyl Acrylate).[249] The reduced degradation of active PFP-esters in NB-PFPE compared to PFPA was most likely caused by the increased distance of reactive C=C double bond from the PFP-ester group. Additionally, double bonds with non-polar alkyl substituents are known to undergo IV more readily compared to polar acrylate double bonds, which typically are unreactive without accelerator and thereby favor side reactions.[56,140]

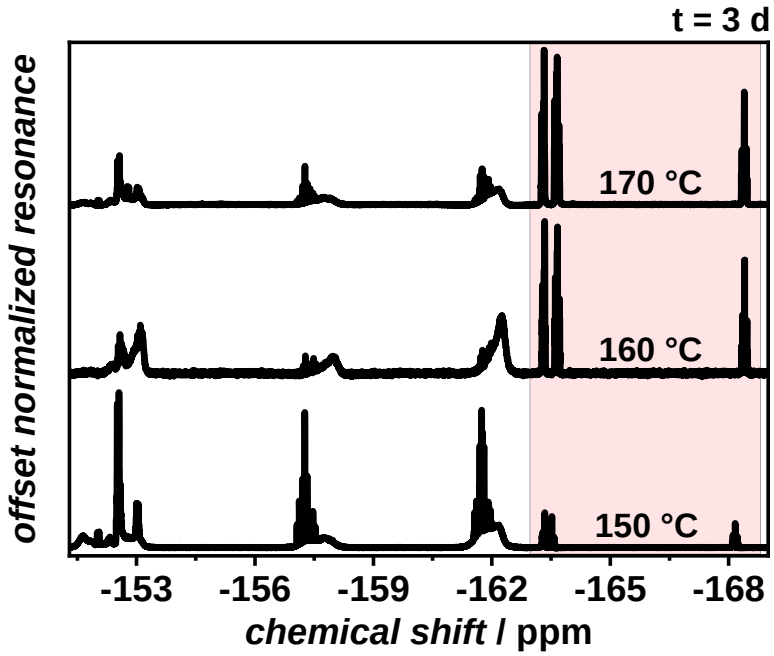

Figure 35. ^{19}F NMR spectra of poly(S-*r*-NB-PFPE) after 3 d of reaction time at 150 °C (bottom), 160 °C (middle), and 170 °C (top). The presence of PFP was found by characteristic resonances in the highlighted area. Solvent: THF-d_8.

Notably, the formation of norbornene-derived polysulfides has been previously investigated by POPLE et al.,[250] who demonstrated that norbornenes tend to form cyclic trisulfides capable of undergoing electrochemical or anionic polymerization.[251] These polysulfides can also be depolymerized at high temperatures, presenting a potential pathway for the recyclability of sulfur-rich materials based on norbornene units.[250] Based on these findings, we propose that the reaction proceeds through a cyclic intermediate, which subsequently undergoes ring-opening polymerization to form poly(S-*r*-NB-PFPE). Additional TGA and IR analysis have been performed to further characterize the synthesized poly(S-*r*-NB-PFPE) and the respective thermogram and ATR FT-IR spectrum can be found in the appendix (refer to **Appendix 6**).

In summary, norbornenyl pentafluorophenyl ester can withstand IV conditions while retaining its reactive functionality when temperatures do not exceed 150 °C for long times. Higher temperatures promote undesired cross-linking and depolymerization due to the reactive nature of aromatic fluorinated esters. This optimized synthesis approach establishes a sustainable and versatile platform for polymeric materials through PPM *via* the active ester functionality of this sulfur-rich precursor polymer. Polymers containing activated PFP-ester groups are well-known for their ability to undergo quantitative amidation with primary or secondary amines under mild conditions, facilitating functionalization and tunability the respective parent polymer.[187] However, since polysulfides are known to undergo nucleophilic activation in the presence of amines, leading to dynamic S-S bond cleavage, a control experiment was conducted to verify the stability of norbornene-derived polysulfides under such conditions. Literature-known poly(sulfur-*random*-dicyclopentadiene) (poly(S-*r*-DCPD)) was exposed to benzylamine, and no significant molecular weight reduction, shift in T_g, or change in IR and ^{1}H NMR spectra was observed, indicating that amine-induced cleavage of polysulfides did not occur under the chosen conditions (refer to **Figure 36**). Given this stability against amine-induced degradation, four commercially available primary amines were selected to demonstrate the versatility of poly(S-*r*-NB-PFPE) as a platform material for various applications via selective amidation of the active ester.

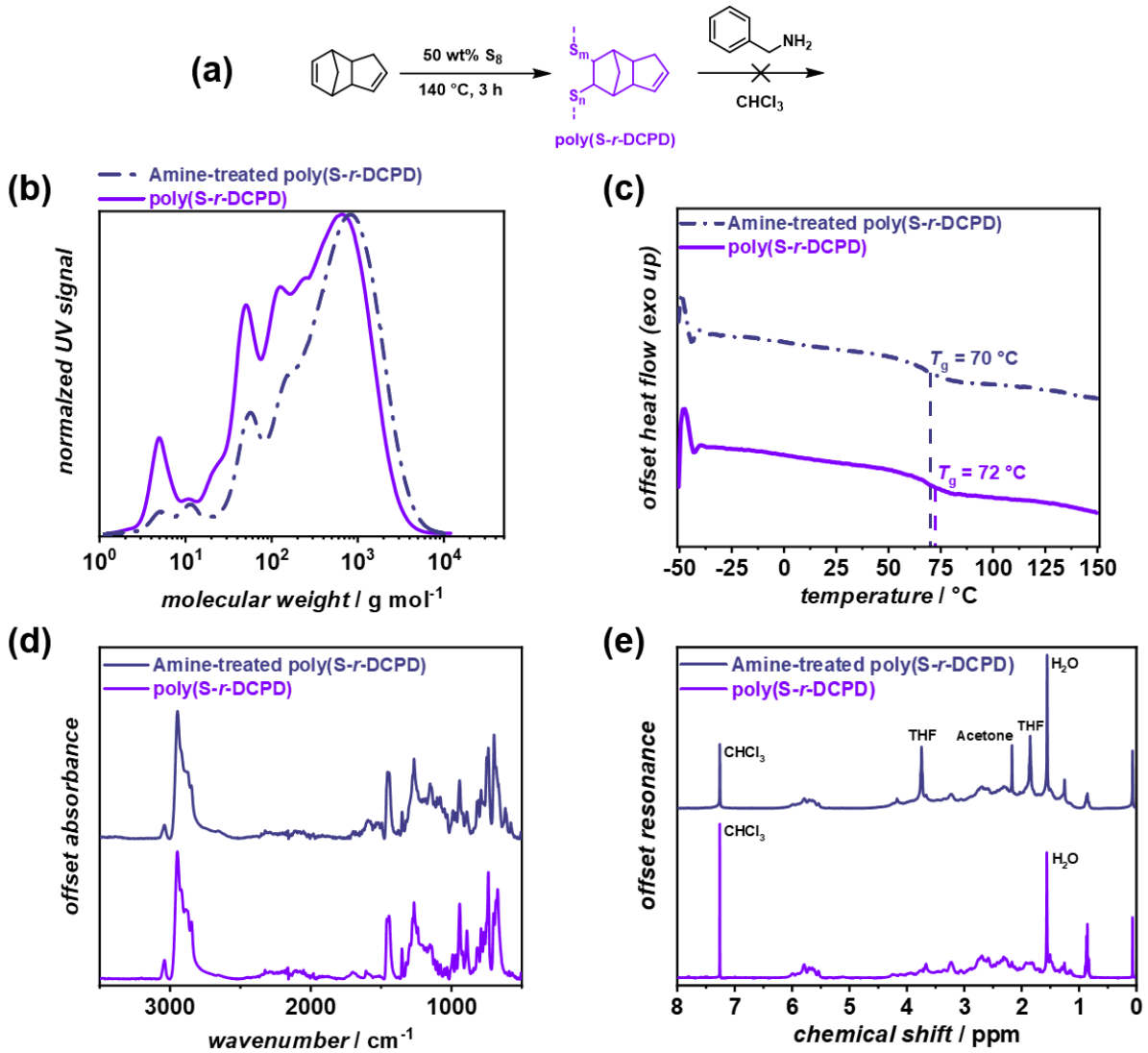

Figure 36. a) Reaction scheme of the IV of DCPD with elemental sulfur. Under the chosen condition, the norbornenyl bonds react predominantly.[252] Subsequent treatment of poly(S-*r*-DCPD) with benzyl amine in chloroform did not show a significant change in molecular weight (b) or thermal phase transitions (c). ATR FT-IR (d) and ^{1}H NMR (e) spectroscopy showed no reaction taking place. Brackets of repeating units are omitted for clarity and sulfur chains are abbreviated by dashed lines. SEC solvent: THF; SEC calibration: PS; NMR solvent: $CDCl_3$.

3.2.4 PPM with *α*-Amino-*ω*-methoxy Poly(ethylene glycol)

Given the hydrophobic nature of polysulfides and the hydrophilic character of poly(ethylene glycol) (PEG), it was hypothesized that PEGylation of the poly(S-*r*-NB-PFPE) precursor could induce phase separation in aqueous media. However, the high polarity of PEG complicates its direct inverse vulcanization with elemental sulfur, often requiring a catalyst in terpolymer systems.[253,254] To circumvent this challenge and integrate PEG into the polysulfide precursor, PPM of poly(S-*r*-NB-PFPE) with Amino-mPEG was performed. The active PFP-esters of poly(S-*r*-NB-PFPE) were selectively substituted with 1.20 equivalents of Amino-mPEG in solution, followed by precipitation

(details can be found in the experimental section; refer to **Chapter 5.3.2.9** poly(S-r-NB-Amino-mPEG)). ^{19}F NMR spectroscopy confirmed the complete conversion of aromatic PFP ester groups, as no residual signals were detected in the −152.5 to −162.5 ppm range (refer to **Figure 37a**). Additionally, ^{1}H NMR and ^{13}C NMR spectra displayed strong resonances at 3 – 4 ppm and 71 – 73 ppm, respectively, corresponding to the PEG backbone protons and carbon atoms (refer to **Figure 37b and c**).[255] Notably, ^{13}C NMR analysis of poly(S-*r*-NB-Amino-mPEG) showed no evidence of thioester or thione formation, indicating that selective amidation of the active esters was the predominant reaction pathway. ATR FT-IR spectroscopy further confirmed the successful conversion of PFP esters. The characteristic ester C=O vibration band at 1778 cm^{-1} disappeared, while the newly formed amide C=O band was observed at 1665 cm^{-1}. Additionally, strong C-H and C-O vibration bands appeared at 2864 cm^{-1} and 1095 cm^{-1}, respectively (refer to **Figure 37d**).[256]

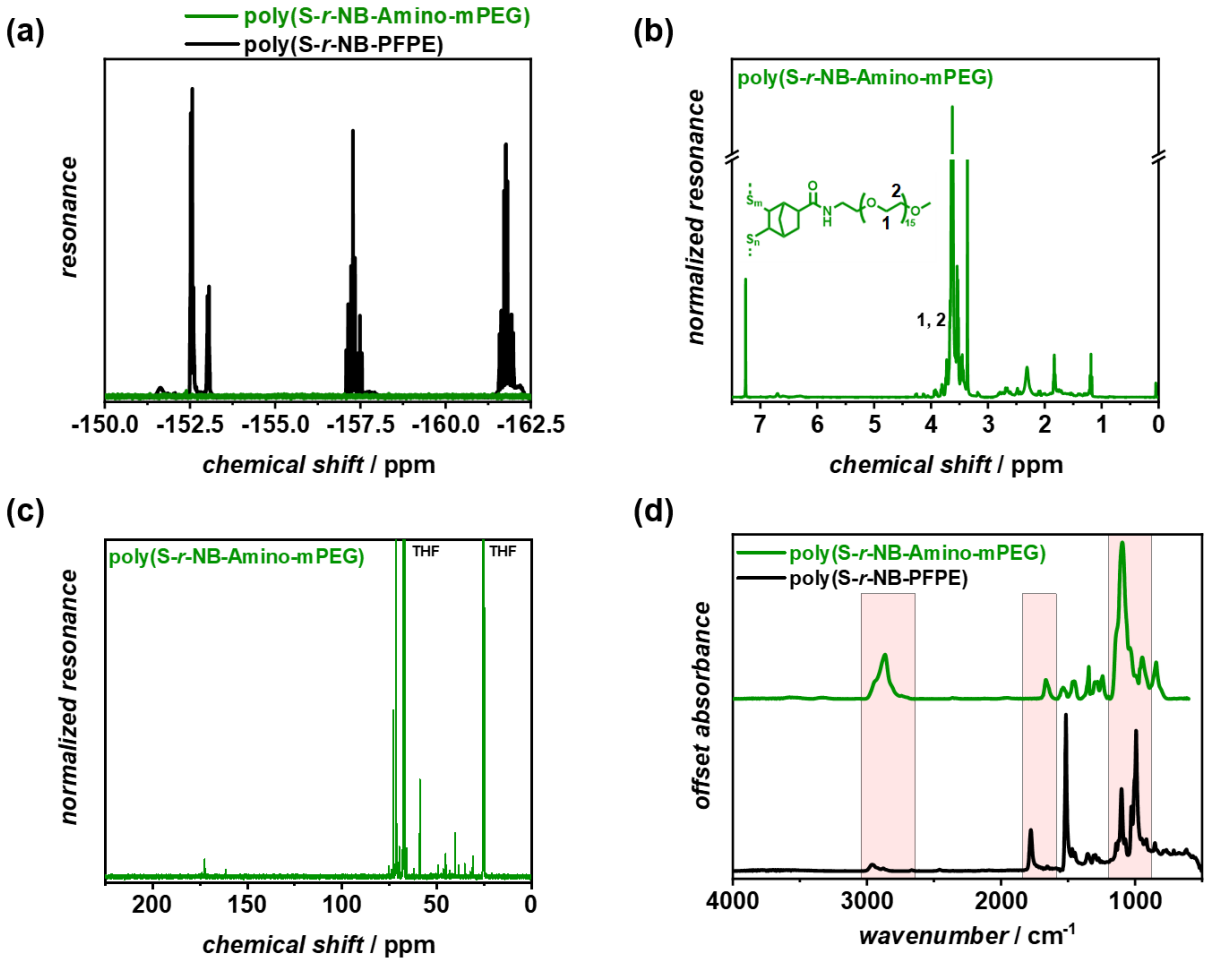

Figure 37. a) ^{19}F-NMR spectra of poly(S-*r*-NB-PFPE) (black) and poly(S-*r*-NB-Amino-mPEG) (green). Absence of aromatic fluorine atoms confirms the full conversion of PFP-esters. b) Normalized ^{1}H NMR spectrum of poly(S-*r*-NB-Amino-mPEG) in $CDCl_3$. The strong resonance between 3 and 4 ppm proves the presence of PEG-chains in the material. The Y-axis was discontinued for scaling visibility purposes. c) ^{13}C NMR spectrum of poly(S-*r*-NB-Amino-mPEG) in THF-d_8. Norbornenyl carbon atoms were found in the region of 30 - 50 ppm. The strong resonance at 71 – 73 ppm can be attributed to the PEG-carbon atoms. Sulfur-bound carbon atoms were found between 65 and 75 ppm. No more C=C double bonds are found in the region between 130 – 150 ppm, confirming the removal of the PFP ring. d) Offset ATR FT-IR spectra of poly(S-*r*-NB-PFPE) (bottom) and poly(S-*r*-NB-Amino-mPEG) (top). The vibrations identified in the highlighted areas prove the successful PEGylation of poly(S-*r*-NB-PFPE). Resolution: 2 cm^{-1}.

SEC analysis revealed a molecular weight increase from M_n = 770 g mol^{-1} to M_n = 3200 g mol^{-1} after amidation. Although the absolute values may be influenced by the use of polystyrene calibration standards,[8] a 4.2-fold increase in M_n was observed, aligning well with the theoretical 4.1-fold increase expected for complete PFP ester substitution by Amino-mPEG (M_n = 750 g mol^{-1}). Precipitation efficiently removed low-molecular-weight species, reducing $Đ$ from 2.11 to 1.60 (refer to **Figure 38a**). TGA and DSC were used to examine the thermal properties of poly(S-*r*-NB-Amino-mPEG). TGA showed an increase in $T_{5\%}$ from 168 °C to 234 °C, attributed to the high PEG content and confirming full PFP ester conversion (refer to **Figure 38b**).[257]

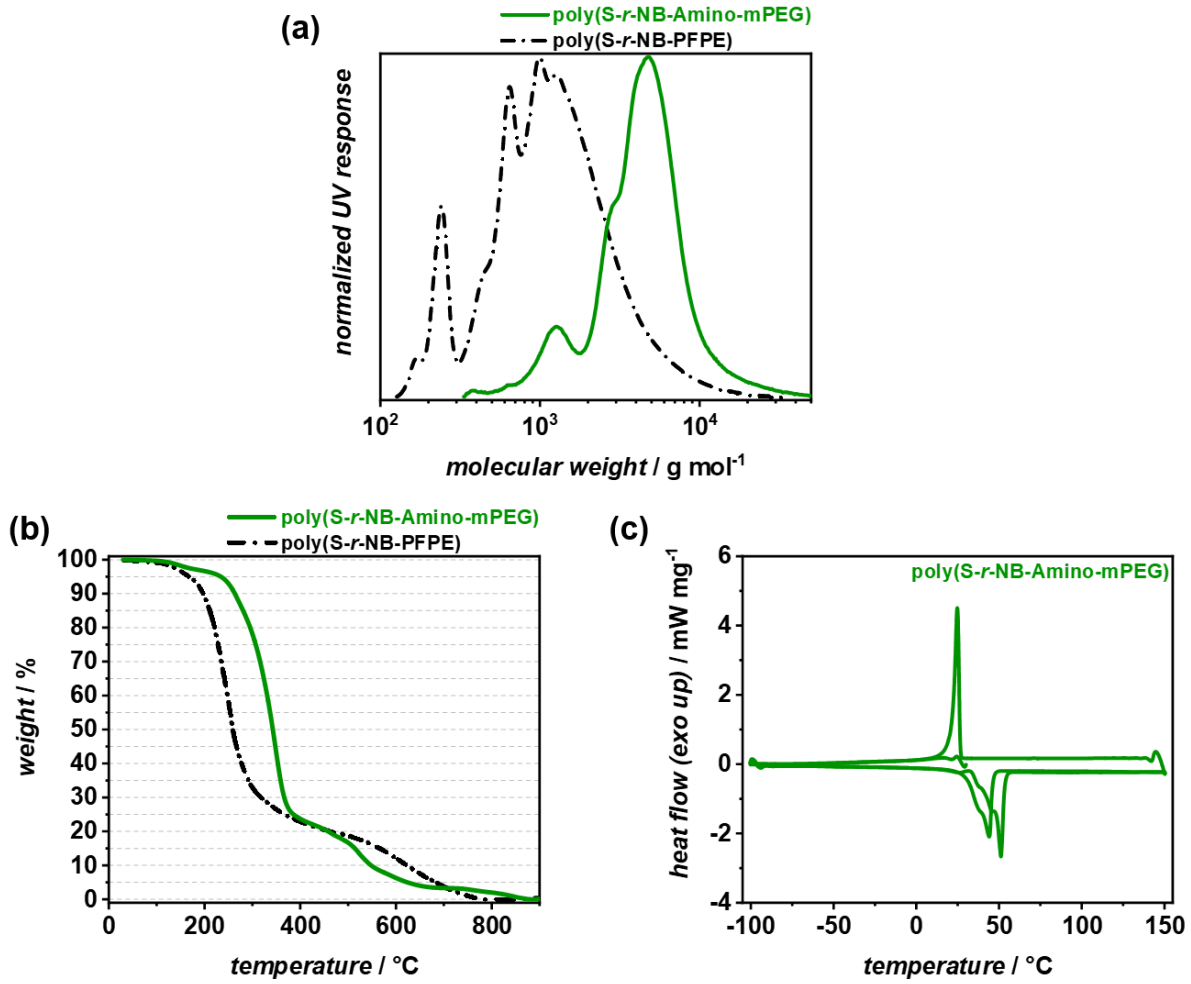

Figure 38. a) Normalized SEC traces of poly(S-*r*-NB-PFPE) (black) and poly(S-*r*-NB-Amino-mPEG) (green). poly(S-*r*-NB-Amino-mPEG): M_w = 5100 g mol^{-1}, M_n = 3200 g mol^{-1}, and $Đ$ = 1.60. Solvent: THF; calibration: PS. b) TGA thermograms of poly(S-*r*-NB-PFPE) and poly(S-r-NB-Amino-mPEG) up to 900 °C. Poly(S-*r*-NB-PFPE): $T_{5\%}$ = 168 °C; $T_{95\%}$ = 684 °C. Poly(S-*r*-NB-Amino-mPEG): $T_{5\%}$ = 234 °C; $T_{95\%}$ = 624 °C. Heating rate: 10 K min^{-1}. c) DSC curve of poly(S-*r*-NB-Amino-mPEG) from -100 to 150 °C. Melting of PEG segments occurred in the range of 25 – 58 °C. Recrystallization begins at 27 °C upon cooling. Heating/cooling rate: 10 K min^{-1}.

DSC analysis revealed a melting range of 32 – 58 °C in the first heat run, which shifted to 25 – 51 °C in the second heat run, indicating the melting of crystalline PEG segments (refer to **Figure 38c**).[258] The shift toward lower temperatures in the second run is likely due to rapid formation of small crystallites during cooling, which have a lower melting point than fully grown equilibrated crystallites.[259] Given the hydrophobicity of polysulfides and norbornenes and the hydrophilicity of PEG, it was hypothesized that poly(S-*r*-NB-Amino-mPEG) would self-assemble into micelles in aqueous environments. A core-shell structure was proposed where sulfur/norbornene-rich domains form the hydrophobic core, while PEG chains extend into the surrounding aqueous phase, acting as a stabilizing corona (refer to **Figure 39a**).

To investigate this, solutions of poly(S-*r*-NB-Amino-mPEG) (3.5 mg mL^{-1}) were prepared in a THF/H_2O (1:1 v/v) mixture. Aggregate formation was induced by gradual THF evaporation in an open vial overnight, thereby increasing the aqueous fraction and driving phase separation of the sulfur segments. Dynamic light scattering (DLS) measurements confirmed the formation of aggregates with a hydrodynamic radius of 17 nm and a narrow dispersity (refer to **Appendix 7**).

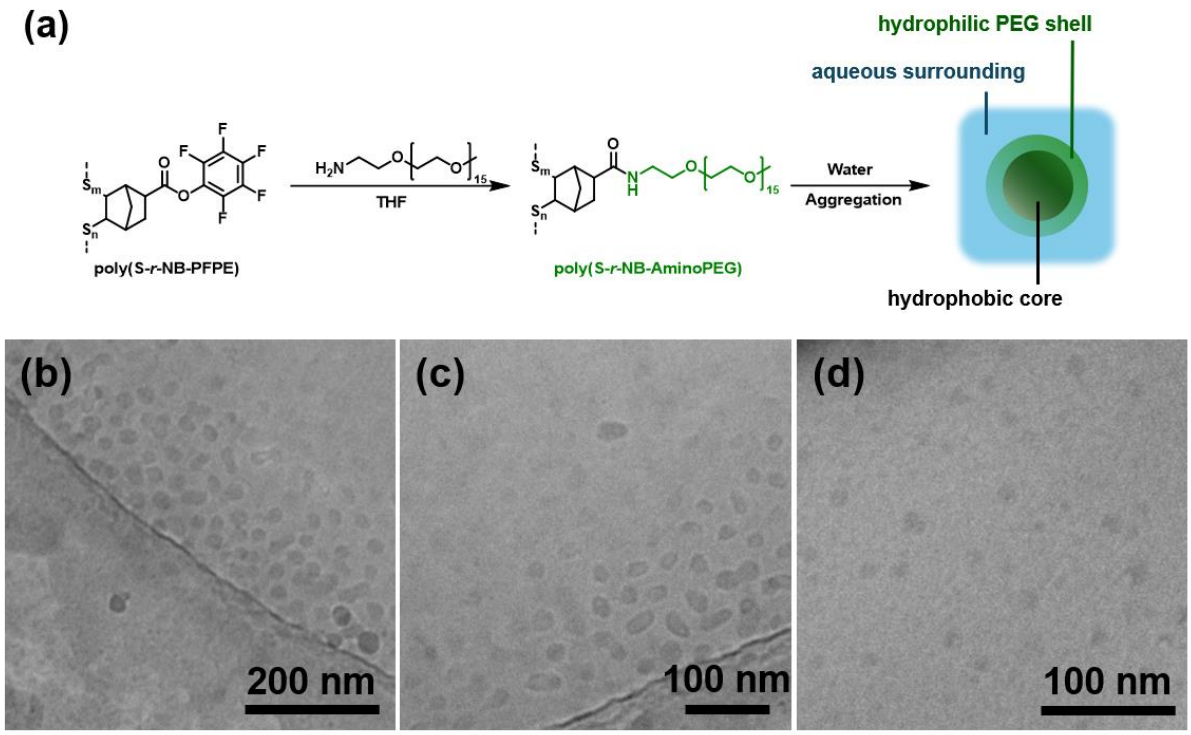

Figure 39. a) Schematic preparation of poly(S-*r*-NB-Amino-mPEG) by amidation of poly(S-*r*-NB-PFPE) followed by particle formation. In an aqueous environment, poly(S-*r*-NB-Amino-mPEG) is able to form spherical particles with hydrophobic cores and hydrophilic shells. Brackets of repeating units are omitted for clarity and sulfur chains are abbreviated by dashed lines. b) – d) Cryo-TEM micrographs of poly(S-*r*-NB-Amino-mPEG) particles with different magnifications. In aqueous environments, nanometer scale particles were observed (mean radius: 12 ± 2 nm). The sharp line seen in b) and c) is the edge of a grid hole of the sample holder. The particles mainly accumulate on the edge of the ice film.

Since the proposed micelle structures are stable only in aqueous environments, cryo-transmission electron microscopy (cryo-TEM) was used to visualize their morphology. **Figure 39b – d** shows spherical particles with an average radius of 12 nm (standard deviation: 2 nm), consistent with the DLS results (hydrodynamic radius: 17 nm). Notably, regular TEM (dry conditions) did not reveal any ordered structures (refer to **Appendix 8**), indicating that the micelles disassemble in non-aqueous environments. This suggests a potential mechanism for controlled substance capture and release by modulating environmental polarity or hydration levels.

This strategy successfully demonstrated that phase separation of sulfur polymers in aqueous media can be achieved through PPM with hydrophilic PEG chains. The straightforward synthesis of hydrophilic spherical nanoparticles from inherently hydrophobic, high-sulfur-content polymers highlights the versatility of poly(S-*r*-NB-PFPE) as a platform material for controlled transport of sulfur-based micelles in aqueous environments. This approach has promising implications for future applications in homogeneous heavy metal capture, drug delivery, and responsive nanomaterials, paving the way for innovative sulfur polymer-based technologies.[254,260]

3.2.5 PPM with Aminopropyl Trimethoxy Silane

Trialkoxysilanes are a crucial class of chemicals widely used for functionalizing surfaces such as glass, metals, silica, and even sand. Organosilanes serve as essential coupling agents in surface coatings,[261] magnetic materials,[262] cross-linkers,[263] and adsorption materials.[264] To demonstrate the extended applicability of silane chemistry to the presented precursor polymer, poly(S-*r*-NB-PFPE) was amidated in THF with aminopropyl trimethoxy silane (APTMS) using 1.20 equivalents of APTMS, yielding in poly(S-*r*-NB-APTMS) (refer to **Figure 40a**). However, due to the rapid hydrolysis and polycondensation of methoxy silanes in presence of water, the resulting polymer was stored in a dry solution until further use. Building on previous research,[119] the potential of poly(S-*r*-NB-APTMS) in synthesizing sulfur-containing silica particles for mercury adsorption was investigated. To achieve this, poly(S-*r*-NB-APTMS) in THF was introduced into a mixture of aqueous ammonia and ethanol at a.t. (refer to **Chapter 5.3.2.11** poly(S-r-NB-APTMS) particles for detailed procedure). A precipitate formed within seconds, as a result of the generation of insoluble silica particles by polycondensation. ATR FT-IR analysis of the purified poly(S-*r*-NB-APTMS) particles confirmed successful amidation of the PFP ester groups, as evidenced by the disappearance of the ester C=O vibration band at 1779 cm^{-1} and the emergence of the amide C=O vibration band at 1640 cm^{-1} (refer to **Figure 40b**). Additionally, an increase in C−H vibration intensity in the 3000 – 2800 cm^{-1} range confirmed the incorporation of propyl CH_2 groups into the material. The formation of a cross-linked siloxane network was further confirmed by the strong, broad absorption band of the asymmetric Si−O−Si stretching vibration at 1090 cm^{-1}, aligning with expectations.[237] TGA of poly(S-*r*-NB-APTMS) particles showed two main thermal decompositions at around 200 °C and

600 °C which are attributed to the decomposition of sulfur and organic rests respectively (refer to **Figure 40c**).

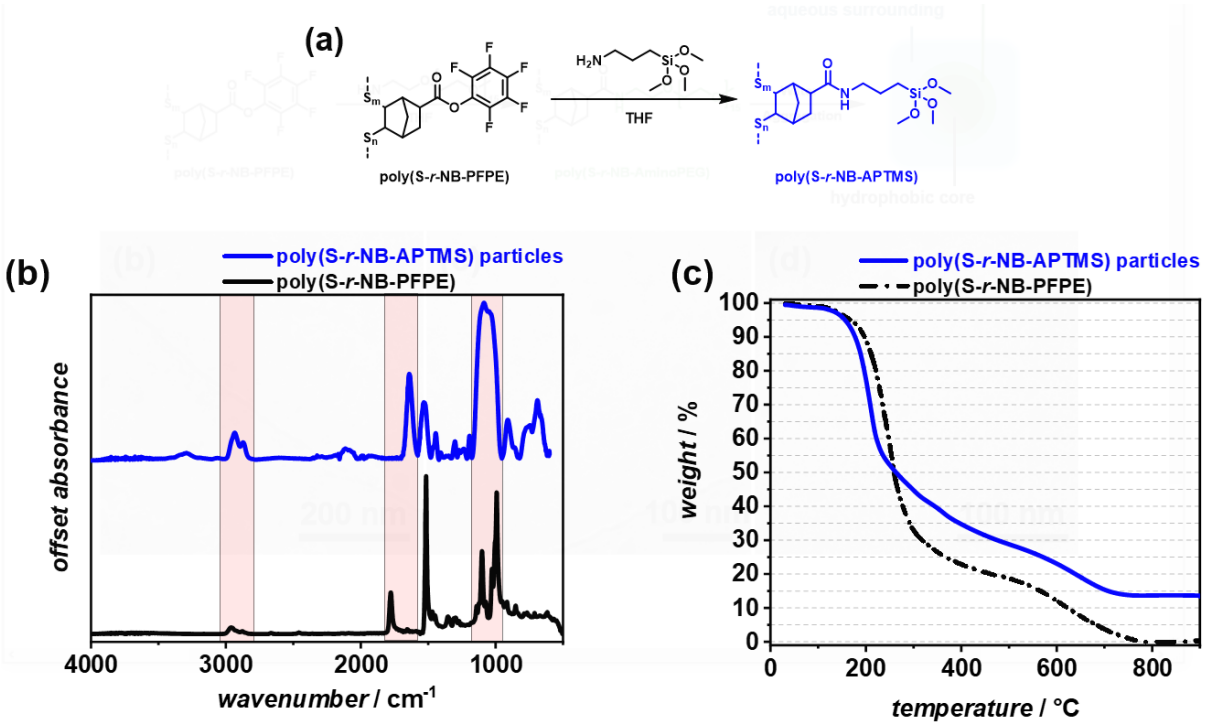

Figure 40. a) Synthesis scheme of poly(S-*r*-NB-APTMS) (blue) by amidation of poly(S-*r*-NB-PFPE) with APTMS in THF under ambient conditions. Brackets of repeating units are omitted for clarity and sulfur chains are abbreviated by dashed lines. b) Offset ATR FT-IR spectra of poly(S-*r*-NB-PFPE) (bottom) and poly(S-*r*-NB-APTMS) particles after polycondensation via the STÖBER method (top). The vibrations identified in the highlighted areas prove the successful conversion of the PFP-ester and the formation of Si-O-Si networks. Resolution: 2 cm^{-1}. c) TGA curves of poly(S-*r*-NB-PFPE) (black) and poly(S-*r*-NB-APTMS) particles (blue) up to 900 °C. Poly(S-*r*-NB-PFPE): $T_{5\%}$ = 168 °C; $T_{95\%}$ = 684 °C. Poly(S-*r*-NB-APTMS) particles: $T_{5\%}$ = 156 °C; weight at 900 °C = 14 wt%. Heating rate: 10 K min^{-1}.

The residual weight at 900 °C can be explained by non-decomposing cross-linked siloxane residues which are known to be thermally stable to very high temperatures. DSC analysis of poly(S-*r*-NB-APTMS) particles showed no phase transition between -50 °C and 150 °C in the first heat run and can be found in the appendix (refer to **Appendix 9**). Scanning electron microscopy (SEM) of the poly(S-*r*-NB-APTMS) particles revealed spherical particles with an average diameter of 810 nm with a standard deviation of 215 nm (refer to **Figure 41**). The high standard deviation was attributed to the broad molecular weight distribution of the original precursor polymer, leading to a wider particle size distribution. EA concluded a final sulfur content of 37 wt% in the poly(S-*r*-NB-APTMS) particles which is twice the amount found in trimethoxyvinylsilane-based particles synthesized via inverse vulcanization in a previous study.[119] Polymers derived from IV are particularly valuable for heavy metal

adsorption, with polysulfides showing strong affinity for toxic mercury ions, a key area of research in materials science.[118] To evaluate the mercury adsorption capability of poly(S-*r*-NB-APTMS) particles, aqueous solutions of Hg^{2+} at varying concentrations were prepared. Four solutions containing $HgCl_2$ in 50 mL of deionized (DI) water were created with initial Hg^{2+} concentrations of 1, 10, 100, and 1000 ppm, respectively. To each solution 100 mg of poly(S-*r*-NB-APTMS) particles were added under vigorous stirring. After 24 h at room temperature, the particles were filtered off, and the remaining Hg^{2+} concentrations were determined *via* cold-vapor atomic absorption spectroscopy (CV-AAS) which were then compared to the concentrations before addition of poly(S-*r*-NB-APTMS) particles.

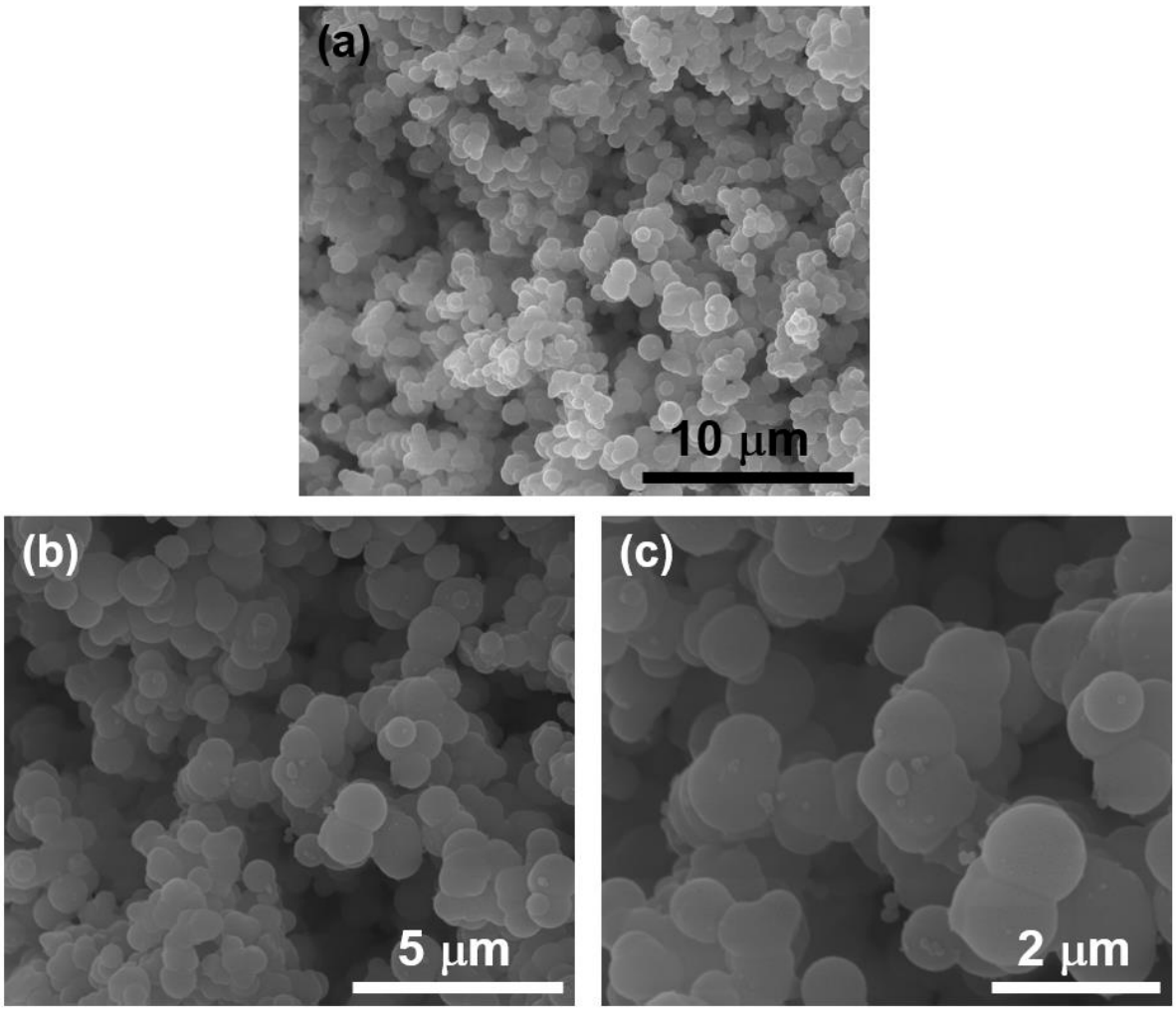

Figure 41. SEM images of poly(S-*r*-NB-APTMS) particles at 5000x (a), 10000x (b), and 20000x (c) magnification, respectively. The average particle size was 810 ± 215 nm.

Results showed that for initial Hg^{2+} concentrations of 1 – 100 ppm, over 99 % of mercury was successfully removed from solution within 24 h at a.t. Even at an initial

mercury concentration of 1000 ppm, 40.8 % could be adsorbed by poly(S-r-NB-APMTS) particles. This represents a significant improvement compared to previous studies (refer to **Figure 42**). This enhanced adsorption performance can be explained by the higher sulfur content in the particles, as well as the presence of coordinating amide groups compared to the direct IV of trimethoxyvinylsilane particles.[119,265]

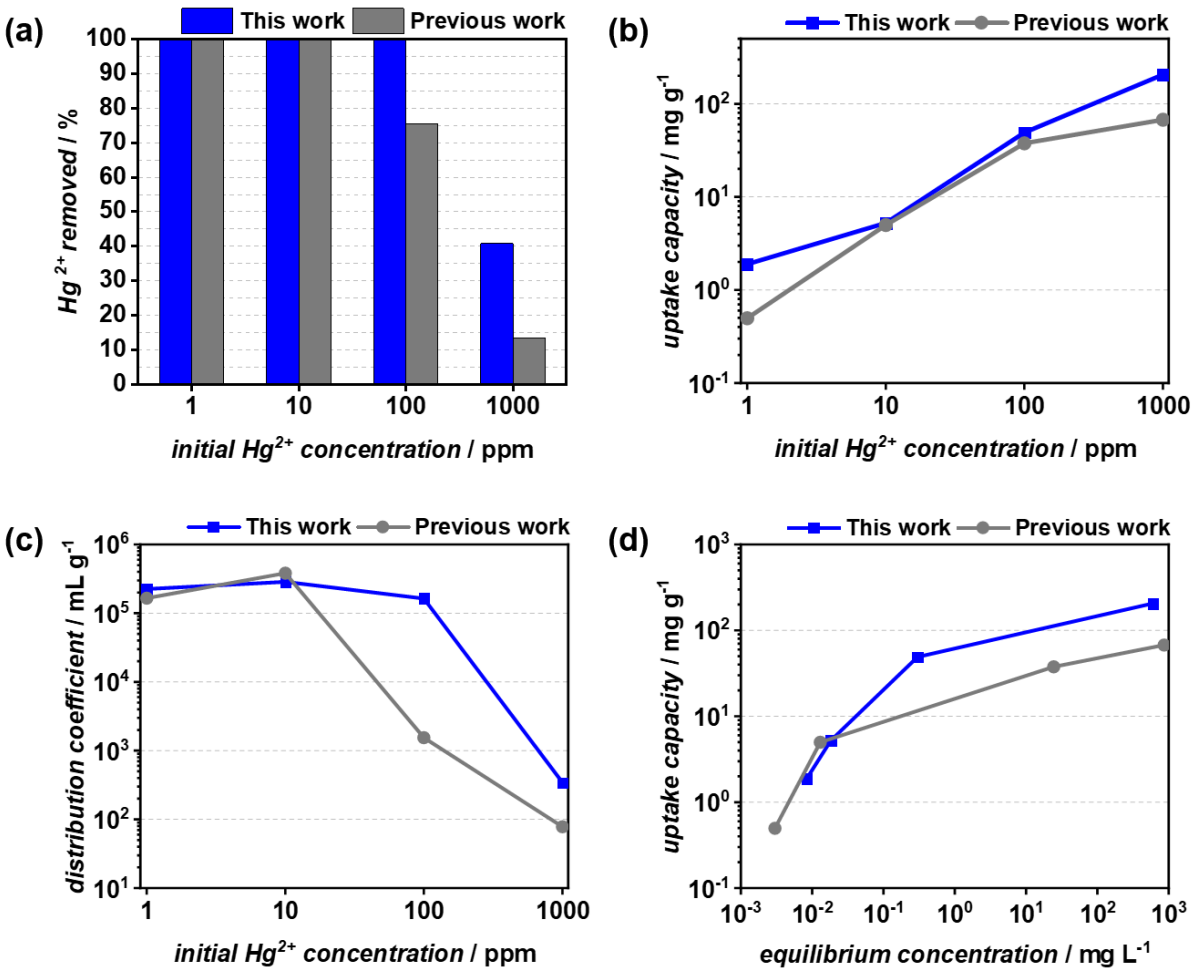

Figure 42. Removed Hg^{2+} ions (a) and uptake capacity (b) of poly(S-*r*-NB-APTMS) particles from aqueous solutions depending on the initial concentration of Hg^{2+} ions in comparison to a previous study (gray).[119] c) Distribution coefficients K_d determined for the adsorption of Hg^{2+} ions from aqueous solution by poly(S-*r*-NB-APTMS) particles in dependence of the initial concentration of Hg^{2+} ions. d) Uptake capacity Q_e vs. equilibrium concentration of Hg^{2+} ions after 24 h of adsorption at ambient temperature. For each adsorption test, 100 mg of poly(S-*r*-NB-APTMS) particles in 50 mL $HgCl_2$ (c = 1 – 1000 ppm) solution were used, respectively.

Distribution coefficients K_d and uptake capacities of poly(S-*r*-NB-APTMS) particles were calculated using the following equations. K_d is defined as:

$$K_d = \frac{(c_i - c_f)}{c_f} \times \frac{V}{m} \qquad \text{(Eq. 2)}$$

where c_i is the initial concentration of the respective metal ion (mg L^{-1}), c_f is the concentration of the respective metal ion after the adsorption experiment (mg L^{-1}), V is the volume of the solution (mL for K_d; L for Q_e), and m is the mass of the adsorbent (g). The distribution coefficient describes the performance of a solid sorbent for metal ion adsorption where values of $1.0 \cdot 10^5$ mL g^{-1} and above are considered excellent. The uptake capacity Q_e (mg g^{-1}) of poly(S-*r*-NB-APTMS) particles was calculated by the mass balance equation:[129]

$$Q_e = (c_i - c_f) \times \frac{V}{m} \quad \text{(Eq. 3)}$$

K_d and Q_e values of poly(S-r-NB-APTMS) particles for Hg^{2+} ions from aqueous solutions are summarized in the following **Table 2** showing outstanding adsorption performance of the synthesized material and substantiate the applicability of PPM of IV polymers towards broad applications.

Table 2. Distribution coefficients K_d and uptake capacities Q_e of Hg^{2+} ions of poly(S-*r*-NB-APTMS) particles from aqueous solutions. V = 50 mL/0.05 L, m = 100 mg, t = 24 h, T = a.t.

initial Hg^{2+} concentration / ppm	*removed* / %	*distribution coefficient* / mL g^{-1}	*uptake capacity* / mg g^{-1}
1	99.78	$2.25 \cdot 10^5$	$1.89 \cdot 10^0$
10	99.83	$2.86 \cdot 10^5$	$5.24 \cdot 10^0$
100	99.70	$1.64 \cdot 10^5$	$4.91 \cdot 10^2$
1000	40.79	$3.44 \cdot 10^2$	$2.06 \cdot 10^2$

A previous study has shown that inverse vulcanized polymers containing hydrolysable silane groups can be used to effectively create sulfur coatings through dip or spin coating.[131] To further expand the applicability of silane coupling chemistry, poly(S-*r*-NB-APTMS) was applied as a coating material on silicon surfaces. For this purpose, the original amidation solution of poly(S-*r*-NB-PFPE) with APTMS was directly used for spin coating onto silicon wafers (details can be found in the experimental section; refer to **Chapter 5.2.5** Spin coating of poly(S-r-NB-APTMS) on silicon wafers).

Coatings were prepared with one, two, and three spin-coating cycles, and a washing step with ethanol after each coating cycle. Ellipsometry measurements confirmed that the film thickness increased with the number of coating cycles, from 317 nm (one cycle) to 410 nm (two cycles) and 422 nm (three cycles) (refer to **Table 3**). However, the

increase in thickness was not strictly linear, likely due to partial dissolution of previously deposited layers during subsequent coating cycles.

Table 3. Film thicknesses and static water contact angles of poly(S-*r*-NB-APTMS) coated on silicon wafers *via* spin-coating. Increasing the number of coating cycles increased the resulting thickness of the coating but had no impact on the water contact angle. Spinning speed = 1500 rpm, t = 15 s, uncertainty given from standard deviation of 4 and 10 measurements of ellipsometry and water contact angle, respectively.

coating cycles	coating thickness / nm	static water contact angle / °
0	-	47.7 ± 1.8
1	317 ± 9	86.0 ± 0.9
2	410 ± 9	85.6 ± 0.9
3	422 ± 4	86.8 ± 1.0

The thickness of poly(S-*r*-NB-APTMS) coatings was found to be comparable to previously reported spin-coated inverse vulcanized polymers on glass surfaces, which can be attributed to the high polymer concentration in the spinning solution (0.1 g mL^{-1}). The hydrophobicity of poly(S-*r*-NB-APTMS)-coated silicon wafers was assessed through water contact angle measurements, which showed that the static water contact angle increased from 47.7 ± 1.8 ° for clean silicon wafers to approximately 86 ° after coating with poly(S-*r*-NB-APTMS), regardless of the number of coating cycles (refer to **Table 3**). To verify the presence of the amide bonds and polysulfides in poly(S-*r*-NB-APTMS) and in order to assess the coating homogeneity, time-of-flight secondary ion mass spectrometry (ToF-SIMS) was conducted on spin-coated silicon wafers.

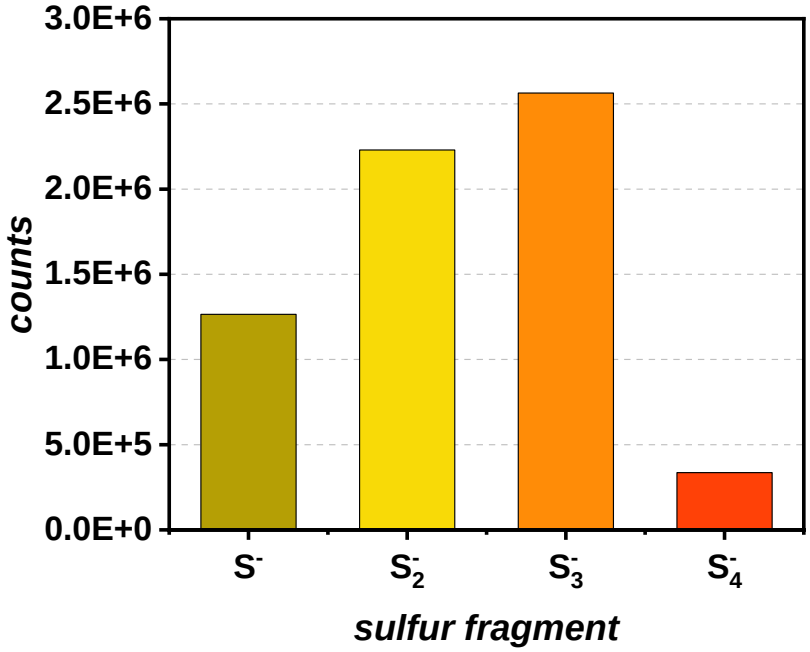

Figure 43. ToF-SIMS analysis of silicon wafers spin-coated with poly(S-*r*-NB-APTMS), confirming the presence of polysulfide species with S_2^- and S_3^- being the predominant sulfur rank.

Consistent with a previous study, S_2^- and S_3^- fragments were the dominant sulfur species, with no significant detection of fragments larger than S_4^- (refer to **Figure 43**).[131] The absence of larger $S_{n>4}^-$ fragments was likely due to their lower binding energy, causing further fragmentation into smaller S^-, S_2^-, and S_3^- fragments during ion cluster bombardment.[266] Consequently, the presence of polysulfide species larger than S_4^- in poly(S-*r*-NB-APTMS) and on the coated surfaces that were cannot be entirely ruled out. Surface S_n^- fragment mapping confirmed a homogeneous sulfur distribution across all detected fragments (refer to **Figure 44**; ToF-SIMS mass spectra of each individual fragment can be found in the appendix, refer to **Appendix 11**).

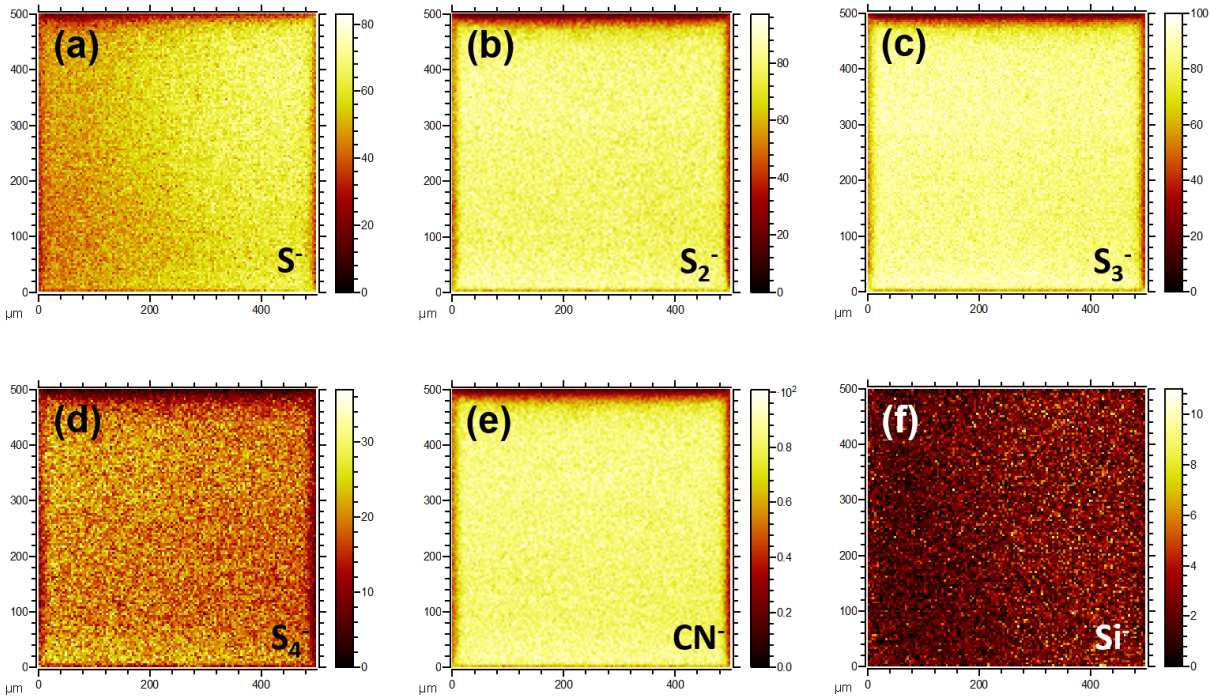

Figure 44. 500 x 500 µm ToF-SIMS images of silicon wafers once spin-coated with poly(S-*r*-NB-APTMS) solution one time at 1500 rpm for 15 seconds. Aerial distributions of all observed fragments were found to be homogenous throughout the observed area. a) S^-, b) S_2^-, c) S_3^-, d) S_4^-, e) CN^-, and f) Si^-. The predominant sulfur ranks of polysulfides S_n^- were n = 2 and 3.

Additionally, ToF-SIMS depth profiling of poly(S-r-NB-APTMS)-coated silicon wafers demonstrated a uniform distribution of polymer-related fragments. The presence of CNO^- fragments confirmed the formation of amide bonds, while $SiCHO^-$ fragments indicated methoxy silane groups on the silicon wafer surface (refer to **Figure 45a** and **Appendix 12**). Interestingly, sulfur-coated silicon wafers exhibited visible color variations, shifting from green to blue to purple with the number of spin-coating cycles, which can be attributed to thin-film interference effects.[267] Digital microscopy revealed some surface inhomogeneity, with micrometer-scale spherical pores present across all coatings (refer to **Figure 45b**). These pores are likely a result of polymerization-induced self-assembly of siloxanes combined with THF evaporation.[131]

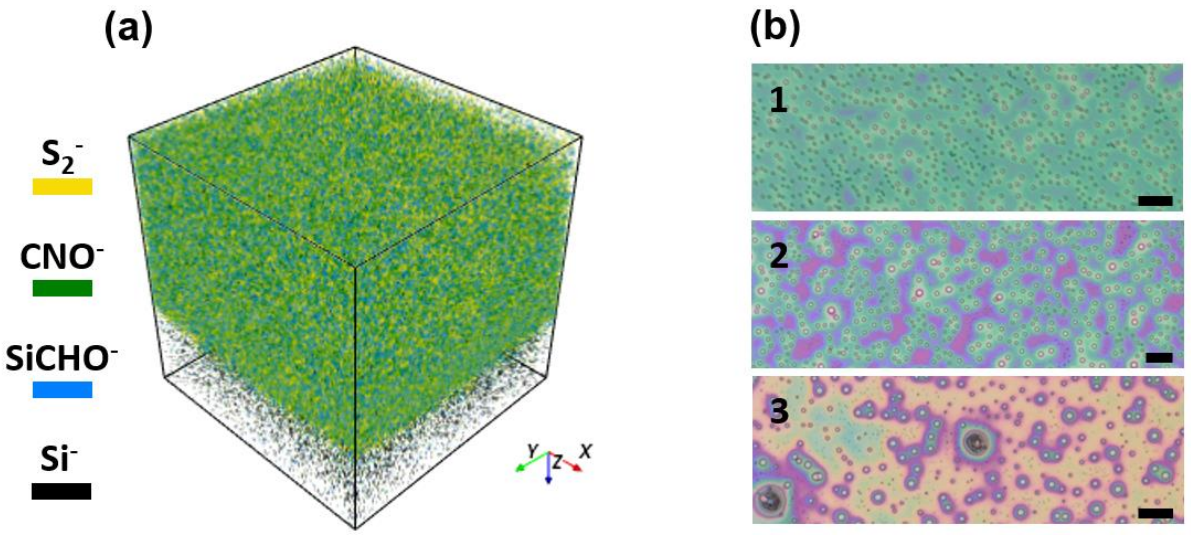

Figure 45. a) 3D representation of S_2^-, CNO^-, $SiCHO^-$, and Si^- fragment distribution determined via ToF-SIMS. The spin-coated poly(S-*r*-NB-APTMS) is clearly distinguishable from the silicon wafer. b) Digital microscopy images of silicon wafers coated with poly(S-*r*-NB-APTMS) with 1, 2, and 3 coating cycles, respectively. The coloration is caused by thin film interference. Scalebars are 10 µm.

Given the exceptional performance of poly(S-*r*-NB-APTMS) particles in removing toxic Hg^{2+} ions from water and the good homogeneity of its coatings, it is believed that amidation of poly(S-*r*-NB-PFPE) with amino silanes represents a promising approach for developing novel high-sulfur-content materials derived from the IV of activated esters.

3.2.6 PPM with Allylamine

Due to the harsh conditions of classic IVs (*i.e.,* radical sulfur melt at ca. 150 °C), unsaturated compounds cannot be employed in the polymerization step, when double or triple bonds ought to remain unreacted in foreseeable quantities after the IV. Therefore, in order to incorporate unsaturated moieties into inverse vulcanized polymers, PPM methods need to be employed. Following the methodology described for poly(S-*r*-Amino-mPEG) and poly(S-*r*-NB-APTMS), poly(S-r-NB-PFPE) was reacted with 1.20 equivalents of allylamine (AA) at ambient temperature to introduce the chemical motif of C=C double bonds into the parent polymer (refer to **Scheme 20, step 1**).

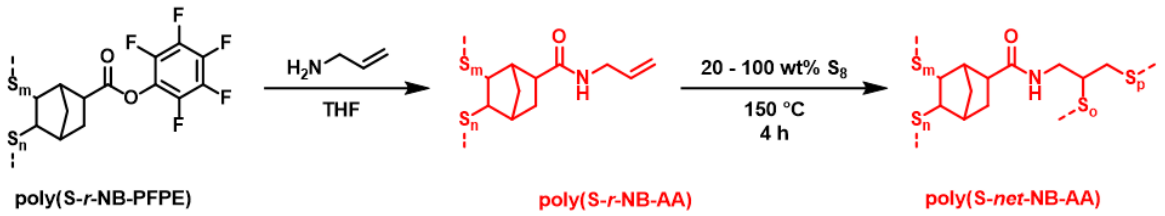

Scheme 20. Synthesis and thermal analysis of poly(S-r-NB-AA) (step 1) and cross-linked poly(S-*net*-NB-AA) (step 2). The second cross-linking step was conducted by dry-mixing different amounts of elemental sulfur with poly(S-*r*-NB-AA) and heating to 150 °C for 4 h. Brackets of repeating units are omitted for clarity and sulfur chains are abbreviated by dashed lines.

Characterization of poly(S-*r*-NB-AA) via ^{1}H NMR and ^{13}C NMR spectroscopy revealed new resonances at 5 – 6 ppm and at 115 and 136 ppm, respectively, confirming the presence of allylic double bonds (refer to **Figure 46a and b**). Norbornenyl carbon atoms were found in the region of 30 - 50 ppm. Sulfur-bound carbon atoms were found between 65 ppm and 75 ppm.

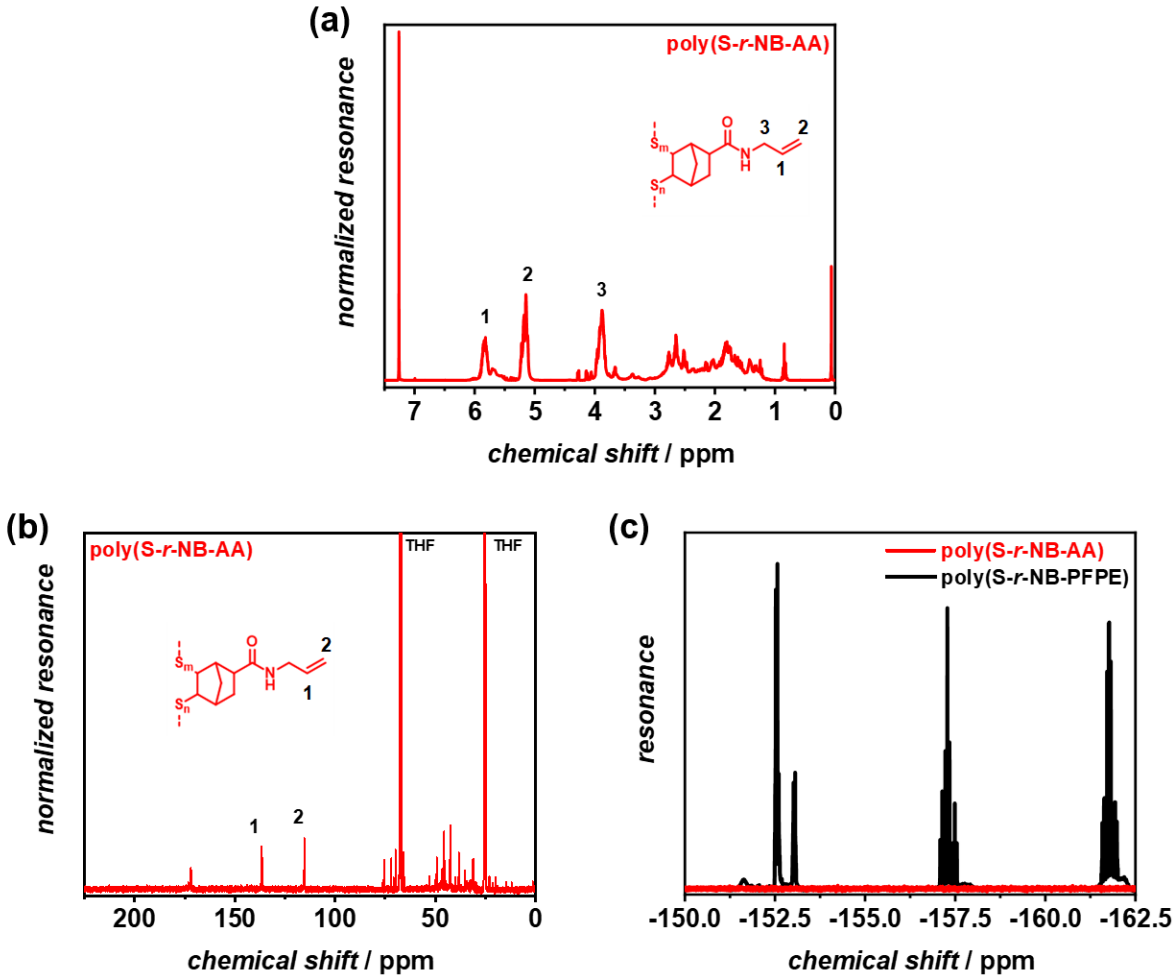

Figure 46. a) Normalized ^{1}H NMR spectrum of poly(S-*r*-NB-AA) in $CDCl_3$. Proton resonances in the area of 5 – 6 ppm found in poly(S-*r*-NB-AA) confirm the successful amidation of poly(S-*r*-NB-PFPE) with allylamine. b) ^{13}C NMR spectrum of poly(S-*r*-NB-AA) in THF-d_8. c) ^{19}F NMR spectra of poly(S-*r*-NB-PFPE) (black) and poly(S-*r*-NB-AA) (red). Absence of aromatic fluorine atoms confirms the full conversion of PFP-esters.

Because sulfur radicals can attach to the C=C double bonds of norbornene in either *exo* or *endo* orientations, four product orientations can occur. This variety accounts for the numerous observed C-S bond peaks. The presence of allyl C=C double bonds was confirmed by resonances at 115 and 136 ppm, respectively. Notably, the carbonyl ester carbon atom was found at 170 ppm, indicating no sulfuration of esters towards thioesters or trithiocarbonates which are expected to appear above 200 ppm.[268] Additionally, ^{19}F NMR spectroscopy showed the disappearance of aromatic PFP resonances (refer to **Figure 46c**).

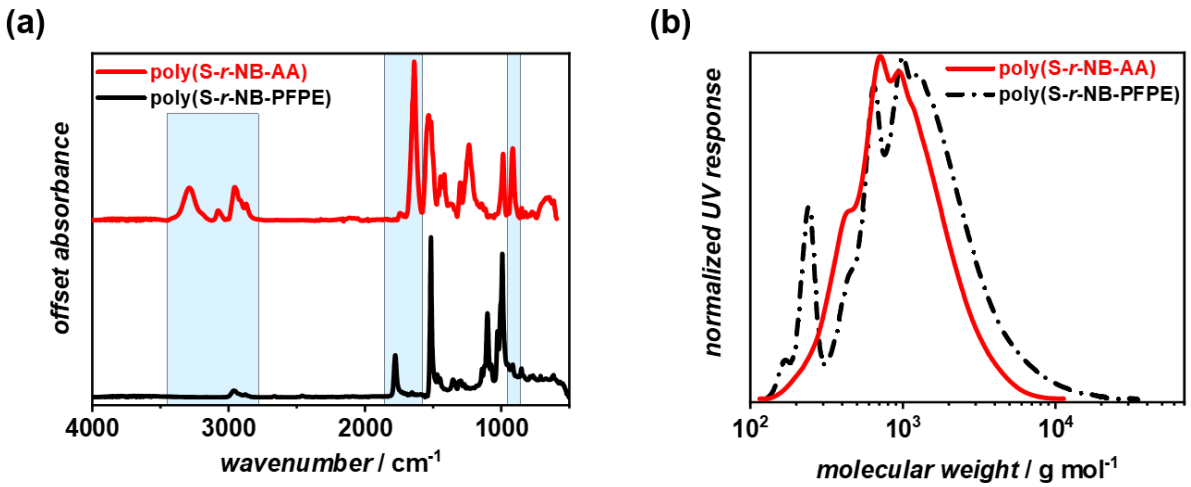

Figure 47. a) ATR FT-IR spectra of poly(S-*r*-NB-PFPE) (black) and poly(S-*r*-NB-AA) (red). The C=O ester and aromatic C=C vibrations of poly(S-*r*-NB-PFPE) at 1776 cm^{-1} and 1100 cm^{-1} disappeared, respectively. Formation of the proposed amide was confirmed by identification of the characteristic amide C=O vibration at 1638 cm^{-1} as well as a vibration at 3080 cm^{-1} associated with unsaturated C-H stretch vibrations. Resolution: 2 cm^{-1}. b) Normalized SEC traces of poly(S-*r*-NB-PFPE) (black) and poly(S-*r*-NB-AA) (red). poly(S-*r*-NB-AA): M_w = 1200 g mol^{-1}, M_n = 580 g mol^{-1}, and $Đ$ = 2.08. Solvent: THF; calibration: PS.

ATR FT-IR spectroscopy further supported successful amidation, with the emergence of a broad amide N−H stretch vibration at 3286 cm^{-1} and an allyl C−H stretch vibration at 3076 cm^{-1} (refer to **Figure 47a**). Moreover, an increase in the intensity of the saturated C−H stretch vibration band at 2955 cm^{-1} was observed, alongside characteristic amide C=O stretch vibration at 1638 cm^{-1}, replacing the ester bond vibration at 1776 cm^{-1}. A C=C bending vibration at 915 cm^{-1} provided additional confirmation of the successful reaction. The molecular weight distribution of poly(S-*r*-NB-AA) was determined via SEC revealing M_w = 1200 g mol^{-1} ($Đ$ = 1.62), corresponding to an estimated weight loss of 25 % compared to the precursor poly(S-*r*-NB-PFPE) (M_w = 1600 g mol^{-1}, $Đ$ = 2.08) (refer to **Figure 47b**). This closely aligns

with the theoretical weight loss of 22 %, assuming complete amidation, confirming the successful synthesis of poly(S-*r*-NB-AA) from poly(S-*r*-NB-PFPE).

To explore the reactivity of the allyl groups, a thiol-ene reaction with benzyl mercaptan was attempted using AIBN at 60 °C for 2 h (refer to **Figure 48a**).[269] However, the reaction produced unsatisfactory results, yielding only analytical amounts after precipitation. SEC analysis showed a molecular weight of approximately 600 g mol^{-1}, contradicting the expected increase in molecular weight from benzyl mercaptan addition (refer to **Figure 48b**). Instead, this suggests partial degradation of the polymer. Although ^{1}H NMR spectroscopy confirmed the incorporation of aromatic species, it is likely that the radical thiol-ene mechanism led to polysulfide chain degradation, reducing the molecular weight (refer to **Figure 48c**).

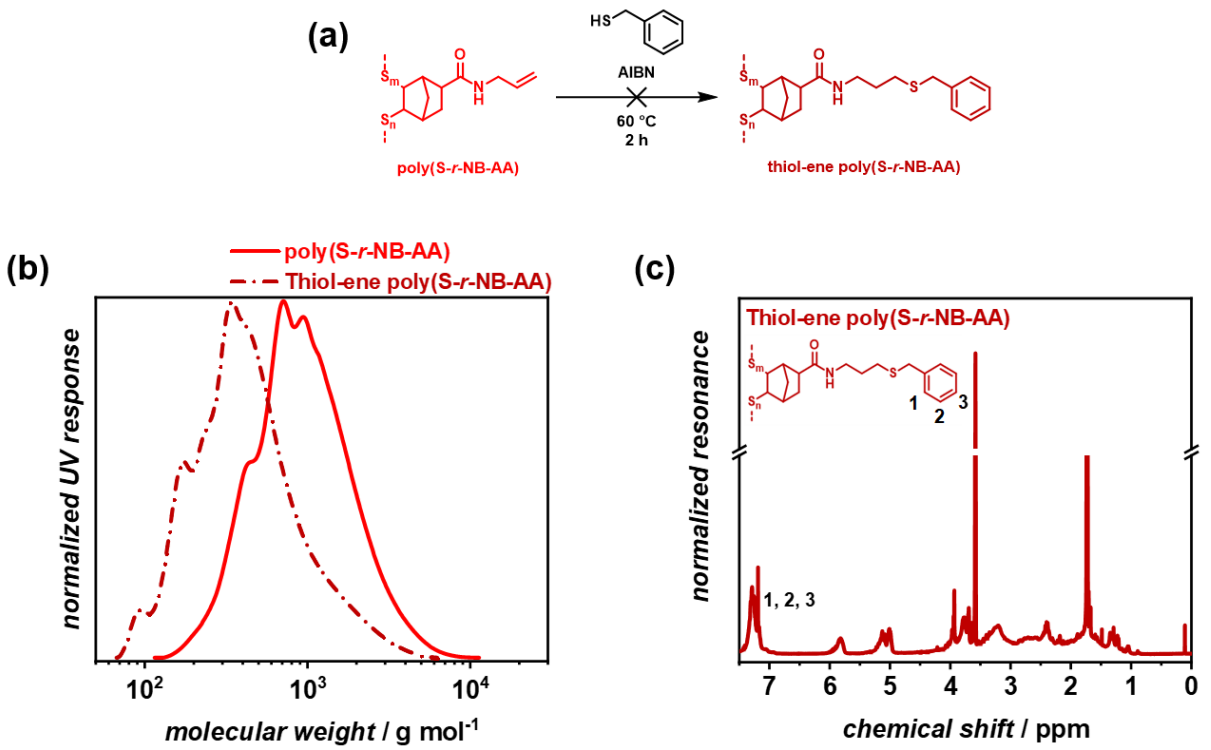

Figure 48. a) Proposed reaction of the thiol-ene reaction of poly(S-*r*-NB-AA) with benzyl mercaptan. Brackets of repeating units are omitted for clarity and sulfur chains are abbreviated by dashed lines. b) SEC traces of poly(S-*r*-NB-AA) before (solid line) and after (dashed line) thiol-ene reaction with benzyl mercaptan. The decrease of the molecular weight indicates the decomposition of sulfur chains during the radical mechanism of the AIBN-initiated thiol-ene reaction, proving it unsuitable for PPM of inverse vulcanized materials. Thiol-ene poly(S-*r*-NB-AA): M_w = 560 g mol^{-1}, M_n = 320 g mol^{-1}, and $Đ$ = 1.74. Solvent: THF; calibration: PS. c) Normalized ^{1}H NMR spectrum of poly(S-*r*-NB-AA) after thiol-ene reaction with benzyl mercaptan in THF-d_8. Presence of aromatic proton resonances in the region of 7 to 7.5 ppm confirm the partially successful reaction. Residual resonances in the area from 5 to 6 ppm indicates incomplete conversion of allylic double bonds. The Y-axis was discontinued for scaling visibility purposes.

Given the dynamic nature of S−S bonds in polysulfides, a DCP approach was taken to create a cross-linked sulfur network with controlled sulfur content by utilizing the allyl moieties as additional binding sites in a second IV step. For this, poly(S-*r*-NB-AA) was dry-mixed with 20, 40, 60, 80, and 100 wt% elemental sulfur and heated to 150 °C under stirring for 4 h (refer to **Scheme 20, step 2**). Weight percentages refer to the total mass of poly(S-*r*-NB-AA). The resulting cross-linked materials (poly(S-*net*-NB-AA)) exhibited low solubility in THF, DCM, acetone, and EtOH, regardless of sulfur content (refer to **Figure 49**).

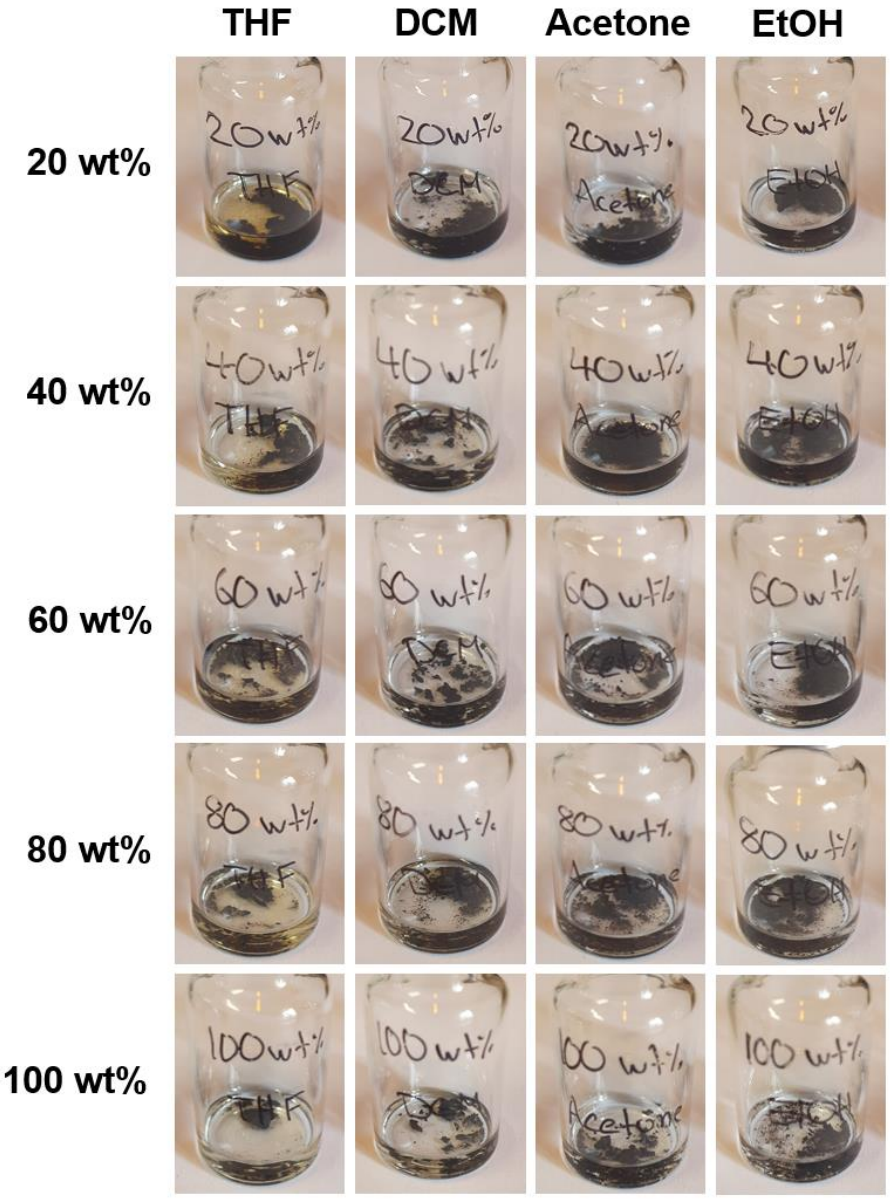

Figure 49. Solubility tests of poly(S-*net*-NB-AA) after a second inverse vulcanization step subsequent to the amidation of poly(S-*r*-NB-PFPE) with AA. All materials were found to be virtually insoluble in THF, DCM, acetone, and EtOH, regardless of the amount of sulfur added during the second cross-linking. Weight percentages refer to the amount of sulfur added to the cross-linking with poly(S-*r*-NB-AA). In a typical solubility test, 50 mg of poly(S-*net*-NB-AA) were mixed with 1 mL of the respective solvent and stirred for 24 h at a.t.

EA determined the final sulfur content of poly(S-*net*-NB-AA) after cross-linking with 20 – 100 wt% sulfur, with results summarized in **Figure 50** and **Appendix 13**.

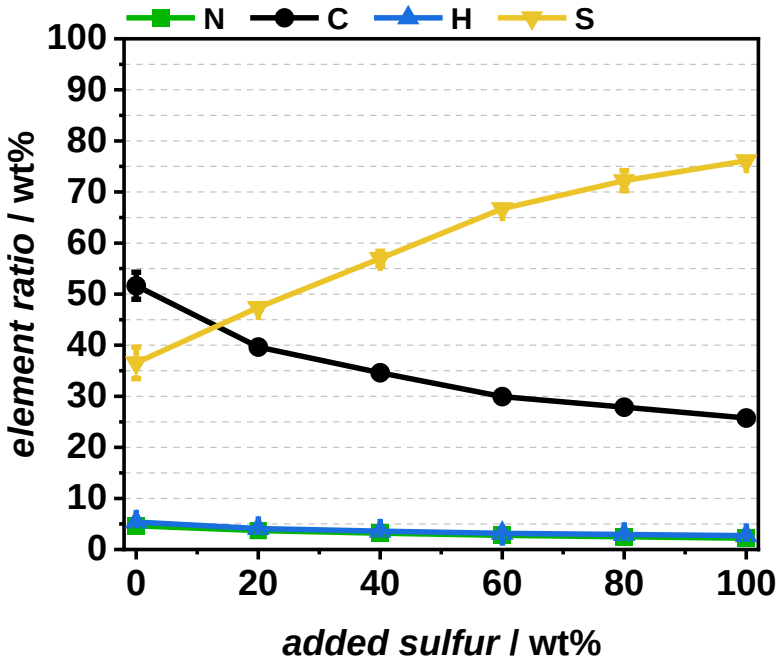

Figure 50. Elemental composition of poly(S-*net*-NB-AA) after the second cross-linking step with different amounts of sulfur. In a typical secondary inverse vulcanization, 100 mg of poly(S-*r*-NB-AA) were reacted with 20 – 100 wt% (20 – 100 mg) elemental sulfur. The resulting final elemental compositions were determined by EA.

DSC was used to assess the consumption of elemental sulfur, which confirmed complete sulfur conversion in samples containing 20 and 40 wt% added sulfur. However, as the sulfur content increased beyond this range (from 60 to 100 wt%), residual crystalline sulfur was detected in the material (refer to **Figure 51**). The T_g of poly(S-*net*-NB-AA) decreased as sulfur content increased, which is known to be caused by easier movement of longer polysulfide chains due to their elongation.[230] The crystallinity *C* [%] of the samples was determined by calculating the melting enthalpy through integration of the sulfur melting peak by the following equation:

$$C = \frac{H_m\big(poly(S-net-NB-AA)\big)}{H_m(S)} \times 100 \qquad \text{(Eq. 4)}$$

where H_m(poly(S-*net*-NB-AA)) and H_m(S) is the melting enthalpy of poly(S-*net*-NB-AA) and pure elemental sulfur, respectively, in J g^{-1}.

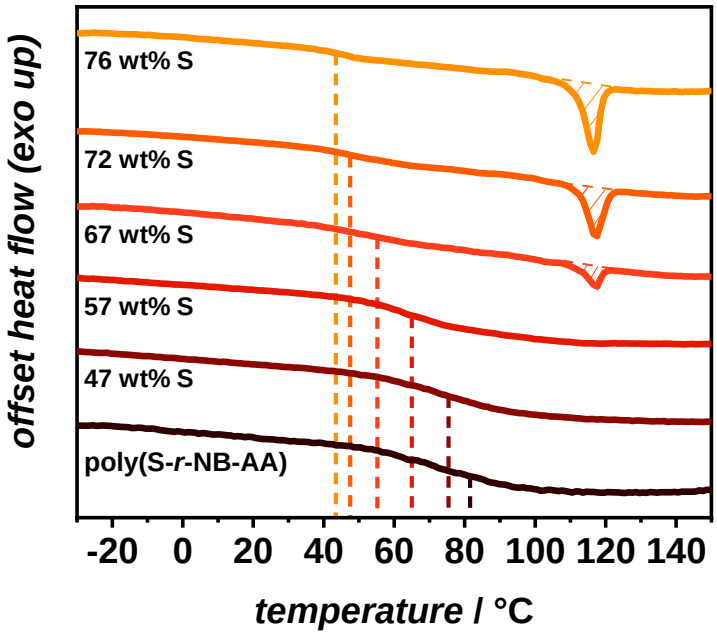

Figure 51. DSC thermograms of poly(S-*r*-NB-AA) and poly(S-*net*-NB-AA) with increasing sulfur content. Full sulfur conversion was found up to 40 wt % of added sulfur in the cross-linking step, while the T_g decreased with increasing added amount of sulfur.

Through comparison of the melting enthalpy of poly(S-*net*-NB-AA) with that of pure elemental sulfur, the crystallinity of the synthesized materials was estimated (refer to **Table 4**).

Table 4. Melting enthalpy and calculated crystallinity of elemental sulfur and poly(S-*net*-NB-AA) in dependency of the amount of added sulfur in the second cross-linking step.

material	*added sulfur* / wt%	*melting enthalpy* / J g^{-1}	*crystallinity* / %
elemental sulfur	-	62.32	100
poly(S-*net*-NB-AA)	20	-	0
poly(S-*net*-NB-AA)	40	-	0
poly(S-*net*-NB-AA)	60	0.83	1.34
poly(S-*net*-NB-AA)	80	2.68	4.29
poly(S-*net*-NB-AA)	100	3.37	5.40

TGA of poly(S-*net*-NB-AA) with varying sulfur contents revealed a primary decomposition step occurring between 200 °C and 500 °C, corresponding to the breakdown of polysulfide species (refer to **Figure 52**). Notably, the networked poly(S-

net-NB-AA) remained partially intact even at temperatures up to 900 °C, demonstrating enhanced thermal stability.

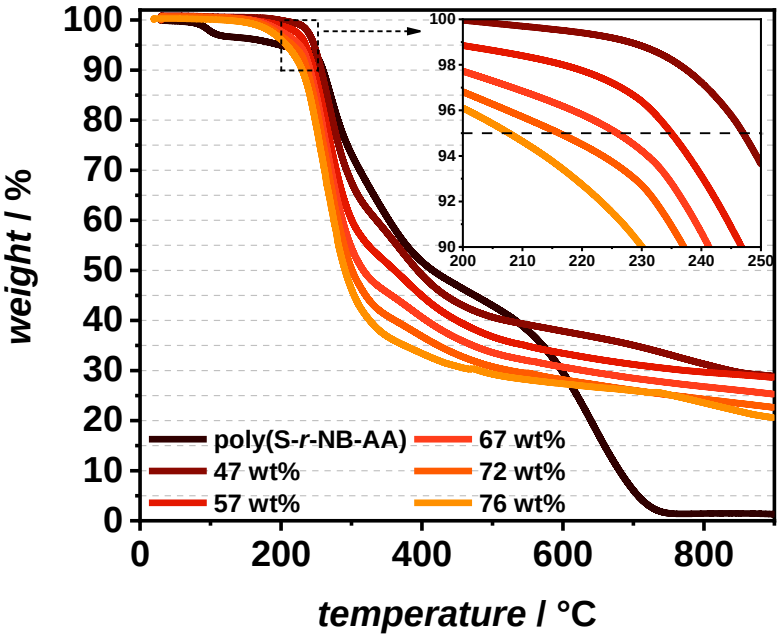

Figure 52. TGA curves of poly(S-*r*-NB-AA) and poly(S-*net*-NB-AA) with increasing sulfur content. $T_{5\%}$ decreased with increasing sulfur content of poly(S-*net*-NB-AA). The inset shows the magnified area from 200 to 250 °C.

Interestingly, the thermal properties of poly(S-*net*-NB-AA) were directly influenced by its sulfur content. Both T_g and thermal stability exhibited a linear decrease as sulfur content increased (refer to **Figure 53**). This correlation enables precise control and tunability of thermal properties by effectively cross-linking poly(S-*r*-NB-AA) through DCP with elemental sulfur.

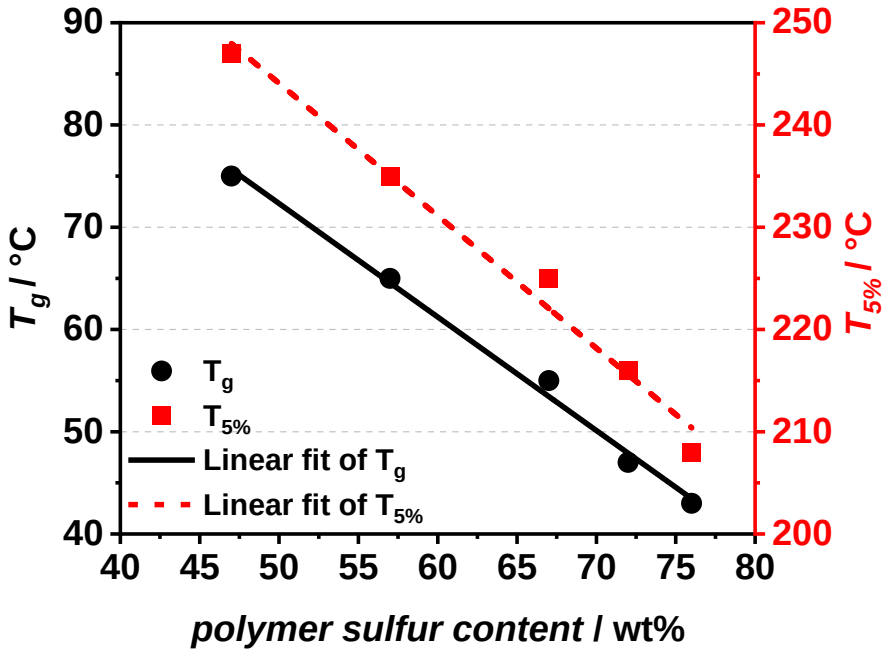

Figure 53. T_g and $T_{5\%}$ plotted against determined sulfur content of poly(S-*net*-NB-AA). A linear correlation was found and approximated with a linear fit, indicating tunability of thermal properties of poly(S-*net*-NB-AA).

3.2.7 PPM with Ferrocenyl Methylamine

As discussed in **Chapter 3.1.2** All-cis-2,3,4,5,6-pentafluorocyclohexyl Acrylate, IV-based materials are known to be applicable as electrochemical materials due to the redox potentials of sulfur against a suitable redox partner. To further investigate the tunability of poly(S-*r*-NB-PFPE) as versatile platform material for various applications, PPM with ferrocenyl methyl amine (FcMA) was conducted (refer to **Figure 54a**). Analogue to its PPM with Amino-mPEG, APTMS, and AA, poly(S-r-NB-PFPE) was dissolved in THF and 1.20 eq of FcMA were added. After stirring for 18 h at a.t., poly(S-r-NB-FcMA) was obtained after precipitation with cold petrol ether and subsequent drying. ^{1}H NMR and ^{19}F NMR spectroscopy confirmed the successful substitution of PFP-rings by the presence of aromatic ferrocene protons at 4.16 ppm (refer to **Figure 54b**) as well as the complete disappearance of fluorine atoms from the material (refer to **Figure 54c**).

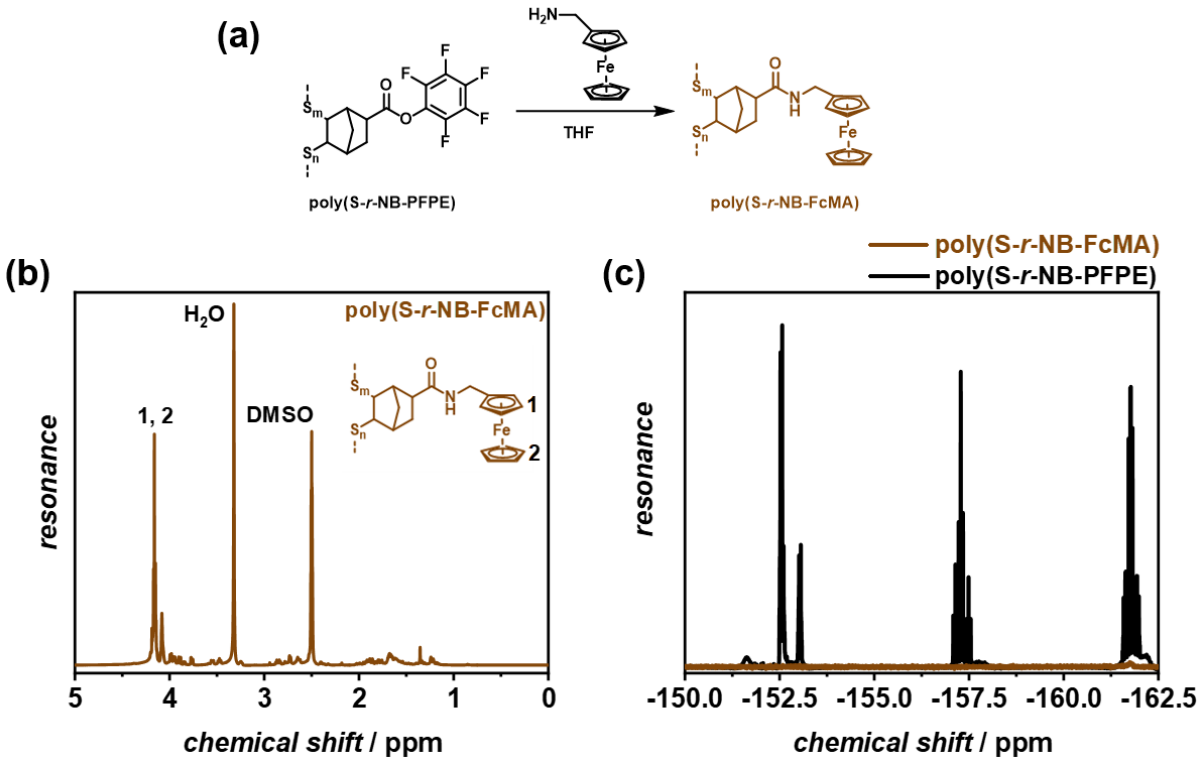

Figure 54. a) Amidation of poly(S-*r*-NB-PFPE) with FcMA, yielding poly(S-*r*-NB-FcMA). Brackets of repeating units are omitted for clarity and sulfur chains are abbreviated by dashed lines. ^{1}H NMR (b) and ^{19}F NMR (c) spectra of poly(S-*r*-NB-FcMA) (brown) and poly(S-*r*-NB-PFPE) in DMSO-d_6. Aromatic ferrocene protons were identified at 4.16 ppm and full conversion of PFP-rings was confirmed by absence of fluorine resonances.

The structure of poly(S-*r*-NB-FcMA) was further confirmed by ATR FT-IR spectroscopy (refer to **Figure 55**). Comparison of the IR spectrum of poly(S-*r*-NB-FcMA) with poly(S-*r*-NB-PFPE) showed the appearance of characteristic C=O absorbance peaks that could be assigned to the formation of amide bonds (1639 cm^{-1}) from ester bonds (1781 cm^{-1}). Additionally, amide N-H and C=C stretch vibrations were identified in the form of a broad absorption band at 3300 cm^{-1} and a weak absorbance at 3090 cm^{-1}, respectively. Characteristic ferrocene vibrations validated the successful synthesis of poly(S-*r*-NB-FcMA) by presence of medium absorbance bands at 1215 cm^{-1}, 816 cm^{-1}, and 608 cm^{-1} which were assigned to in-plane C-H bending, out-of-plane C-H bending, and ring deformation bending vibrations, respectively.[270]

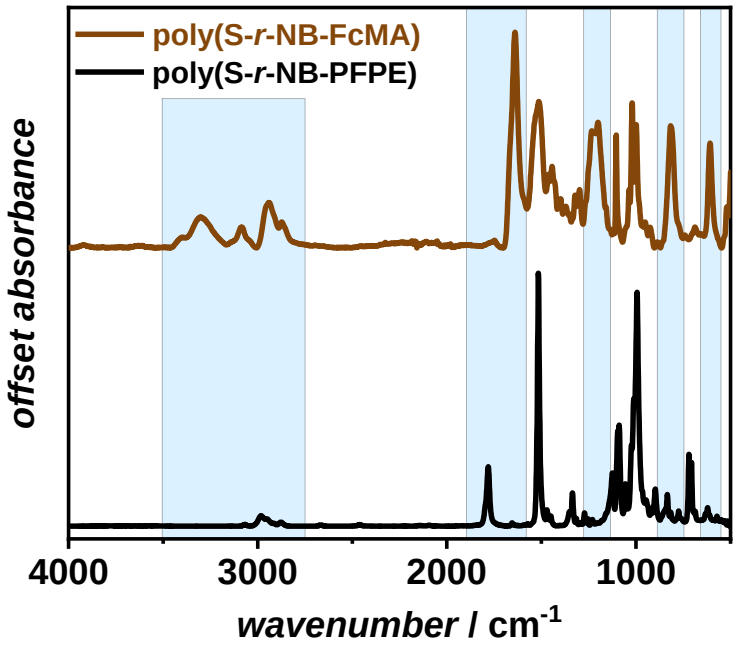

Figure 55. ATR FT-IR spectra of poly(S-*r*-NB-PFPE) (black) and poly(S-*r*-NB-FcMA) (brown). The highlighted areas show identified characteristic bond vibrations that confirm the proposed polymer structure. Resolution: 2 cm^{-1}.

SEC of poly(S-*r*-NB-FcMA) showed a strong increase in M_n of a factor of 5.7 and a decrease of *Đ* from 2.08 to 1.16 (refer to **Figure 56a**). While the decrease in *Đ* may be explained by the removal of low molecular species by precipitation, the shift in molecular weight does not reflect the theoretically expected increase of 5 % calculated from the polymer structure after the amidation. One explanation for the fast elution of poly(S-*r*-NB-FcMA) is a weaker interaction of the polymer with the column material which is not reflected by the calibration standard. DSC analysis of poly(S-*r*-NB-FcMA) revealed a shift of T_g of from 32 °C to 63 °C after amidation with FcMA which can be explained by the relatively short linkers between the bulky ferrocene units and is in accordance with earlier studies on ferrocene-containing polymers (refer to **Figure 56b**).[271]

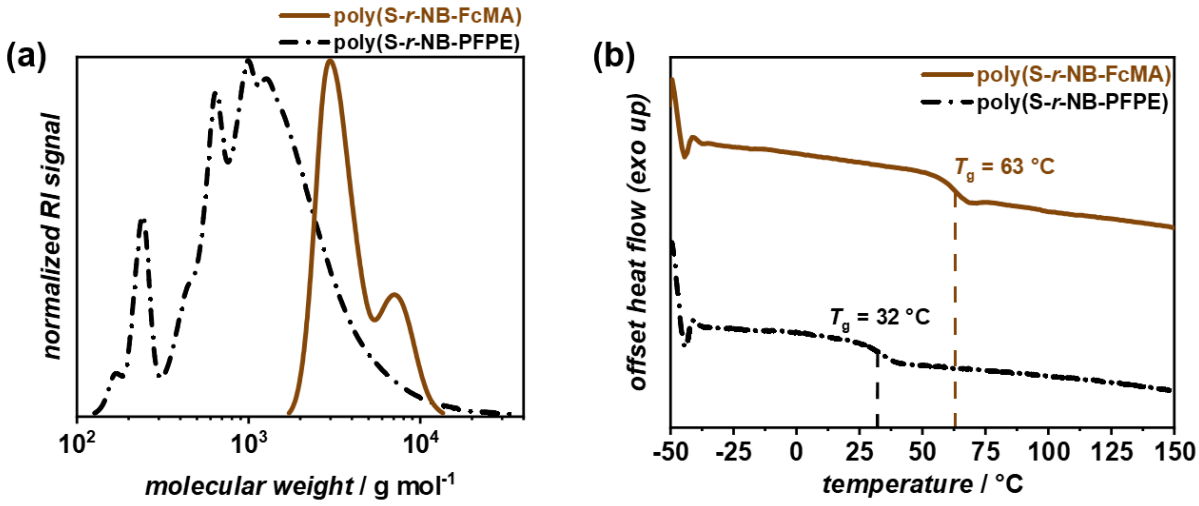

Figure 56. SEC (a) and DSC (b) traces of pol(S-*r*-NB-PFPE) (black) and poly(S-*r*-NB-FcMA) (brown). Poly(S-*r*-NB-FcMA): M_n = 4410 g mol^{-1}, M_w = 5120 g mol^{-1}, $Đ$ = 1.16. SEC solvent: THF; SEC calibration: PS; DSC heating rate: 10 K min^{-1}.

Ultimately, to uncover the electrochemical activity of poly(S-*r*-NB-FcMA), CV measurements against Ag/Ag$^+$ at varying scan rates were conducted (refer to **Figure 57a**). Cathodic peaks were identified at -0.80 V and -1.96 V which were attributed to the multi-step reduction of long chain oligosulfides ($S_{n\approx6}$) to short chain oligosulfides ($S_{n\approx4}$) and sulfides, respectively. The anodic peaks at 0.16 V and 0.89 V in turn could be assigned to the reverse process of oxidation of sulfides and oligosulfides back to polysulfides.[272]

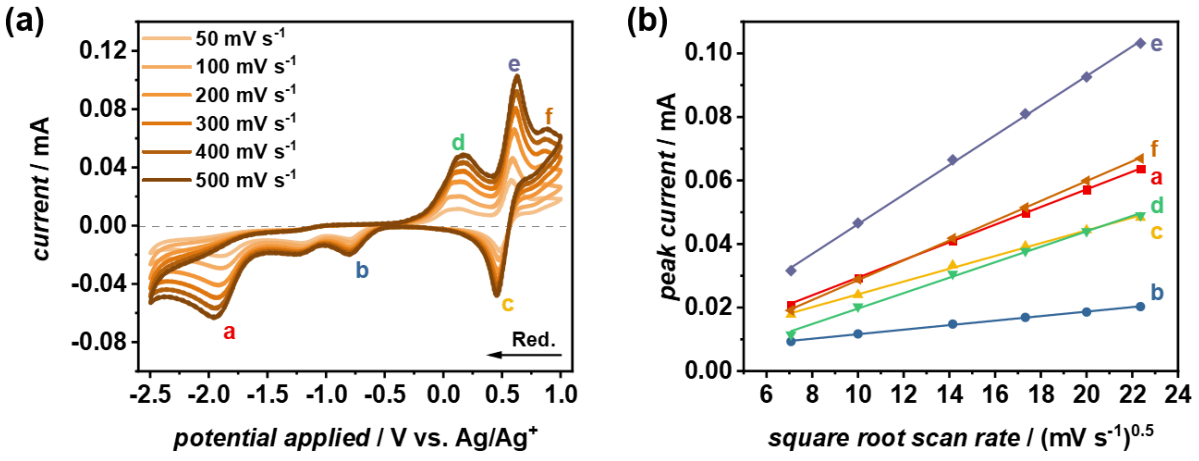

Figure 57. a) Cyclic voltammogram of poly(S-*r*-NB-FcMA) in DMSO against Ag/Ag$^+$ at different scan rates. Peaks were identified and labelled a – f. b) Plot of peak current against square root of the scan rate for each identified CV peak with linear fits. The fits show good linear correlation between peak current and square root of the scan rate which indicated diffusion-controlled redox processes.[273]

Importantly, in addition to these reactions, the CV spectrum of poly(S-*r*-NB-FcMA) also clearly shows the presence of a characteristic redox peak at 0.45 V and 0.64 V respectively which can be assigned to the redox reaction of Fe^{2+}/Fe^{3+} in the ferrocene units.[273] The peak currents were found to correlate linearly with the square root of the scan rate which is in accordance with the expected scan rate dependence and indicates diffusion-controlled redox processes (refer to **Figure 57b**).[273] This confirms the successful incorporation of FcMA and highlights the versatility of poly(S-*r*-NB-PFPE) as platform for potential future applications in electrochemical materials.

3.2.8 Summary

In this chapter, the IV of NB-PFPE with elemental sulfur was investigated, leading to the successful formation of poly(S-*r*-NB-PFPE). This polymer served as a versatile platform for amidation reactions, leveraging the active ester functionality of the PFP groups. Amidation of poly(S-*r*-NB-PFPE) was conducted in solution under mild conditions with four different primary amines: α-amino-ω-methoxy poly(ethylene glycol) (Amino-mPEG), aminopropyl trimethoxy silane (APTMS), allylamine (AA), and ferrocenyl methyl amine (FcMA). The reaction with Amino-mPEG resulted in the formation of spherical nanoscale particles, as confirmed by DLS and cryo-TEM analysis, when exposed to aqueous environments. These particles were unstable under dry conditions and thus may be applied in controlled substance capture and release by modulating environmental polarity or hydration levels in future studies. In a second approach, poly(S-*r*-NB-PFPE) was modified with APTMS, enabling the use of silane coupling chemistry. The siloxane polycondensation of poly(S-*r*-NB-APTMS) with high sulfur content led to the creation of spherical silica-sulfur particles that efficiently adsorb mercury. These silica-sulfur particles removed over 99 % of mercury from aqueous solutions, even at initial concentrations ranging from 1 to 100 ppm Hg^{2+}, with only 100 mg of the particles. Surface coatings of poly(S-*r*-NB-APTMS) were spin-coated onto silicon wafers, yielding homogeneous, hydrophobic, and colored surfaces. Thirdly, the synthesis of an unsaturated inverse vulcanized material was achieved by amidating poly(S-*r*-NB-PFPE) with AA. The glass transition temperature and thermal stability of the resulting poly(S-*r*-NB-AA) were precisely adjusted through additional cross-linking in a subsequent inverse vulcanization step with elemental sulfur. Lastly, poly(S-*r*-NB-PFPE) was modified via amidation with FcMA, which led to the integration of electrochemically active ferrocene units into the material. As was confirmed by CV,

the combination of polysulfide and ferrocene redox processes was achieved in a straightforward manner from PPM of active PFP-esters. The simple synthesis strategy demonstrated here highlights the potential of poly(S-*r*-NB-PFPE) as a platform for a wide array of specialized applications, including release systems, heavy metal remediation, antibacterial surfaces, lacquers, high-sulfur-content materials with tunable thermal properties, and electrochemically active materials.

3.3 Automated Synthesis and Post-polymerization Modification of Polypentafluorophenyl Acrylate in Continuous Flow

3.3.1 Disclaimer

The content of this chapter has been published in Macromolecular Rapid Communications from Wiley-VCH GmbH (Weinheim, Germany).[274] The complete authors list in the original order is Alexander P. Grimm, Dr. Stephen T. Knox, Dr. Clarissa Y. P. Wilding, Harry A. Jones, Björn Schmidt, Olga Piskljonow, Dr. Dominik Voll, Dr. Christian W. Schmitt, Prof. Dr. Nicholas J. Warren, and Prof. Dr. Patrick Théato.

Alexander P. Grimm is the first author of the article. Parts of this chapter and the corresponding parts in the experimental section were adapted with permission from this publication written by the author (Alexander P. Grimm).

The author contributions were as follows: A. P. G.: conceptualization, methodology, validation, formal analysis, investigation, data curation, writing – original draft & review & editing, visualization; S. T. K.: methodology, software, validation, formal analysis, investigation, data curation, writing – review & editing; C. Y. P. W.: software, formal analysis, investigation; H. A. J. and O. P.: formal analysis, investigation; B. S.: methodology, validation, formal analysis, investigation, data curation; C. W. S.: supervision, project administration, writing – review & editing; D.V., N. J. W., and P. T.: supervision, project administration, funding acquisition, writing – review & editing.

3.3.2 Introduction

The integration of ML and autonomous laboratory management has significantly advanced chemical synthesis, particularly in high-throughput data collection and

interpretation.[275] Real-time data analysis enables efficient reaction optimization and material composition investigation through rapid screening and importantly, continuous reaction platforms can be adapted into autonomous systems that rely on intelligent algorithms to iteratively optimize processes.[276] These algorithms analyze real-time data and dynamically control reactions by adjusting reactant concentrations and flow rates.[277] Flow processing offers greater stability and consistency compared to batch processing, thanks to its larger surface area-to-volume ratio, which ensures isothermal conditions, efficient heat dissipation, and straightforward scalability.[278] Furthermore, the continuous nature of flow systems makes them well-suited for online monitoring, as reaction progress can be directly tracked by analyzing the output stream.[32,208] Besides organic and inorganic chemistry, also polymer and supramolecular chemistry have greatly benefited from these advances, allowing precise control over reaction conditions and rapid screening of chemical systems. This has led to optimized polymerization reactions, scalable synthesis, enhanced reaction consistency, improved safety, and increased sustainability.[279] By leveraging large datasets and sophisticated ML algorithms, researchers can predict material properties, optimize reaction conditions, and design novel polymer structures.[280] A major challenge in synthetic polymer chemistry lies in balancing process efficiency and product quality. Controlled polymerization techniques, particularly reversible deactivation radical polymerization, are essential for achieving control of desired polymer properties such as molecular weight and *Đ*. Among these, RAFT polymerization stands out for its robustness and ease of application.[281] However, optimizing polymerization conditions requires careful balancing between reaction speed and product quality. By systematically exploring the relationship between conversion rates and dispersity, researchers can identify optimal conditions for improved efficiency and quality in polymer synthesis, making RAFT polymerization even more effective.[282] Recent innovations in RAFT polymerization have led to techniques such as photo-iniferter RAFT,[283] electro-RAFT,[284] sono-RAFT,[285] polymerization-induced self-assembly (PISA),[286] single-unit monomer insertion (SUMI),[287] and automated high-throughput RAFT polymerization.[225,288] Alongside controlled polymerization, PPM has gained increasing relevance.[289] Among various modification strategies, amidation and transesterification of active ester-containing polymers are among the most effective PPM methods where PFP-esters offer broad applicability, supporting advanced polymer architectures,[290] metal-catalyzed small molecule synthesis,[291] and next-

generation data storage and cryptography materials.[292] The exploration of poly(PFPA) as a precursor polymer for functional materials via flow chemistry presents a promising avenue for achieving complex polymer architectures with unprecedented speed, control, and efficiency. A noteworthy advancement in ML-assisted polymer synthesis was demonstrated in 2021 by REIS *et al.*, who utilized ^{19}F NMR spectroscopy to develop fluorinated copolymers for ^{19}F MRI agents through AI.[293] Despite the high natural abundance of ^{19}F, its strong gyromagnetic ratio, and a broad chemical shift range, ^{19}F NMR remains underutilized in flow chemistry.[294] To date, the RAFT polymerization of fluorinated active ester polymers and their post-polymerization modification in a continuous flow context remain largely unexplored.

3.3.3 Strategy

As known in literature, and demonstrated in **Chapter 3.2** Inverse Vulcanization of Norbornenyl-Pentafluorophenyl-Ester, the PPM of active PFP-ester containing polymers is a highly efficient reaction and the combination with characteristic advantages inherent to flow-based chemistry such as high reproducibility, easy upscaling, and precise control is believed to represent an important step to expand the toolbox of polymer chemists. In the current chapter, the automated optimization of the polymerization of PFPA by a self-optimizing algorithm and the derived implications for future remote-controlled, cloud-based reaction control are discussed (refer to **Chapter 3.3.4** Closed-loop Multi Objective Optimization of the Polymerization). Additionally, PPM of poly(PFPA) in continuous flow was investigated and the precise control over the resulting polymer by virtue of continuous reaction operation is presented and the results are discussed (refer to **Chapter 3.3.5** Post-polymerization Modification of poly(PFPA) and **Scheme 21**).

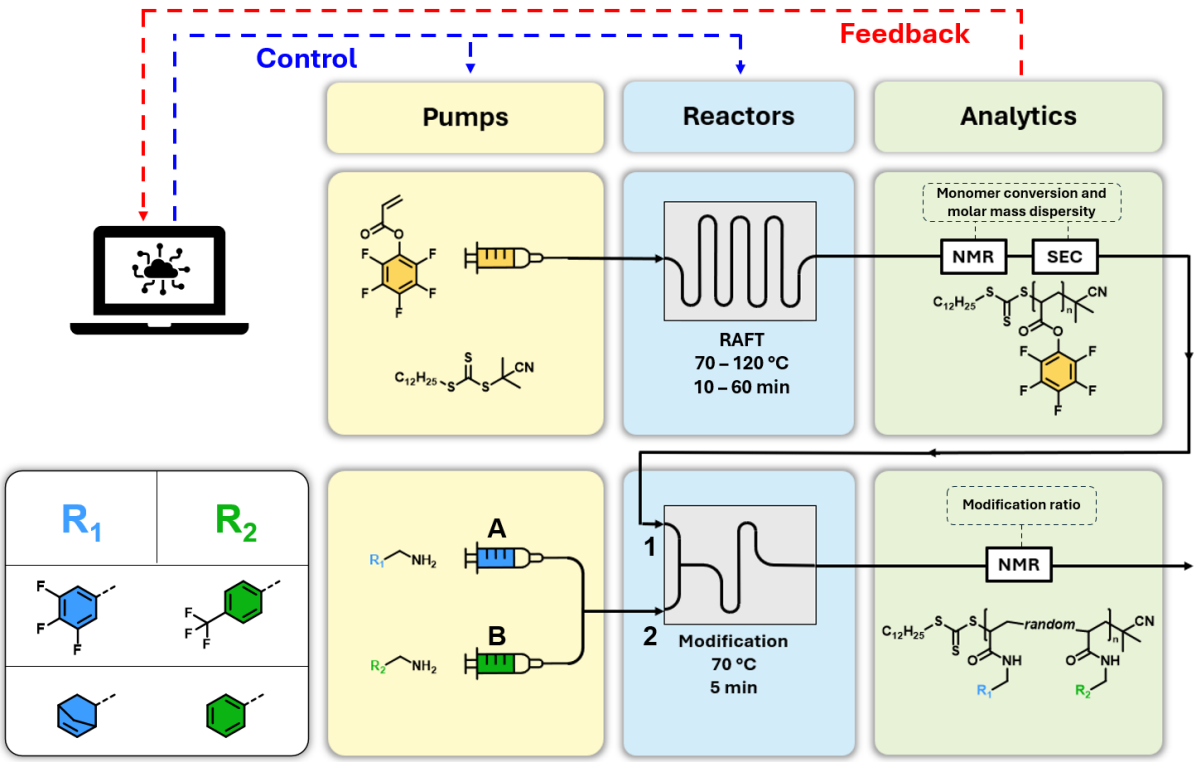

Scheme 21. Visualization of the flow reaction setup used in this chapter. Top: Automated polymerization platform for the RAFT polymerization of PFPA with software-based feedback and control loop. Bottom: Schematic of the PPM of poly(PFPA) with two different pairs of primary amines. Control over the flow rate facilitates the direct control over the modification ratio of the active polymer.

3.3.4 Closed-loop Multi Objective Optimization of the Polymerization

PFPA was synthesized following an established literature procedure, with successful preparation confirmed via NMR and ATR FT-IR spectroscopy (refer to **Appendix 1**).[227] The automated RAFT polymerization optimization platform was located in Leeds, UK and featured a stainless steel tubular flow reactor capable of heating and pressurization. The reaction output was analyzed using inline benchtop NMR spectroscopy for monomer conversion and online SEC for determination of molecular weight and *Đ*. Flow rates, t_r, and reaction temperatures were controlled via a custom-built MATLAB™ interface (details can be found in the experimental section; refer to **Chapter 5.2.7** Automated reactor platform (Leeds, UK)).

The polymerization was conducted using a pre-mixed solution of PFPA, cyanopropyl dodecyl trithiocarbonate (CPDT), and azobisisobutyronitrile (AIBN) in anisole, with concentrations set at 50:1:0.2 ([PFPA]:[CPDT]:[AIBN]) and a monomer concentration of 20 wt% (refer to **Figure 58a**). Optimization explored temperatures between 70 – 120 °C and residence times from 10 – 60 minutes. NMR spectra were acquired on demand at steady-state and processed using an automated script for phase and

baseline correction.[295] Monomer conversion was determined by comparing vinyl region peak integrals (5.0 – 6.0 ppm) before and after the reaction. Additionally, a programmable switching valve extracted approximately 3 µL samples for SEC, which provided M_n, M_w , and $Đ$ based on PMMA standards. A dataset was generated without human intervention, mapping conversion and $Đ$ across temperature and residence time variables. This data was visualized as a color-mapped surface plot, showing conversion (z-axis) and dispersity trends (color; refer to **Figure 58b**). Optimization was performed using the Thompson sampling efficient multi-objective (TSEMO) algorithm, which employs a Gaussian process-based model to iteratively select reaction conditions.[296] The algorithm sought optimal reaction conditions balancing 100 % conversion and $Đ$ = 1.0 within the predefined temperature and residence time range. It explored the trade-off between these two objectives, constructing a Pareto front of optimal conditions.[297] While TSEMO does not guarantee identification of all optima, it efficiently maps the Pareto front, allowing for rapid selection of the best reaction conditions.

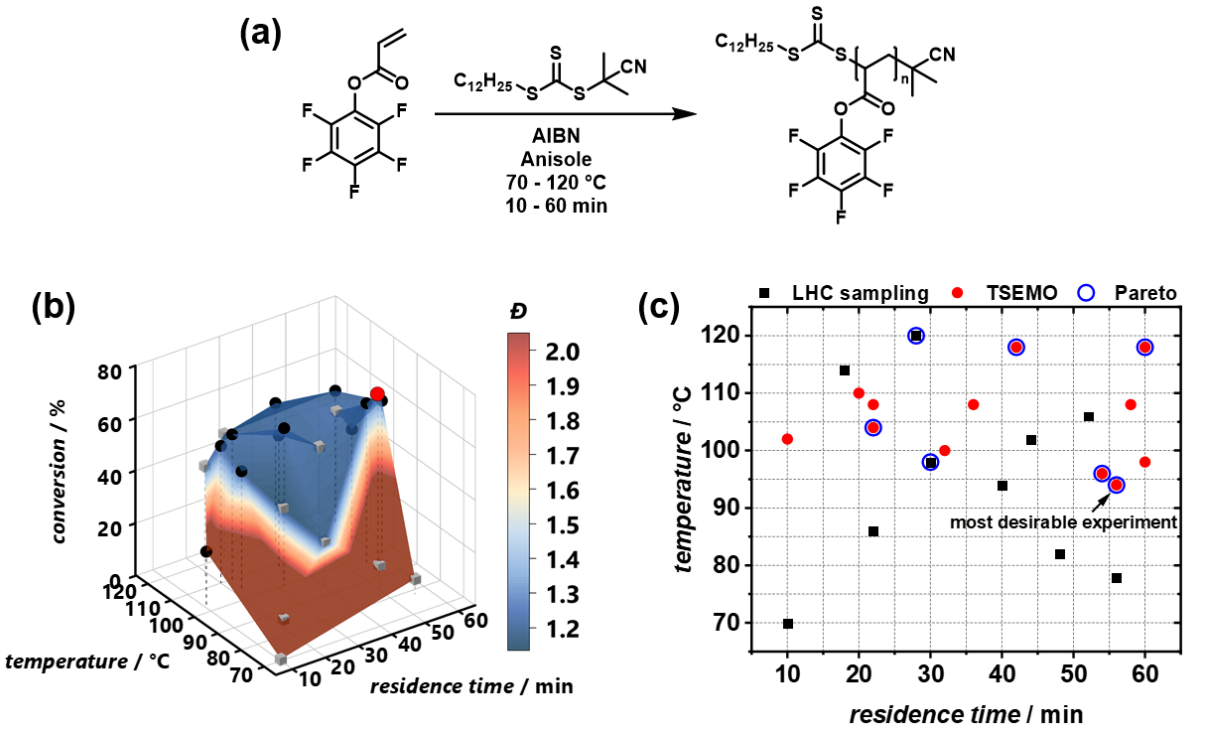

Figure 58. a) Reaction scheme of the polymerization of PFPA with CPDT and AIBN in anisole. b) Monomer conversion and molar mass dispersity for the automated polymerization of PFPA with CPDT and AIBN in anisole. LHC sampling training experiments are shown in gray; optimization results are shown in black. Red: reaction conditions explored by the TSEMO algorithm (parameter space: T = 70 – 120 °C, t_r = 10 – 60 min; optimal: T = 94 °C, t_r = 56 °C). c) Temperature and residence time pairs investigated by the automation algorithm. Black squares: experiments chosen by LHC sampling for training of the algorithm. Red circles: Suggested experiments for the multi objective optimization of high monomer conversion and low dispersity. Blue circles: non-dominated solutions of the optimization problem (Pareto front).

The optimization process began with 10 initial training experiments generated via Latin hypercube (LHC) sampling, ensuring diverse parameter coverage. For a workflow diagram of the automated optimization experiment, refer to **Appendix 14**. These initial experiments (gray data points in **Figure 58b**) were executed autonomously, with conversion and molecular weight distributions determined independently. The algorithm then suggested new reaction conditions, which were tested iteratively (black data points in **Figure 58b**), refining the search toward higher temperatures (> 90 °C), where improved performance was observed (refer to **Figure 58c**).

The study found that achieving substantial conversion required high temperatures and long residence times, leading to well-controlled polymerization with low dispersities (Đ ≈ 1.2) (refer to **Figure 59**).

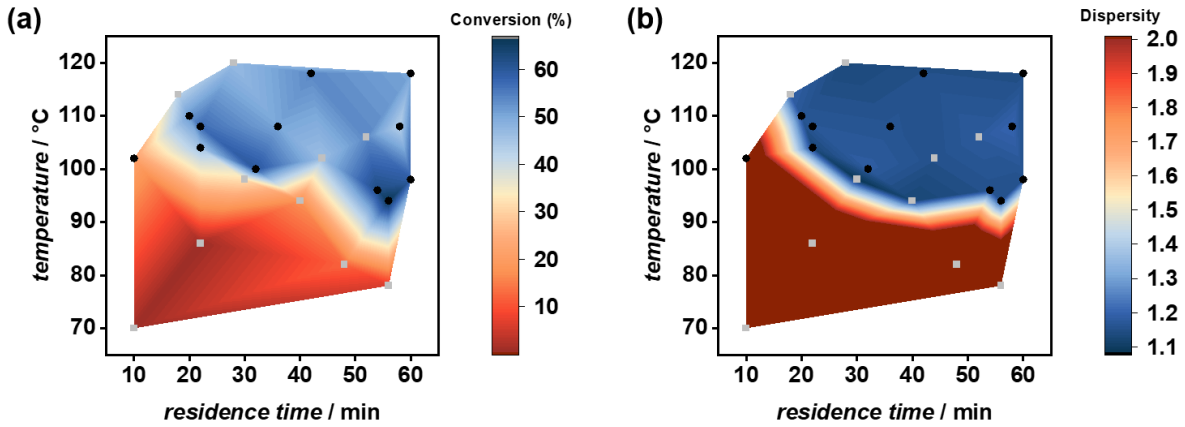

Figure 59. Conversion map (a) and dispersity map (b) of the automated optimization of the polymerization of PFPA in the investigated parameter space. Above 90 °C and 20 min residence time, the polymerization was found to run very controlled with reasonable monomer conversions. The loss of control over the polymerization mostly overlaps with the areas of low monomer conversion. Gray: LHC sampling experiments, black: algorithm-suggested optimization experiments.

Optimization was halted after 12 iterations once no significant improvements in hypervolume were detected by further exploring by the algorithm (refer to **Figure 60**). A detailed list of investigated reaction parameters with resulting monomer conversion, M_n, $Đ$, and hypervolume can be found in **Appendix 15**.

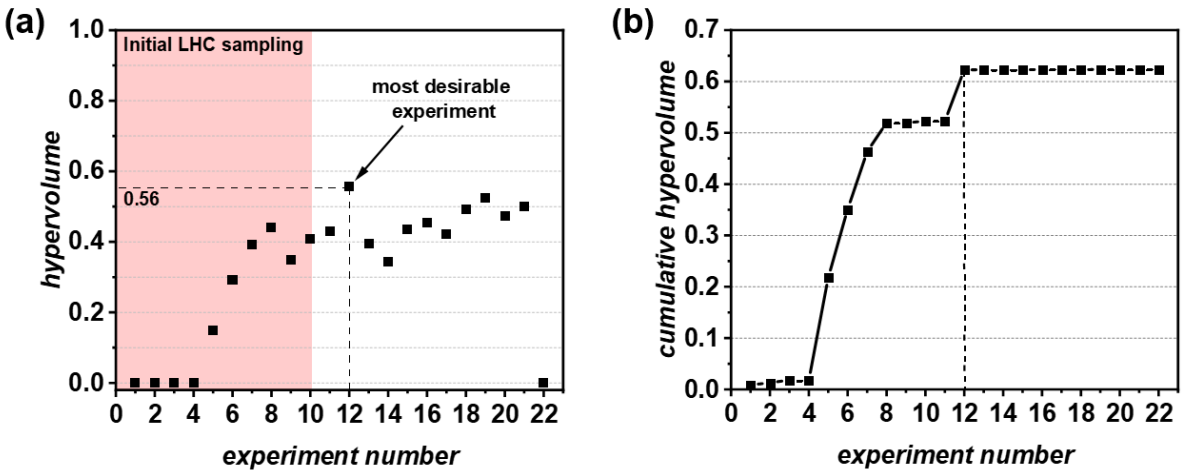

Figure 60. Hypervolume (a) and cumulative hypervolume (b) vs. experiment number. Highlighted area represents experiments derived from LHC sampling. Experiment 12 (highlighted) exhibited the highest hypervolume (0.56), making it the experiment with the most desirable reaction conditions with no significant improvement afterwards.

The final Pareto front comprised 7 optimal conditions, with 5 identified by the algorithm. However, from a chemical and polymer materials perspective, certain conditions were more desirable. To select a single optimum PPM, individual hypervolume contributions were analyzed and ultimately, iteration 12 (T = 94 °C, t_r = 56 min) was chosen,

contributing the highest hypervolume and emerging as the second suggested experiment by the algorithm (refer to **Figure 61**).[298]

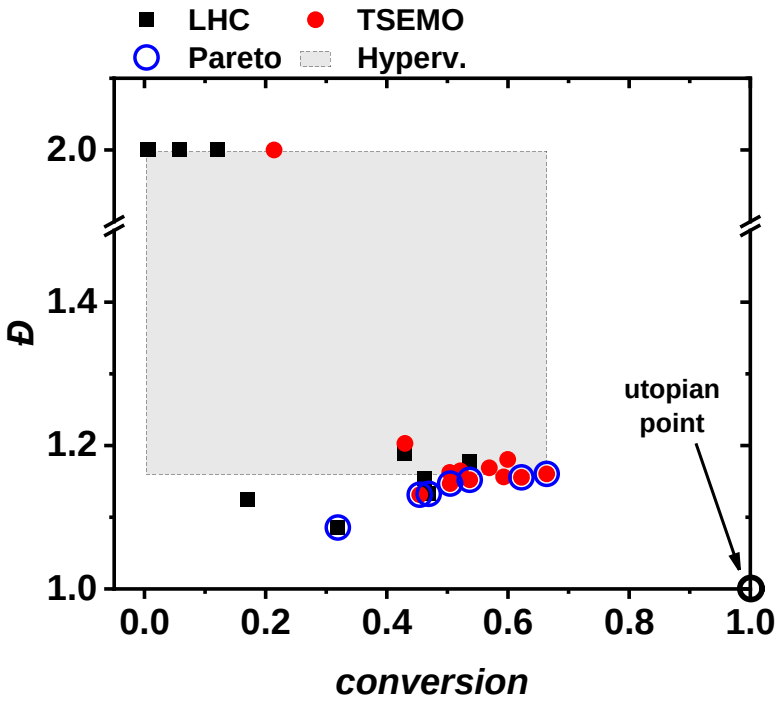

Figure 61. Visualization of the hypervolume during the optimization process. Black squares: experiments chosen by LHC sampling for training of the algorithm. Red circles: Suggested experiments for the multi objective optimization. Blue circles: non-dominated solutions of the optimization problem (Pareto front). The area created by the points on the Pareto front, the hypervolume, is an indicator of proximity to the utopian point, here: conversion = 1.0, Đ = 1.0. The hypervolume is examplatory visualized for only the right-most Pareto point. The dispersity of 2.0 was set as the upper limit to represent no control over the polymerization as in free radical polymerization. Measured dispersities exceeding this threshold were set to 2.0.

To validate the optimization results and demonstrate the robustness of automated polymer synthesis optimization in continuous flow, the ideal reaction parameters were tested in a comparative experiment in a different lab with a different flow setup located in Germany (details can be found in the experimental section; refer to **Chapter 5.2.8** Flow polymerization and PPM setup (Karlsruhe, Germany)). Although both experiments were based on flow chemistry, the reactor configurations differed slightly. A reaction solution with identical reactant concentrations ([PFPA] : [CPDT] : [AIBN] = 50 : 1 : 0.2; 20 wt% PFPA in anisole) was purged with nitrogen gas and introduced into a flow reactor setup. This system consisted of a syringe pump connected to a heated custom-made 3D-printed metal flow reactor (refer to **Figure 62a and c**), followed by sample collection.

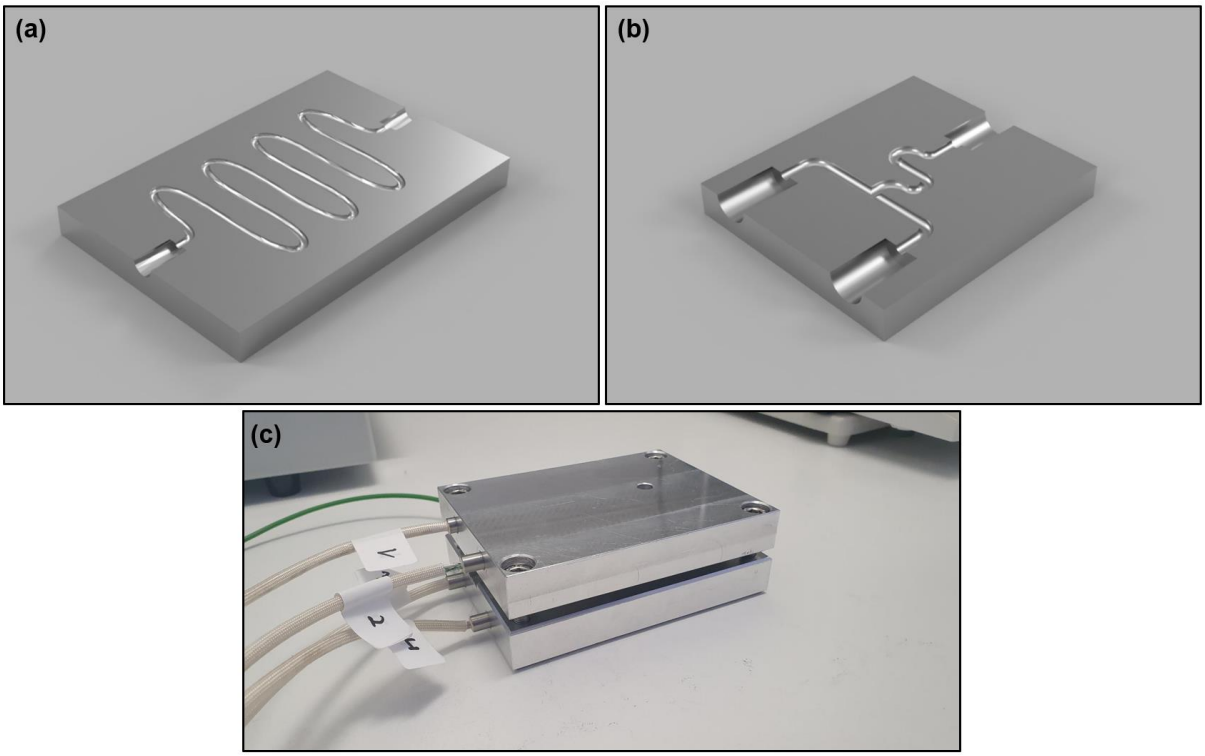

Figure 62. 3D-rendered cross-sections of a) the reactor used for heated flow-reactions (material: 316L, 1.4404 stainless steel, channel radius: 1 mm) and b) the mixer used to combine streams at ambient temperature (material: commercial 3D-printed methacrylic plastics, channel radius: 1 mm). c) Photography of the heating jackets (material: aluminum) with four inserted heating cartridges.

Monomer conversion was monitored via low-field (60 MHz) ^{1}H NMR spectroscopy by analyzing the vinyl region of the stock solution. The molecular weight distribution was determined via SEC using crude polymer solutions diluted in DMAc. Additionally, a batch polymerization was performed under identical conditions for further comparison. **Table 5** summarizes the monomer conversion and *Đ* for the optimized reaction, validation experiments, and batch polymerization.

Table 5. Monomer conversion and molar mass dispersity of the polymerization of PFPA conducted in two different, independent flow reactor setups and in batch. The most desirable reaction parameters found by the optimization algorithm were T = 94 °C and t_r = 56 min.

	optimization (flow, United Kingdom)	*validation* (flow, Germany)	*batch*
monomer conversion / %	66	64	63
Đ	1.16	1.26	1.30

The conversion rates of both flow polymerizations were found to be highly consistent, despite variations in reactor setup, demonstrating the reproducibility and robustness of autonomous polymerization automation. This high level of reproducibility further highlights the universality of automated polymer synthesis, even for functional polymers such as poly(PFPA). The observed 8 % deviation in $Đ$ can be attributed to multiple factors, including differences in flow rates, solvents, SEC columns, calibration methods, and the intrinsic variability of SEC measurements.[299] Noteworthy, the overall efficiency of PFPA polymerization in flow surpasses that of conventional batch polymerization, primarily due to enhanced heat transfer enabled by the higher surface-to-volume ratio in flow reactors. While these findings support the broad applicability of the optimized process, further advancements could be made by utilizing digital twin reactors to precisely map reactor fingerprints and develop scalable models.[300] Given the broad applicability of poly(PFPA) and its reactive ester functionality, continuous-flow polymerization offers an efficient high-throughput approach to accelerated material development, benefiting from enhanced reproducibility, efficiency, and safety.[301]

3.3.5 Post-polymerization Modification of poly(PFPA)

In addition to the polymerization of PFPA, high-throughput PPM of poly(PFPA) was performed in continuous flow. A pre-mixed solution of poly(PFPA) in DMF or DMAc was prepared at a concentration of 100 mg mL^{-1} and loaded into a syringe pump (flow rate = 0.1 mL min^{-1}). Two additional syringe pumps, labeled A and B, were each filled with solutions of different amines in DMF or DMAc, with amine concentrations chosen to match the active ester group concentration in the polymer solution.

In the modification process, the amine solutions from syringes A and B were combined and then merged with the polymer solution from syringe 1 in a custom-designed 3D-printed flow channel (refer to **Figure 62b**). The flow rates of streams A and B were adjusted so that their combined flow rate matched the flow rate of the polymer solution from syringe 1. The combined stream (Stream 2) was split into ratios of 10 – 90 mol% amine A and 90 – 10 mol% amine B, respectively, ensuring that the total flow rate after mixing remained 0.2 mL min^{-1} for all reaction compositions (refer to **Figure 63**). The 3D-printed flow channel had a 1.0 mL reactor volume, resulting in a residence time of 5 min for each modification.

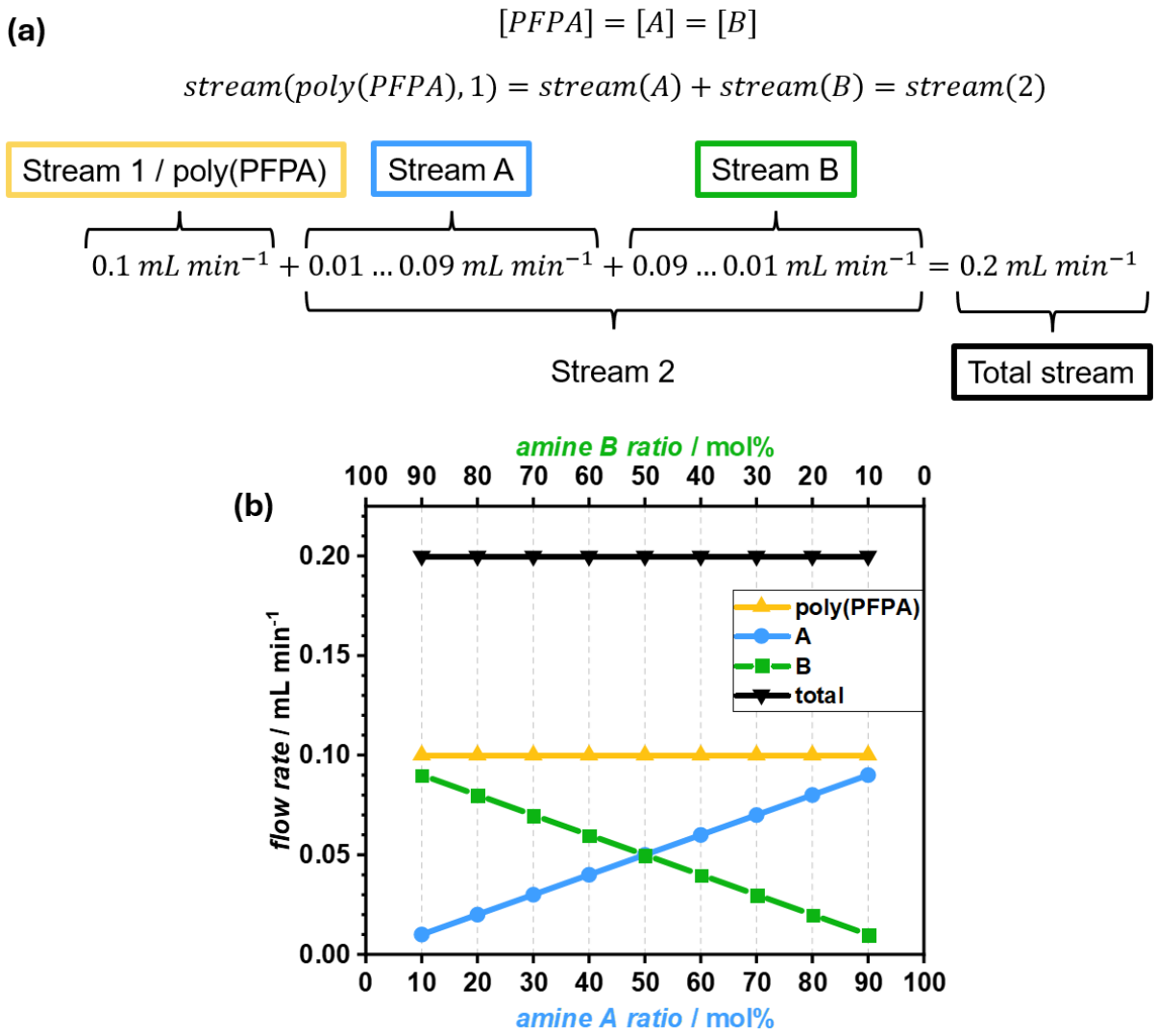

Figure 63. Mathematical (a) and graphical (b) relations of flow rates and ratios during the PPM of poly(PFPA) with two different amines (A and B) in continuous flow. Yellow refers to the stream of polymer solution, blue and green refer to the stream of amines A and B, respectively.

The modification of poly(PFPA) with two different amines was precisely controlled by adjusting the flow rates of the amine streams at known concentrations. The lower half of **Scheme 21** illustrates the flow path of the reaction setup for the PPM of poly(PFPA) in flow. Notably, when the PPM step was linked to the preceding polymerization step, a side reaction involving residual PFPA double bonds was observed in the ^{1}H NMR spectra after the addition of the amines. This side reaction likely occurred due to the Aza-Michael addition of the primary amine to the acrylate, as acrylates feature a carbonyl-activated double bond.[302]

While ^{19}F NMR spectroscopy confirmed the successful amidation of the PFP esters, the side reaction interfered with the double bond resonance in the ^{1}H NMR spectra,

preventing the accurate calculation of monomer conversion during polymerization (refer to **Figure 64**).

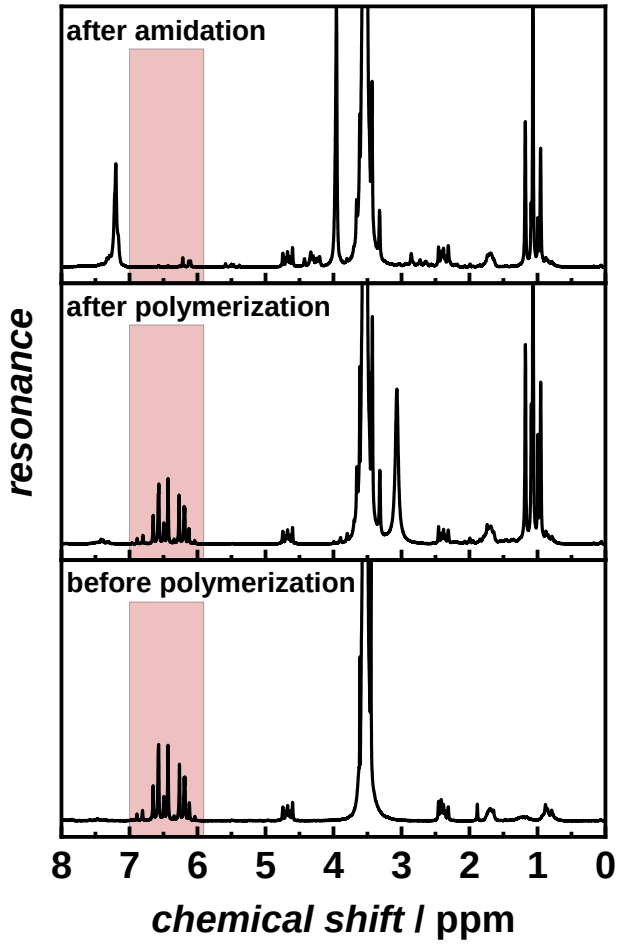

Figure 64. Low-field ^{1}H NMR spectra of the reaction solutions before the polymerization (bottom), after polymerization (middle), and after amidation with benzylamine (top) directly inline after polymerization. The highlighted area shows the vinyl double bond region. The double bonds were found to react with benzylamine in an Aza-Michael reaction, necessitating separation of polymerization and modification of PFPA. Solvent: 1,4-dioxane.

To obtain optimized results, the polymerization and PPM were thus studied separately. To enable simultaneous analysis of both polymerization and PPM in a single process, the reaction setup would need to be expanded, for example by integrating additional selective analysis steps, or a different chemical approach may need to be adopted.

3.3.5.1 PPM of poly(PFPA) *via* ^{19}F NMR

To demonstrate the flexibility and effectiveness of benchtop ^{19}F NMR analysis in continuous flow, an experiment was designed to control the modification of functional

poly(PFPA). Poly(PFPA) was modified using two different fluorinated primary amines, 3,4,5-trifluorobenzylamine (TFBA) and 4-(trifluoromethyl)benzyl amine (TFMBA) (refer to **Scheme 22**). The modified polymers were named poly(trifluoro benzyl acrylamide-*random*-trifluoromethyl benzyl acrylamide) (poly(TFBAAm-*r*-TFMBAAm)).

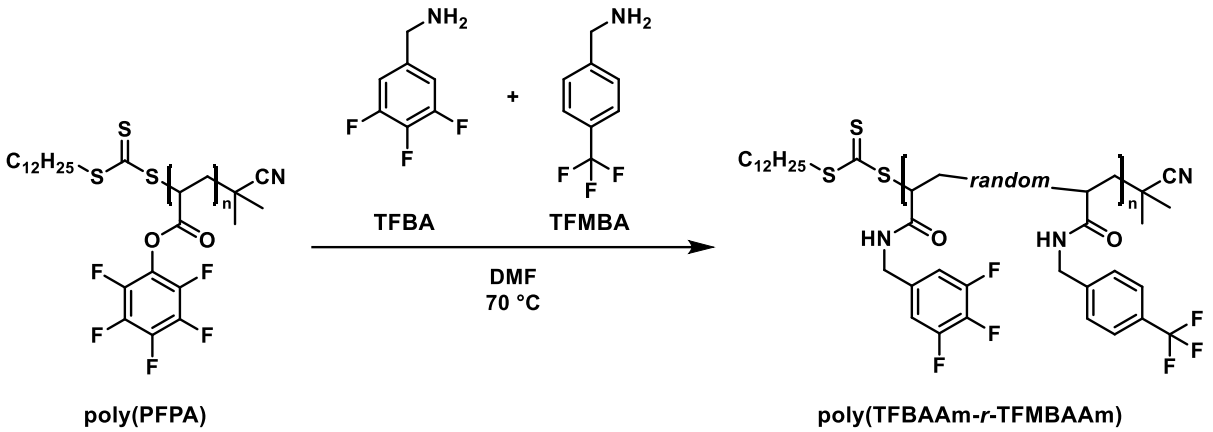

Scheme 22. Reaction scheme of the PPM of poly(PFPA) with TFBA (A) and TFMBA (B), yielding poly(TFBAAm-*r*-TFMBAAm).

It was hypothesized that the distinct chemical environments of aliphatic and aromatic fluorine substituents would allow clear differentiation between the two amine species. The ^{19}F NMR spectra of TFBA and TFMBA confirmed this, with the aliphatic fluorine atoms in TFMBA showing a resonance around -61 ppm, while TFBA showed two resonances at -136 ppm and -165 ppm corresponding to *meta* and *para* fluorine atoms, respectively (refer to **Figure 65**). By calculating the integral ratios of the *meta*-fluorine atoms from TFBA and the $-CF_3$ fluorine atoms from TFMBA, the amine ratio could be determined. Given the high reactivity of poly(PFPA) toward primary amines, it was hypothesized that the amidation of PFP active esters could be precisely controlled by adjusting the flow rates of the amine streams at known concentrations of PFPA units and amines.

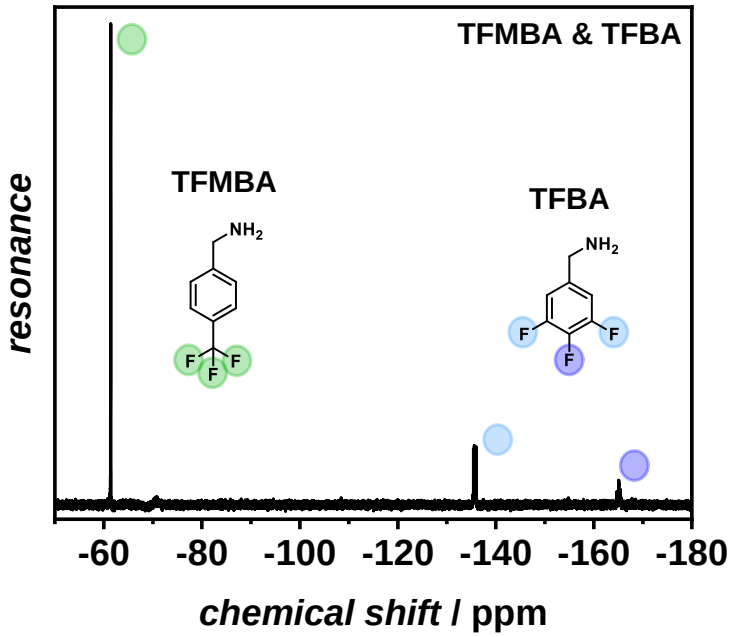

Figure 65. High-field ^{19}F NMR spectrum of a mixture of TFBA and TFMBA in DMSO-d_6. Aromatic and aliphatic fluorine atoms exhibit significantly different chemical shifts, allowing the calculation of the amount of the respective species by integration. Solvent: DMSO-d_6.

Solutions of poly(PFPA), TFBA, and TFMBA were prepared at equal concentrations and loaded into three separate syringe pumps. The flow rates of these solutions were screened as shown in **Figure 63**. The amidation of poly(PFPA) with primary amines occurs at room temperature, but for a balance between experiment time and conversion, the PPM was carried out with DMF as the solvent at 70 °C, with a residence time of 5 minutes for each reaction solution composition.[185] After adjusting the flow rates of amines A and B to achieve the desired modification ratio, the reactor was equilibrated with the new solution by passing 4 mL through the system (which took 20 minutes). Afterwards, 4 mL of the reaction solution were collected in a vial, and the polymer samples were isolated by precipitation in cold methanol, followed by centrifugation and vacuum drying. The modification ratios of TFBA and TFMBA were determined via ^{19}F NMR spectroscopy.

It was found that for each modification reaction, the amidation of PFP active esters was quantitative, as no PFP ester signals remained in the ^{19}F NMR spectra (refer to **Figure 66**).

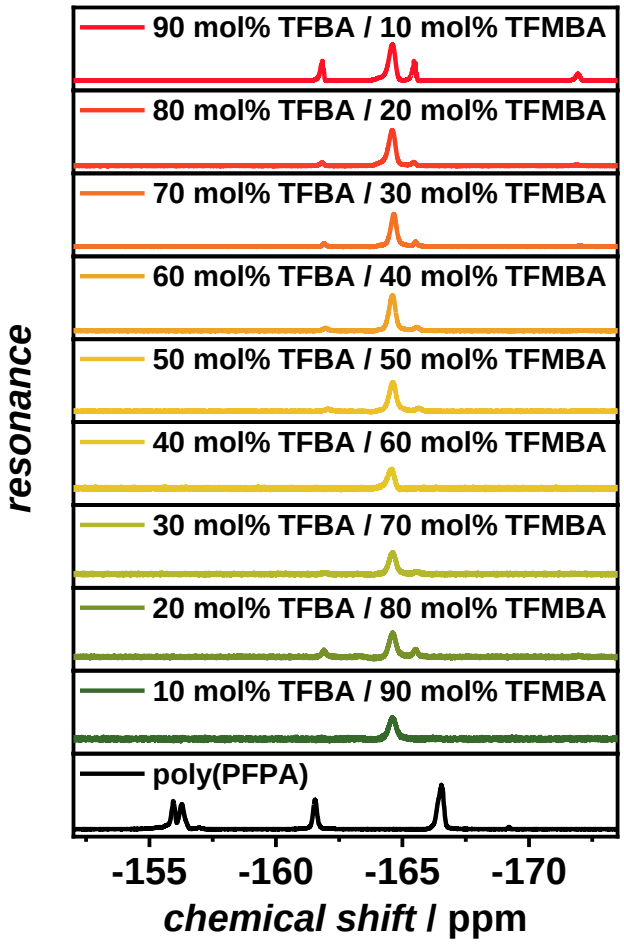

Figure 66. Stacked low-field ^{19}F NMR spectra of poly(PFPA) (black) and poly(TFBAAm-*r*-TFMBAAm) (colored) modified with different rations of TFBA and TFMBA. No more signals in the region of aromatic poly(PFPA) resonances were found which confirms the quantitative conversion of PFP-ester groups in 5 minutes at 70 °C. The singlet at -164.6 ppm can be attributed to the *para*-fluorine atom of TFBAAm, while the signals at -161.8, 165.5, and -172.0 ppm are assigned to detached PFP species. The amount of TFBA increased from green to red (10 – 90 mol%) while the amount of TFMBA increased from red to green (10 – 90 mol%), respectively. Solvent: DMSO-d_6.

The ratios of TFBA to TFMBA in the resulting polymers were calculated by comparing the *meta*-fluorine peaks of TFBA and the -CF_3 fluorine peaks of TFMBA (refer to **Figure 67a** and **Appendix 16**). Importantly, the final modification ratios in the polymers closely matched the input ratios of TFBA and TFMBA fed into the reactor, which were linked to the flow rates of the respective amine solutions. The precision of the modification was found to exceed 95 % across the composition range from 10 to 90 mol% (refer to **Figure 67b**). This excellent precision and control highlighted the power of ^{19}F NMR spectroscopy in controlling the PPM of poly(PFPA) in continuous flow, a method that, while widely used in batch polymerization, has seen limited application in continuous reaction control.

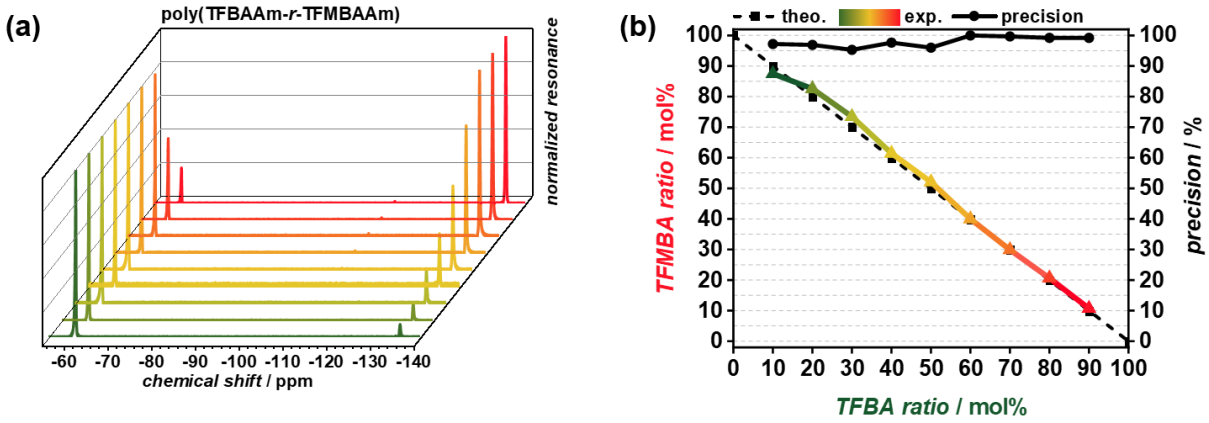

Figure 67. a) Normalized ^{19}F NMR spectra of poly(TFBAAm-*r*-TFMBAAm) in the region between -55 and -140 ppm. The left peaks at -61 ppm are attributed to the -CF_3 group of TFMBA while the right peaks at -135 ppm are attributed to the *meta*-fluorine atoms of TFBA. b) Theoretical and experimental modification ratios of poly(PFPA) with TFBA and TFMBA, respectively. The black dashed line represents the theoretical input ratios of TFBA and TFMBA which are directly correlated to the flow rates of the reactor setup while the colored solid line represent the found ratios in the final polymers. The precision (black circles) shows that almost perfect control over the modification was obtained. The amount of TFBA increased from green to red (10 – 90 mol%) while the amount of TFMBA increased from red to green (10 – 90 mol%), respectively. Solvent: DMSO-d_6.

Additionally, ^1H NMR spectroscopy was used to investigate its potential in determining the modification ratios with TFBA and TFMBA. The trends in the resonances corresponding to the aromatic protons were clear (refer to **Figure 68**). However, due to the similarity in the chemical environment of the protons in TFBA and TFMBA, it was not possible to isolate the integrations of the respective protons.

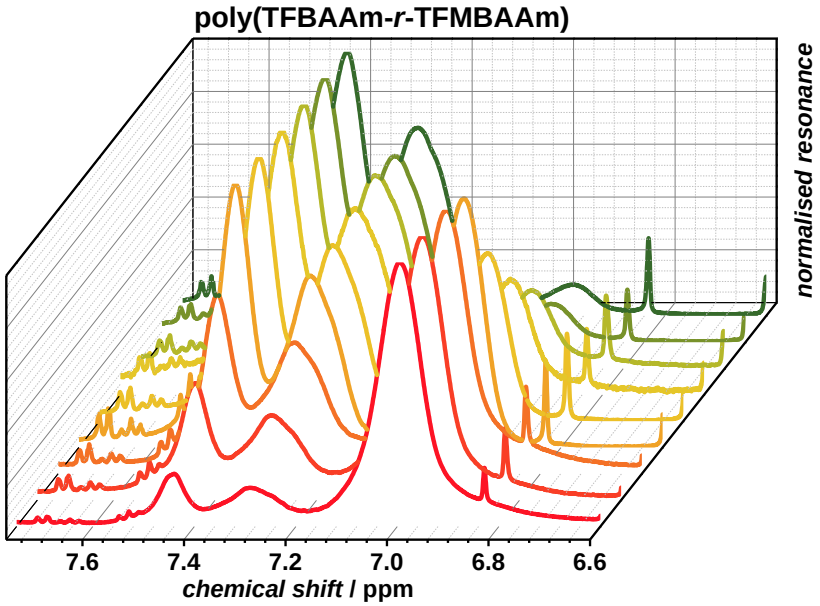

Figure 68. Waterfall plot of the normalized ^{1}H NMR spectra of poly(TFBAAm-*r*-TFMBAAm) in the region between 7.75 and 6.60 ppm recorded on a high-field device. A distinction between TFBAAm and TFMBAAm groups can be made, however no quantitative integration of characteristic signals was possible due to signal overlap. The amount of TFBA increased from green to red (10 – 90 mol%) while the amount of TFMBA increased from red to green (10 – 90 mol%), respectively. Solvent: DMSO-d_6.

Interestingly, the modification of poly(PFPA) with different ratios of TFBA and TFMBA influenced the polymer's IR absorbance (refer to **Figure 69a**). As the TFBA content increased, the absorbance of C-C ring vibrations from fluorine-substituted aromatics increased at 1527 cm^{-1}, 1448 cm^{-1}, and 1356 cm^{-1} (peaks A to C).[303] Meanwhile, the decrease of TFMBA content resulted in a reduction of IR absorbance at wavenumbers attributed to -CF_3 groups (1322 cm^{-1}, 1162 cm^{-1}, 1120 cm^{-1}, and 1065 cm^{-1}, peaks D to G).[304,305] The correlation between absorbance and amine ratio was linear, demonstrating the applicability of IR spectroscopy for controlling PPM of poly(PFPA) in continuous flow and broadening the range of modifying agents that can be selectively analyzed based on functional groups incorporated into the polymer (refer to **Figure 69b**).

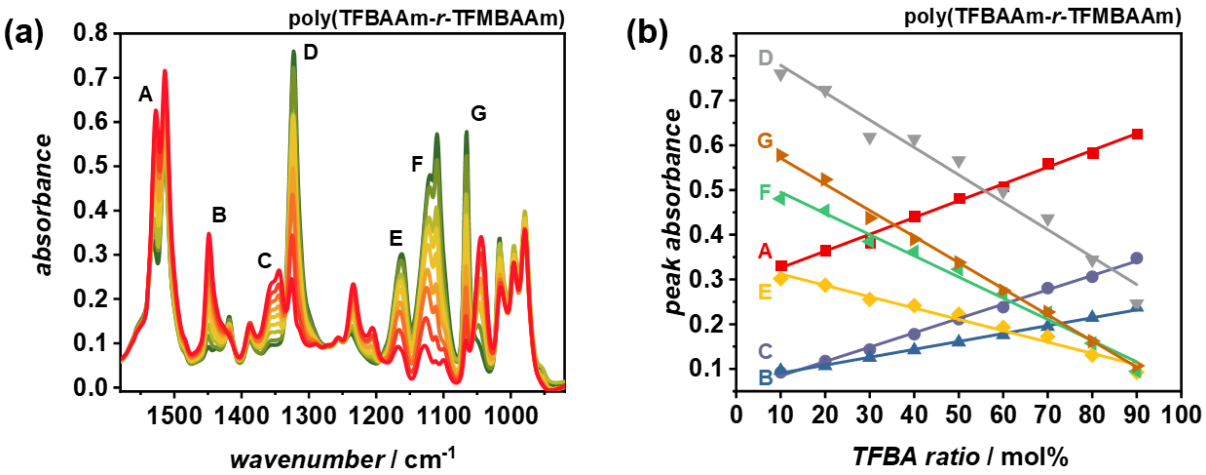

Figure 69. a) ATR FT-IR spectra of poly(TFBAAm-*r*-TFMBAAm) in the range of 1580 cm^{-1} to 920 cm^{-1}. The amount of TFBA increased from green to red (10 – 90 mol%) while the amount of TFBA increased from red to green (10 – 90 mol%), respectively. Characteristic peaks assigned to TFBA and TFMBA, respectively were identified which were found to increase or decrease linearly with the amount of respective amine. Resolution: 2 cm^{-1}. b) Linear fits of the peak absorbance against the ratio of TFBA of peaks A – G.

SEC analysis of poly(TFBAAm-*r*-TFMBAAm) showed an overall increase in molecular weight with the incorporation of the heavier TFMBA groups, consistent with the proposed modification of poly(PFPA), while the dispersity remained relatively unchanged (refer to **Figure 70**). Detailed information about M_n and $Đ$ are displayed in **Appendix 17**.

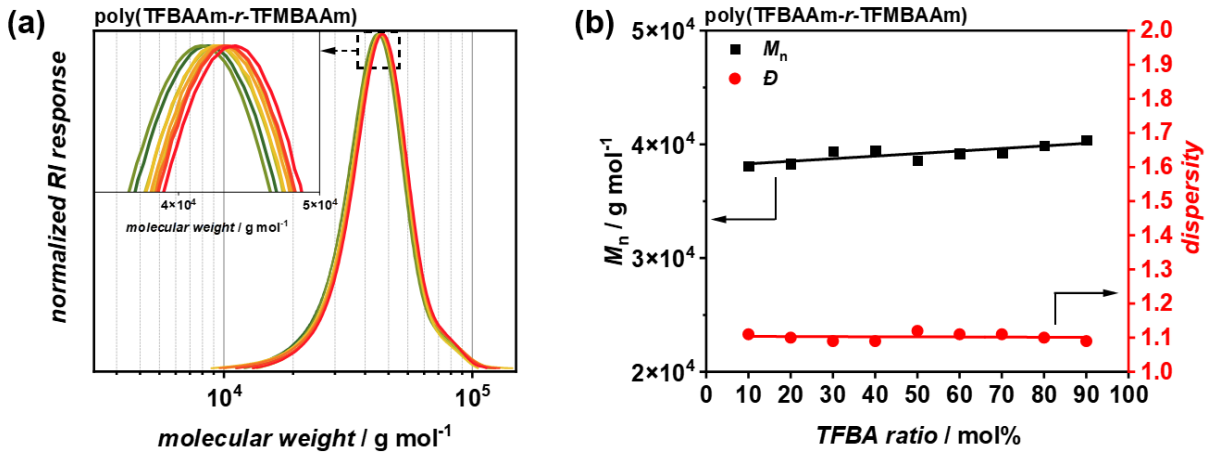

Figure 70. a) SEC traces of poly(TFBAAm-*r*-TFMBAAm) in DMAc. A slight increase in molecular weight was observed with increasing amounts of heavier TFMBAAm in the polymer. The amount of TFBA increased from green to red (10 – 90 mol%) while the amount of TFBA increased from red to green (10 – 90 mol%), respectively. Calibration: PMMA. b) M_n and $Đ$ vs. TFBAAm content in poly(TFBAAm-*r*-TFMBAAm) with linear fits. The M_n (black) was found to slightly increase, while $Đ$ (red) remained virtually unchanged. Solvent: DMAc; calibration: PMMA.

Thermal properties of the modified polymers were studied using TGA and DSC. TGA revealed a two-step thermal decomposition process for poly(TFBAAm-*r*-TFMBAAm), with the first decomposition starting at approximately 140 °C ($T_{5\%} \approx 155$ °C). This initial decomposition was dependent on the polymer composition, with higher TFBA content leading to greater weight loss. The second decomposition began around 340 °C and resulted in complete polymer decomposition ($T_{95\%} \approx 436$ °C) (refer to **Figure 71a**). DSC analysis showed a T_g of 20 °C for all poly(TFBAAm-*r*-TFMBAAm) compositions regardless of the modification ratio between A and B (refer to **Figure 71b**).

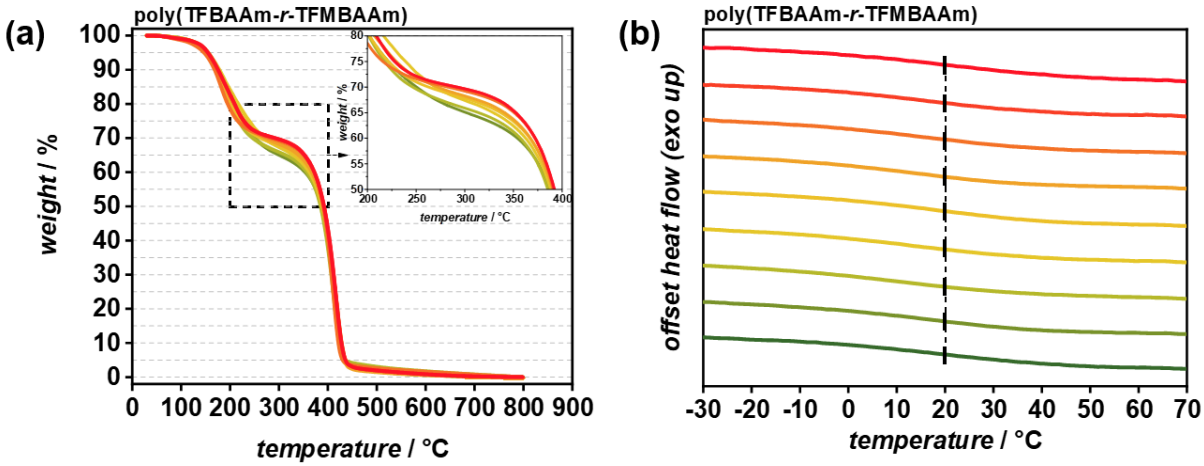

Figure 71. a) Thermal decomposition profile of poly(TFBAAm-*r*-TFMBAAm) with different amounts of TFBAAm and TFMBAAm incorporated into the polymer. b) Offset DSC thermograms of poly(TFBAAm-*r*-TFMBAAm) from -30 to 70 °C. The glass transition temperatures (black lines) were found to be 20 °C, regardless of the modification ratio. The amount of TFBA increased from green to red (10 – 90 mol%) while the amount of TFMBA increased from ref to green (10 – 90 mol%), respectively.

Thus, while the thermal properties of poly(TFBAAm-*r*-TFMBAAm) could not be significantly tuned due to the similarity between TFBA and TFMBA, this strategy provides a highly controlled and versatile approach for modifying poly(PFPA) in continuous flow, facilitated by ^{19}F NMR and IR spectroscopy in combination with continuous flow polymer reaction control.

3.3.5.2 PPM of poly(PFPA) *via* ^{1}H NMR

Building on the strategy outlined in the previous chapter, an experiment was designed to extend the presented methodology to not only ^{19}F NMR but also ^{1}H NMR spectroscopy to monitor the modification ratio of poly(PFPA). It was hypothesized that by utilizing modifying agents with distinct proton resonances, the range of applicable amines could be extended beyond fluorinated compounds. Given the unique chemical

environments of aromatic and olefinic protons, it was believed that these two groups would be sufficiently distinguishable in ^{1}H NMR spectra, allowing for quantitative integration and calculation of modification ratios based on aromatic and C=C double bond signals. A mixture of 5-norbornenyl-2-methylamine (NBMA) and benzylamine (BA) exhibited separate aromatic and olefin proton resonances, which were suitable for integration and ratio calculation (refer to **Figure 72**).

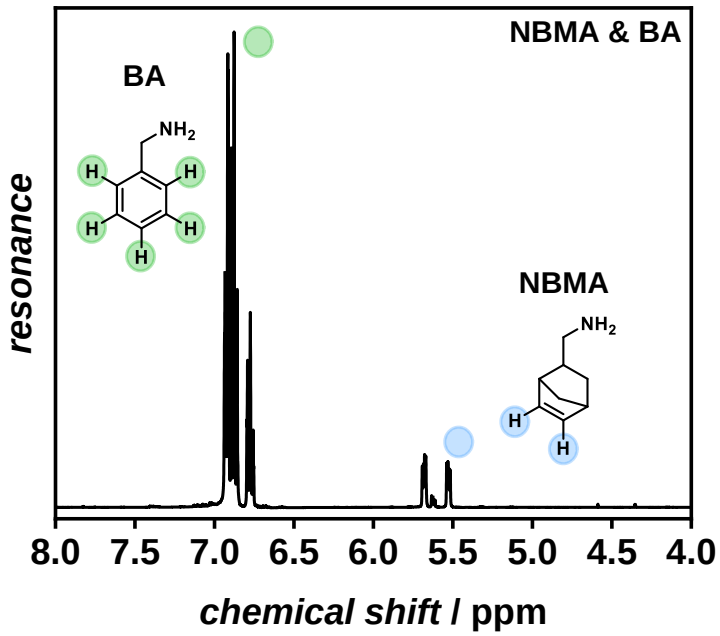

Figure 72. High-field ^{1}H NMR spectrum of a mixture of NBMA and BA in DMSO-d_6. Aromatic and double bond protons exhibit significantly different chemical shifts, allowing the calculation of the amount of the respective species by integration. Solvent: DMSO-d_6.

As a result, the PPM of poly(PFPA) with NBMA and BA was carried out in continuous flow, screening the ratio of NBMA (A) to BA (B) (refer to **Scheme 23**). The resulting polymers were named poly(5-norbornenyl-2-methyl)acrylamide-*random*-benzyl acrylamide) (poly(NBMAAm-*r*-BAAm)).

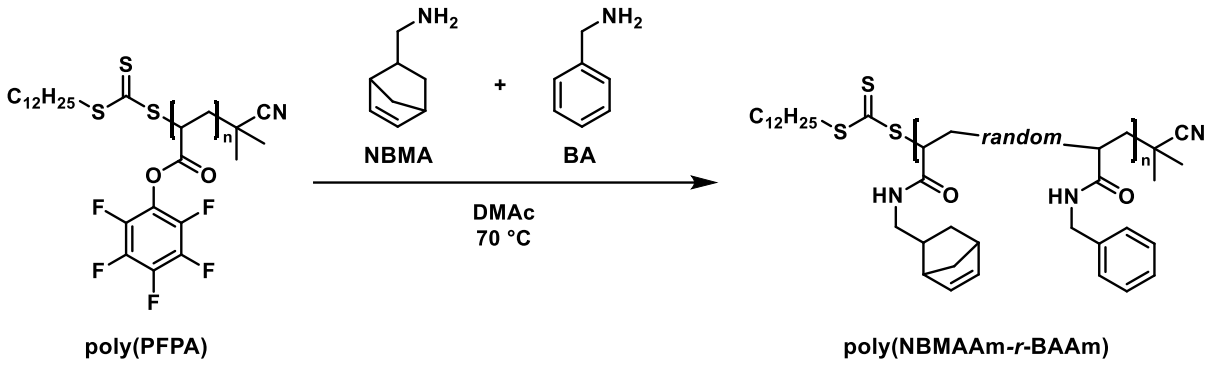

Scheme 23. Reaction scheme of the PPM of poly(PFPA) with NBMA (A) and BA (B), yielding poly(NBMAAm-*r*-BAAm).

Solutions of poly(PFPA), NBMA, and BA were prepared with equal concentrations and loaded into three separate syringe pumps. The flow rates of the three solutions were adjusted as shown in **Figure 63**. The PPM of poly(PFPA) was conducted using DMAc as the solvent instead of DMF to avoid solvent peaks overlapping with the aromatic proton resonance area (δ aromatic protons ≈ 7 – 8 ppm; δ DMF-CH proton ≈ 8 ppm; DMAc-*α*-CH_3 protons ≈ 2 ppm).[306] The reaction temperature was set to 70 °C, with a residence time of 5 minutes for each reaction solution composition. Polymer samples were collected and isolated by precipitation into cold methanol, centrifugation, and vacuum drying. The modification ratios of NBMA and BA were determined via ^{1}H NMR spectroscopy. **Figure 73a and b** show the normalized ^{1}H NMR spectra of poly(NBMAAm-*r*-BAAm) in the region of C=C double bonds and aromatic protons, where the resonance between 7.00 and 7.50 ppm is attributed to the five aromatic protons of BAAm, and the split signal between 5.75 and 6.25 ppm is assigned to the two double bond protons of the norbornene group in NBMAAm.

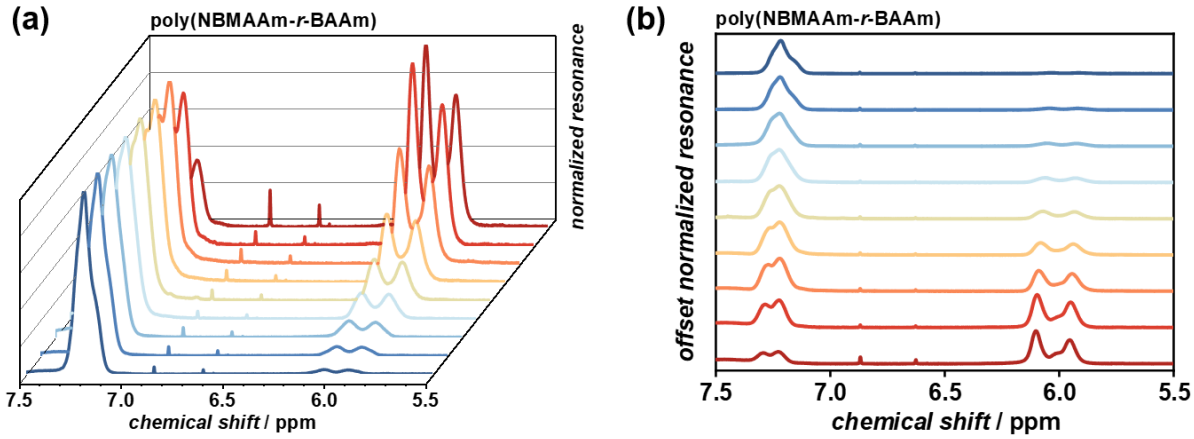

Figure 73. Normalized ^{1}H NMR spectra of poly(NBMAAm-*r*-BAAm) as waterfall (a) and stacked (b) plot in the region between 7.5 and 5.5 ppm. The left peak at around 7.25 ppm is attributed to the aromatic ring of BA while the right peaks at around 6 ppm are attributed to double bond protons of NBMA. The amount of NBMA increased from blue to red (10 – 90 mol%) while the amount of BA increased from red to blue (10 – 90 mol%), respectively. Solvent: DMSO-d_6.

Notably, the final modification ratios in the polymers closely matched the input ratios of NBMA and BA fed into the flow reactor. However, the modification was slightly less precise compared to the PPM of poly(PFPA) with fluorinated amines. The amount of incorporated BA was slightly higher than expected based on the input ratio (refer to **Figure 74**).

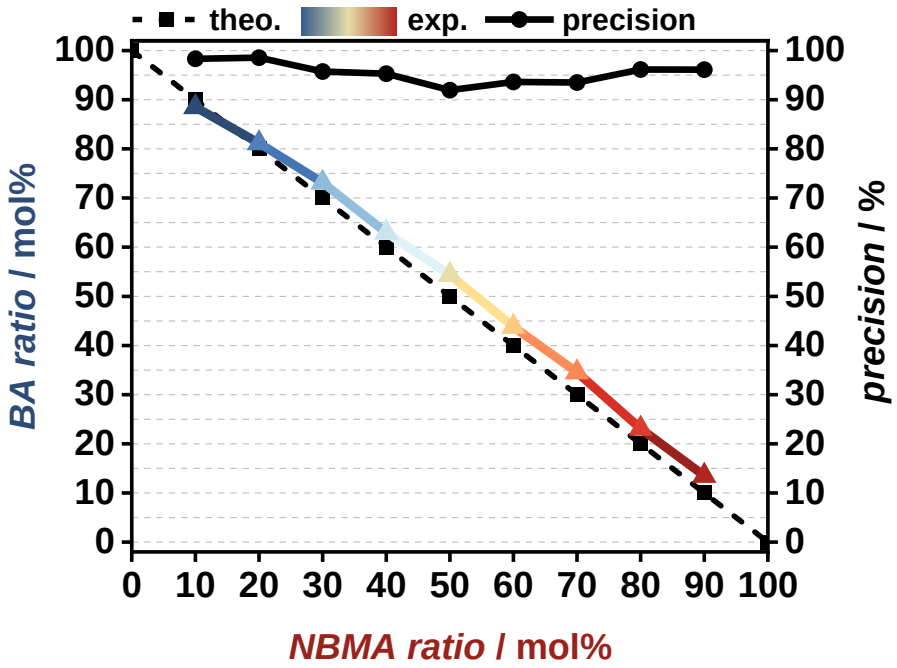

Figure 74. Theoretical and experimental modification ratios of poly(PFPA) with NBMA and BA, respectively. The black dashed line represents the theoretical input ratios of NBMA and BA which are directly correlated to the flow rates of the reactor setup while colored solid line represents the found ratios in the final polymers. The precision (black circles) shows that exceptionally good control over the modification was obtained. The amount of NBMA increased from blue to red (10 – 90 mol%) while the amount of BA increased from red to blue (a0 – 10 mol%), respectively.

The slightly higher incorporation of BA compared to NBMA may be due to differences in the nucleophilicity of aromatic and aliphatic amines,[307] and the possible but negligible loss of C=C double bond protons from side reactions of the norbornene moiety, which typically requires harsh conditions or catalysts.[308] Nonetheless, the precision of modification control was found to be above 90 % throughout the investigation range of 10 – 90 mol% NBMA or 90 – 10 mol% BA, respectively. The effect of varying modification ratios on the absorbance of poly(NBMAAm-*r*-BAAm) was also examined using IR spectroscopy (refer to **Figure 75a**). C-H stretch vibrations associated with C=C double bonds at 3030 cm^{-1} (peak A) decreased with the reduced amount of aromatic benzyl groups in the polymers.[309] This result aligned with the expected modification, as C=C double bonds were more prominent in BA than in NBMA. Peaks B to D at 2965 cm^{-1}, 2936 cm^{-1}, and 2868 cm^{-1} were assigned to the asymmetric CH_2 stretch, ring CH stretch, and symmetric CH_2 stretch vibrations of the norbornene ring, respectively, and increased as the input ratio of NBMA increased.[310] The correlation between peak absorbance and amine ratio was found to be linear (refer to **Figure 75b**), supporting the linear modification ratio predicted by the experimental design. However, due to the structural similarity between NBMA and BA, IR analysis of poly(NBMAAm-*r*-BAAm) remained challenging.

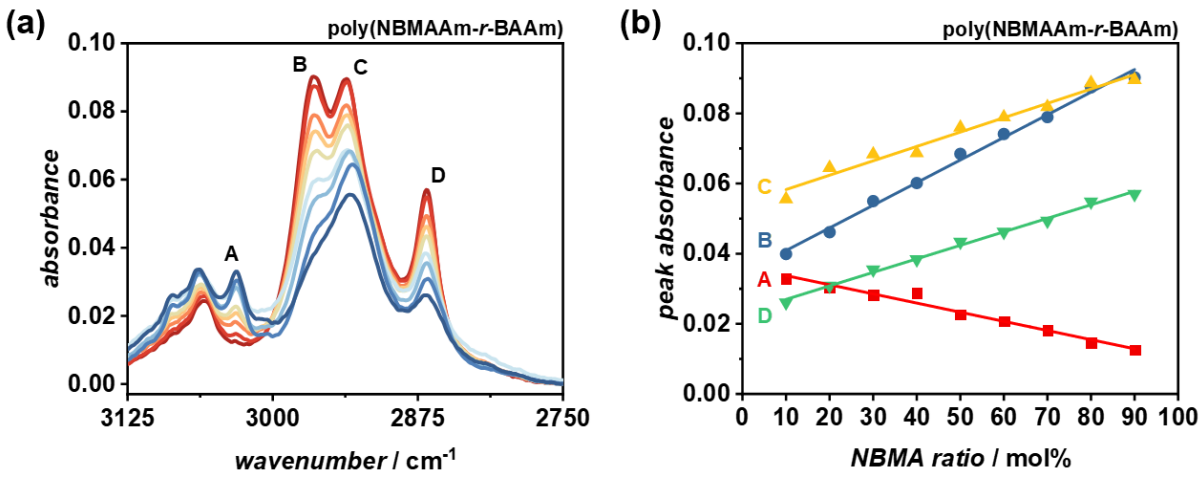

Figure 75. a) ATR FT-IR spectra of poly(NBMAAm-*r*-BAAm) in the range of 3125 cm^{-1} to 2750 cm^{-1}. The amount of NBMA increased from blue to red (10 – 90 mol%) while the amount of BA increased from red to blue (10 – 90 mol%), respectively. Characteristic peaks assigned to NBMA and BA, respectively were identified which were found to increase or decrease linearly with the amount of respective amine. Resolution: 2 cm^{-1}. b) Linear fits of the peak absorbance against the ratio of NBMA of peaks A – D.

SEC analysis of poly(NBMAAm-*r*-BAAm) showed a slight increase in molecular weight with higher NBMA content, consistent with the incorporation of the heavier norbornene groups. The dispersity remained unchanged (refer to **Figure 76**). Detailed information about M_n and $Đ$ of poly(NBMAAm-*r*-BAAm) is displayed in **Appendix 18**.

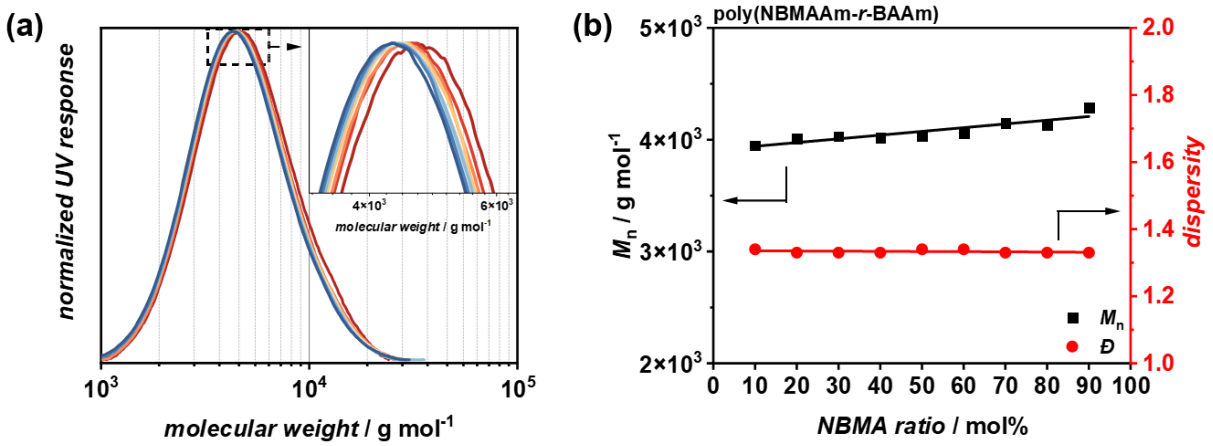

Figure 76. a) SEC traces of poly(NBMAAm-*r*-BAAm) in DMAc. A slight increase in molecular weight was observed with increasing amounts of heavier NBMA in the polymer. The amount of NBMA increased from blue to red (10 – 90 mol%) while the amount of BA increased from red to blue (10 – 90 mol%), respectively. Calibration: PMMA. b) M_n and $Đ$ vs. NBMAAm content in poly(NBMAAm-*r*-BAAm). The M_n (black) was found to slightly increase, while the dispersity (red) remained unchanged. Solvent: THF; calibration: PMMA.

The thermal decomposition profiles of poly(NBMAAm-*r*-BAAm) were investigated via TGA. Interestingly, an increase in norbornene content led to enhanced expression of gradual thermal decomposition, with $T_{5\%}$ values ranging from 107 °C to 161 °C (refer to **Figure 77** and **Appendix 19** for detailed information). The multi-step decomposition of poly(NBMAAm-*r*-BAAm) with higher NBMAAm content (above 50 mol%) is believed to be caused by the thermal lability of norbornene moieties due to ring strain, compared to the more stable aromatic benzyl groups.[311]

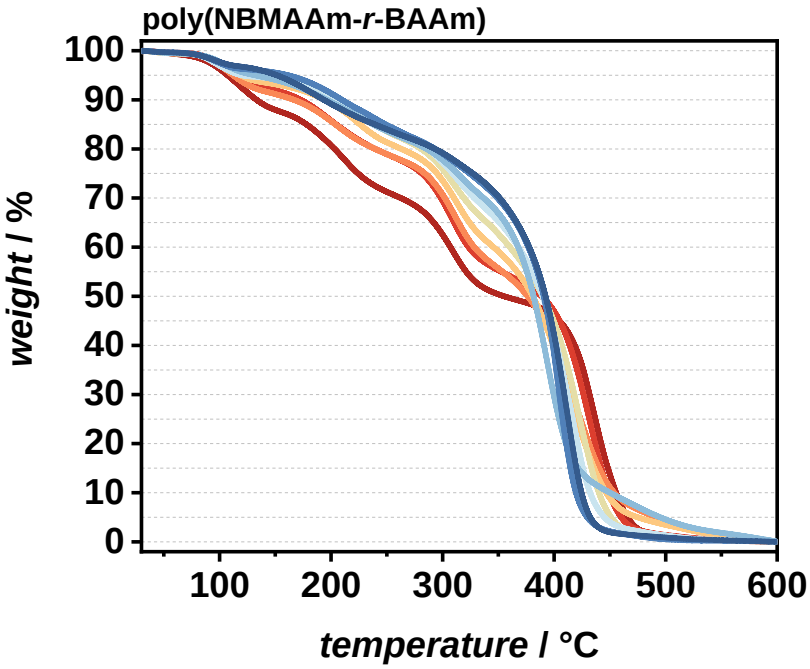

Figure 77. Thermal profile of poly(NBMAAm-*r*-BAAm) with different amounts of NBMA and BA incorporated into the polymer. The amount of NBMA increased from blue to red (10 – 90 mol%) while the amount of BA increased from red to blue (10 – 90 mol%), respectively.

The phase transition behavior of poly(NBMAAm-*r*-BAAm) was studied by DSC. The T_g of poly(NBMAAm-*r*-BAAm) was found to depend on the NBMAAm to BAAm ratio (refer to **Figure 78a**). As the amount of NBMAAm increased from 10 to 50 mol%, the T_g decreased from 80 °C to 63 °C. With further increase in NBMAAm content (from 50 to 90 mol%), the T_g increased from 63 °C to 87 °C, resulting in a V-shaped T_g profile across the amine ratio (refer to **Figure 78b**). It is believed that the change in T_g is due to alterations in chain mobility caused by the side group effects. A higher ratio of foreign pendant chains may hinder optimal chain orientation, leading to less stable chain stacking and increased chain mobility, which in turn results in a minimum T_g at a 50:50 mol% modification mixture.[312,313]

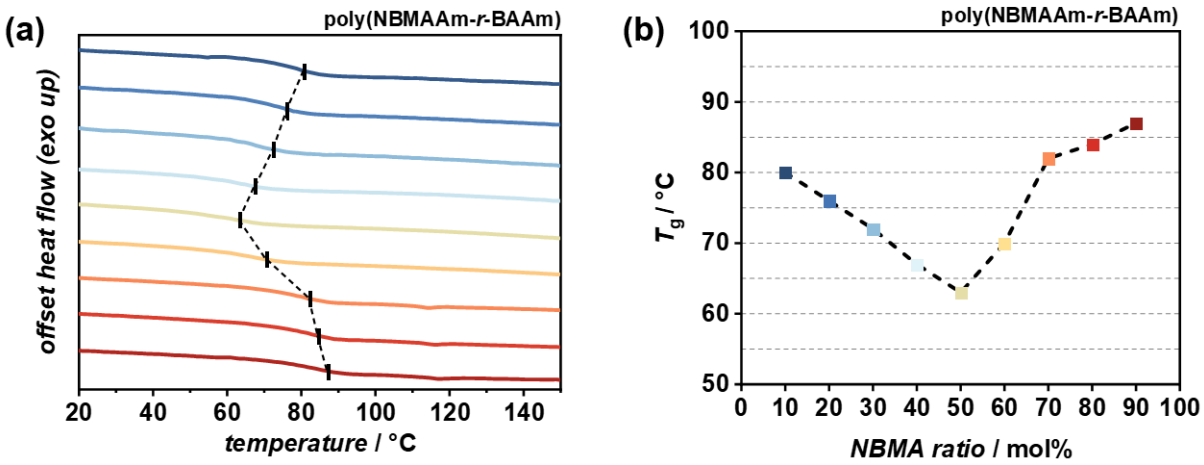

Figure 78. a) DSC thermograms of poly(NBMAAm-*r*-BAAm) polymers showing the tunability of T_g (black line) with the modification ratio of poly(PFPA) with NBMA and BA. b) Plot of T_g of poly(NBMAA-*r*-BAAm) with different modification ratios. The T_g exhibits a minimum at a 50/50 modification ratio, which is believed to be caused by the hinderance of optimal chain orientation which causes less stable chain stacking.[312,313] The amount of NBMA increased from blue to red (10 – 90 mol%) while the amount of BA increased from red to blue (10 – 90 mol%), respectively.

Given the precise control over the modification of poly(PFPA) demonstrated in this work, the tunability of polymer material properties facilitated by continuous flow modification represents a promising approach for high-throughput materials synthesis and analysis.

3.3.6 Summary

In summary, an automated flow reactor, integrated with orthogonal online analytics, was successfully utilized for ML-driven self-optimization of PFPA polymerization. The optimized polymerization parameters, determined algorithmically, were subsequently implemented in a different and independent flow reactor in a separate laboratory, yielding comparable polymeric materials. While equivalent batch experiments achieved similar conversion levels, they resulted in an undesirable broadening of molar mass dispersity.

Additionally, an adapted flow platform enabled precise control over the post-polymerization modification of poly(PFPA) through amidation with primary amines with over 90 % precision. The applicability of this strategy was validated using ^{19}F and ^{1}H NMR spectroscopy, demonstrating successful modification with both fluorinated and non-fluorinated amines containing NMR-active groups. ATR FT-IR spectroscopy of the modified polymers revealed a linear correlation between absorbance band intensities

and the degree of modification, further highlighting the utility of IR spectroscopy in flow polymer chemistry.

Thermal analysis using TGA and DSC confirmed the tunability of material properties through controlled poly(PFPA) modification in flow. While this study focused on amidation of poly(PFPA) homopolymers with specific amine pairs, the approach is expected to be applicable to other active ester-based polymers, such as NHS-containing systems, as well as more complex amine mixtures detectable via NMR. Future extensions may include transesterification or thiolysis, potentially enabling the construction of intricate polymer architectures through flow chemistry.

Overall, this work presents a powerful strategy for high-throughput exploration of novel functional polymeric materials. More broadly, it highlights the potential for sustainable and efficient global collaboration between research labs with complementary expertise.

3.4 High-throughput Polymerization and Post-polymerization Modification of Pentafluorostyrene in Continuous Flow

3.4.1 Introduction

In addition to the closed-loop, algorithm-based optimization discussed in **Chapter 3.3** Automated Synthesis and Post-polymerization Modification of Polypentafluorophenyl Acrylate in Continuous Flow, continuous flow polymer chemistry can be utilized for kinetic screening of polymerization reactions by a method called transient timesweeping (TT). In these experiments, a flow reactor is stabilized at a given flow rate before an instant change in flow rate is introduced. This leads to a transient reaction volume which incrementally contains samples resembling the residence times between prior and successive flow rate. A more in-depth introduction to TT in polymer chemistry can be found in **Chapter 2.5.2** Kinetic Screening *via* Transient Timesweeping as well as an article published by JOREN VAN HERCK and TANJA JUNKERS in 2022.[37] The transient reactor volume contains kinetic information about the polymerization in the form of conversion and molecular weight evolution over reaction time and can be used to calculate polymerization rate constants via inline and online analyses such as benchtop NMR and SEC. As a consequence, the TT method generates much more data compared to CLMOO and allows kinetic screening of a polymerization on the scale of minutes, depending on the residence times of interest.[38] In recent years, monomers employed in TT analysis and method development were

mainly limited on non-functional acrylates such as methyl (meth)acrylate,[314] butyl acrylate,[39] or styrene.[315] The investigation of functional polymers able to undergo PPM remains underrepresented in the field of flow polymer chemistry in general, and in the use of TT for kinetic investigations in particular.

3.4.2 Strategy

In this chapter, the kinetic screening via TT of pentafluorostyrene (PFSty) is discussed in order to gain valuable insight into kinetic parameters for the polymerization of this commercial, functional, and readily polymerizable monomer. Building on the results presented in **Chapter 3.3** Automated Synthesis and Post-polymerization Modification of Polypentafluorophenyl Acrylate in Continuous Flow, the PPM of poly(PFSty) was conducted by PFT reaction with different fluorinated thiols in continuous flow, as well as an automated robotic platform to demonstrate the versatility of automated and continuous reaction control (refer to **Scheme 24**).

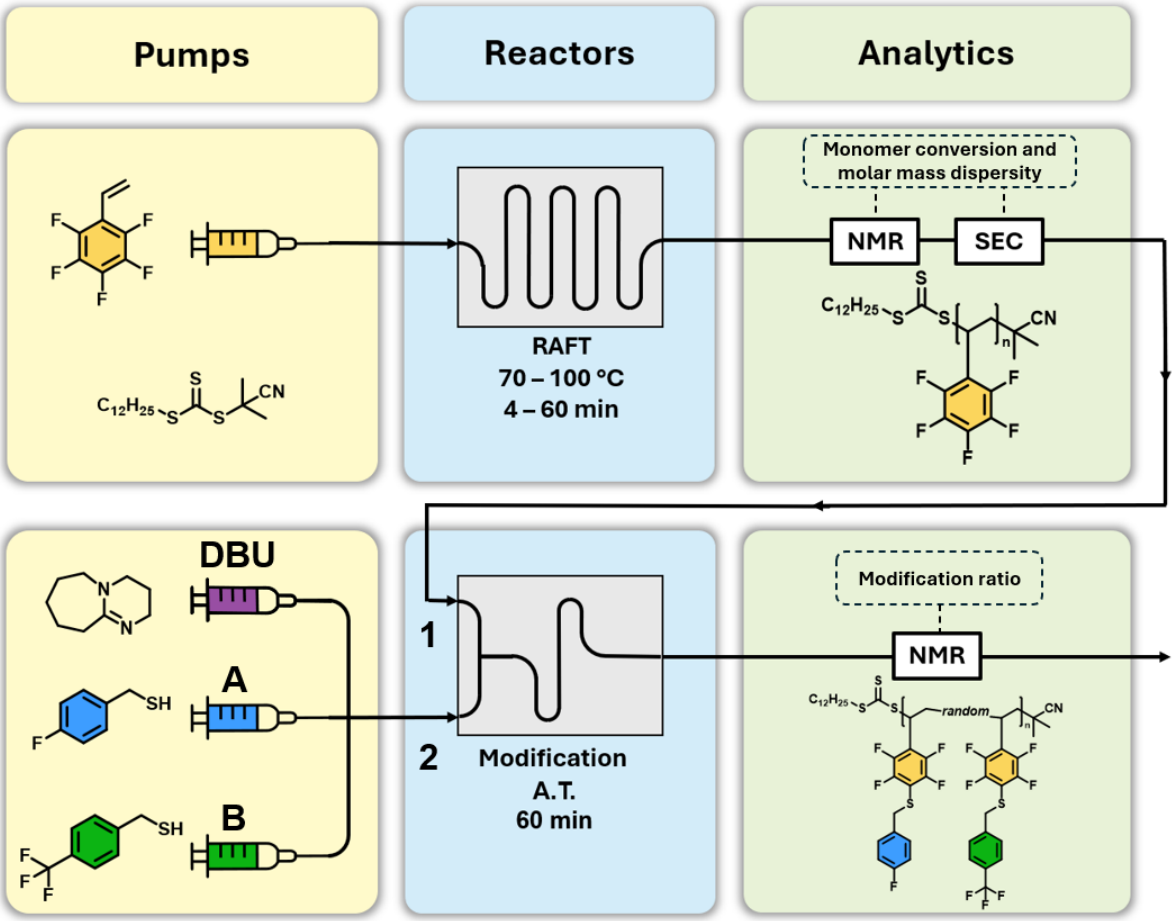

Scheme 24. Visualization of the flow reaction setup used in this chapter. Top: High-throughput polymerization of PFSty using TT for kinetic investigation of the reaction. Bottom: Schematic of the PPM of poly(PFSty) with two different thiols under presence of DBU. Control over the flow rate and liquid dosing facilitates the direct control over the modification ratio of the active polymer.

3.4.3 Kinetic Screening of the Polymerization of PFSty

The synthetic platform used for the high-throughput polymerization and analysis and of the polymerization of PFSty was located at the Monash University in Melbourne, Australia and essentially consisted of a pre-loaded syringe pump with the reaction solution, a tubular coil reactor heated by an oil bath (material: PFA), a 60 MHz benchtop NMR, a 6-port injection valve, and an SEC column. Syringe pump, and thus the flow rate, and NMR spectrometer were controlled by one computer, while the SEC injection was controlled by another computer (refer to **Scheme 25**). Both computers were connected to a server for communication and timed the experiment by precise determination of NMR and SEC measurement windows based on the dead volume of the flow path and the current flow rate. Thereby the transient volume was intercepted by the NMR and SEC devices and linked to the respective residence time of each analyte volume.[225]

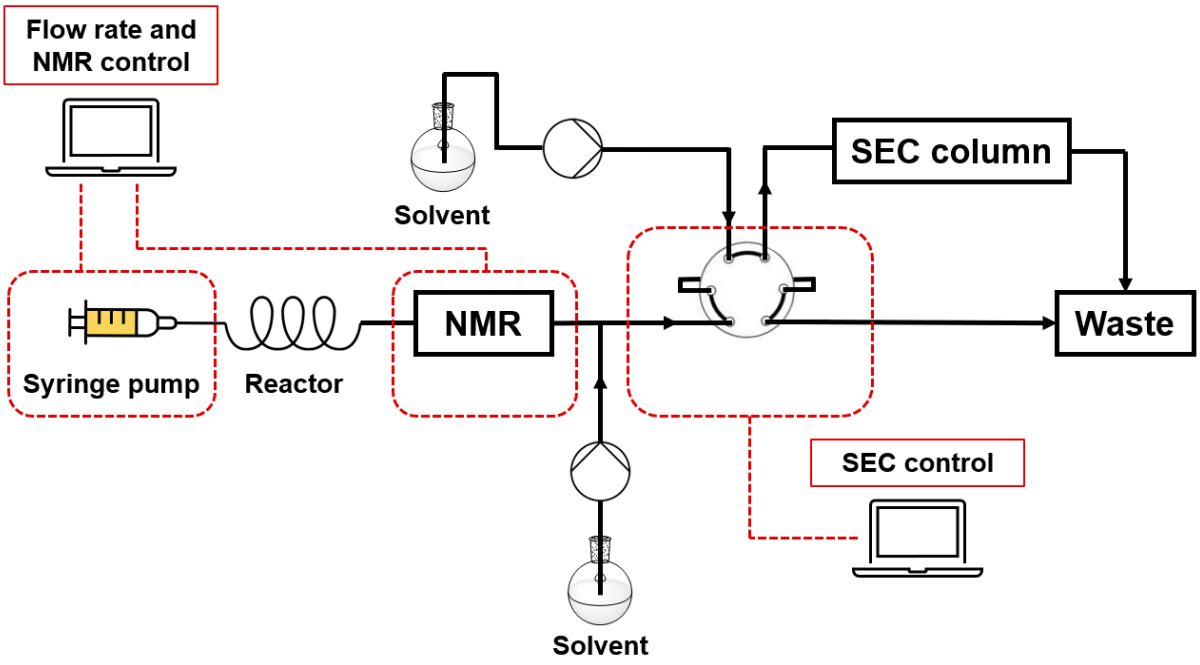

Scheme 25. Schematic setup used for the high-throughput investigation of the polymerization of PFSty via TT. Dashed red lines indicate software communication between computer and the respective elements for control.

In a typical TT experiment, a solution of PFSty, RAFT-agent, and AIBN in DMF was prepared with molar ratios of 50 : 1 : 0.2 equivalents, respectively. The mass ratio of PFSty in the whole reaction mixture was 30 wt% for each experiment. The solution was degassed by bubbling with argon for 10 minutes before being loaded to a gastight

syringe in a syringe pump. The reactor was a tubular coil reactor made from PFA with a volume of 1.0 mL which was submerged in a pre-heated oil bath and purged with 2 mL of reaction solution prior to the experiment. Each experiment was divided into 4 timesweeps (4 – 8 min, 8 – 16 min, 16 – 32 min, and 32 – 60 min residence time), in order to prevent non-ideal flow behavior caused by large flow rate changes.[37] Monomer conversion was determined by ^{1}H NMR spectroscopy using the standard *Magritek* flow reaction monitoring protocol which recorded a single NMR scan every 17 seconds which ran throughout the whole experiment time. Removal of the conversion data during stabilization and wait periods allowed combination of each individual timesweep into one total conversion-residence time profile.[37] Calculation of monomer conversion was done by comparing the signal of C=C double bond protons to the constant signal of the DMF H-C=O formamide proton in the inert solvent. The ratio of these signals at known signal ratio prior to the reaction allowed the calculation of the monomer conversion *p* [%] via the following formula:

$$p = 100 \times \left(\frac{\frac{PFSty_i}{DMF_i} - \frac{PFSty_x}{DMF_X}}{\frac{PFSty_x}{DMF_x}} \right) \times \frac{1}{3} \qquad \text{(Eq. 5)}$$

Where $PFSty_i$ and DMF_i are the initial signals of PFSty and DMF protons before the reaction and $PFSty_x$ and DMF_x are the respective signals at a given residence time. The factor 1/3 accounts for the proton ratio of 1 to 3 in DMF and PFSty at the respective chemical shift ranges. Assuming pseudo-first-order kinetics for the polymerization,

$$[PFSty] = [PFSty]_0 e^{-kt} \qquad \text{(Eq. 6)}$$

the rate constant of propagation (k_{prop}) can be calculated from the slope of the linear progression of the natural logarithm of conversion over time:

$$p = \frac{[PFSty]_0 - PFSty}{[PFSty]_0} \qquad \text{(Eq. 7)}$$

$$[PFSty]_0(1 - X) = [PFSty]_0 e^{-k_{prop}t} \qquad \text{(Eq. 8)}$$

$$ln(1 - X) = -k_{prop}t \qquad \text{(Eq. 9)}$$

SEC measurements were done by a continuous injection of samples after a wait period to account for the dead volume between reactor and injection valve. During passing of

the transient volume, a SEC measurement was injected every 90 seconds and at the new equilibrium flow rate. Consequently, the number of SEC measurements and therefore their relative density within a transient volume was dependent on the flow rate and the individual timesweeps. For instance, the timesweep from 4 to 8 minutes allowed recording of four SEC traces (at 4, 5.5, 7, and 8 minutes of residence time). The timesweep from 8 to 16 minutes on the other hand allowed recording of twelve SEC traces (at 8, 9.5, 11, 12.5, 14, 15.5, and 16 minutes of residence time). To profile the control and kinetic behavior of the polymerization of PFSty at different temperatures, TT experiments were conducted in the range of 70 – 100 °C using CPDT as RAFT-agent (refer to **Figure 79** and **Table 6**).

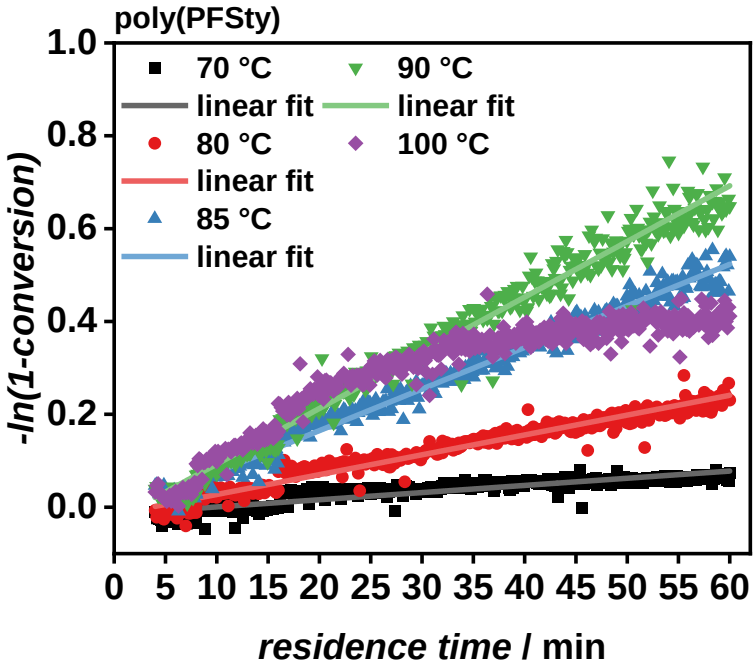

Figure 79. Pseudo-first-order kinetics plot of poly(PFSty) from four individual timesweeps at different polymerization temperatures with linear fits. The composition of the reaction mixture was constant at 50 : 1 : 0.2 eq. [PFSty : RAFT-agent : AIBN].

It was found that a polymerization temperature of 70 °C resulted in a low conversion of below 10 % after 1 h of residence time and is therefore not feasible for the polymerization of PFSty under the chosen conditions. Furthermore, the linear fit of the 70 °C experiment showed unsatisfactory overlap with the experimental data. At 100 °C on the other hand, the control over the polymerization was lost as is indicated by non-linear conversion-time correlation. This can be explained by the increased occurrence of terminating reactions due to high temperature and a shift towards a free radical polymerization mechanism.[170] In the intermediate region from 80 °C to 90 °C however,

the polymerization of PFSty was found to be well controlled with satisfactory conversions after only 60 minutes of residence time with a good correlation of the linear fits.

Table 6. Conversion after 60 minutes residence time, propagation rate constant, and quality of the linear fit at different polymerization temperatures.

temperature / °C	*p after 60 min* / %	k_{prop} / s^{-1}	*coefficient of determination* R^2
70	7.2	$1.54 \cdot 10^{-3} \pm 4.01 \cdot 10^{-5}$	0.782
80	20.6	$4.27 \cdot 10^{-3} \pm 4.62 \cdot 10^{-5}$	0.954
85	41.7	$8.96 \cdot 10^{-3} \pm 5.72 \cdot 10^{-5}$	0.983
90	47.7	$1.20 \cdot 10^{-2} \pm 9.09 \cdot 10^{-5}$	0.977
100	33.7	-	-

The rate constant for the propagation was found to increase with increasing temperature which is in line with the expectations based on the ARRHENIUS equation:

$$k_{prop} = Ae^{-\frac{E_a}{RT}} \quad \text{(Eq. 10)}$$

However, it was found that the rate constant at 80 °C was lower than theoretically expected which was most likely caused by inaccuracies during the preparation of the experiment or shimming errors of the NMR spectrometer during long term operation (refer to **Figure 80**).

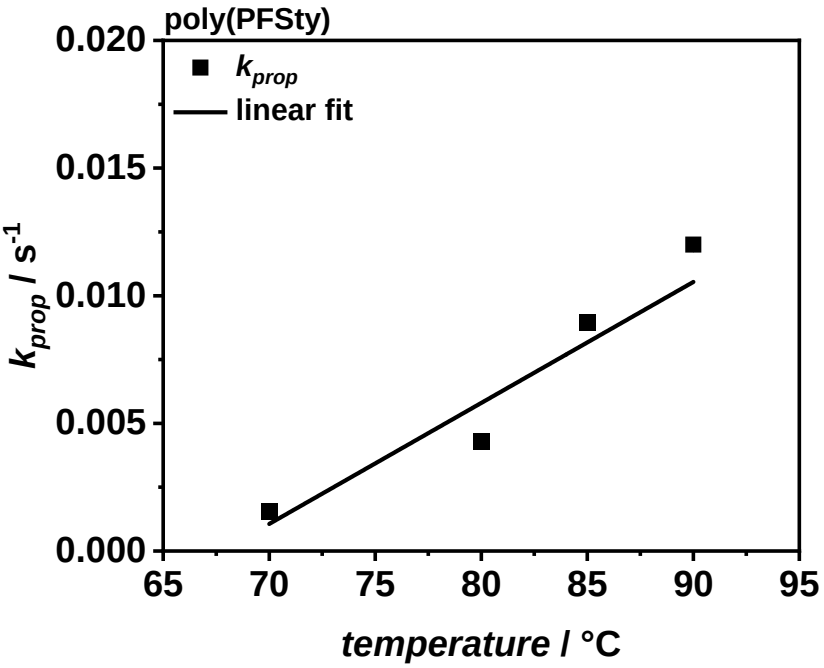

Figure 80. Relation of the rate constant of the polymer propagation of poly(PFSty) with reaction temperature. Linear fit coefficient of determination R^2: 0.908.

Nevertheless, the obtained results highlight the power of TT as a rapid method for acquisition of valuable kinetic data in the preparation of functional polymers. Notably, the calculation of the monomer conversion via ^{19}F NMR was not possible with this method since the signal-to-noise ratio was insufficient to separate monomer from polymer signals necessary for calculation of the conversion. To overcome this, each individual NMR measurement would need to be performed at lower flow rates and with a higher number of scans which, however, contradicts the concept of TT in its essence by disrupting the flow continuity (refer to **Appendix 20**). Automated SEC data acquisition during the continuous polymerization of poly(PFSty) allowed monitoring of the molecular weight and *Đ* over the course of the reaction (refer to **Figure 81**). SEC traces of the polymerizations carried out at 70, 80, 90, and 100 °C can be found in the appendix (refer to **Appendix 21**).

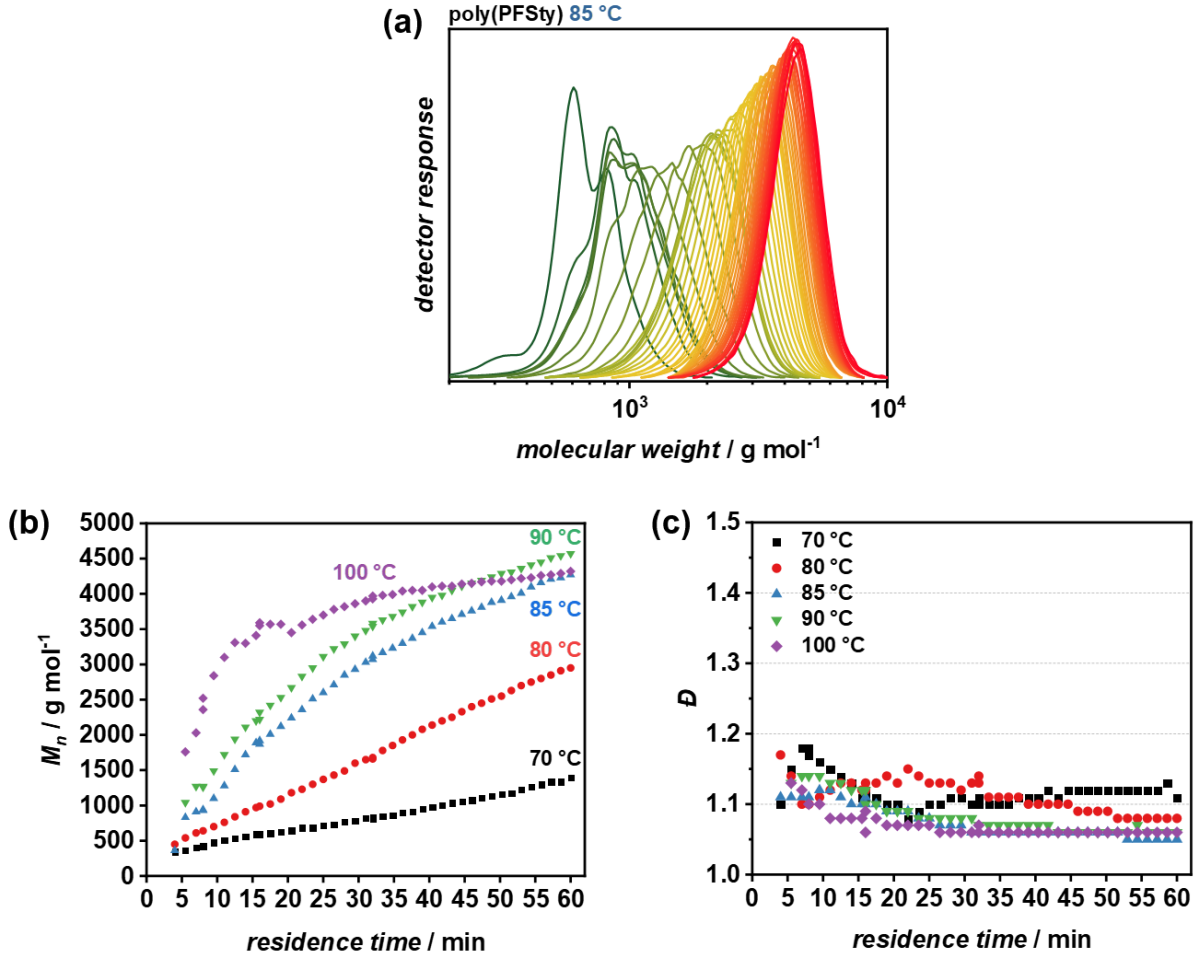

Figure 81. a) SEC traces of poly(PFSty) during a TT experiment at 85 °C. The shift from green to red resembles the increasing residence time from 4 to 60 minutes. Progression of M_n (b) and $Đ$ (c) with increasing residence time. Good control is achieved at 70 °C and 80 °C. A slight curvature of the M_n profile appeared at 85 °C and propagation quickly stops at 100 °C. Solvent: THF; calibration: PS.

M_n of poly(PFSty) was found to increase linearly over time at 70 °C and 80 °C. Increasing the temperature to 85 °C and 90 °C resulted in faster formation of longer chains which is in line with the increased propagation rate constant discussed earlier. However, at higher temperatures the M_n profile shows a slight curvature, indicating the depletion of radicals and propagating chains at higher temperatures. At temperatures as high as 100 °C, no significant increase in chain lengths was observed after 30 minutes which can be explained by the consumption of initiator and the termination of propagating polymer chains due to termination reactions which is in line with the monomer conversion profile obtained from ^{1}H NMR analysis (refer to **Figure 79**).[170] The dispersity of all polymers was found to be below 1.20 throughout all experiments which indicates good compatibility of CPDT with PFSty to obtain polymers with low dispersity. However, it was found that the dispersity of poly(PFSty) can be as low as 1.05 when the temperature does not exceed 85 – 90 °C which can be considered a

very high degree of control over the polymerization by virtue of CDPT which was further confirmed by plotting M_n against conversion. According to the theory of controlled polymerizations, this correlation should be linear when good control is achieved.[316] Indeed, the M_n of poly(PFSty) was found to increase linearly with conversion for temperatures up to 90 °C (refer to **Figure 82**).

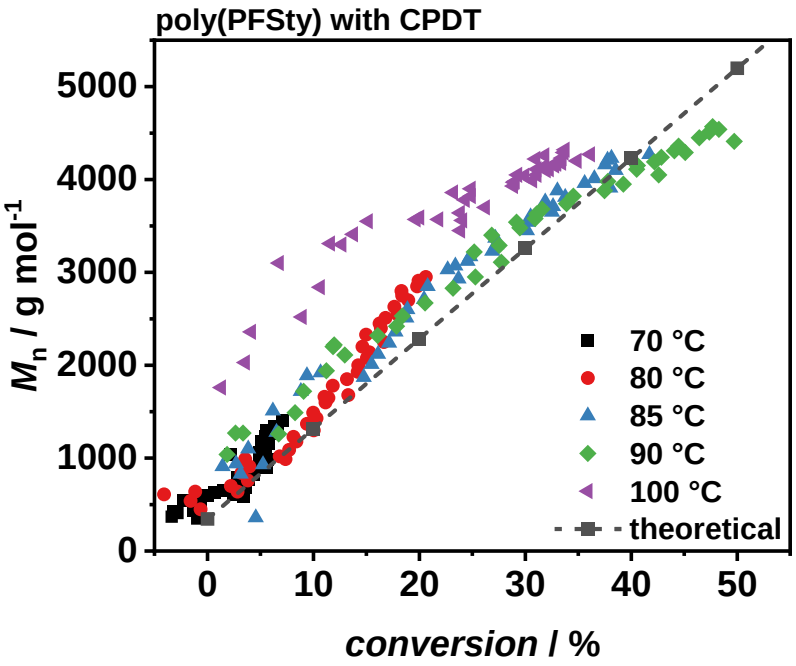

Figure 82. M_n vs. conversion for the polymerization of PFSty at temperatures between 70 and 100 °C. Experiments below 100 °C show good agreement with the theoretical linear increase of M_n with conversion associated with controlled polymerizations.

This highlights the feasibility of high-throughput polymerization of PFSty as while maintaining good control over the polymer architecture for further application in PPM and confirms the quality of the kinetic data obtained by TT.

Additionally, a screening of different RAFT-agents at 85 °C polymerization temperature was conducted to investigate their influence on the polymerization behavior. Investigated RAFT-agents included CPDT, 4-cyano-4-[[(dodecylthio) carbonothioyl]thio] pentanoic acid (CDCTPA), 2-(dodecylthiocarbonothioylthio) propanoic acid (DoPAT), and 2-cyano-2-butyl-4-chloro-3,5-dimethyl-1H-pyrazole-1-carbodithioate (CBCDMPC) (refer to **Figure 83**).

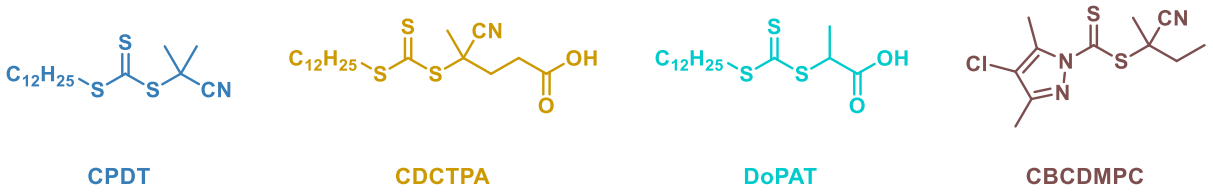

Figure 83. Chemical structures of CPDT, CDCTPA, DoPAT, and CBCDMPC used for the polymerization of PFSty in this study.

TT experiments with CPDT, CDCTPA, DoPAT, and CBCDMPC as RAFT-agents at 85 °C revealed a mostly linear increase in monomer conversion over residence time (refer to **Figure 84**).

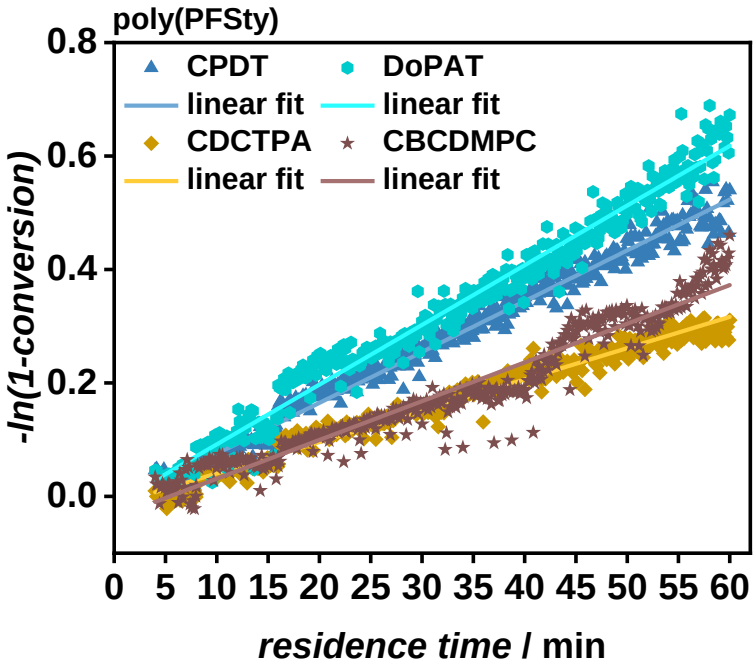

Figure 84. Pseudo-first-order kinetics plot of poly(PFSty) from four individual timesweeps using different RAFT-agents at 85 °C with linear fits. The composition of the reaction mixture was constant at 50 : 1 : 0.2 eq. [PFSty : RAFT-agent : AIBN].

However, the experiment with CBCDMPC showed some irregularities at residence times from 35 to 40 minutes and 45 to 52 minutes which were caused by an error in the material stream, as it also occurred in SEC measurements which lead to an incomplete M_n and $Đ$ profile due to missing injections (refer to **Figure 85b and c**). Overall, DoPAT showed the highest propagation rate and monomer conversion of 49.0 % after 60 minutes residence time (refer to **Table 7**).

Table 7. Conversion after 60 minutes residence time, propagation rate constant, and quality of the linear fit using different RAFT-agents for the polymerization of PFSty.

RAFT-agent	*p after 60 min / %*	*k / s^{-1}*	*coefficient of determination R^2*
CPDT	41.7	$8.96 \cdot 10^{-3} \pm 5.72 \cdot 10^{-5}$	0.983
CDCTPA	27.0	$5.52 \cdot 10^{-3} \pm 4.53 \cdot 10^{-5}$	0.973
DoPAT	49.0	$1.05 \cdot 10^{-2} \pm 7.79 \cdot 10^{-5}$	0.978
CBCDMPC	36.7	$6.83 \cdot 10^{-3} \pm 8.77 \cdot 10^{-5}$	0.936

Despite the high conversion achieved with DoPAT, SEC analysis showed its incompatibility with PFSty compared to the other investigated RAFT-agents (refer to **Figure 85**). SEC traces of TT experiments with CDCTPA and CBCDMPC can be found in the appendix (refer to **Appendix 22**).

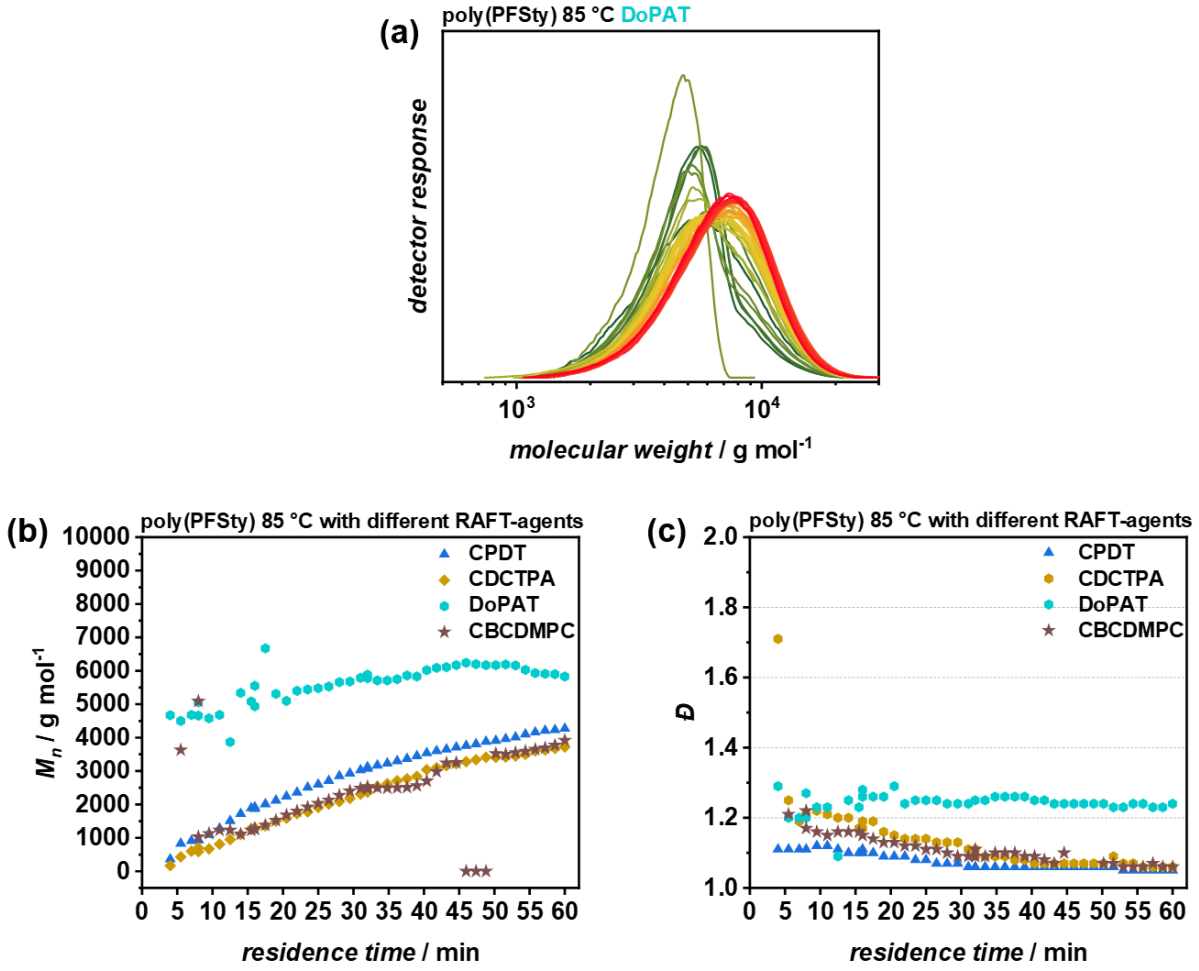

Figure 85. a) SEC traces of poly(PFSty) prepared with DoPAT as RAFT-agent. The shift from green to red resembles the increasing residence time from 4 to 60 minutes. Progression of M_n (b) and $Đ$ (c) with increasing residence time. Good control was achieved using CPDT, CDCTPA, and CBCDMPC. DoPAT proved non-satisfactory for the polymerization of PFSty in continuous flow due to the high dispersity and non-controlled increase in M_n. Solvent: THF; calibration: PS.

The molecular weight of poly(PFSty) with DoPAT was found to be around 4670 g mol^{-1} after only 4 minutes of residence time and only increased slightly to around 5830 g mol^{-1} after 60 minutes. Additionally, the dispersity was found to be significantly higher with $Đ$ > 1.20 throughout the experiment when using DoPAT in comparison to all other investigated RAFT-agents. Even though $Đ$ was found to be smaller than the characteristic dispersity of 2.0 associated with FRP,[317] it is concluded that the polymerization did not undergo the RAFT equilibria and the rapid increase in M_n is caused by direct polymerization of PFSty by AIBN, ignoring DoPAT as RAFT-agent. CDCTPA and CBCDMPC yielded comparative SEC results with low $Đ$ at higher conversions and almost perfectly linear M_n-residence time profiles but exhibited significantly lower monomer conversions and were therefore less efficient compared to CPDT. The M_n-conversion plot of poly(PFSty) synthesized by TT in continuous flow further confirmed CPDT to be the most suitable of all investigated RAFT-agents for this reaction (refer to **Figure 86**). The DoPAT-containing reaction clearly did not show a controlled linear correlation of M_n with conversion and CPDT was able to achieve the highest conversion with lowest $Đ$ at 85 °C.

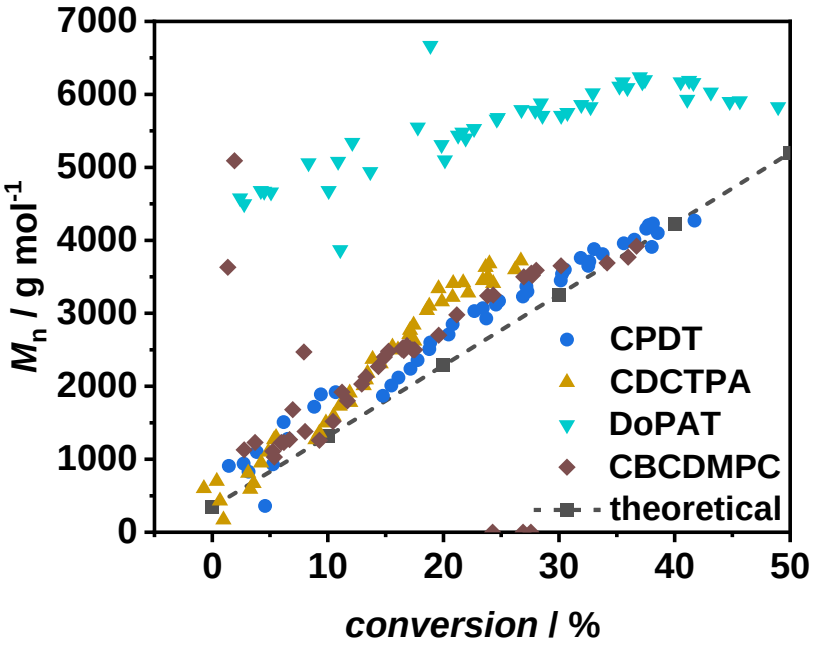

Figure 86. M_n vs. conversion for the polymerization of PFSty using different RAFT-agents. DoPAT was found to not control the polymerization of PFSty, rendering it unsuitable for this reaction. Experiments with CPDT, CDCTPA, and CBCDMPC showed good agreement with the theoretical linear increase of M_n with conversion associated with controlled polymerizations.

3.4.4 Post-polymerization Modification of poly(PFSty)

PPM of poly(PFSty) via PFT reaction and following the strategy introduced in **Chapter 3.3.5** Post-polymerization Modification of poly(PFPA) and displayed in the bottom half of **Scheme 24**. In addition to the PPM in continuous flow via syringe pumps, a commercial and programmable robotic liquid handler (RLH) was used for dosing of reaction solutions. A RLH is a pipette robot which can automatically and precisely transfer and mix liquids from reservoirs into well plates at known locations within its perimeter. RLH are commonly used in automated biomedical and biochemical research where large numbers of pipetting steps are necessary.[318] The PFT reaction was carried out with 4-fluoro benzyl mercaptan (FBM; A) and 4-trifluoromethyl benzyl mercaptan (TFBM; B), which feature aromatic and aliphatic fluorine atoms, respectively, and would therefore be traceable via ^{19}F NMR spectroscopy. For simplicity reasons, the obtained polymer was entitled poly(FBM-*r*-TFBM) which does not describe the exact polymer structure but is sufficient in order to describe the PPM aspect of the approach presented here. The ratio of modification of the polymer can be determined by the integral ratio of aromatic and aliphatic fluorine atoms, as was described in **Chapter 3.3.5.1** PPM of poly(PFPA) *via* ^{19F} NMR and thus, control over polymer properties can be achieved in an automated high-throughput manner. However, the S_nAr of *para*-fluorine atoms with thiols does not occur spontaneously and the use of a deprotecting base (here DBU) is necessary to enable nucleophilic attack of a sulfide anion.[201] Thus the reaction platform needs to be able to precisely handle and dose four components. In continuous flow, this was realized by designing a 4-pump flow setup using syringe pumps with two mixing steps (refer to **Figure 87**). At the first mixing step, A, B, and DBU were mixed at a.t. to allow deprotonation of thiols before this combined stream was mixed with the polymer solution stream. The resulting output stream was allowed to react at a.t. for 1 h before precipitation with H_2O/MeOH (1:1 v/v) and analysis of the resulting polymers.

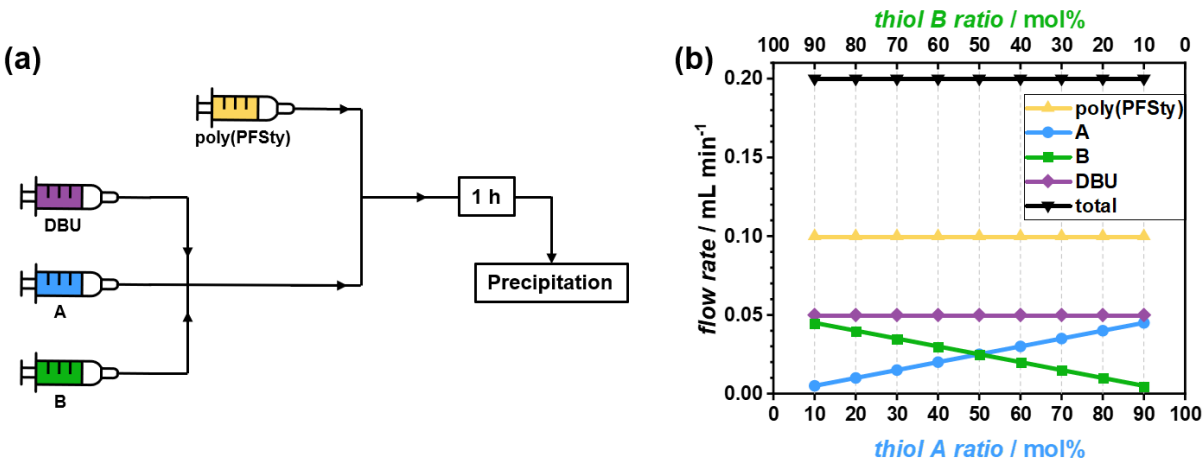

Figure 87. Schematic flow path (a) and graphical relations of flow rates (b) for the PPM of poly(PFSty) with thiols A and B and DBU as base in continuous flow. Yellow refers to the stream of polymer solution, blue and green refer to the stream of thiols A and B, respectively and purple refers to the stream of DBU.

PPM using an RLH was done by preparing four reservoirs with solutions of the four reactants (A, B, DBU, and poly(PFSty)) from which the robot automatically dosed predefined amounts in predefined containers in a well plate (refer to **Figure 88**). Due to the limited volume of the wells, each polymer modification composition was executed five times and the wells with the same compositions were combined after 1 h reaction at a.t prior to precipitation using a solution of MeOH/H_2O (1:1 v/v). to increase the yield. Given the limited compatibility of commercial pipette tips with organic solvents, the PPM of poly(PFSty) was conducted in EtOAc in both the continuous flow approach as well as the RLH approach. The concentrations of the solutions were adjusted so that the combined amount of thiols A and B would resemble 1.0 equivalents of pentafluorophenyl groups and DBU molecules in the reaction solutions after mixing.

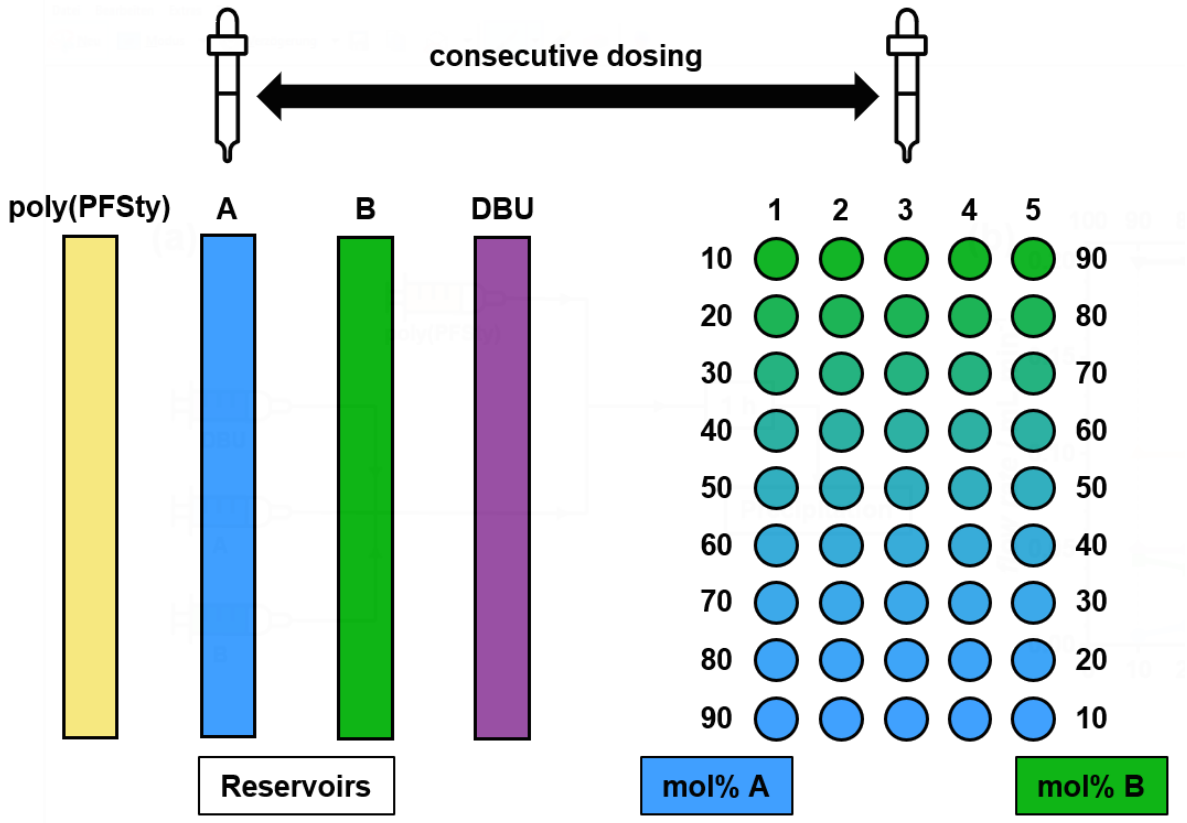

Figure 88. Visualization of the dosing and mixing process of reaction solutions during PPM of poly(PFSty) using an RLH. The pipette head consecutively dosed predefined amounts of solutions from the reservoirs to the different well plate positions. The order of dosing was: 1. poly(PFSty), 2. A, 3. B, 4. DBU. After addition of DBU, each well was thoroughly mixed by repeated aspiration and dispensing of the reaction solution.

^{19}F NMR and ^{1}H NMR spectroscopy of the obtained poly(FBM-*r*-TFBM) polymers was conducted and the ratio of FBM and TFBM was calculated from the integral ratios between the aromatic fluorine atoms in FBM and the aliphatic -CF_3 group in TFBM. **Figure 89b and c** show the ^{19}F NMR and ^{1}H NMR spectra of poly(FBM-*r*-TFBM) obtained from the continuous flow PPM approach. NMR spectra of poly(FBM-*r*-TFBM) obtained from the RLH approach can be found in the Appendix (refer to **Appendix 23**). The complete conversion of *para* fluoro atoms in poly(PFSty) was confirmed by the complete disappearance of the respective resonance at -157 ppm (refer to **Appendix 24**). The *ortho* and *meta* fluorine atoms at -144 ppm and -164 ppm in poly(PFSty) were found to shift to -134 ppm and -143 ppm in poly(FBM-*r*-TFBM), respectively.

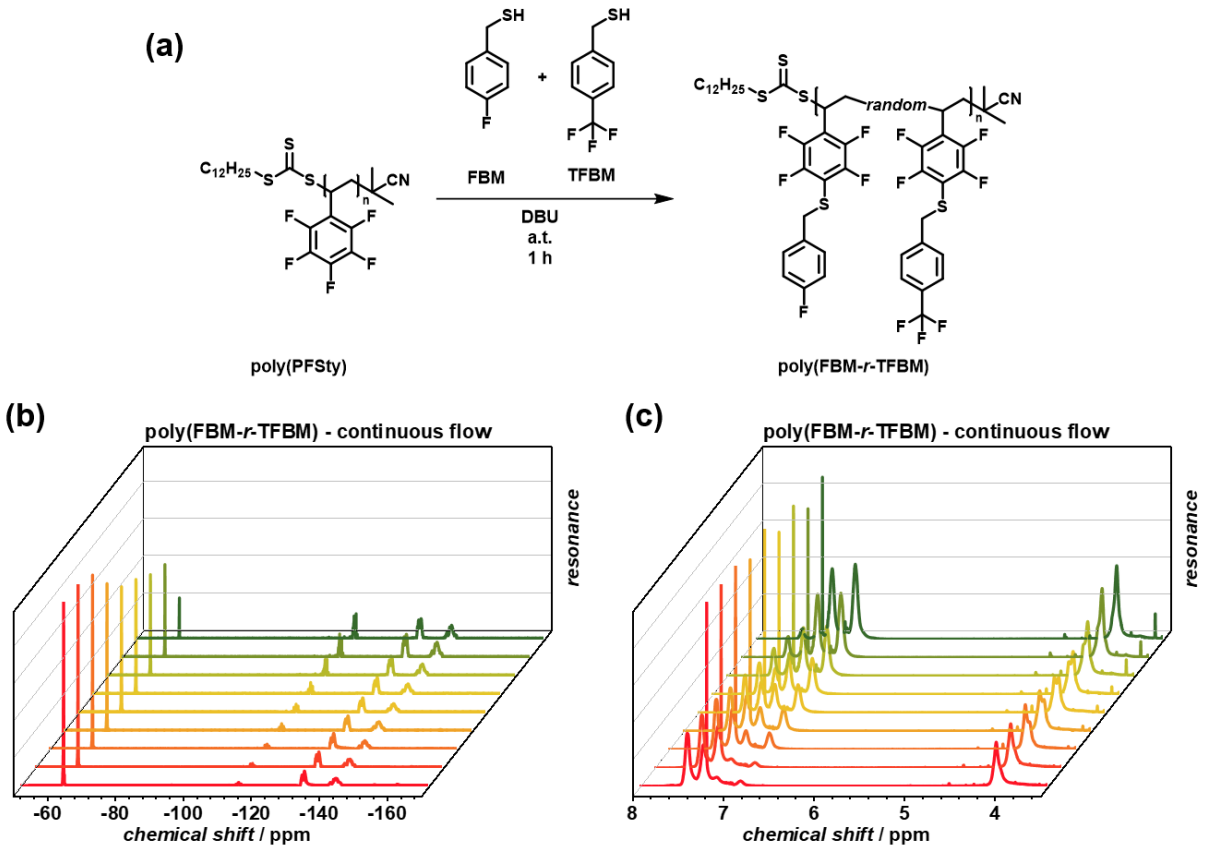

Figure 89. a) Reaction scheme of the PPM of poly(PFSty) with FBM and TFBM via PFT reaction with DBU. b) ^{19}F NMR and c) ^{1}H NMR spectra of poly(FBM-r-TFBM) with different ratios of FBM and TFBM. The amount of FBM increased from red to green (10 – 90 mol%) while the amount of TFBM increased from green to red (10 – 90 mol%), respectively. Solvent: $CDCl_3$.

Interestingly, the ^{1}H NMR spectra of poly(FBM-*r*-TFBM) also show a distinct difference in proton resonance depending on the amount of FBM and TFBM in the final polymer. Despite the chemical similarity of FBM and TFBM protons, the aromatic region between 6.8 ppm and 7.8 ppm revealed the same trend found in the ^{19}F NMR spectra where the resonances of FBM groups increased with increasing FBM content in the polymer and vice versa for TFBM proton resonances (refer to **Figure 89c**). However, due to the overlap of the proton resonances of FBM and TFBM groups, the modification ratio could not be calculated from the ^{1}H NMR spectra alone. NMR devices with stronger magnetic field might be necessary in order to separate the resonance areas sufficiently.[319] Calculation of the modification ratio in poly(FBM-*r*-TFBM) revealed a very close agreement with the theoretically expected ratio derived from the input streams at continuous flow (refer to **Figure 90**). The precision of control over the modification was found to be around 90 % and above, except for the 50:50 mol% composition where the precision dropped to approximately 80 % which is still considerable.

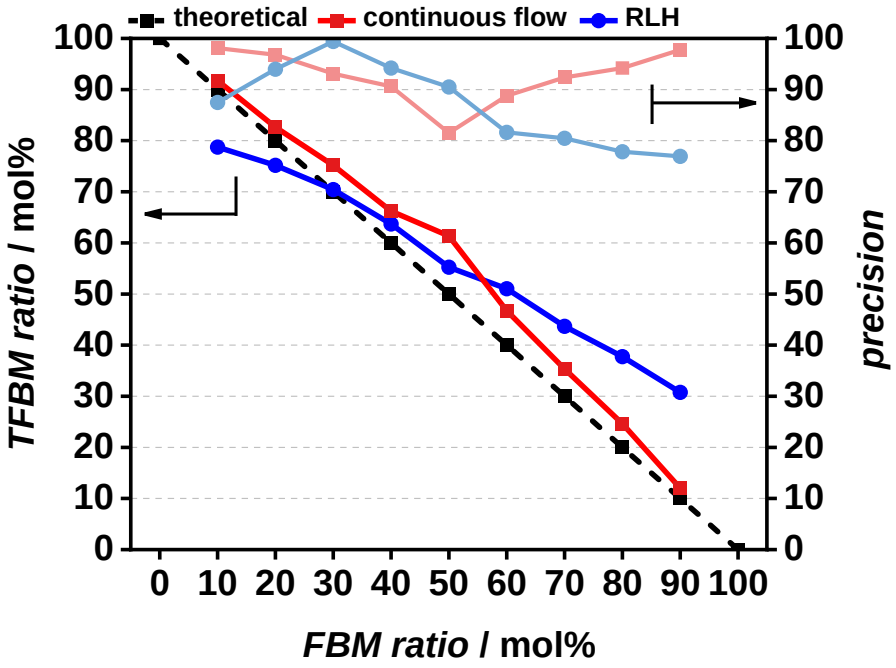

Figure 90. Theoretical and experimental modification ratios of poly(PFSty) with FBM (thiol A) and TFBM (thiol B) in continuous flow (red) and using a RLH (blue), respectively. The black dashed line represents the theoretical input ratios of FBM and TFBM which are directly correlated to the flow rates of the reactor setup and dosed volumes while colored solid line represents the found ratios in the final polymers. The precision (lightly colored) shows that good control over the modification was obtained in continuous flow.

Interestingly, the determined modification ratios of polymers modified by the RLH were found to significantly differ from the theoretically expected ratios. The reason for this is not entirely clear, given the accuracy of RLHs to precisely dose liquids in predefined amounts. It is hypothesized that solvent evaporation from the reservoirs or inaccuracies during solution preparation might cause these deviations and future experiments are necessary to validate this and further elucidate the applicability of RLHs for PPM of poly(PFSty). However, SEC analysis of poly(FBM-*r*-TFBM) made by PPM in continuous flow and using an RLH exhibited bimodal distributions of the molecular weight (refer to **Figure 91**). The pure poly(PFSty) used for PPM exhibited an M_n of 8130 g mol^{-1} with a peak molecular weight (M_p) of 8500 g mol^{-1}. After PFT reaction in continuous flow the molecular weight distribution exhibited two peaks, one with an $M_{p,1}$ of 11600 g mol^{-1} and one with an $M_{p,2}$ of 22300 g mol^{-1}. Poly(FBM-*r*-TFBM) made using the RLH also showed bimodal distributions with $M_{p,1}$ = 11800 g mol^{-1} and $M_{p,2}$ = 21400 g mol^{-1}, which increased with increasing ratio of heavier TFBM groups. The increase in polymer molecular weight can be explained by the addition of FBM and TFBM onto the PFSty monomer units which results from the substitution of a light fluorine atom with heavier FBM and TFBM units. The theoretical average increase in

molecular weight of each repeating unit was 76 %, however, the measured shift of $M_{p,1}$ was calculated to resemble an increase in weight of only 34 %. This can be explained by a strong deviation of the analyzed polymer from the PS calibration material and thus the absolute values of molecular weights of poly(FBM-*r*-TFBM) derived from SEC need to be treated cautiously.

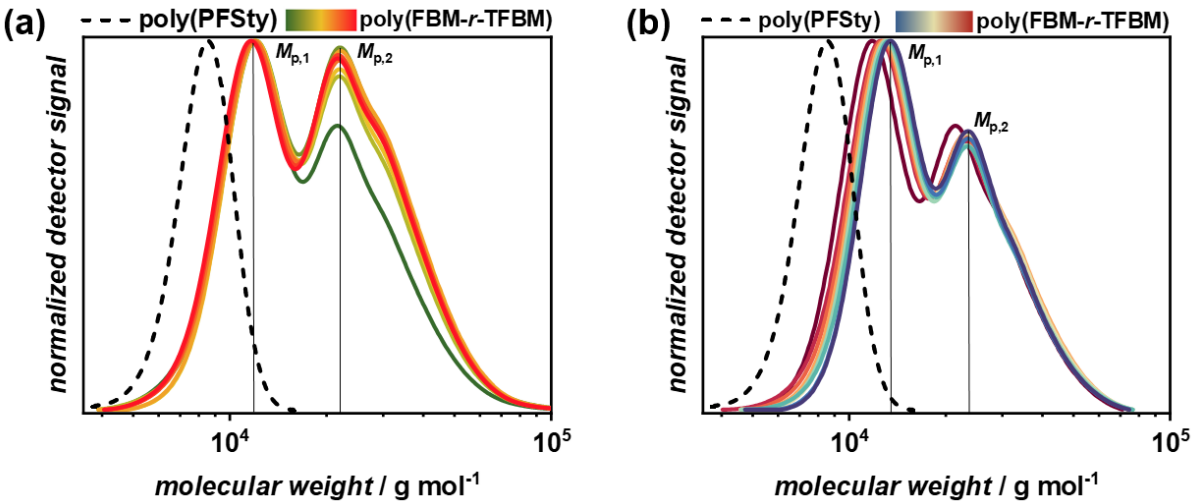

Figure 91. SEC traces of poly(PFSty) (dashed black lines) and poly(FBM-*r*-TFBM) (colored solid lines) made by PPM in continuous flow (a) and using an RLH (b). The peak molecular weights ($M_{p,1}$ and $M_{p,2}$) are exemplary visualized. The amount of FBM increased from red to green (a) and blue to red (b), respectively (10 – 90 mol%). Calibration: PS.

The bimodal molecular weight distribution found in the SEC elugrams is indicative for the occurrence of a side reaction during the PPM of poly(PFSty) with FBM and TFBM. Given the fact that NMR analysis proved the presence of intact tetrafluorostyrene and FBM and TFBM units, the multiple substitution of aromatic fluorine atoms via S_nAr could be ruled out. Furthermore, the $M_{p,2}$ was found to be the precise double of $M_{p,1}$ which indicates the formation of polymer dimers. A detailed list of the molecular weights and dispersities of poly(FBM-*r*-TFBM) can be found in the appendix (refer to **Appendix 25** and **Appendix 26**). One possible explanation is the cleavage of the RAFT end group into thiols by DBU which could then in turn have reacted under oxidative formation of disulfides (refer to **Scheme 26a**). This would explain the double molecular weight of the second SEC peak. Given the necessity of DBU or other bases during PFT reactions, this side reaction might by be prevented by deliberate cleavage of the RAFT end groups by excess AIBN (refer to **Scheme 26b**).[320]

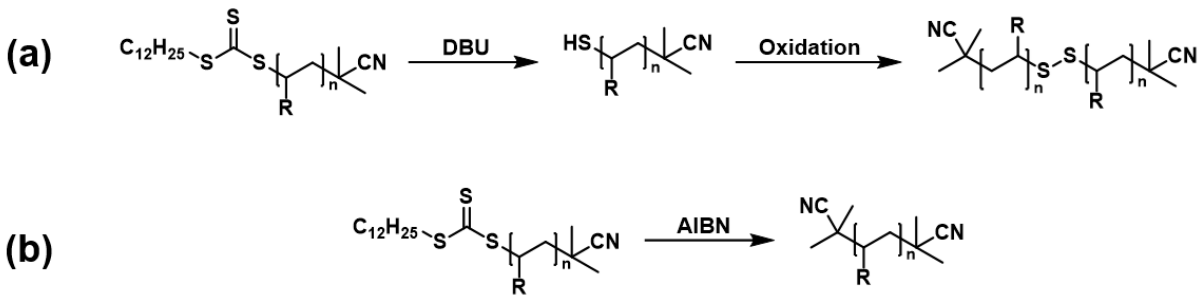

Scheme 26. a) Proposed cleavage of the RAFT end group und formation of a thiol end group with subsequent oxidative formation of polymeric disulfide dimers, doubling the apparent molecular weight. b) Cleavage of the RAFT end group with AIBN prior to PPM could prevent the formation of polymer dimers. For clarity, PFSty and substituted PFSty pendant groups are abbreviated as R.

Thermal properties of poly(FBM-*r*-TFBM) were investigated by DSC and TGA measurements. Interestingly, DSC thermograms of polymers made by PPM in continuous flow and by using an RLH differed in absolute T_g values as well as T_g trends over the ratio of modification (refer to **Figure 92**). Although the T_g of poly(FBM-*r*-TFBM) was found to be in the range of 46 °C to 59 °C throughout every experiment and modification ratio, the T_g itself was found to only shift significantly when the PPM was conducted in continuous flow. There the T_g increased with increasing ratio of FBM groups which can be explained by stronger interactions between smaller FBM units with less steric hinderance and more π-π stacking compared to -CF_3 group-containing TFBM pendant chains.[321] However, when modifying poly(PFSty) in small batches using an RLH, the T_g of the resulting polymer increased only once from 51 °C at 10 mol% to 59 °C at 20 mol% FBM content before remaining constant at approximately 59 °C regardless of the modification ratio (refer to **Appendix 27**).

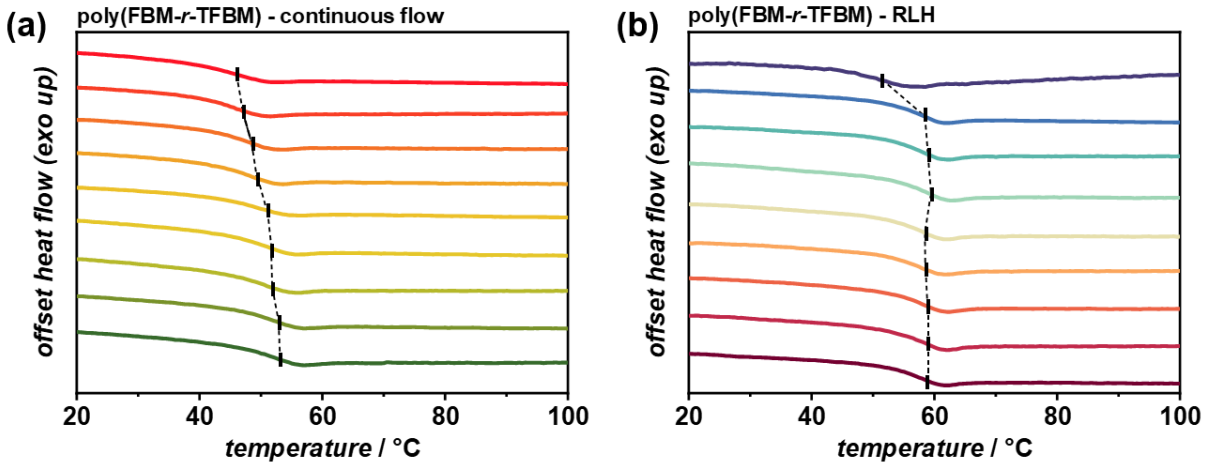

Figure 92. DSC traces of poly(FBM-r-TFBM) made by PPM in continuous flow (a) and using an RLH (b). T_gs are marked in black. The amount of FBM increased from red to green (a) and blue to red (b), respectively (10 – 90 mol%). Heating rate: 10 K min^{-1}.

The reason for the discrepancy in T_g profiles depending on the PPM method is not fully understood but might be explained by a difference in the polymer microstructure depending on the different mixing of reaction solutions between PPM in continuous flow and subsequent dosing in small wells by the RLH.

Poly(PFSty) exhibited a three-step thermal decomposition profile with onset decomposition temperatures of 136 °C, 264 °C, and 427 °C, respectively. The overall $T_{5\%}$ temperature of poly(PFSty) was 275 °C. Although no overall trend regarding the thermal stability of poly(FBM-*r*-TFBM) depending on the ratio and method of modification with FBM and TFBM can be identified, the modified polymers also exhibited three-step decomposition profiles with $T_{5\%}$ temperatures of approximately 316 °C (refer to **Figure 93**). In general, the weight loss during the first and second thermal decomposition increased with FBM content in the polymers which indicates a faster thermal degradation of aromatic fluorine atoms compared to aliphatic -CF_3 groups.

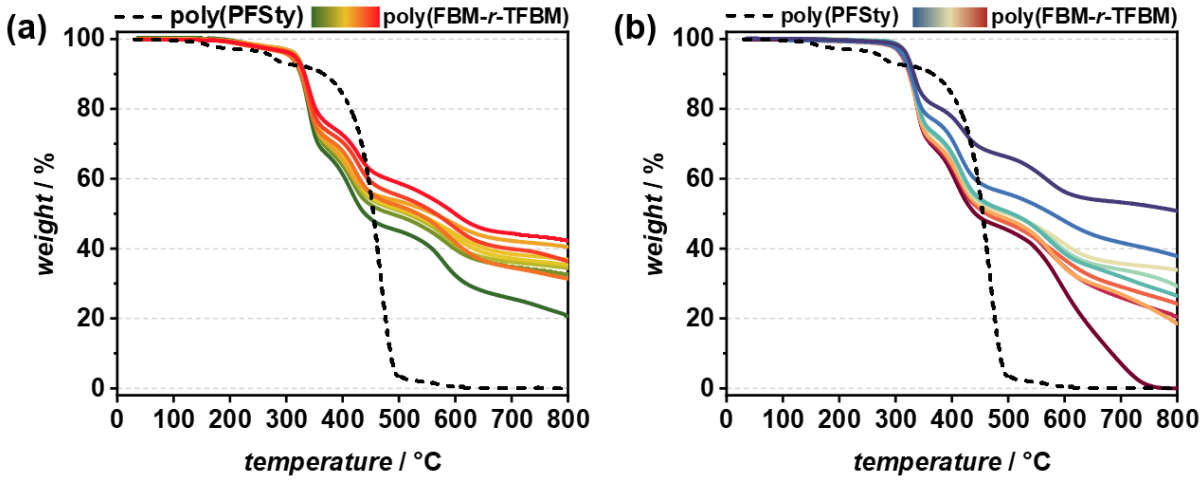

Figure 93. TGA profiles of poly(PFSty) (dashed black line) and poly(FBM-*r*-TFBM) (solid colored lines) made by PPM in continuous flow (a) and using an RLH (b). The amount of FBM increased from red to green (a) and blue to red (b), respectively (10 – 90 mol%). Heating rate: 10 K min^{-1}.

3.4.5 Summary

In this chapter, the polymerization and PPM of PFSty in continuous flow was investigated. TT allowed the rapid acquisition of large kinetic data sets from which valuable rate constants of the propagation of the polymerization were conveniently obtained with little to no operator input. For the RAFT polymerization of PFSty with CPDT and AIBN in DMF, the best compromise between monomer conversion and

control over the polymerization were obtained at 85 – 90 °C. Lowering the temperature resulted in unsatisfactory conversion while increasing the temperature resulted in the loss of control necessary to create defined polymer structures. Furthermore, additional RAFT agents were screened in order to evaluate their influence on poly(PFSty) synthesis. DoPAT, CDCTPA, and CBCDMPC were chosen, all of which were outperformed by CPDT in terms of monomer conversion and polymerization control. Building on the PPM method introduced in **Chapter 3.3.5.1** PPM of poly(PFPA) *via* ^{19F} NMR, the PPM of poly(PFSty) via PFT reaction with FBM and TFBM was demonstrated both in continuous flow and using a RLH for reactant dosing. The PFT reaction was found to proceed quantitatively and selectively in 1 h at a.t. with DBU as base in EtOAc. ^{19}F NMR spectroscopy of the obtained polymers was used to determine the ratio and therefore the precision of modification with the different thiols derived from the theoretically expected modification ratio by input. The precision with which the modification could be controlled was found to be above 80 % in continuous flow and above 75 % with an RLH. Polymers after PPM exhibited bimodal molecular weight distributions which was believed to be caused by the formation of polymer dimers *via* disulfide bridging facilitated by the cleavage of RAFT end groups by DBU. This may be prevented in future studies by transformation of the RAFT group into an unreactive end group with AIBN prior to PPM. Interestingly, the T_g of poly(FBM-*r*-TFBM) was found to be in the range of 46 ° to 59 °C but was only dependent on the ratio of modification when PPM was conducted in continuous flow. Analysis of the thermal stability of poly(FBM-*r*-TFBM) revealed a faster thermal degradation of polymers with increased amount of aromatic fluorine atoms compared to aliphatic -CF_3 containing pendant groups. The strategy presented herein highlights the power of TT and continuous reaction control to obtain kinetic information about the polymerization of functional monomers which would be time and material consuming to achieve from traditional batch-based reactions. Furthermore, the PPM of poly(PFSty) by PFT reaction in a continuous automated manner presents itself as a promising approach toward controlled fabrication of novel materials by virtue of a selective and highly efficient PPM method beyond the amidation of PFPA using a commercial and established feedstock.

3.5 Post-polymerization Modification of poly(S-*r*-NB-PFPE) in Continuous Flow

3.5.1 Introduction

The investigation of IV polymers in a continuous flow context has to this day never been explored. Due to the harsh reaction conditions associated with IV, *i.e.* high temperatures and reactive sulfur radical concentration without inert solvent, no IV polymerization in continuous flow has ever been reported. Realization of the polymerization itself in a high-throughput manner would require scientists to design a reactor setup capable to overcome two major hurdles:

1. Continuous transport of reactants: Elemental sulfur at ambient temperature is a ponderous solid, and as such it is not as easily conveyed and dosed as liquids.[322] One conceivable method might be the usage of screw conveyers and conveyer belts to transport elemental sulfur through a heated reactor. However, this poses a significant engineering challenge and is not feasible on a laboratory scale. Another method might be the transport of sulfur in a dissolved state. However, sulfur is known to be not well soluble, and the best solvent is CS_2 which has a boiling point of 46.3 °C and is therefore not applicable for a typical IV at over 120 °C.[46]

2. Solubility of IV polymers: High sulfur content materials prepared by IV are typically known for their poor solubility in organic solvents. Depending on the number of unsaturated groups in the cross-linker, IV polymers exist in the form of cross-linked networks which are completely insoluble.[22] This means that as the polymerization progresses, the resulting polymer solidifies and/or precipitates which would lead to a blockage of the tubing. Additionally, inline and online analyses, one of the key advantages of flow polymer chemistry over batch chemistry such as NMR and SEC rely on the analysis of dissolved samples and would therefore not be accessible to IV polymers in continuous flow.[32]

Therefore, the realization of IV polymerizations themselves in flow remains elusive to this point and PPM needs to be employed in order to combine the benefits of IV (abundant feedstock, facile synthesis) with the advantages of flow polymer chemistry (user-independent control, upscaling, high reproducibility).

3.5.2 Strategy

As shown previously, poly(S-*r*-NB-PFPE) was found to be an effective platform polymer for PPM with primary amines owing to its solubility in organic solvents while maintaining its reactive PFP-ester functionality throughout polymerization. Thus, it was hypothesized that poly(S-*r*-NB-PFPE) might be applicable to flow-assisted PPM analogous to the PPM of poly(PFPA) demonstrated in **Chapter 3.3** Automated Synthesis and Post-polymerization Modification of Polypentafluorophenyl Acrylate in Continuous Flow. Poly(S-*r*-NB-PFPE) was modified with two different amine pairs (4-fluorobenzylamine (FBA) and TFMBA as well as NBMA and BA) as described in **Chapters 3.3.5.1** PPM of poly(PFPA) *via* ^{19F} NMR and **3.3.5.2** PPM of poly(PFPA) *via* ^{1H} NMR (refer to **Scheme 27**). The application of the PPM methodology presented previously on poly(S-*r*-NB-PFPE) represents the logical combination of **Chapters 3.2** Inverse Vulcanization of Norbornenyl-Pentafluorophenyl-Ester and **3.3** Automated Synthesis and Post-polymerization Modification of Polypentafluorophenyl Acrylate in Continuous Flow and is believed to be a promising approach to advance both the field of IV and the field of flow polymer chemistry by gaining control over IV polymers (a notorious downside of IV) while at the same time demonstrating the power of flow-PPM.

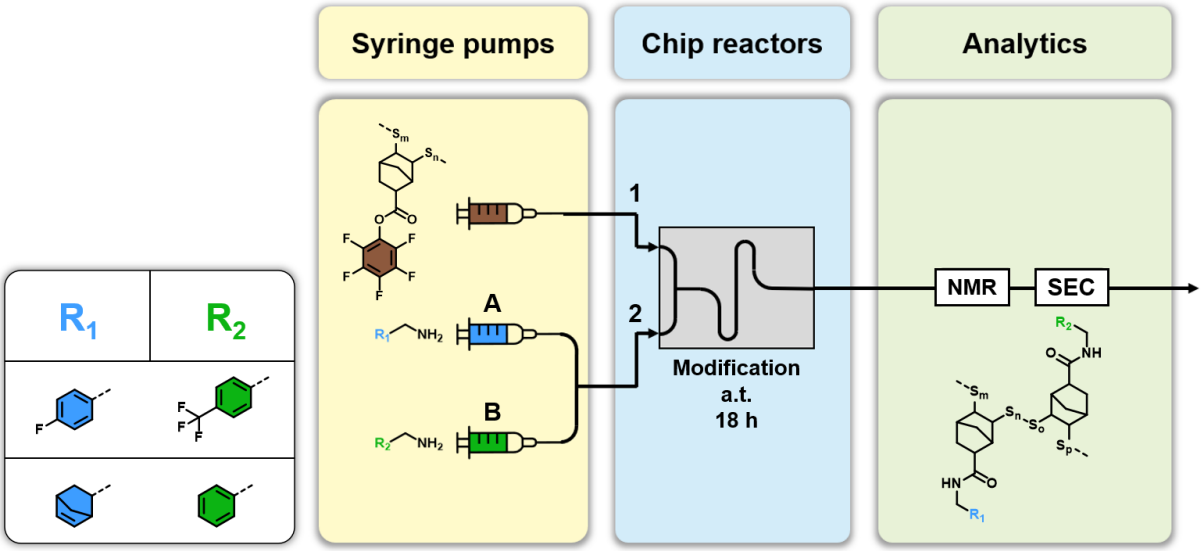

Scheme 27. Visualization of the flow reaction setup used for the PPM of poly(S-*r*-NB-PFPE) (brown) with two pairs of primary amines (blue and green). Control over the flow rate and liquid dosing facilitates the direct control over the modification ratio of the active polymer. A is either FBA or NBMA and B is either TFMBA or BA, depending on if modification is traced *via* ^{19}F NM or ^{1}H NMR, respectively. Brackets of repeating units are omitted for clarity and sulfur chains are abbreviated by dashed lines.

3.5.3 PPM of poly(S-*r*-NB-PFPE) *via* ^{19}F NMR

The PPM of poly(S-*r*-NB-PFPE) with FBA and TFMBA was conducted following the procedure described in **Chapter 3.3.5.1** PPM of poly(PFPA) *via* ^{19F} NMR. In general, solutions of poly(S-*r*-NB-PFPE), FBA, and TFMBA were prepared with equal concentrations of active ester units and amine groups, respectively. The streams of amines were mixed before being combined with the polymer-containing stream at a.t. Samples with the desired compositions were collected and rested for 18 h prior to precipitation with petrol ether. The resulting polymers were entitled poly(sulfur-*random*-norbornenyl-fluorobenzylamide-*random*-trifluoromehtylbenzylamide) (poly(S-*r*-NB-FBAm-*r*-TFMBAm)) (refer to **Scheme 28**).

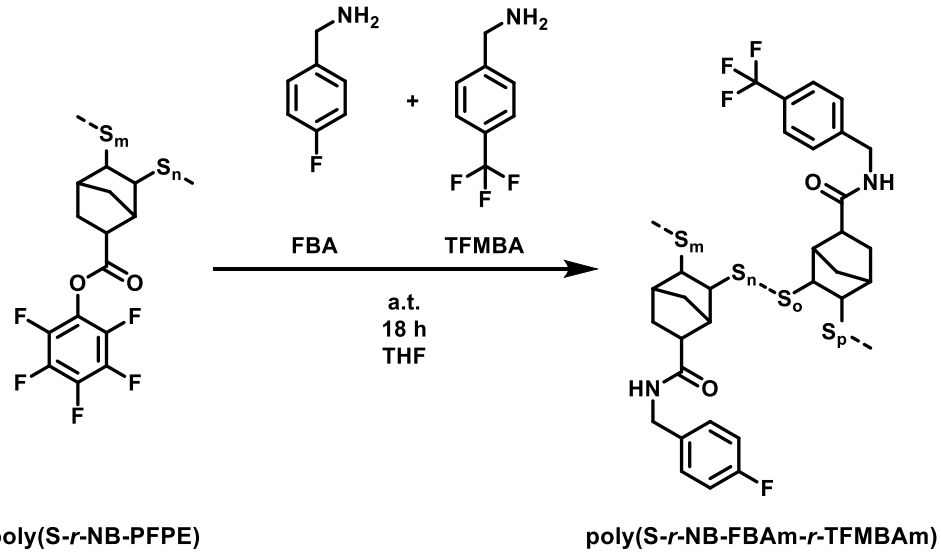

Scheme 28. Reaction scheme of the PPM of poly(S-*r*-NB-PFPE) with FBA and TFMBA in continuous flow.

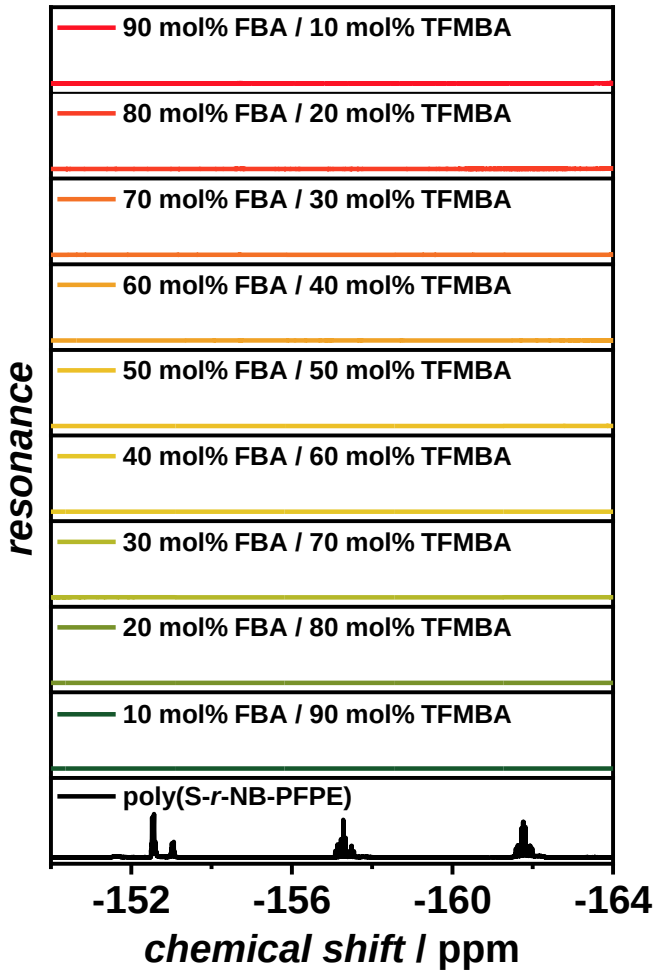

Figure 94. Stacked ^{19}F NMR spectra of poly(S-*r*-NB-PFPE) (black) and poly(S-*r*-NB-FBAm-*r*-TFMBAm) (colored) modified with different rations of FBA and TFMBA. No more signals in the region of aromatic poly(S-*r*-NB-PFPE) resonances were found which confirms the quantitative conversion of PFP-ester groups. The amount of FBA increased from green to red (10 – 90 mol%) while the amount of TFMBA increased from red to green (10 – 90 mol%), respectively.

The full conversion of PFP-ester moieties was confirmed by the disappearance fluorine resonances at -152.6 ppm, 157.3 ppm, and -161.8 ppm attributed to poly(S-*r*-NB-PFPE) (refer to **Figure 94**). However, calculation of the ratio of modification by integration of aromatic para fluorine atoms and aliphatic -CF_3 fluorine atoms showed a very strong deviation between the input and the resulting ratio according to which almost no FBA was incorporated into the polymer (refer to **Figure 95**). The calculated modification ratios according to ^{19}F NMR spectroscopy can be found in the appendix (refer to **Appendix 28**).

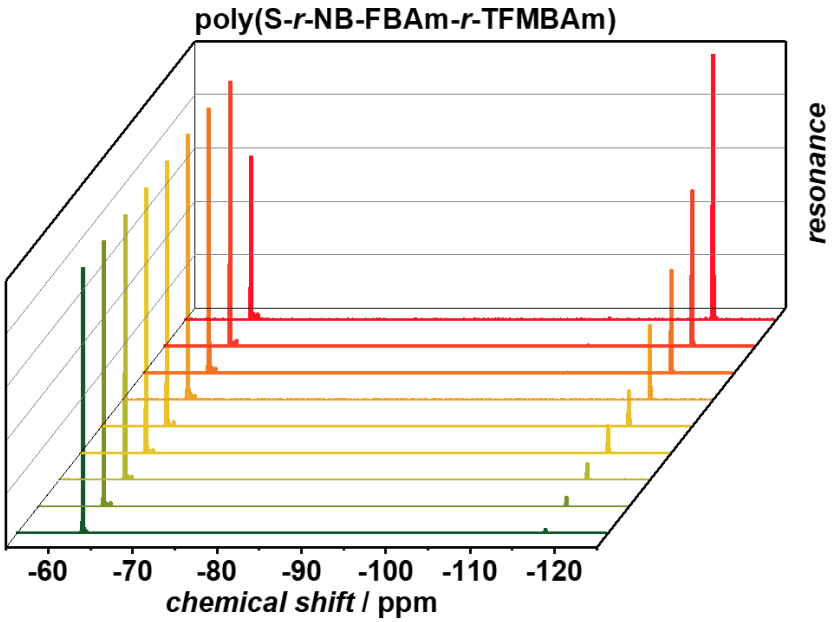

Figure 95. Waterfall plot of normalized ^{19}F NMR spectra of poly(S-*r*-NB-FBAm-*r*-TFMBAm) in the region of aliphatic and aromatic fluorine resonances. The peak at -63 ppm was assigned to -CF_3 groups and the peak at -118 ppm was assigned to aromatic para fluorine atoms. The amount of FBA increased from green to red (10 – 90 mol%) while the amount of TFMBA increased from red to green (10 – 90 mol%), respectively.

The reason of this drastic deviation is not fully understood but might have been caused by the substitution of fluorine atoms by sulfide anions potentially present in the IV polymer, which resulted in lower FBA resonance integrals than expected. As discussed previously (refer to **Chapter 3.3.5.1** PPM of poly(PFPA) *via* ^{19F} NMR), the modification of PFP-ester containing polymers by amidation with different aromatic amines could also be observed by ^{1}H NMR. Given the sufficient separation of chemical shift of FBA from TFMBA, the ratio of modification in poly(S-*r*-NB-FBAm-*r*-TFMBAm) was calculated by integration of the respective aromatic resonance regions in the ^{1}H NMR spectra (refer to **Figure 96a**). It was found that according to ^{1}H NMR spectroscopy, the final ratios of FBAm and TFMBAm units in the sulfur polymer matched the input ratios very precisely with accuracies over 95 % (refer to **Figure 96b**).

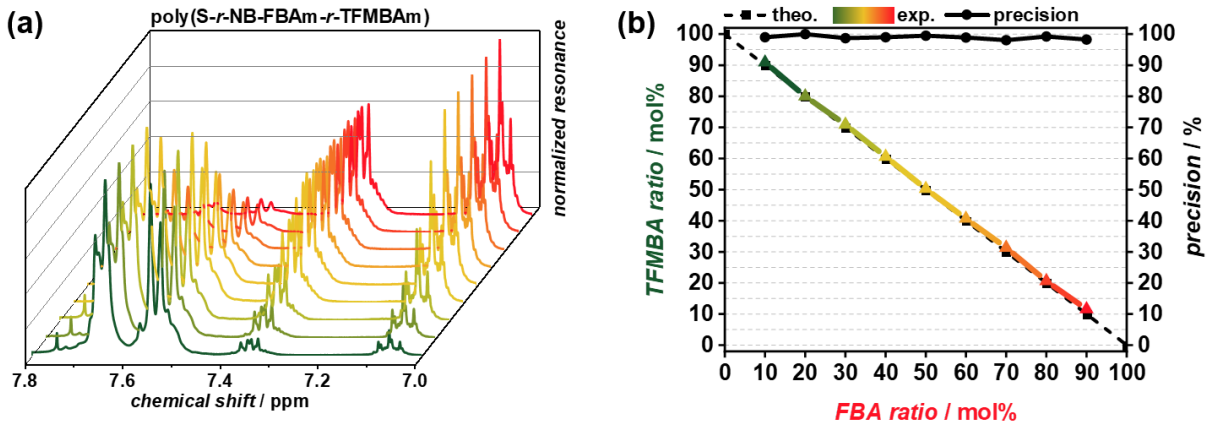

Figure 96. a) Waterfall plot of ^{1}H NMR spectra of poly(S-r-NB-FBAm-r-TFMBAm) in the aromatic region. FBAm and TFMBAm groups were separately integrated for calculation of the ratio of modification. b) Theoretical and experimental modification ratios of poly(S-r-NB-PFPE) with FBA and TFMBA calculated from ^{1}H NMR spectra. The black dashed line represents the theoretical input ratios of FBA and TFMBA which are directly correlated to the flow rates of the reactor while the colored solid line represents the found ratios in the final polymers. The precision (black dots) shows that excellent control over the modification was obtained in continuous flow.

This excellent precision and control highlighted the power of continuous reaction operation in controlling the PPM of poly(S-*r*-NB-PFPE) in continuous flow, which further highlights the applicability of the presented sulfur precursor polymer as platform material able to be modified in a highly controlled manner. The modification of poly(S-*r*-NB-PFPE) was additionally investigated by ATR TF-IR spectroscopy, as described in **Chapter 3.3.5.1** PPM of poly(PFPA) *via* ^{19F} NMR, which revealed the linear correlation between the peak absorbance of characteristic FBA and TFMBA groups with the input ratios of these respective amines (refer to **Figure 97**).The absorbance bands at 1510 cm^{-1}, 1352 cm^{-1}, and 1223 cm^{-1} (peaks A, B, and D) could be attributed to the vibrations C-C ring bonds in fluorine-substituted aromatics which were found to increase with the increasing molar amount of FBAm in the polymers.[303] Absorbance bands at 1324 cm^{-1}, 1163 cm^{-1}, 1110 cm^{-1}, and 1067 cm^{-1} (peaks B, and E – G) were assigned to aliphatic -CF_3 group vibrations, which decreased with the decreasing ratio of TFMBA and increasing amount of FBA, respectively.[304,305]

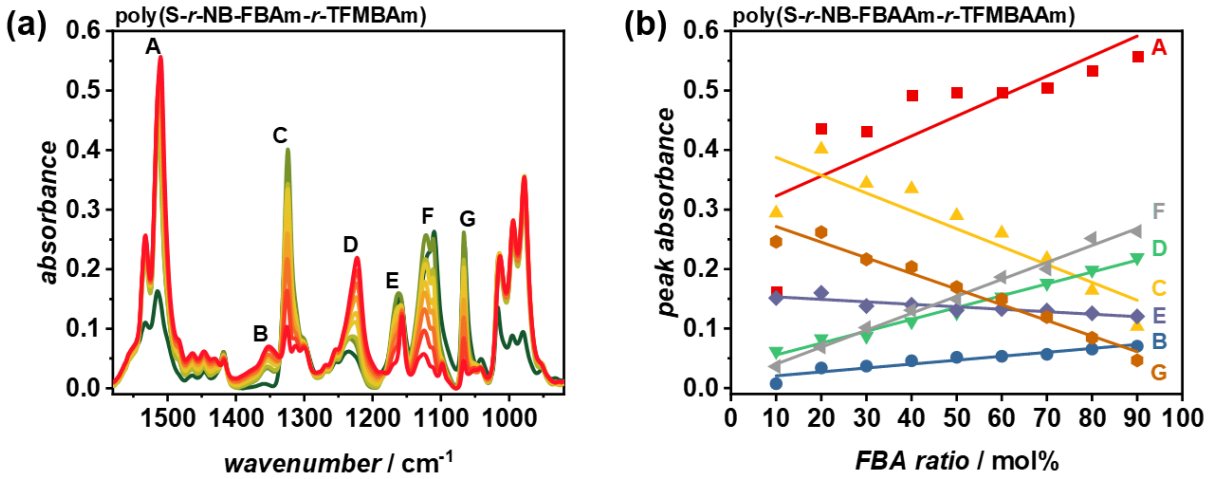

Figure 97. ATR FT-IR spectra of poly(S-*r*-NB-FBAm-*r*-TFMBAm) in the range of 1580 cm^{-1} to 920 cm^{-1}. The amount of FBA increased from green to red (10 – 90 mol%) while the amount of TFMBA increased from red to green (10 – 90 mol%), respectively. Characteristic peaks assigned to FBA and TFMBA, respectively were identified which were found to increase or decrease linearly with the amount of respective amine. Resolution: 2 cm^{-1}. b) Linear fits of the peak absorbance against the ratio of FBA of peaks A – G.

SEC analysis of poly(S-*r*-NB-FBAm-*r*-TFMBAm) showed a reduction in molecular weight from $M_n \approx 930$ g mol^{-1} to $M_n \approx 890 – 710$ g mol^{-1} caused by the substitution of PFP groups by lighter FBA and TFMBA groups. The M_n followed the trend of smaller resulting molecular weight with increasing substitution with lighter FBA groups compared to TFMBA groups (refer to **Figure 98**). However, as described previously, absolute molecular weights determined by SEC need to be viewed with caution as no proper polysulfide standards exists today and thus M_n values are likely to be prone to error. Dispersity $Đ$ was as low as 1.09, which can be explained by the purification of the polymers by precipitation that was not done with poly(S-*r*-NB-PFPE). Detailed information about M_n and $Đ$ are displayed in **Appendix 29**.

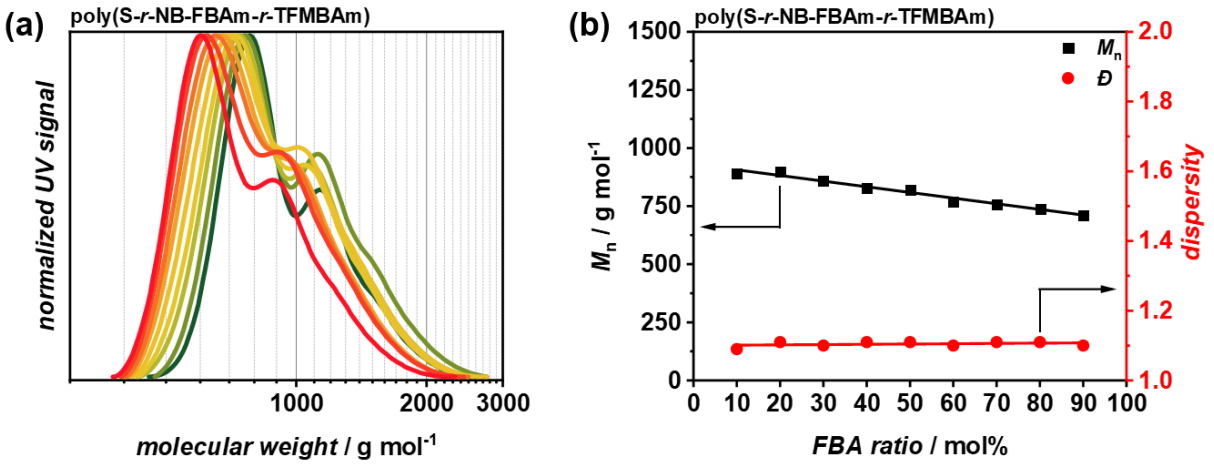

Figure 98. SEC traces of poly(S-*r*-NB-FBAm-*r*-TFMBAm). b) M_n (black) and *Đ* (red) against the input ratio of FBA. The M_n was found to decrease with increasing modification with lighter FBA compared to TFMBA while *Đ* did not change significantly. Solvent: THF; calibration: PS.

The reaction was additionally conducted using TFBA and TFMBA at 50 °C with a residence time of 5 min. It was found that the conversion of PFP-ester units was quantitative after 5 min which was proven by the disappearance of PFPE resonances in the ^{19}F spectra which highlights applicability of the continuous flow approach for the controlled and rapid modification of IV polymers in a controlled manner (refer to **Appendix 30**). However, it has been shown that amidation of active PFP-esters already occurs at a.t. Therefore, to avoid undesired side reactions at higher temperatures and to ensure comparability with the PPM of poly(S-*r*-NB-PFPE) in batch, the PPM of poly(S-*r*-NB-PFPE) in flow was carried out at a.t. for 18 h, as described previously (refer to **Chapter 3.2** Inverse Vulcanization of Norbornenyl-Pentafluorophenyl-Ester). An in-depth study of the PPM of poly(S-*r*-NB-PFPE) in flow at elevated temperatures and with different residence times represents an important and promising subject of future studies to fully exploit the advantages of flow chemistry over batch chemistry.

3.5.4 PPM of poly(S-*r*-NB-PFPE) *via* ^{1}H NMR

In addition to the amidation of poly(S-*r*-NB-PFPE) with intricate fluorinated amines, the flow-PPM and control thereof using a non-fluorinated amine pair was investigated with NBMA and BA. As described previously (refer to **Chapter 3.3.5.2** PPM of poly(PFPA) *via* ^{1H} NMR), NBMA and BA exhibit distinguishable characteristic proton resonances caused by their aromatic and olefinic protons. Integration of these resonance regions

therefore allows determination of the modification ratio of polymers bearing different amounts of these amines. Solutions of poly(S-*r*-NB-PFPE), NBMA, and BA were prepared, ensuring equal concentrations of active ester units and amine groups. The amine-containing streams were mixed before being introduced into the polymer-containing stream at a.t. Samples with the intended compositions were collected and allowed to rest for 18 hours before being precipitated using petrol ether. The resulting polymers made by amidation of poly(S-*r*-NB-PFPE) with NBMA and BA were named poly(sulfur-*random*-norbornenyl-norbornenylmethylamide-*random*-benzylamide) (poly(S-*r*-NB-NBMAm-*r*-BAm)) (refer to **Scheme 29**).

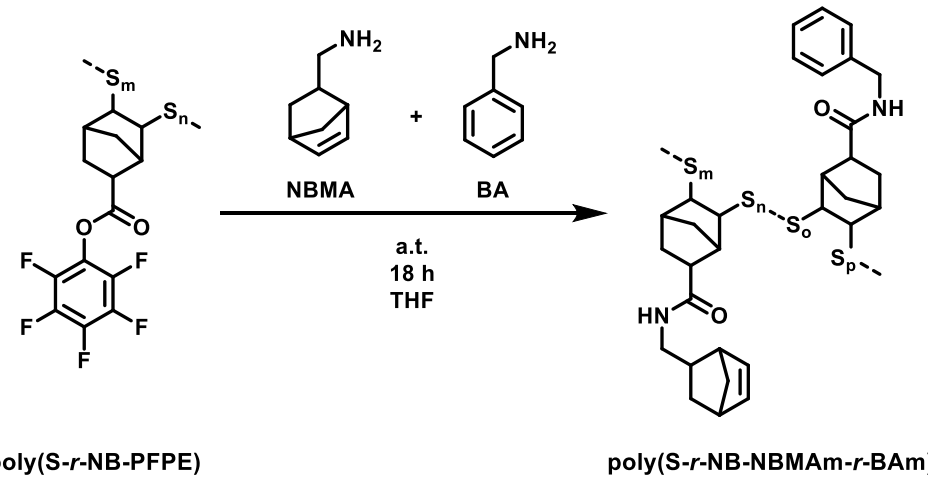

Scheme 29. Reaction scheme of the PPM of poly(S-*r*-NB-PFPE) with NBMA and BA in continuous flow.

The complete conversion of PFP-ester groups was confirmed by ^{19}F NMR spectroscopy of the resulting polymers which showed the complete disappearance of PFP-ester fluorine atoms at -152.6 ppm, 157.3 ppm, and -161.8 ppm, respectively (refer to **Figure 99**). The signal at -161.8 ppm can be attributed to residual detached PFP.

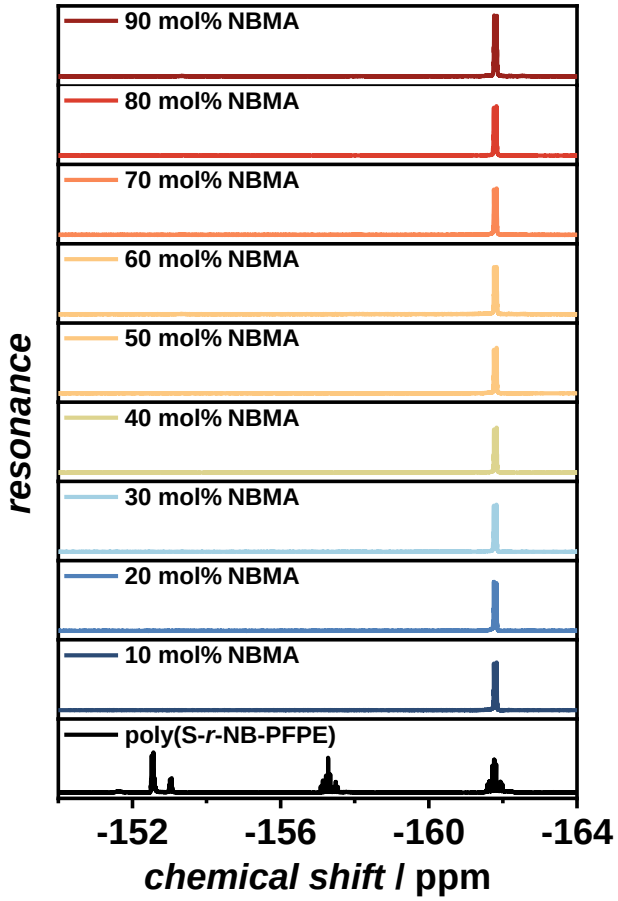

Figure 99. Stacked ^{19}F NMR spectra of poly(S-r-NB-PFPE) (black) and poly(S-*r*-NB-NBMAm-*r*-BAm) (colored) modified with different rations of NBMA and BA. No more signals in the region of aromatic poly(S-*r*-NB-PFPE) resonances were found which confirms the quantitative conversion of PFP-ester groups. The resonance at -161.8 can be explained by the presence of residual detached PFP. The amount of NBMA increased from blue to red (10 – 90 mol%) while the amount of BA increased from red to blue (10 – 90 mol%), respectively.

Evaluation of the resulting modification ratios of poly(S-*r*-NB-PFPE) with NBMA and BA was done by ^{1}H NMR spectroscopy. Integration of the five aromatic benzyl protons in the range of 7.1 ppm – 7.4 ppm and the two C=C double bond protons of norbornenyl groups in the range of 5.9 ppm – 6.2 ppm were used to calculate the ratio of modification with NBMA and BA, respectively (refer to **Figure 100a**). Importantly, the ratio of modification of poly(S-*r*-NB-PFPE) matched very closely the theoretically input ratio between amines NBMA and BA. The precision with which the polymers could be effectively modified using flow-PPM was found to be above 95 % throughout the whole modification range which proves the excellent precision over the control of the presented IV polymer (refer to **Figure 100b**).

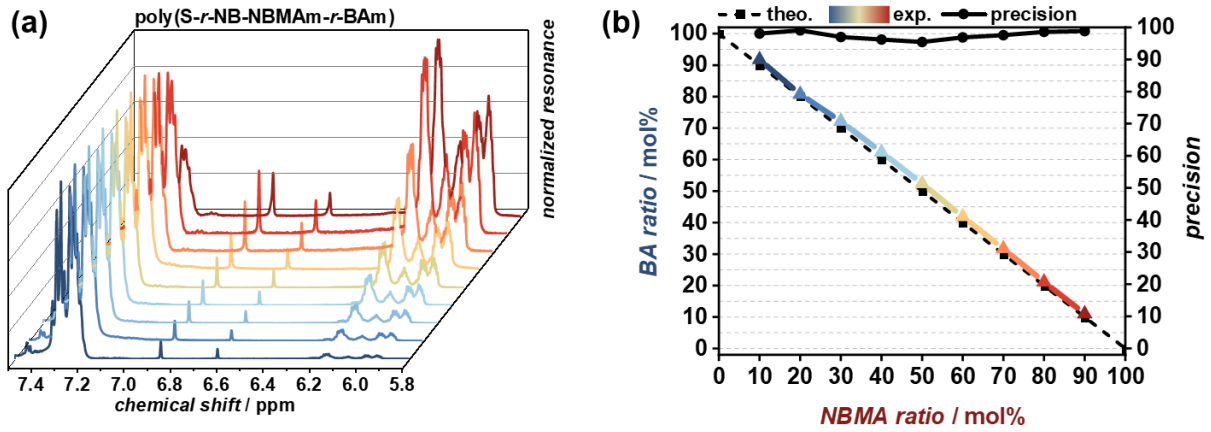

Figure 100. a) Waterfall plot of ^{1}H NMR spectra of poly(S-*r*-NB-NBMAm-*r*-BAm) in the olefinic and aromatic region. NBMAm and BAm groups were separately integrated for calculation of the ratio of modification. b) Theoretical and experimental modification ratios of poly(S-*r*-NB-PFPE) with NBMA and BA calculated from ^{1}H NMR spectra. The black dashed line represents the theoretical input ratios of NBMA and BA which are directly correlated to the flow rates of the reactor while the colored solid line represents the found ratios in the final polymers. The precision (black dots) shows that excellent control over the modification was obtained in continuous flow.

The traceability of the modification *via* ATR FT-IR spectroscopy was investigated by analyzing the range of characteristic benzyl and norbornenyl bond vibrations from 3125 cm^{-1} to 2750 cm^{-1} (refer to **Figure 101a**). Interestingly, the C-H stretch vibration band of unsaturated double bonds at 3030 cm^{-1} was found to decrease with decreasing amount of BA in the polymer which is in line with the expectation as the aromatic phenyl ring in BA contains more protonated C=C bonds compared to NBMA.[309]

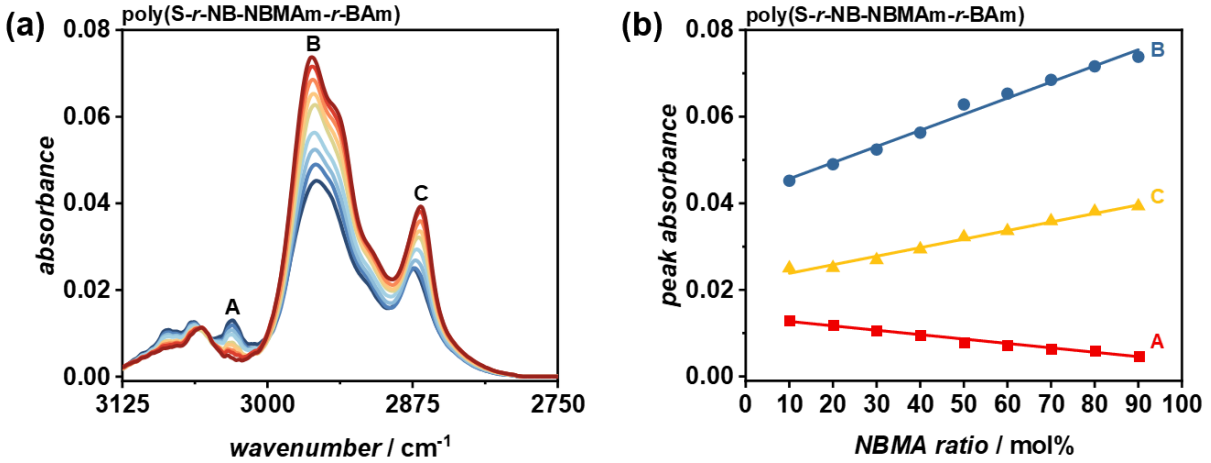

Figure 101. ATR FT-IR spectra of poly(S-*r*-NB-NBMAm-*r*-BAm) in the range of 3125 cm^{-1} to 2750 cm^{-1}. The amount of NBMA increased from blue to red (10 – 90 mol%) while the amount of BA increased from red to blue (10 – 90 mol%), respectively. Characteristic peaks assigned to NBMA and BA, respectively were identified which were found to increase or decrease linearly with the amount of respective amine. Resolution: 2 cm^{-1}. b) Linear fits of the peak absorbance against the ratio of NBMA of peaks A – C.

Additionally, aliphatic, unsaturated C-H stretch vibrations were found at 2961 cm^{-1} and 2868 cm^{-1} and were identified as CH_2 stretch and ring CH stretch vibrations of the norbornene ring.[310] NBMA-associated absorbance bands increased linearly with the linear ratio profile of NBMA found in the polymer while BA-associated decreased linearly, respectively which substantiates the proposed tunable modification (refer to **Figure 101b**). The molecular weight distribution of poly(S-*r*-NB-NBMAm-*r*-BAm) was investigated by SEC, which showed an overall decrease in molecular weight from $M_n \approx 930$ g mol^{-1} of poly(S-*r*-NB-PFPE) to $M_n \approx 800$ g mol^{-1} of poly(S-*r*-NB-NBMAm-*r*-BAm) (refer to **Figure 102a**). Over the change of in poly(S-*r*-NB-NBMAm-*r*-BAm) with different ratios of NBMA and BA, no significant trend in M_n and $Đ$ was observed by SEC. The dispersity before and after PPM of poly(S-*r*-NB-PFPE) changed slightly with a shift from $Đ$ = 1.35 before PPM to approximately $Đ$ = 1.10 after PPM (refer to **Figure 102b**). Detailed information on M_n and $Đ$ of poly(S-*r*-NB-NBMAm-*r*-BAm) are displayed in **Appendix 31**. Similar to the PPM of poly(S-*r*-NB-PFPE) with FBA and TFMBA discussed previously, the lower $Đ$ is believed to be caused by the purification through precipitation which was not done with the poly(S-*r*-NB-PFPE) precursor polymer.

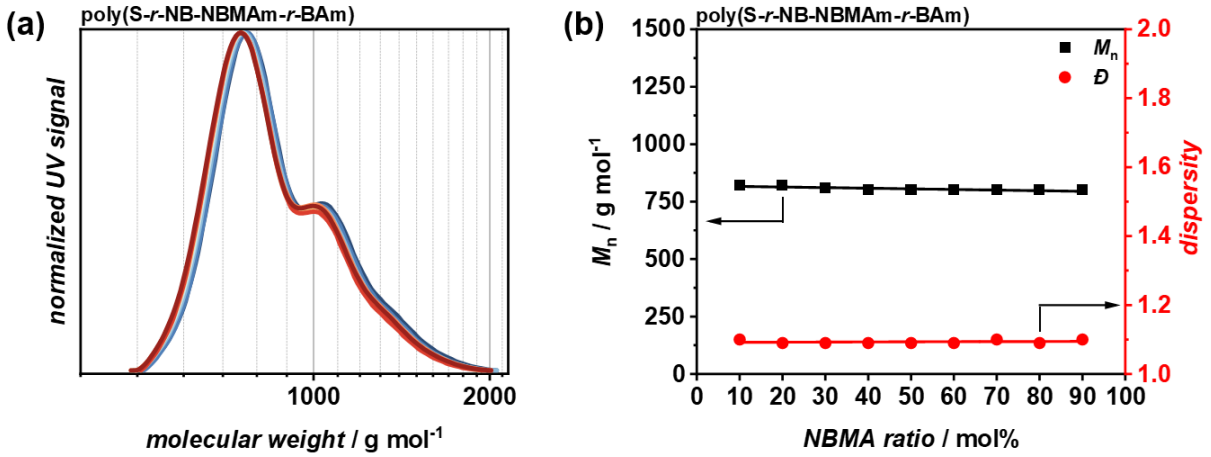

Figure 102. SEC traces of poly(S-*r*-NB-NBMAm-*r*-BAm). b) M_n (black) and $Đ$ (red) against the input ratio of NBMA. The M_n and $Đ$ did not change significantly over the modification ratio range. The amount of NBMA increased from blue to red (10 – 90 mol%) while the amount of BA increased from red to blue (10 – 90 mol%), respectively. Solvent: THF; calibration: PS.

3.5.5 Summary

In this chapter, the PPM of poly(S-*r*-NB-PFPE) in continuous flow was investigated and discussed. Poly(S-*r*-NB-PFPE) was reacted by continuous dosing and mixing with two pairs of primary amines: FBA and TFMBA as fluorinated amine pair and NBMA and BA as non-fluorinated amine pair. By virtue of the highly efficient amidation of active PFP-esters with primary amines, the PPM of poly(S-*r*-NB-PFPE) could be controlled directly by the flow rates set at the dosing syringe pumps which could be computer controlled and thus required little to no human intervention for high throughput synthesis of functional sulfur polymers derived from inverse vulcanization. The precision with which the predefined modification ratio could be controlled was found by ^{1}H NMR spectroscopy to be over 95 % for both amine pairs which demonstrated outstanding control over polymer structures, an unresolved issue associated with IV polymers in general. Additionally, IR spectroscopy proved to be a valuable and straightforward tool to further validate the proposed modification trend by a linear correlation between characteristic peak absorbances and ratio of modification. In general, this chapter represents itself as the combination of **Chapters 3.2** Inverse Vulcanization of Norbornenyl-Pentafluorophenyl-Ester and **3.3** Automated Synthesis and Post-polymerization Modification of Polypentafluorophenyl Acrylate in Continuous Flow and is believed to be a significant step towards establishing control over IV polymers by the means of flow polymer chemistry.

4 Conclusion and Outlook

The use of elemental sulfur as abundant resource for polymeric materials has been recognized by the scientific community for decades and has recently experienced an upswing with the invention IV. However, the harsh reaction conditions associated with IV limit the range of applicable cross-linkers and control over the final polymer structures. The approach of PPM offers the possibility to create functional polymers from reactive precursors to create materials that would not be accessible *via* direct polymerization. This concept is widely used in chemical polymer research but remains underused in combination with high sulfur content polymers derived from IV which dramatically limits the range of applications of IV polymers. In addition, the emergence of automated polymer reaction design and optimization has revolutionized all fields of chemical research in recent years, allowing safer, more sustainable, and more efficient polymer research and development. Despite its power and chemical versatility, PPM also remains underrepresented in the context of flow polymer chemistry and material science.

This thesis aimed to investigate the PPM of reactive precursor materials based on active fluorine-containing polymers derived from IV, as well as conventional carbon-based polymer chemistry in continuous flow. Synergies between IV, as efficient polymerization method, and flow chemistry, as next-generation high-throughput technology, in terms of PPM were demonstrated while advancing each individual field at the same time.

Even though the IV of PFPA, an established acrylate-based active monomer, was found to yield unsatisfactory results when reacted with elemental sulfur at elevated temperatures. The all-*cis* hydrogenated counterpart of PFPA, PFCHA, was found to undergo IV alongside TEVS which underwent PPM in the form of silane hydrolysis and polycondensation. The high dipolar moment stemming from an all-*cis*-fluorinated cyclohexyl ring was found to have beneficial impact on the electrochemical performance and cycling stability of Li-S batteries by suppressing polysulfide shuttling. Even though the intricate electrochemical mechanisms occurring in Li-S cells under presence of PFCHA have not been exhaustively studied in this thesis, the approach of advancing next-generation Li-S batteries through confinement of polysulfides by JANUS-faced coordination motifs was found to be a promising field of future research which will revolve around elucidating precise polysulfide coordination structures.

As an alternative to PFPA, IV of NB-PFPE was conducted, resulting in the formation of a polymeric material with 50 wt% sulfur while maintaining its active PFP-ester moieties to undergo PPM *via* amidation with primary amines. The versatility of poly(S-*r*-NB-PFPE) was demonstrated by the amidation with α-amino-ω-methoxy polyethylene glycol, aminopropyl trimethoxy silane, allylamine, and ferrocenyl methyl amine under mild conditions. The PPM with these functionally different amines highlighted the versatility with which poly(S-*r*-NB-PFPE) could be tuned and tailored towards special applications such as microphase separation, mercury adsorption, surface coating, cross-linking, and electrochemical activity, respectively. This represents the first report on PPM of active ester containing polymers made by IV and dramatically broadens the scope of IV for future applications such as drug delivery systems, heavy metal adsorbents, hydrophobic coatings, and electrochemical materials. Given the vast amount of commercially available primary amines, the methodology presented herein can be used to dramatically increase the number of possible polymer structures based on inverse vulcanization.

Meanwhile, the RAFT polymerization of PFPA in continuous flow was investigated by utilization of an automated flow polymerization platform able to autonomously optimize polymerization reactions. The results from the optimization were validated in an independent flow setup equipped with a different reactor in order to demonstrate the universality of experimental data generated from user-independent and ML-assisted autonomous reaction platforms. This is believed to be a crucial step towards the development of fully autonomous and even remote-controlled reactor platforms which can produce universally applicable data on polymerization reactions. However, in-depth identification of reactor fingerprints and scale models by digital twin reactors remain elusive but represent a promising approach of current research to further advance the usage of PFPA in flow polymerizations techniques based on this work. As the concept of PPM is not established in flow-based polymer research, the PPM of poly(PFPA) in continuous flow was performed and the control over the tunability of polymer properties and structure using ^{19}F NMR, ^{1}H NMR, and IR spectroscopy was demonstrated. Specifically, the precision with which two pairs of amines (two fluorinated and two non-fluorinated) could be efficiently incorporated into the parent polymer by virtue of continuous reaction control and precise dosing was highlighted. Given the broad application of poly(PFPA) in batch-based polymer reactions, the introduction thereof to the field of flow chemistry is believed to have the potential to

rapidly advance polymer research by unlocking PPM as a powerful tool of next-generation material design guided by ML. Synthesis and modification of intricate polymer architectures with multiple building blocks is certainly a promising opportunity for future research alongside the investigation of their selective PPM by orthogonal chemistry.

In addition to the investigation of the polymerization and PPM of PFPA in continuous flow, the kinetic RAFT polymerization behavior of PFSty was studied by transient timesweeping. Rate constants of the polymer propagation were obtained depending on polymerization temperature and RAFT-agent. Importantly, poly(PFSty) is known to be a reactive precursor polymer for PPM via *para*-fluoro-thiol reaction which was done in this thesis to demonstrate the control over modification achievable using this chemistry and showcasing the applicability of continuous flow to not only precisely tune poly(PFPA) but also poly(PFSty) which potentially allows investigation of more complex copolymer structures in future research.

Finally, the results from the PPM of poly(S-*r*-NB-PFPE) as IV polymer in batch were combined with the PPM of poly(PFPA) in continuous flow, resulting in the investigation of the PPM of poly(S-*r*-NB-PFPE) in continuous flow. Indeed, it was found that poly(S-*r*-PFPE) could be precisely tuned with defined amounts of primary amines under mild conditions by virtue of continuous reaction control. Desired amine ratios could be incorporated into the sulfur polymer with precisions over 95 %, proving outstanding control over polymer structures of high sulfur content materials made by IV.

To conclude, this thesis was dedicated to the investigation of PPM of IV polymers on one hand, and the PPM of conventional carbon-based polymers in continuous flow on the other. PPM over IV polymers could be achieved by usage of poly(S-*r*-NB-PFPE) as precursor material for various applications. PPM in continuous flow using poly(PFPA) and poly(PFSty) revealed excellent tunability of these polymers facilitated by continuous flow. By combining these two approaches, the PPM of IV polymers in continuous flow could be realized which offers unprecedented control over polymer structure and material properties derived from elemental sulfur as alternative feedstock for next generation materials. This work demonstrates the synergies between IV as sustainable, straightforward, and economic polymerization technique and flow polymer chemistry as emerging technology to advance science in general and chemistry in particular in our modern society.

5 Experimental Section

5.1 Analysis

This section lists information about the analysis devices and respective procedures used in this thesis in alphabetical order.

5.1.1 Attenuated Total Reflection Fourier-Transform Infrared Spectroscopy (ATR FT-IR)

IR spectra were recorded on a *Bruker Alpha II* or a *Bruker Vertex 80* IR device in ATR operation mode from 600 cm^{-1} to 4000 cm^{-1} at 22 °C. Resonance bands are categorized after their relative intensity and denoted as very weak (*vw*), weak (*w*), medium (*m*), strong (*s*), very strong (*vs*), and broad (*br*).

5.1.2 Brunauer-Emmett-Teller Analysis (BET)

The specific surface areas were determined by nitrogen physisorption via the BET method. The analysis was performed with a *BELSORP-mini II* from *Rubotherm*. Particles were pretreated in vacuum at 100 °C for 2 h prior to N_2 dosing.

5.1.3 Cold-vapor Atom Absorption Spectroscopy (CV-AAS)

Cold vapor atomic absorption spectroscopy measurements were performed using a *QuickTrace M-7600* from *Teledyne Leeman Labs*. Bromination reagent was added prior to measurements.

5.1.4 Cyclic Voltammetry against Ag/Ag^+ in solution

Cyclic voltammetry of poly(S-*r*-NB-FcMA) was done in DMSO solution with tetrabutylammonium fluorine as electrolyte salt at a concentration of 0.1 mol L^{-1}. A three-electrode cell was used attached to an *Autolab PGSTAT128N* galvanostat from *Metrohm*. The working electrode was glassy carbon, the counter electrode was platinum, and the reference electrode was $Ag/AgNO_3$. Working and counter electrodes were thoroughly cleaned prior to use. Three scan cycles at each scan rate were recorded.

5.1.5 Cyclic Voltammetry against Li in Li-S cells

Cyclic voltammetry of Li-S cells was conducted using a *BioLogic VMP-300* potentiostat from *BioLogic Science Instruments* with a potential window from 1.6 – 2.8 V. The scan rate was kept at 0.2 mV s^{-1} for 3 cycles in electrochemical stability measurements. Scan rate sweeps were conducted with scan rates between 0.02 – 0.5 mV s^{-1} for three cycles.

5.1.6 Cycling of Li-S cells

Galvanostatic cycling of Li-S cells was conducted with a *BT-2143* battery cycler from *Arbin Instruments* between 1.7 – 2.7 V under different C-rates (1 C = 1675 mA g^{-1}).

5.1.7 Differential Scanning Calorimetry (DSC)

Differential scanning calorimetry was performed on a *214 Polyma* DSC device from *NETZSCH*. Around 5 mg of sample were precisely (Δ = 0.005 mg) weighed in an aluminum pan with a pierced lid for measurement. An aluminum pan filled with air was used as a reference and the heating rate was typically set to 10 K min^{-1} for all measurements unless specified otherwise. Only the first heating run was used for discussion unless stated otherwise.

5.1.8 Dynamic Light Scattering (DLS)

DLS measurements were conducted at a scattering angle of 90° using a light scattering setup equipped with an *ALV-SP125* goniometer, an *ALV/LSE5004* multi tau correlator, a fiber optical *ALV/High QE APD* avalanche photodiode with pseudo-cross correlation and a uniphase He/Ne laser (632.8 nm). The temperature was controlled by a *Huber Pilot One* thermostat and kept at 25 °C. Correlation is recorded over 3 runs of 30 s, with runs containing count rate spikes of more than 2x the average count rate being discarded, since such spikes are likely caused by contaminants.

5.1.9 Electrochemical Impedance Spectroscopy (EIS)

Electrochemical impedance spectroscopy was conducted on Li-S cells in the frequency range of 0.5 Hz – 5 MHz using a *VMP-300* potentiostat from *BioLogic Science Instruments*. Data fitting of EIS spectra was done using RelaxIS 3 by rhd instruments.

5.1.10 Elemental Analysis (EA)

Elemental analysis was performed via thermal combustion with an *Elementar Vario Microtube* device from *Elementar* at a temperature of about 1100 °C.

5.1.11 Ellipsometry

Ellipsometry measurements were performed on a *M2000* from *Woollam.* Samples were prepared via spin-coating on silicon wafers. Measurements were taken at an angle of incidence of 65° in the spectral range of 370 – 900 nm. To evaluate the experimental data, an optical box model was applied using the instrument software *CompleteEase (V6.51).* Silicon substrates were fitted with database values for Si and SiO_2 as defined in the software. The thickness and the optical properties of the polymer layers were fitted with a Cauchy relation model.

5.1.12 High-resolution Mass-Spectrometry (HR-MS)

High-resolution mass-spectrometry was performed using a Fourier-Transform Ion Cyclotron Resonance (FT-ICR) mass spectrometer *solariX* from *Bruker Daltonik GmbH* equipped with a 7.0 T superconducting magnet in APCI mode.

5.1.13 Nuclear Magnetic Resonance Spectroscopy (NMR)

High-field ^{1}H NMR, ^{13}C NMR, and 19F NMR spectra were acquired using a Bruker Ascend III 400 MHz spectrometer, with operating frequencies of 400 MHz for protons, 101 MHz for carbon atoms, and 376 MHz for fluorine atoms, respectively.
Low-field ^{1}H NMR and ^{19}F NMR spectra were acquired using a *Magritek Spinsolve 60 Ultra* benchtop spectrometer with operating frequencies of 60 MHz for protons and 57 MHz for fluorine atoms, respectively.
All samples were dissolved in deuterated solvents as specified in the respective figure captions and the chemical shifts are referenced to the residual solvent signals. Resonances are characterized by their multiplicity and are denoted as singlet (*s*), doublet (*d*), double of a double (*dd*), triplet (*t*), multiplet (*m*), broad (*br*), and the coupling constant (*J*).

5.1.14 Scanning Electron Microscopy (SEM)

Scanning electron microscopy imaging was done using a *Quanta 200 F* from *FEI* with an accelerating voltage of 15 kV. Samples were sputtered with gold for 240 seconds prior to measurement.

5.1.15 Self-discharge of Li-S cells

Self-discharge was investigated by recording the open circuit voltage of fresh cells over time after two discharge-charge cycles at 0.2 C using a *BT-2143* battery cycler from *Arbin Instruments.*

5.1.16 Size Exclusion Chromatography (SEC)

Size exclusion chromatography in THF was performed using a *Tosoh Bioscience HLC-8320GPC EcoSEC* system, which was equipped with an autosampler, three PSS SDV columns (5 µm, 100 Å, 1000 Å, 100000 Å; 8 × 300 mm), and both UV and differential refractive index (RI) detectors. The system operated at a temperature of 35 °C with a flow rate of 1 mL min^{-1}. The system was calibrated with *ReadyCal* standards, using PMMA standards with molecular weights ranging from 800 to 2200000 Da, and PS standards from 370 to 2520000 Da. Typically, 50 µL of a filtered 2.0 mg mL^{-1} sample solution was injected onto the columns. The eluent contains 0.55 g BHT per 2.5 L HPLC grade THF.

Size exclusion chromatography in DMAc was performed an *Agilent Technologies 1260 Infinity II* system, equipped with both a refractive index (RI) detector. The system was calibrated with *ReadyCal* standards, using PMMA standards with molecular weights ranging from 800 to 2200000 Da, and PS standards from 370 to 2520000 Da. The columns used were a front Mixed-C and a Mixed-E column from *Agilent*. The eluent consisted of DMAc (HPLC grade) with 0.79 g of LiBr per 2.5 L of solvent. Typically, 50 µL of a filtered 2.0 mg mL^{-1} sample solution was injected onto the columns. The system operated at a temperature of 50 °C with a flow rate of 1 mL min^{-1}.

5.1.17 Thermogravimetric Analysis (TGA)

All thermogravimetric analysis measurements were performed on a TGA 5500 from TA Instruments in Platinum HT pans under nitrogen atmosphere. Samples were

equilibrated at 30 °C and heated to 900 °C at a heating rate of 10 K min^{-1}. 5 – 10 mg of sample were used per measurement.

5.1.18 Time-of-Flight Secondary Ion Mass Spectrometry (ToF-SIMS)

ToF-SIMS was performed on a *TOF.SIMS5* instrument. The spectrometer was equipped with a bismuth liquid cluster primary ion source and a reflectron type time-of-flight analyzer. UHV base pressure was < $5 \cdot 10^{-8}$ mbar. For high mass resolution the bismuth source was operated in the 'high current bunched' mode providing 1.69 ns Bi^{3+} primary ion pulses at 25 keV energy, a lateral resolution of approximately 4 µm, and a target current of 0.46 pA at 100 µs cycle time. The primary ion beam was scanned across a 500 × 500 $µm^2$ field of view on the sample, and 128 × 128 data points were recorded. Spectra were calibrated on the omnipresent C^-, CH^-, C_2H^-, Si^-, and S^- and peaks. Based on these datasets, the chemical assignments for characteristic fragments were determined. For depth profiling a dual beam analysis was performed in non-interlaced mode. The sputter gun operated with Ar_{1500}^+ ions, 10 keV, scanned over a concentric field of 750 × 750 $µm^2$. A target current of 5.79 nA, was applied to erode the sample. The primary ion beam was scanned across a 500 × 500 $µm^2$ field of view centered in the crater, and 128 × 128 data points were recorded with a target current of 0.46 pA at 100 µs cycle time. Shift of the calibration due to not expected charging effects during the depth profiling were corrected using Advanced ToF Correction (Depth) of the onboard software.

5.1.19 Transmission Electron Microscopy (TEM)

For both TEM and cryo-TEM, a 200 kV *FEI Tecnai G2 20* microscope equipped with a 1k × 1k *Olympus MegaView* camera was used, with the acceleration voltage set to 120 kV. For conventional TEM, 10 µL of the sample solution were deposited on a carbon support film on a 400-mesh copper grid manufactured by *Quantifoil Micro Tools*. The films were hydrophilized in an Argon plasma produced by a *Diener Electronics* plasma oven for 120 s prior to sample deposition. After blotting the excess with filter paper, the samples were allowed to air dry before introduction to the microscope. For Cryo-TEM, holey carbon films (3.5/1) on copper grids also manufactured by *Quantifoil Micro Tools* were prepared identically. 8.5 µL of the sample solution were deposited on the grid, with a portion of the sample being placed on either side, blotted using a *Thermo Fisher*

Vitrobot Mark IV, and plunge-frozen in liquid ethane. The grid was then transferred to the microscope using a *Gatan* transfer stage.

5.1.20 Water Contact Angle (WCA)

Water contact angle values were determined by the sessile drop method using a *DSA 100* drop shape analyzer from *KRÜSS*. Briefly, 10 µL (2.67 µL s^{-1}) of double distilled water was placed on an uncoated silicon wafer and on poly(S-*r*-NB-APTMS) spin-coated silicon wafers at a.t. Subsequent to incubation for 15 s, a photographic image of the drop was recorded. Image analysis was conducted with the DSA software (DSA Version 1.7.0.8).

5.2 Methods

This chapter contains information on general procedures used for the application of the described materials. Additionally, information about the flow reactor setups discussed in this thesis can be found in this chapter. Subsections are sorted by occurrence in the discussion section.

5.2.1 Solubility tests of poly(S-PFCHA-TEVS) and poly(S-CHA-TEVS)

100 mg of the respective polymer were placed in a 5 mL crimp vial and 2 mL of the solvent to investigate were added (THF, NMP, or DME/DOL 1:1 v/v). The vial was sealed and stirred at room temperature before resting for 24 hours. Solubility was estimated qualitatively by coloration of the solution.

5.2.2 Fabrication of Li-S cells

80 wt% poly(S-PFCHA-TEVS) or poly(S-CHA-TEVS), 15 wt% Ketjenblack and 5 wt% LA133 (3 %) latex were mixed until a slurry was obtained. Then the slurry was coated on an aluminum foil, dried at ambient temperature for 18 h and then at 60 °C under vacuum for additional 6 h. Then the dried electrodes were punched into small disk with a diameter of 12 mm as sulfur cathodes. The areal sulfur loading was around 1.0 mg S cm^{-2}. 2025-type coin cells were fabricated where a piece of Li foil with a diameter of 14.0 mm was used as the anode and a piece of Celgard 2500 served as

the separator. 1.0 mol L^{-1} LiTFSI and 1 wt% $LiNO_3$ dissolved in DOL/DME (v/v = 1:1) was adopted as the electrolyte. The E/S ratio was 20 µL electrolyte per mg sulfur.

5.2.3 Formation of poly(S-*r*-NB-Amino-mPEG) nanoparticles

20.0, 35.0, and 50.0 mg of poly(S-*r*-NB-Amino-mPEG) were separately dissolved in 10 mL anhydrous THF in a glass vial. To each solution, 10 mL DI water were added, and the vials were kept in a fume hood without a cap under stirring for 24 hours, allowing the THF to evaporate and trigger particle formation. Final poly(S-*r*-NB-Amino-mPEG) concentrations were 2.0, 3.5, and 5.0 mg mL^{-1}, respectively and the obtained solutions were directly used for Cryo-TEM and DLS measurements.

5.2.4 Mercury adsorption of poly(S-*r*-NB-APTMS) particles

Four solutions of $HgCl_2$ in 100 mL DI water were prepared with concentrations of 1, 10, 100, 1000 ppm, respectively. 50 mL of each solution were separated to determine the initial Hg^{2+} concentrations. To the other 50 mL solutions, 100 mg of poly(S-*r*-NB-APTMS) particles were added, and the suspensions were vigorously stirred for 24 h at a.t. The particles were filtered off and the final Hg^{2+} concentration of each solution was determined via CV-AAS.

5.2.5 Spin coating of poly(S-*r*-NB-APTMS) on silicon wafers

Pristine silicon wafers were cleaned with EtOH and acetone prior to use and covered with poly(S-*r*-NB-APMTS) solution (c = 0.1 g mL^{-1} in THF). Spin-coating was performed at 1500 rpm for 15 sec one to three times. After each coating cycle, the coated surfaces were washed with ethanol and acetone.

5.2.6 Solubility tests of poly(S-*net*-NB-AA)

The solubility of poly(S-*net*-NB-AA) was evaluated by mixing 50 mg of the respective polymer with 1 mL of THF, DCM, acetone, or EtOH and stirring for 24 hours at a.t. Solubility was estimated qualitatively by coloration of the solution.

5.2.7 Automated reactor platform (Leeds, UK)

The reactor platform used for the optimization of the polymerization of PFPA was located at the *University of Leeds* (UK) and has previously been described elsewhere.[41,297] Generally, the automated reactor platform included one *JASCO-PU 980* pump, and an aluminum heating block equipped with two *Elmatic Max K* cartridge heaters regulated by a *Eurotherm 3210* temperature controller. The reactor vessel was formed by coiling 1/16 inch stainless steel tubing with an internal volume of 1 mL around the heating block. The equipment was managed by a custom MATLAB™ interface, enabling autonomous kinetic experiments. GPC data was collected online using an *Agilent Rapide M* with a 5 µm guard column employing RI detection by a *Knauer K2301* RI detector. The eluent used was DMF treated with 0.1 wt/wt LiBr. The GPC system was calibrated using PMMA standards. Conversion monitoring was conducted with a *Magritek Spinsolve 60 Ultra* (7 µs excitation pulse, 6.4 s acquisition time, and 10 s repetition time for 2 scans). Kinetic samples were collected after three reactor volumes to ensure steady-state conditions.

5.2.8 Flow polymerization and PPM setup (Karlsruhe, Germany)

The setup located at *Karlsruhe Institute of Technology* (Germany) was comprised of three *CETONI Nemesys M* syringe pumps (volumes = 1 x 50 mL and 2 x 25 mL) equipped with a 3-way high-pressure *Contiflow* ball valve from *CETONI GmbH*. The 50 mL syringe pump was attached to a 3D-printed metal flow reactor made from 316L stainless steel (Type 1.4404) and fabricated by selective laser sintering (refer to **Figure 62**). The reactor volume was 1 mL with a flow channel radius of 1.00 mm. The reactor was heated by custom-made heating jackets made from aluminum equipped with 4 heating cartridges (160 W heating power each) with integrated Type K thermocouples from *Horst GmbH*. Temperature control was done by a *F4T 4-zone* benchtop temperature controller from *Zesta Engineering Ltd.* The flow reactor was placed inside the heating jackets and screwed together firmly for good contact and heat transfer. The output streams of the two 25 mL syringe pumps were fed together with a *Swagelok* T-piece which was attached to a 3D-printed mixing channel made from a commercial *Formlabs Form 2* 3D-printer with *Clear V4* resin. This setup was used for the PPM of poly(PFPA) and poly(S-*r*-NB-PFPE) in continuous flow.

5.2.9 Flow polymerization setup for transient timesweeping (Melbourne, Australia)

The automated flow polymerization platform used for the investigation of the polymerization of PFSty via TT was located at the *Monash University* in Melbourne (Australia) and has previously been described elsewhere.[37,225] Generally, the setup was comprised of a syringe pump equipped with a gastight 50 mL syringe from *Trajan Scientific* attached to a PFA tubing with an inner diameter of 1/16 inch and a total volume of 2 mL submerged in a thermostated oil bath which served as reactor. The reactor output was fed though a *Spinsolve 60 Ultra* benchtop NMR by *Magritek* in a PFA tubing before being diluted with THF and injected to a SEC system. The SEC component was equipped with a 5 µm *SDV PSS* analytical column (50 x 8 mm) with varying porosity (1000 Å, 100 000 Å, and 1 000 000 Å) and a *SDV PSS* 5 µm guard column. THF was used as eluent and PS standards were used for calibration and the solvent stream was filtered through a PTFE membrane with 0.22 µm pore size. A custom-made Python™ script controlled the flow rate of the syringe pump and timed the SEC injections by known dead volumes between reactor and SEC at known flow rates. ^{1}H NMR spectra were recorded using the default continuous measurement protocol provided by *Magritek* with a 7 µs excitation pulse, 6.4 s acquisition time, and 10 s repetition time. The spectrometer was shimmed using the default powershim protocol (approximately 40 min) prior to each experiment. All spectra were automatically phased and baseline corrected by the *Spinsolve* software prior to analysis.

5.2.10 PPM of poly(PFSty) in continuous flow and using an RLH (Melbourne, Australia)

The PPM of poly(PFSty) in continuous flow was done using custom built a flow setup located at the *Monash University* in Melbourne, Australia, which was comprised of four syringe pumps equipped with gastight syringes from *Trajan Scientific.* Syringe 1 was loaded with a solution of poly(PFSty) while syringes 2 – 4 contained solutions of DBU, FBM, and TFBM, respectively. The streams of syringes 2 – 4 were mixed using a cross-shaped mixer before being combined with the polymer stream from syringe 1 in a Y-shaped mixer. The flow rates were adjusted manually to match the desired modification ratios of poly(PFSty) as depicted in **Figure 87**.

The PPM of poly(PFSty) using a RLH was done with am *OT-2* robotic liquid handler from *opentrons*. Reservoirs containing solutions of poly(PFSty), DBU, FBM, and TFBM were prepared from which the robot dosed and mixed the reactants into 45 individual wells of a 96 well plate. The dosed volumes and target wells were predefined in a Python™ script to match the desired ratio of modification of poly(PFSty) and the dosing proceeded automatically once started. Each polymer composition was prepared five times in order to maximize yield (refer to **Figure 88**).

5.3 Synthesis

This chapter contains information about the synthesis procedures of monomers and polymers discussed in this thesis. Descriptions of syntheses are sorted by occurrence in the discussion section.

5.3.1 Materials and chemicals

Commercially available chemicals and solvents were obtained from abcr (Karlsruhe, Germany), Acros Organics (Geel, Belgium), BLD Pharmatech (Pudong, China), Boron Molecular (Melbourne, Australia), Fluorochem (Hadfield, United Kingdom), Rapp Polymere (Tübingen, Germany), Sigma-Aldrich/Merck (Darmstadt, Germany), TCI (Tokio, Japan), or Thermo Fisher Scientific (Waltham, Massachusetts, USA) and used as received. AIBN was recrystallized from MeOH prior to use.

5.3.2 Synthesis of monomers, polymerizations, and post-polymerization modifications

5.3.2.1 Pentafluorophenyl acrylate (PFPA)

The synthesis of PFPA was carried out following a procedure known to literature.[227] In a round bottom flask equipped with a magnetic stirring bar, pentafluorophenol (30 g, 0.16 mol, 1.00 eq) was dissolved in DCM (280 mL). The mixture was cooled to 0 °C and triethylamine (24 mL, 0.17 mol, 1.10 eq) was added slowly. Acryloyl chloride (15 mL, 0.17 mol, 1.10 eq) was added dropwise via a dropping funnel, and the mixture was stirred overnight to reach ambient temperature. The reaction mixture was washed

with water (3 x 300 mL), dried over $MgSO_4$, filtered, and concentrated under reduced pressure. The product was obtained after column chromatography with petrol ether as eluent (80 %).

^{1}H NMR (400 MHz, $CDCl_3$): δ (ppm) = 6.72 (*dd*, 1H), 6.37 (*m*, 1H), 6.18 (*dd*, 1H).

^{13}C NMR (101 MHz, $CDCl_3$): δ (ppm) = 161.83, 142.68, 140.95, 140.17, 139.33, 138.44, 136.80, 135.63, 125, 50.

^{19}F NMR (376 MHz, $CDCl_3$) δ (ppm) = -152.9 (*m*, 2F, *ortho*-F), -158.4 (*t*, 1F, *para*-F), -162.8 (*m*, 2F, *meta*-F).

ATR FT-IR: ν (cm^{-1}) = 1770 *w br*, 1657 *vw*, 1634 *vw*, 1515 *vs*, 1471 *vw*, 1406 *w*, 1293 *vw br*, 1218 *w br*, 1149 *vw*, 1111 *m br*, 1069 *vw*, 1030 *w*, 992 *vs br*, 870 *vw br*, 797 *vw*, 732 *vw*, 636 *vw br*, 618 *vw*

5.3.2.2 poly(S-*r*-PFPA)

500 mg PFPA (2.10 mmol, 50 wt%) and 500 mg elemental sulfur (1.95 mmol, 50 wt%) were mixed in a 20 mL crimp vial equipped with a magnetic stirred. For accelerated reactions, 50 mg $Zn(DTC)_2$ (0.14 mol, 5 wt%) or 50 mg MIA (0.61 mol, 5 wt%) were additionally added, and the vial was sealed. The vial was heated to 160 °C for 4 hours (for reactions without accelerator) or heated to 150 °C for 1 h (for reactions with accelerator) while stirring. The product was obtained in quantitative yield in the form of a deep brown solid after cooling the reaction mixture to a.t.

5.3.2.3 all-*cis*-2,3,4,5,6-pentafluorocyclohexyl acrylate (PFCHA)

All-*cis*-2,3,4,5,6-pentafluorocyclohexan-1-ol (1.00 eq) and 2,6-Luitidine (3.00 eq) were dissolved in anhydrous THF, and the reaction mixture was cooled to 0 °C. Then acryloyl chloride (1.20 eq) was added dropwise. The reaction was then stirred at ambient temperature for 18 hours. Silica was added to the reaction mixture and the solvents were evaporated. Subsequently, column chromatography was performed using acetone and DCM as eluents (acetone:DCM 20:80 v/v). The solvents were removed under reduced pressure to yield all-*cis*-2,3,4,5,6-pentafluorocyclohexyl acrylate as white solid (92 %).

^{1}H NMR (400 MHz, acetone-d_6): δ (ppm) = 6.50 (*dd*, *J* = 17.2, 1.5 Hz, 1H), 6.27 (*s*, 1H), 6.05 (*d*, *J* = 10.3 Hz, 1H), 5.64 – 4.91 (*m*, 6H).

^{13}C NMR (101 MHz, acetone-d_6): δ (ppm) = 165.60, 133.74, 128.66, 89.13, 87.14, 85.20, 68.00.

^{19}F NMR (376 MHz, acetone-d_6): δ (ppm) = -211.56 (*br s*, 2F), -216.10 (*br s*, 2F), -217.90 (*br s*, 1F).

HR-MS (APCI) m/z = Calculated for $C_9H_{10}F_5O_2$: 245.0601, observed: 245.0597 $[M+H]^+$.

5.3.2.4 poly(S-PFCHA)

In a 20 mL crimp vial equipped with a magnetic stirring bar, 500 mg sulfur (1.95 mmol, 50 wt%) and 500 mg PFCHA(2.04 mmol, 50 wt%) were mixed. 3.00 mL NMP were added, and the vial was sealed. The vial was heated to 150 °C for 18 h in a thermostated metal heating block. The reaction was stopped by cooling to a.t. and the product was precipitated into DI water. The crude product was dried in a vacuum oven at 40 °C for 18 hours before qualitative solubility tests were performed.

5.3.2.5 poly(S-PFCHA-TEVS) and poly(S-CHA-TEVS)

In a 20 mL crimp vial equipped with a magnetic stirring bar, 500 mg sulfur (1.95 mmol, 50 wt%), 250 mg PFCHA(1.02 mmol, 25 wt%), and 250 mg TEVS (1.31 mmol, 25 wt%) were mixed. 3.00 mL NMP were added, and the vial was sealed. The vial was heated to 150 °C for 18 h in a thermostated metal heating block. The reaction was stopped by cooling to a.t. and the product was precipitated into DI water. The mixture was stirred for 24 hours before filtration. The crude product was dried in a vacuum oven at 40 °C for 5 days before washing with THF, EtOH, and DME/DOL solution (1:1 v/v) until the washings remained colorless. The product was dried again in a vacuum oven for 24 hours to yield poly(S-PFCHA-TEVS) in the form of a black powder.

poly(S-CHA-TEVS) was obtained as a yellow powder by following the same procedure but replacing PFCHA with 500 mg CHA (1.62 mmol, 25 wt%).

ATR FT-IR: ν (cm^{-1}) = 2930 *w*, 2854 *vw*, 1722 *m br*, 1447 *vw*, 1406 *vw*, 1323 *vw*, 1254 *w*, 1210 *w*, 1116 *vs br*, 1034 *vs br*, 1006 *vs br*, 908 *m br*, 755 *s br*.

EA: wt% (calculated) = N: 0.03 (0.00), C: 26.92 (25.50), H: 3.61 (3.31), S: 60.85 (57.25).

5.3.2.6 Norbornenyl-pentafluorophenyl ester (NB-PFPE)

NB-PFPE was synthesized according to literature. In general, pentafluorophenol (10.08 g, 54.76 mmol, 1.10 eq) and 5-norbornene-2-carboxylic acid (6.89 g, 49.87 mmol, 1.00 eq) were dissolved in anhydrous dichloromethane (100 mL). The mixture was cooled to 0 ºC and *N*,*N'*-dicyclohexylcarbodiimide (11.30 g, 54.77 mmol, 1.10 eq) was added. 4-dimethylaminopyridine (670 mg, 5.48 mmol, 0.11 eq) in anhydrous THF (10 mL) was added drop-wise via a syringe. After 1 h, the reaction mixture was warmed to a.t. and stirred for additional 24 h. The crude was filtered and washed with hexane (20 mL). The obtained solution was concentrated and purified by column chromatography with hexane as the eluent to provide the colorless liquid product with a yield of 83 % (12.55 g, 41.25 mmol).

^{1}H NMR (400 MHz, $CDCl_3$): δ (ppm) = 6.35 – 6.00 (*m*, 2 H), 3.42 (*br s*, 0.7 H, endo-H), 3.32 (*m,* 0.7 H, endo-H), 3.27 (*br s*, 0.3 H, exo-H), 3.01 (*br s*, 1 H), 2.58 (*m*, 0.3 H, exo-H), 2.05 (*m*, 1 H), 1.63 – 1.33 (*m*, 3 H).

^{19}F NMR (376 MHz, $CDCl_3$) δ (ppm) = -152.8 – -153.3 (*m*, 2 F, ortho-F), -158.3 – -158.7 (*m*, 1 F, para-F), -162.4 – -162.9 (*m*, 2 F, meta-F).

ATR FT-IR: ν (cm^{-1}) = 3067 *vw*, 2983 *w*, 1781 *m*, 1516 *vs*, 1336 *w*, 1272 *vw*, 1125 *w*, 1096 *m*, 1089 *m*, 1056 *w*, 994 *vs*, 898 *w*, 834 *w*, 774 *vw*, 719 *m*, 706 *m*, 621 *vw*.

5.3.2.7 poly(S-r-NB-PFPE)

In a typical reaction, NB-PFPE (5 g, 16.44 mmol, 50 wt%) and sulfur (5 g, 19.49 mmol, 50 wt%) were placed in a round bottom flask equipped with a magnetic stirring bar. The mixture was heated to 150 °C in a thermostated oil bath for 3 d under stirring. The reaction became visible by homogenization of the components as well as a color change from orange to deep brown after 2 hours. The reaction was stopped by cooling to ambient temperature and gave poly(S-*r*-NB-PFPE) as deep brown solid in quantitative yield.

ATR FT-IR: ν (cm^{-1}) = 2966 *w br*, 1777 *m*, 1515 *vs*, 1353 *w*, 1296 *vw*, 1101 *m*, 992 *s*, 915 *vw*, 815 *w*.

5.3.2.8 poly(S-*r*-DCPD)

Dicyclopentadiene (500 mg, 3.78 mmol, 50 wt%) and sulfur (500 mg, 1.96 mmol, 50 wt%) were placed in a 20 mL crimp vial, equipped with a magnet stirring bar. The reaction vessel was sealed and heated to 140 °C for 3 h under stirring. The reaction was stopped by cooling to ambient temperature to afford poly(S-*r*-DCPD) as deep brown solid in quantitative yield. The treatment of poly(S-*r*-DCPD) was done by dissolving 500 mg poly(S-*r*-DCPD) 10 mL anhydrous chloroform in a round bottom flask. Under stirring, 210 mg benzyl amine were added dropwise. The flask was sealed, and the reaction mixture was stirred at ambient temperature for 18 h before the product was precipitated into cold petrol ether. The liquid phase was decanted, and the isolated product was dried in a vacuum oven at 40 °C overnight (yield: 83 %).

5.3.2.9 poly(S-*r*-NB-Amino-mPEG)

n a 100 mL round bottom flask equipped with a magnetic stirring bar, poly(S-r-NB-PFPE) (1.00 g, 1.64 mmol (PFP units), 1.00 eq (PFP units)) was dissolved in anhydrous THF (40 mL) under stirring. Once the precursor polymer was completely dissolved, *α*-amino-*ω*-methoxy poly(ethylene glycol) (1.48 g, M_n = 750 g mol^{-1}, 2.00 mmol, 1.20 eq) was added in one portion. The rection mixture was stirred at ambient temperature for 18 h and the product was precipitated into cold petrol ether (400 mL). The liquid phase was decanted, and the isolated product was dried in a vacuum oven at 40 °C overnight (yield: 1.37 g).

ATR FT-IR: ν (cm^{-1}) = 2865 *m br*, 1666 *w br*, 1538 *w br*, 1463 *w br*, 1345 *w*, 1289 *w br*, 1242 *w br*, 1094 *vs br*, 1039 *m br*, 945 *w br*, 842 *w br*.

5.3.2.10 poly(S-*r*-NB-APTMS)

The modification with aminopropyl trimethoxy silane was done following the procedure described above. In a 100 mL round bottom flask equipped with a magnetic stirring bar, poly(S-*r*-NB-PFP-E) (1.00 g, 1.64 mmol (PFP units), 1.00 eq (PFP units)) was dissolved in anhydrous THF (40 mL) under stirring. Once the precursor polymer was completely dissolved, APTMS (352 mg, 2.00 mmol, 1.20 eq) was added in one portion.

The rection mixture was stirred at ambient temperature for 18 h and directly used for further silica particle formation and spin-coating.

5.3.2.11 poly(S-*r*-NB-APTMS) particles

60 mL of anhydrous ethanol were placed in a 250 mL round bottom flask equipped with a magnetic stirring bar. 12 mL aqueous ammonia solution (25 wt%) were added and the solution was stirred for 5 min. 30 mL of the amidation solution of poly(S-*r*-NB-APMTS) were added and the mixture was stirred at ambient temperature for 1 h. The resulting solid product was filtered off and washed thoroughly with DI water, ethanol, and THF until the washings remained colorless. Drying in vacuum at 40 °C for 18 h gave poly(S-*r*-NB-APTMS) particles in the form of a brown powder (yield: 518 mg).

ATR FT-IR: ν (cm^{-1}) = 3290 *vw br*, 2930 *w br*, 2872 *w br*, 1640 *s*, 1532 *m*, 1444 *w*, 1302 *w*, 1194 *w*, 1089 *vs br*, 909 *w*, 750 *w br*, 690 *m br*.

5.3.2.12 poly(S-*r*-NB-AA)

The modification with allylamine was done following the procedure described above. In a 100 mL round bottom flask equipped with a magnetic stirring bar, poly(S-*r*-NB-PFP-E) (1.00 g, 1.64 mmol (PFP units), 1.00 eq (PFP units)) was dissolved in anhydrous THF (40 mL) under stirring. Once the precursor polymer was completely dissolved, allylamine (112 mg, 2.00 mmol, 1.20 eq) was added in one portion. The rection mixture was stirred at ambient temperature for 18 h and the product was precipitated into cold petrol ether (400 mL). The liquid phase was decanted, and the isolated product was dried in a vacuum oven at 40 °C overnight (yield: 523 mg).

ATR FT-IR: ν (cm^{-1}) = 3285 *w br*, 3076 *vw br*, 2959 *w br*, 1638 *vs*, 1532 *s br*, 1444 *w*, 418 *w*, 1300 *w*, 1236 *m br*, 987 *m*, 915 *m*.

5.3.2.13 Thiol-ene reaction of poly(S-*r*-NB-AA)

100 mg of poly(S-*r*-NB-AA) and 30.0 mg AIBN were dissolved in anhydrous THF. 185 mg benzyl mercaptan were added and the solution was flushed with N_2 for 15 min and then heated to 60 °C under stirring for 2 h. The product was precipitated with cold petrol ether, decanted, and dried in a vacuum oven 40 °C for 18 h (yield: analytical amount).

ATR FT-IR: ν (cm^{-1}) = 3287 *w br*, 3061 *vw br*, 2957 *w br*, 1639 *vs*, 1547 *m*, 1536 *s*, 1530 *s*, 1518 *s*, 1494 *vs*, 1484 s, 1469 *m*, 1452 *s*, 1421 *m*, 1300 *w*, 1238 *m br*, 1091 *m br*, 1071 *m*, 985 *m*, 960 *m*, 916 *m*, 863 *vw*, 766 *w*, 697 *vs*, 613 *w*.

5.3.2.14 poly(S-*net*-NB-AA)

100 mg poly(S-*r*-NB-AA) were placed in a 20 mL crimping vial equipped with a magnetic stirring bar. 20 – 100 mg sulfur were added, and the solids were thoroughly mixed. The vial was sealed and heated to 150 °C for 4 h. The obtained product was removed from the vial used without further purification (yield: quantitative).

5.3.2.15 poly(S-*r*-NB-FcMA)

The modification with allylamine was done following the procedure described above. In a 100 mL round bottom flask equipped with a magnetic stirring bar, poly(S-*r*-NB-PFP-E) (1.00 g, 1.64 mmol (PFP units), 1.00 eq (PFP units)) was dissolved in anhydrous THF (40 mL) under stirring. Once the precursor polymer was completely dissolved, ferrocenyl methyl amine (430 mg, 2.00 mmol, 1.20 eq) was added in one portion. The rection mixture was stirred at ambient temperature for 18 h and the product was precipitated into cold petrol ether (400 mL). The liquid phase was decanted, and the isolated product was dried in a vacuum oven at 40 °C overnight (yield: 865 mg).

ATR FT-IR: ν (cm^{-1}) = 3304 *w br*, 3083 *w*, 2941 *w br*, 2871 *w*, 1639 *vs*, 1515 *s br*, 1444 *m*, 1398 *w*, 1379 *w*, 1322 *w*, 1298 *w*, 1234 *m br*, 1201 *m br*, 1104 *m*, 1020 *s*, 999 *m*, 951 *vw*, 925 *vw*, 817 *m br*, 687 *vw br*, 609 *m*.

5.3.2.16 Automated synthesis of poly(PFPA) (Leeds, UK)

The automated polymerization was conducted in the laboratories of the University of Leeds (UK). In a 500 mL round bottom flask, PFPA (58.20 g, 0.24 mol, 50.0 eq), CPDT (1.71 g, 4.93 mmol, 1.00 eq), and AIBN (181 mg, 1.10 mmol, 0.02 eq) were dissolved in 232 mL anhydrous anisole. The reaction mixture was degassed by purging with nitrogen gas for 15 minutes. The flask containing the reaction mixture was kept under nitrogen gas and connected to the flow platform by submerging one end of a steel tubing which was connected to one of the pumps. The complete tubing of the reactor

platform was purged with the reaction solution and initial ^{1}H spectra were recorded from which the monomer conversion was calculated. The parameter space was set to a reaction time of 10 – 60 minutes (resolution = 2 minutes) and a reaction temperature of 70 – 120 °C (resolution = 2 °C). The number of initial training steps was set to 10 for Latin hypercube sampling. Each analysis was conducted at identical conditions with the NMR performed on the production stream flowing at 0.1 mL min^{-1}. The SEC setup used a rapid column and as such a single injection took 6 mins for a result. To improve reproducibility of measurement, a triple overlaid injection sequence was used which allowed for triplicate analysis in 12 min. The entire analysis window required 15 min and as such consumed approximately 1.5 mL of material. In total, each datapoint required < 9 mL of reaction solution.

5.3.2.17 Synthesis of poly(PFPA) in continuous flow (Karlsruhe, Germany)

The optimal polymerization parameters obtained from the automated optimization of the polymerization of PFPA were employed in a second, independent flow reactor setup allocated at Karlsruhe Institute of Technology (Germany). In a 25 mL round bottom flask, PFPA (6.27 g, 26.33 mmol, 50.0 eq), CPDT (184 mg, 0.531 mmol, 1.00 eq), and AIBN (19.5 mg, 0.118 mmol, 0.02 eq) were dissolved in 25 mL anhydrous anisole. The reaction mixture was degassed by purging with nitrogen gas for 15 min. A sample was withdrawn for measuring a pilot 60 MHz ^{1}H NMR spectrum for monomer conversion calculation before loading to the 50 mL syringe pump of the flow setup. The reactor was heated to 94 °C and the flowrate was set to 0.01786 mL min^{-1} which resembled a residence time of 56 minutes. Three reactor volumes were passed through the reactor to ensure steady-state and around 1 mL of reaction mixture was collected for calculation of monomer conversion and SEC analysis.

5.3.2.18 Synthesis of poly(PFPA) in batch

Poly(PFPA) for PPM experiments was synthesized in multiple batches with varying reaction times and temperatures. PFPA (6.27 g, 26.33 mmol, 50.0 eq), CPDT (184 mg, 0.531 mmol, 1.00 eq), and AIBN (19.5 mg, 0.118 mmol, 0.02 eq) were placed in a 50 mL round bottom flask and dissolved in 25 mL anhydrous anisole. The reaction mixture was degassed by purging with nitrogen gas for 15 min before heating to 80 – 90 °C for 8 h – 3 d under stirring. The reaction was stopped by exposure to air and cooling to a.t. Poly(PFPA) was obtained after precipitation after threefold precipitation

with MeOH from THF, centrifugation, and drying in vacuum at 40 °C. poly(PFPA) were obtained in the form of a yellow solid (yield varied from 39 – 82 %).

^{19}F NMR (57 MHz, $CDCl_3$) δ (ppm) = -155.0 – -156.5 (*m*, 2 F, *ortho*-F), -161.5 (*m*, 1 F, *para*-F), -166.5 (*m*, 2 F, *meta*-F).

ATR FT-IR: ν (cm^{-1}) = 1781 *w*, 1656 *vw*, 1515 *vs*, 1473 *vw*, 1451 *vw*, 1387 *vw br*, 1225 *vw br*, 1079 *w br*, 1077 *w*, 987 *vs*, 884 *vw*, 856 *vw*, 783 *vw*, 757 *vw*, 720 *vw*, 621 *vw*.

5.3.2.19 poly(TFBAAm-*r*-TFMBAAm)

2.00 g poly(PFPA) were dissolved in 20 mL anhydrous DMF and loaded to syringe pump 1. 1.02 g 3,4,5-trifluorobenzylamine (6.30 mmol) and 1.10 g 4-(trifluoromethyl)benzylamine (6.30 mmol) were separately dissolved in 15 mL anhydrous DMF and the solutions were loaded to syringe pumps 2 and 3, respectively. The 3D-printed metal flow reactor was heated to 70 °C and dosing of the syringe pumps was started (flow rates, refer to **Figure 63**). After each flow rate change, a total of 4 mL was passed through the system before 4 mL of sample were collected. The polymers were isolated by precipitation in cold methanol, followed by centrifugation and drying in vacuum at 40 °C for 18 hours.

^{19}F NMR (376 MHz, $CDCl_3$) δ (ppm) = -61.2 (*s*, 3 F, CF_3), -135.5 (*m*, 2 F, *meta*-F), -164.6 (*s*, 1 F, *para*-F).

ATR FT-IR: ν (cm^{-1}) = 3304 v*w br*, 3062 *w*, 2964 v*w br*, 2871 *w*, 2932 *vw br*, 2869 *vw*, 1643 *m br*, 1513 *vs*, 1454 *w*, 1337 w, 1231 *w br*, 1079 *vw br*, 1013 *w*, 995 *m*, 979 *m*, 907 *vw*, 823 *vw*, 722 *w*, 698 *m*. IR intensities are given for polymers with a 50:50 modification ratio between TFBA and TFMBA as they vary with the amount of the respective functional group.

5.3.2.20 poly(NBMAAm-*r*-BAAm)

2.00 g poly(PFPA) were dissolved in 20 mL anhydrous DMF and loaded to syringe pump 1. 776 mg norbornenyl methylamine (6.30 mmol) and 675 mg benzylamine (6.30 mmol) were separately dissolved in 15 mL anhydrous DMAc and the solutions were loaded to syringe pumps 2 and 3, respectively. The 3D-printed metal flow reactor was heated to 70 °C and dosing of the syringe pumps was started (flow rates, refer to

Figure 63). After each flow rate change, a total of 4 mL was passed through the system before 4 mL of sample were collected. The polymers were isolated by precipitation in cold methanol, followed by centrifugation and drying in vacuum at 40 °C for 18 hours.

ATR FT-IR: ν (cm^{-1}) = 3296 *vw br*, 3061 *vw br*, 3032 *vw br*, 2962 *vw br*, 2936 *vw br*, 2869 *vw br*, 1781 *vw br*, 1633 *w br*, 1532 *w*, 1512 *vs*, 1454 *vw*, 1357 *vw*, 1338 *vw*, 1312 *vw*, 1253 *vw br*, 1231 *vw br*, 1190 *vw*, 1081 *vw*, 1013 *w*, 994 *w*, 979 *w*, 932 *vw*, 907 *vw*, 823 *vw br*, 788 *vw*, 721 *w br*, 698 *w*, 606 *vw*, 559 *vw*. IR intensities are given for polymers with a 50:50 modification ratio between NBMA and BA as they vary with the amount of the respective functional group.

5.3.2.21 Synthesis of poly(PFSty) in continuous flow

The automated flow reactor platform for the continuous polymerization of PFSty was located at the Monash University in Melbourne, Australia. In a 25 mL round bottom flask, PFSty (7.50 g, 38.64 mmol, 50.0 eq), RAFT-agent (1.00 eq), and AIBN (25 mg, 0.16 mmol, 0.02 eq) were dissolved in 18.5 mL anhydrous DMF. Investigated RAFT-agents were CPDT, CDCTPA, DoPAT, and CBCDMPC. The reaction mixture was degassed by purging with argon gas for 15 min. The mixture was loaded to a gastight 50 mL syringe and attached to the syringe pump of the flow setup. The reactor was heated to 70 °C – 100 °C and the Python™ script was started. Flowrates were 0.5, 0.25, 0.125, 0.0625 or 0.0333 mL min^{-1} which resembled a residence times of 4, 8, 16, 32, and 60 minutes, respectively. The transient volumes exiting the heated reactor were automatically incrementally analyzed by inline NMR and online SEC.

5.3.2.22 Synthesis of poly(PFSty) in batch

Poly(PFSty) for PPM experiments was synthesized in batch by dissolving PFSty (10.00 g, 51.52 mmol, 50.0 eq), CPDT (356 mg, 1.03 mmol, 1.00 eq), and AIBN (34 mg, 0.21 mmol, 0.02 eq) in 24.7 mL anhydrous DMF in a 50 mL round bottom flask. The reaction mixture was degassed by purging with argon gas for 15 min before heating to 85 °C for 3 d under stirring. The reaction was stopped by exposure to air and cooling to a.t. Poly(PFSty) was obtained after precipitation after threefold precipitation with MeOH from THF, centrifugation, and drying in vacuum at 40 °C. poly(PFSty) was obtained in the form of a yellow solid (yield: 87 %).

^{19}F NMR (376 MHz, $CDCl_3$) δ (ppm) = -140.0 – -145.0 (*m*, 2 F, *ortho*-F), -157.0 (*s*, 1 F, *para*-F), -163.5 (s, 2 F, *meta*-F).

ATR FT-IR: ν (cm^{-1}) = 2943 *vw br*, 2872 *vw br*, 1680 *w*, 1654 *vw*, 1520 *m*, 1495 *vs*, 1459 *w*, 1418 *vw*, 1386 *vw*, 1364 *vw br*, 1302 *vw*, 1260 *vw br*, 1222 *vw br*, 1130 *vw br*, 1087 *w br*, 979 *w*, 959 *m*, 867 *w br*, 765 *vw*, 737 *vw*, 659 *vw*.

SEC (THF, 35 °C, Calibration: PS): M_n = 8130 g mol^{-1}, M_w = 8450 g mol^{-1}, $Đ$ = 1.04.

5.3.2.23 Synthesis of poly(FBM-*r*-TFBM) in continuous flow

Four solutions of reactants were prepared: 1. Poly(PFSty) (3.00 g, 15.5 mmol PFSty) in 30 mL EtOAc, 2. 3.92 g DBU (25.8 mmol) in 25 mL EtOAc, 3. 1.47 g FBM (10.3 mmol) in 10 mL EtOAc, 4. 1.98 g TFBM (10.3 mmol) in 10 mL EtOAc. The solutions were transferred to gastight syringe pumps and the dosing was started with flow rates according to the desired ratio of modification (refer to **Figure 87**). The flow reactor was equilibrated by constant dosing for 3 minutes before 25 minutes of sample collection for each product composition. After each sample collection, the flow rate of pumps 3 and 4 were adjusted to match the new desired ratio of modification of the next sample. The obtained samples were rested at a.t. for 1 h before precipitation with H_2O/MeOH (1:1 v/v). The polymers were centrifuged and dried in vacuum at 40 °C for 18 h.

^{19}F NMR (376 MHz, $CDCl_3$) δ (ppm) = -62.7 (*s*, 3 F, CF_3), -114.8 (*br m*, 1 F, *para*-F), -133.2 (*br m*, 2 F, *ortho*-F), -142.8 (*br m*, 2 F, *meta*-F).

ATR FT-IR: ν (cm^{-1}) = 2933 *vw br*, 2868 *vw br*, 1642 *vw br*, 1619 *vw*, 1510 *w*, 1471 *s*, 1456 *m*, 1417 *vw*, 1365 *vw*, 1321 *vs*, 1261 *vw*, 1227 *w*, 1164 *m*, 1120 *s*, 1106 *s*, 1066 *vs*, 1014 *w*, 949 *m*, 891 *vw*, 822 *m br*, 752 *vw*, 671 *vw br*, 618 *w*, 590 *vw*, 531 *vw*.

5.3.2.24 Synthesis of poly(FBM-*r*-TFBM) with RLH

Three solutions of reactants were prepared: 1. Poly(PFSty) (1.30 g, 6.70 mmol PFSty) in 10 mL EtOAc, 2. 1.19 g FBM (8.37 mmol) in 5 mL EtOAc, 3. 1.61 g TFBM (8.38 mmol) in 5 mL EtOAc. Each solution was transferred to a reservoir container placed in the perimeter of the *opentrons OT-2* RLH. 20.0 g DBU were added to another reservoir without solvent. A Python™ script defined the volumes of each reactant and the position of the target well for mixing. First, poly(PFSty) was added to each well.

Then FBM and TFBM were added subsequently in the amounts resembling the desired ratio of modification. In the last dosing step, DBU was added to each well and the contents were mixed by consecutive aspiration and dispensing. Each polymer composition was created five times in order to maximize yield (refer to **Figure 88**). The wells were rested at a.t. for 1 h and wells with the same composition were combined before precipitation with H_2O/MeOH (1:1 v/v). The polymers were centrifuged and dried in vacuum at 40 °C for 18 h.

^{19}F NMR (376 MHz, $CDCl_3$) δ (ppm) = -62.7 (*s*, 3 F, CF_3), -114.2 (*br m*, 1 F, *para*-F), -133.8 (*br m*, 2 F, *ortho*-F), -142.8 (*br m*, 2 F, *meta*-F).

ATR FT-IR: ν (cm^{-1}) = 2937 *vw br*, 2872 *vw br*, 1639 *vw*, 1618 *vw*, 1509 *w*, 1471 *vs*, 1456 *s*, 1416 *w*, 1362 *vw*, 1322 *vs*, 1260 *w*, 1224 *w*, 1159 *m*, 1123 *s*, 1107 *m*, 1066 *vs*, 1018 *w*, 948 *s*, 890 *vw*, 822 *s br*, 753 *vw*, 658 *vw br*, 618 *w*, 590 *vw*, 529 *vw*.

5.3.2.25 Synthesis of poly(S-*r*-NB-FBAm-*r*-TFMBAm) and poly(S-*r*-NB-NBMAm-*r*-BAm) in continuous flow

The PPM of poly(S-*r*-NB-PFPE) was done using the same procedure and setup as for the synthesis of poly(TFBAAm-*r*-TFMBAAm) and poly(NBMAAm-*r*-BAAm) (refer to **Chapters 5.3.2.19** poly(TFBAAm-r-TFMBAAm) and **5.3.2.20** poly(NBMAAm-r-BAAm)). For poly(S-*r*-NB-FBAm-*r*-TFMBAm) 2.5 g poly(S-*r*-NB-PFPE) (4.11 mmol NB-PFPE) were dissolved in 40 mL anhydrous THF. 258 mg FBA (2.06 mmol) and 361 mg TFMBA (2.06 mmol) were dissolved in 25 mL anhydrous THF respectively and the three solutions were loaded to the syringe pumps. The 3D-printed flow reactor was kept at a.t. and dosing was started. After each flow rate change, a total of 4 mL was passed through the system before 4 mL of sample were collected. The polymers were isolated by precipitation in cold petrol ether, followed by centrifugation and drying in vacuum at 40 °C for 18 hours.

^{19}F NMR (376 MHz, $CDCl_3$) δ (ppm) = -62.9 (*s*, 3 F, CF_3), -117.7 (*s*, 1 F, *para*-F).

ATR FT-IR: ν (cm^{-1}) = 3296 *vw br*, 3077 *vw br*, 2957 *vw br*, 2877 *vw br*, 1646 *w br*, 1532 *m*, 1513 *vs*, 1464 *vw*, 1447 *vw*, 1418 *vw*, 1354 *vw*, 1325 *m*, 1225 *w*, 1158 *w*, 1124 *w*, 1067 *w*, 1014 *m*, 994 *m*, 978 *s*, 886 *vw br*, 850 *vw br*, 810 *vw*. IR intensities

are given for polymers with a 50:50 modification ratio between FBA and TFMBA as they vary with the amount of the respective functional group.

For poly(S-*r*-NB-NBMAm-*r*-BAm) the procedure was the same, only TFBA was replaced with 254 mg NBMA (2.06 mmol) and TFMBA was replaced with 221 mg BA (2.06 mmol).

ATR FT-IR: ν (cm^{-1}) = 3299 vw br, 3061 vw br, 3030 vw, 2960 vw br, 2870 vw br, 1642 w br, 1532 m, 1513 vs, 1453 vw, 1344 vw br, 1302 vw, 1237 vw br, 1187 vw, 1158 vw, 1133 vw, 1052 vw, 1013 m, 994 m, 978 s, 887 vw, 720 w br, 697 w br. IR intensities are given for polymers with a 50:50 modification ratio between NBMA and BA as they vary with the amount of the respective functional group.

List of Publications

Publications within this Dissertation

[3] A. P. Grimm, S. T. Knox, C. Y. P. Wilding, H. A. Jones, B. Schmidt, O. Piskljonow, D. Voll, C. W. Schmitt, N. J. Warren, P. Théato, A Versatile Flow Reactor Platform for Machine Learning Guided RAFT Synthesis and Amidation of Poly(pentafluorophenyl acrylate), *Macromol. Rapid Commun.* **2025**, 2500264.

[2] A. P. Grimm, B. Deng, S. V. Haridas, D. Voll, C. W. Schmitt, M. von Delius, F. Scheiba, P. Théato, Inverse vulcanization of all-*cis*-fluorinated cyclohexylacrylate: Tailored polymers for Li-S battery cathode materials, *Europ. Polym. J.* **2025**, 113815.

[1] A. P. Grimm, M. Plank, A. Stihl, C. W. Schmitt, D. Voll, F. H. Schacher, J. Lahann, P. Théato, Inverse Vulcanization of Activated Norbornenyl Esters – A Versatile Platform for Functional Sulfur Polymers, *Angew. Chem. Int. Ed.* **2024**, e202411010.

Other Publications

[4] D. Döpping, A. Buchheit, X. Liu, A. Goecke, A. P. Grimm, D. Voll, M. Wilhelm, M. Finsterbusch, G. Brunklaus, P. Théato, Versatile Solvent-free Synthesis of Composite Polymer Electrolytes for Thin High Performance Solid-State Lithium Metal Batteries, *Small* **2025**, *in revison*.

[3] B. Deng, F. Scheiba, A. Zuo, S. Indris, H. Li, H. Radinger, A. P. Grimm, C. Njel, Sulfur Distribution Analysis in Lithium−Sulfur Cathode via Confined Inverse Vulcanization in Carbon Frameworks, *Adv. Energy Mater.* **2024**, 2402996.

[2] A. P. Grimm, J. M. Scheiger, P. W. Roesky, P. Théato, Inverse vulcanization of trimethoxyvinylsilane particles, *Polym. Chem.* **2022**, 13, 5852.

[1] J. M. Scheiger, M. Hoffmann, P. Falkenstein, Z. Wang, M. Rutschmann, V. W. Scheiger, A. P. Grimm, K. Urbschat, T. Sengpiel, J. Matysik, M. Wilhelm, P. A. Levkin, P. Théato, Inverse Vulcanization of Norbornenylsilanes: Soluble Polymers with Controllable Molecular Properties via Siloxane Bonds, *Angew. Chem. Int. Ed.* **2022**, e202114896.

Acknowledgement / Danksagung

An dieser Stelle möchte ich mir die Zeit nehmen allen zu danken die mich auf der Reise dieser Promotion und darüber hinaus begleitet und mir ermöglicht haben diese Arbeit anzufertigen. Jetzt nachdem die Arbeit getan und geschrieben ist blicke ich zurück und bin sehr dankbar für all diejenigen Menschen in meinem Leben die dazu beigetragen haben, direkt oder indirekt, dass diese letzten Jahre wirklich Spaß gemacht haben und auch erfolgreich waren.

At this point I would like to take the time to thank everyone who accompanied me during the journey of this PhD and beyond and who made it possible to write this thesis. Now that the work is done and the thesis is written, I look back and feel very grateful for each and every person in my life that, directly or indirectly, made these last years so fun and successful.

Zuerst gilt mein großer Dank PROF. DR. PATRICK THÉATO dafür, dass ich nicht nur Vertiefer- und Masterarbeit, sondern auch diese Doktorarbeit unter seiner Ägide anfertigen durfte. Vielen Dank für das Vertrauen in meine ganzen Ideen und die Chance sie auch alle so frei auszuprobieren und umzusetzten. Besonders bedanken möchtige ich mich für die Unterstützung bei der Verwirklichung meiner diversen Auslandsaufenthalte in UK und Australien, welche definitiv zu den Highlights meiner Promotion gehören.

Im Zuge dessen bedanke ich mich ebenfalls bei PROF. DR. PETER W. ROESKY. Nicht nur für die freundliche Übernahme des Koreferats dieser Arbeit, sondern auch für die Betreuung meiner Bachelorarbeit vor all diesen Jahren.

I would like to thank all my colleagues and co-authors from outside the Théato research group for the thoroughly pleasant and successful collaboration in the realization of my scientific projects and ideas:

- ANDREAS STIHL *and* PROF. DR. FELIX H. SCHACHER *from the Friedrich-Schiller-University Jena.*

- DR. SHYAMKUMAR V. HARIDAS *and* PROF. DR. MAX VON DELIUS *from the University of Ulm*.

- PROF. DR. PETER W. ROESKY, DR. MARTINA PLANK, PROF. DR. JÖRG LAHANN, DR. BIJIAN DENG, *and* DR. FRIEDER SCHEIBA *from KIT*.

It is one thing to have a synthetic idea but actually doing, analyzing, and publishing it is a whole other thing that requires help and collaboration. I thank you all for your time, effort, and trust put in me during my PhD.

Für die unermüdliche organisatorische und bürokratische Unterstützung der letzten Jahre möchte ich mich bei BÄRBEL SEUFERT-DAUSMANN, BIRGIT HUBER, KATHARINA KUPPINGER, KLARA M. URBSCHAT, MARTINA RITTER, und SASKIA BLOCK bedanken.

Bei DR. CHRISTIAN W. SCHMITT und DR. DOMINIK VOLL bedanke ich mich für die ständige Unterstützung und Betreuung meiner Arbeit und Projekte der letzten Jahre. Ihr gabt mir stets das Gefühl einen guten Job zu machen und dafür bin ich sehr dankbar.

I thank PROF. DR. NICHOLAS J. WARREN *and his research group from the University of Leeds (now Sheffield) for the nice research collaboration but most importantly for hosting me for two visits to the UK. I would like to especially thank* DR. STEPHEN T. KNOX, DR. CLARISSA Y. P. WILDING, DR. JONATHAN GUILD, *and* HARRY A. JONES *for patiently introducing me into the field of flow chemistry and welcoming me in their group. Also thank you for all the tasty pints in the 'Library'.*

Ich bedanke mich beim *Karlsruhe House of Young Scientists* für die Förderung meines *Research Travel Grants* nach Australien. Ich bin sehr dankbar für die tolle Zeit in Melbourne und all die Erfahrungen und Freunde dich dort machen konnte.

With that said, from the bottom of my heart, I thank PROF. DR. TANJA JUNKERS *and the PRD group at Monash University in Australia for the great time I had during my research visit. Special thanks go to* AMNA B. ASGHAR, BO ZHANG, DR. GAYATHRI DEV, IGOR W. F. SILVA, K. LAKSHANI J. WEERARATHNA, KRITTIN THASUNTHORN, LACHLAN ALEXANDER, MENGYUAN "LILY" WEN, MIA HALL, SANDRA SMELTZER, DR. VIANNA JAFARI, *and* WEINIAN "WILL" WONG*. Thank you all for welcoming me with open arms and making my time in Australia truly unforgettable. I hope I could convince you that Germans can indeed be funny.*

At this point I would like to thank all the members of the Théato research group for the nice collaboration, working atmosphere, and scientific discussions. Science lives from discussion and exchange and many problems can be solved when shared with others. Together we are stronger and having a helping group goes a long way. With that in

mind I wish all the current PhD students, namely ALEKSANDRA ORLOVA*,* BJÖRN SCHMIDT*,* CORNELIUS "CORNY" HUB*,* JIAFENG WAN*,* LARS WESTENDARP*,* LUKAS KREUZER*,* SHIYI CHEN*,* T. T. THUY VU*, and* TONGTONG CUI *as well as all the postdocs/group leaders, namely* DR. CHRISTIAN W. SCHMITT*,* DR. DOMINIK VOLL*,* DR. HUIJING "MIA" LI*,* DR. SVEN SCHNEIDER*,* DR. TIMOFEY KOLESNIKOV*, and* DR. YOSUKE AKAE *the best of times for the future.*

Gesondert bedanke ich mich bei meiner HiWin OLGA PISKLJONOW für die tatkräftige Unterstützung im Labor. Danke fürs Säulen und NMR Röhrchen spülen :)

Ein ganz besonderer Dank gebührt meinem direkten Vertiefer- und Masterbetreuer DR. JOHANNES M. SCHEIGER. Du hast mich Selbstvertrauen und Selbstständigkeit im Labor gelehrt und wie man als Doktorand zurechtkommt und sich organisiert. Ich hatte großes Glück dich als Betreuer zu haben und hoffe, dass ich deine Lehren, die mich so weit gebracht haben, an nachfolgende Generationen von Studenten weitergeben konnte.

Ein großer (wenn nicht der größte) Dank geht an all die Freunde, und Familie, die mich die letzten Jahre tagtäglich begleitet haben. Auf viele weitere gemeinsame Jahre!

Zuallererst und von tiefstem Herzen bedanke ich mich beim KCU: BJÖRN SCHMIDT, CORNELIUS "CORNY" HUB, DANIEL A. DÖPPING, GIANNA JÄGER, JAKOB BECKER, KLARA M. URBSCHAT, DR. MORITZ KÖHLER, DR. NICO U. ZUBER, and DR. SVEN SCHNEIDER für all die lustigen Stories, Memes, und die gute Zeit, auch wenn es mal nervig oder schwierig wurde. Ohne euch wären die letzten Jahre nicht halb so unterhaltsam gewesen. Bleibt, wie ihr seid.

Mindestens genauso tief empfunden bedanke ich mich bei den lieben Freunden und Kollegen vom AK Wilhelm: ANIKA GOECKE, MAX G. SCHUßMANN, und TAMARA MEYER die sich allerdings viel zu gern mit einem Kaffee und Gelaber vom Arbeiten ablenken lassen. Sorry, not sorry. Die forschen zwar an ganz seltsamen ("interessanten") Sachen aber wer hätte gedacht, dass man unter Polymerphysikern so liebenswerte Menschen finden kann?

Man sagt im Studium knüpft man Freundschaften, die ein Leben lang halten können und ich bin geneigt dem zuzustimmen. Und weil ich es nicht darauf anlegen will bedanke ich mich an dieser Stelle bei denjenigen die vom ersten Lernbier am AKK im 1. Semester bis zur Fertigstellung dieser Doktorarbeit auf die eine oder andere Weise

an meiner Seite waren und mich begleitet haben: AMÉLIE MOREAU, JAN SCHIEFFER, JOSHUA BIEBERSTEIN, DR. LISA V. HIRSCH, und MARC MAURER. Danke für die tolle gemeinsame Zeit, ich denke immernoch gern an das Quali zurück.

Spezieller Dank gebührt LEONIE WILDERSINN, die immer ein offenes Ohr für mich hatte, wenn ich Rat brauchte, nicht weiterkam, oder einfach keine Motivation mehr fand.

Zum Schluss möchte ich den Leuten danken, die mich außerhalb der Universität schon länger unterstützen als ich mich zum Teil selbst erinnern kann.

Bei meinen Bandkollegen von FANCITY, BERIT GRASEMANN, MARKUS GÖRNERT, und MAXIMILIAN BODEN bedanke ich mich von ganzem Herzen für die jahrelange Freundschaft und Unterstützung. Als Gegengewicht zur wissenschaftlichen Laborarbeit war die musikalische Kreativität ein ungemein wertvoller Ausgleich und ich bin zutiefst dankbar für dieses Privileg und diese Freundschaft.

Des Weiteren gilt mein großer Dank meinen langjährigsten Freunden ANSELM DREHER, DAVID SCHREIBER, JANEK HERZOG, JULIA SCHWÄRZLER, KLARA HARMSEN, LAURA HEMMER, LUCA NOE, LUCA SESTAK, NICHOLAS B. C. ZÖRNER, NILS HANDT, TIM DUNKELBERG, TIM MÜNZINGER, und VANESSA FRANK welche seit meiner Schulzeit an meiner Seite sind und immer für mich da waren. Diesen Leuten verdanke ich wer ich heute bin und einen besseren moralischen Kompass und emotionalen Anker als euch kann ich mir nicht wünschen.

Zu guter Letzt gilt mein Dank meiner Familie. Meinen Eltern HARALD A. GRIMM und EVA SATKE sowie meiner Schwester ANNA S. GRIMM und meinem Schwager KEVIN B. ELSNER. Vielen Dank für die unerschütterliche Unterstützung und das nie endende Vertrauen, das ihr mir entgegenbringt. Ohne euch wäre das alles nicht möglich gewesen. Zu euch schaue ich mein Leben lang auf. Ihr seid meine Vorbilder. Danke für alles.

References

[1] W. J. Ripple, C. Wolf, J. W. Gregg, J. Rockström, M. E. Mann, N. Oreskes, T. M. Lenton, S. Rahmstorf, T. M. Newsome, C. Xu et al., *BioScience* **2024**.

[2] B. P. Grady, *J Surfact & Detergents* **2024**, *27*, 857.

[3] M. J. King, W. G. Davenport, M. S. Moats, *Sulfuric acid manufacture*. *Analysis, control, and optimization*, Elsevier, Amsterdam, **2013**.

[4] E. M. Błońska-Sikora, M. Klimek-Szczykutowicz, M. Michalak, K. Kulik-Siarek, M. Wrzosek, *Applied Sciences* **2024**, *14*, 6912.

[5] C. C. Boswell, D. K. Friesen, *Fertilizer Research* **1993**, *35*, 127.

[6] P. Pangamol, P. Sae-oui, C. Sirisinha, *Energy Procedia* **2014**, *56*, 474.

[7] D. Stirling, *The Sulfur Problem*. *Cleaning Up Industrial Feedstocks*, RSC, La Vergne, **2007**.

[8] W. J. Chung, J. J. Griebel, E. T. Kim, H. Yoon, A. G. Simmonds, H. J. Ji, P. T. Dirlam, R. S. Glass, J. J. Wie, N. A. Nguyen et al., *Nature chemistry* **2013**, *5*, 518.

[9] a) A. Alex, N. K. Singha, S. Choudhury, *Current Opinion in Electrochemistry* **2023**, *39*, 101271; b) P. T. Dirlam, A. G. Simmonds, T. S. Kleine, N. A. Nguyen, L. E. Anderson, A. O. Klever, A. Florian, P. J. Costanzo, P. Theato, M. E. Mackay et al., *RSC Adv.* **2015**, *5*, 24718.

[10] M. P. Crockett, A. M. Evans, M. J. H. Worthington, I. S. Albuquerque, A. D. Slattery, C. T. Gibson, J. A. Campbell, D. A. Lewis, G. J. L. Bernardes, J. M. Chalker, *Angewandte Chemie International Edition* **2016**, *55*, 1714.

[11] M. J. H. Worthington, R. L. Kucera, I. S. Albuquerque, C. T. Gibson, A. Sibley, A. D. Slattery, J. A. Campbell, S. F. K. Alboaiji, K. A. Muller, J. Young et al., *Chemistry (Weinheim an der Bergstrasse, Germany)* **2017**, *23*, 16219.

[12] A. Nayeem, M. F. Ali, J. H. Shariffuddin, *Environmental research* **2023**, *216*, 114306.

[13] J. J. Griebel, N. A. Nguyen, S. Namnabat, L. E. Anderson, R. S. Glass, R. A. Norwood, M. E. Mackay, K. Char, J. Pyun, *ACS Macro Lett.* **2015**, *4*, 862.

[14] D. J. Parker, S. T. Chong, T. Hasell, *RSC advances* **2018**, *8*, 27892.

[15] S. J. Tonkin, C. T. Gibson, J. A. Campbell, D. A. Lewis, A. Karton, T. Hasell, J. M. Chalker, *Chemical science* **2020**, *11*, 5537.

[16] J. J. Griebel, S. Namnabat, E. T. Kim, R. Himmelhuber, D. H. Moronta, W. J. Chung, A. G. Simmonds, K.-J. Kim, J. van der Laan, N. A. Nguyen et al., *Adv. Mater.* **2014**, *26*, 3014.

[17] T. Lee, P. T. Dirlam, J. T. Njardarson, R. S. Glass, J. Pyun, *Journal of the American Chemical Society* **2022**, *144*, 5.

[18] C. King‐Poole, H. Thérien‐Aubin, *Adv Funct Materials* **2024**.

[19] J. M. Chalker, M. J. H. Worthington, N. A. Lundquist, L. J. Esdaile, *Topics in current chemistry (Cham)* **2019**, *377*, 16.

[20] J. Bao, K. P. Martin, E. Cho, K.-S. Kang, R. S. Glass, V. Coropceanu, J.-L. Bredas, W. O. Parker, J. T. Njardarson, J. Pyun, *J. Am. Chem. Soc.* **2023**, *145*, 12386.

[21] a) V. K. Shankarayya Wadi, K. K. Jena, S. Z. Khawaja, K. Yannakopoulou, M. Fardis, G. Mitrikas, M. Karagianni, G. Papavassiliou, S. M. Alhassan, *ACS omega* **2018**, *3*, 3330; b) B. Zheng, L. Zhong, X. Wang, P. Lin, Z. Yang, T. Bai, H. Shen, H. Zhang, *Nat Commun* **2024**, *15*, 5507.

[22] A. S. M. Ghumman, M. M. Nasef, M. R. Shamsuddin, A. Abbasi, *Polymers and Polymer Composites* **2021**, *29*, 1333.

[23] H. Shen, B. Zheng, H. Zhang, *Polymer Reviews* **2024**, 1.

[24] J. M. Scheiger, M. Hoffmann, P. Falkenstein, Z. Wang, M. Rutschmann, V. W. Scheiger, A. Grimm, K. Urbschat, T. Sengpiel, J. Matysik et al., *Angew. Chem.* **2022**.

[25] A. P. Grimm, M. Plank, A. Stihl, C. W. Schmitt, D. Voll, F. H. Schacher, J. Lahann, P. Theato, *Angewandte Chemie International Edition* **2024**.

[26] I. Gomez, A. F. de Anastro, O. Leonet, J. A. Blazquez, H.-J. Grande, J. Pyun, D. Mecerreyes, *Macromol. Rapid Commun.* **2018**, *39*, e1800529.

[27] C. P. Ambulo, K. J. Carothers, A. Hollis, H. N. Limberg, L. Sun, C. J. Thrasher, M. E. McConney, N. P. Godman, *Macromol. Rapid Commun.* **2023**, e2200798.

[28] N. Q. Tufts, N. C. Chiu, E. N. Musa, T. C. Gallagher, D. B. Fast, K. C. Stylianou, *Chemistry (Weinheim an der Bergstrasse, Germany)* **2023**, e202203177.

[29] K.-S. Kang, A. Phan, C. Olikagu, T. Lee, D. A. Loy, M. Kwon, H. Paik, S. J. Hong, J. Bang, W. O. Parker et al., *Angewandte Chemie Intl Edit* **2021**, *60*, 22900.

[30] J. J. Griebel, N. A. Nguyen, A. V. Astashkin, R. S. Glass, M. E. Mackay, K. Char, J. Pyun, *ACS Macro Lett.* **2014**, *3*, 1258.

[31] D. Wang, Z. Tang, R. Huang, H. Li, C. Zhang, B. Guo, *Macromolecules* **2022**.

[32] A. Laybourn, K. Robertson, A. G. Slater, *J. Am. Chem. Soc.* **2023**.

[33] P. A. Beaucage, D. R. Sutherland, T. B. Martin, *Macromolecules* **2024**.

[34] N. Zaquen, M. Rubens, N. Corrigan, J. Xu, P. B. Zetterlund, C. Boyer, T. Junkers, *Progress in Polymer Science* **2020**, *107*, 101256.

[35] S. T. Knox, N. J. Warren, *React. Chem. Eng.* **2020**, *5*, 405.

[36] a) J. H. Vrijsen, I. A. Thomlinson, M. E. Levere, C. L. Lyall, M. G. Davidson, U. Hintermair, T. Junkers, *Polym. Chem.* **2020**, *11*, 3546; b) B. Zhang, A. Mathoor, T. Junkers, *Angewandte Chemie International Edition* **2023**, e202308838; c) P.-J. Voorter, M. Wagner, C. Rosenauer, J. Dai, P. Subramanian, A. I. McKay, N. R. Cameron, J. Michels, T. Junkers, *Polym. Chem.* **2023**.

[37] J. van Herck, T. Junkers, *Chemistry Methods* **2022**, *2*.

[38] J. van Herck, I. Abeysekera, A.-L. Buckinx, K. Cai, J. Hooker, K. Thakur, E. van de Reydt, P.-J. Voorter, D. Wyers, T. Junkers, *Digital Discovery* **2022**, *1*, 519.

[39] T. Junkers, J. P. Hooker, J. van Herck, A. Kumar, G. D. Ammini, *Polym. Chem.* **2023**.

[40] a) S. Parkinson, S. T. Knox, R. A. Bourne, N. J. Warren, *Polym. Chem.* **2020**, *11*, 3465; b) P. M. Pittaway, S. T. Knox, G. Ghasemi, O. J. Cayre, N. Kapur, N. J. Warren, *React. Chem. Eng.* **2023**; c) J. D. Guild, S. T. Knox, S. B. Burholt, E. M. Hilton, N. J. Terrill, S. L. M. Schroeder, N. J. Warren, *Macromolecules* **2023**, *56*, 6426; d) M.-N. Antonopoulou, R. Whitfield, N. P. Truong, D. Wyers, S. Harrisson, T. Junkers, A. Anastasaki, *Nature chemistry* **2021**.

[41] C. Y. P. Wilding, S. T. Knox, R. A. Bourne, N. J. Warren, *Macromolecules* **2023**.

[42] A.-L. Buckinx, M. Rubens, N. R. Cameron, C. Bakkali-Hassani, A. Sokolova, T. Junkers, *Polym. Chem.* **2022**, *13*, 3444.

[43] J. T. Brosnan, M. E. Brosnan, *The Journal of nutrition* **2006**, *136*, 1636S-1640S.

[44] T. B. Nguyen, *Adv. Synth. Catal.* **2017**, *359*, 1066.

[45] D. A. Boyd, *Angewandte Chemie International Edition* **2016**, *55*, 15486.

[46] W. M. Haynes, *CRC Handbook of Chemistry and Physics*, CRC Press, **2014**.

[47] A. F. Holleman, N. Wiberg, E. Wiberg, *Lehrbuch der anorganischen Chemie*, de Gruyter, Berlin, **2007**.

[48] Y. Ingenbleek, H. Kimura, *Nutrition reviews* **2013**, *71*, 413.

[49] G. Kutney, *Sulfur*. *History, Technology, Applications and Industry*, ChemTec Publishing, Toronto, **2023**.

[50] J. J. Griebel, R. S. Glass, K. Char, J. Pyun, *Progress in Polymer Science* **2016**, *58*, 90.

[51] J. Likus-Cieślik, M. Pietrzykowski, *TOBIOTJ* **2021**, *15*, 82.

[52] a) J. S. Eow, *Environ. Prog.* **2002**, *21*, 143; b) M. K. Awasthi, A. Amobonye, P. Bhagwat, V. Ashokkumar, S. C. Gowd, A. M. Dregulo, K. Rajendran, G. Flora, V. Kumar, S. Pillai et al., *The Science of the total environment* **2024**, *914*, 169857.

[53] E. Riedel, C. Janiak, *Anorganische Chemie*, de Gruyter, Berlin, Boston, **2015**.

[54] T. K. Birkham, M. J. Hendry, S. L. Barbour, J. R. Lawrence, *Journal of environmental quality* **2010**, *39*, 834.

[55] a) J. Lim, J. Pyun, K. Char, *Angewandte Chemie International Edition* **2015**, *54*, 3249; b) M. J. H. Worthington, R. L. Kucera, J. M. Chalker, *Green Chem.* **2017**, *19*, 2748.

[56] X. Wu, J. A. Smith, S. Petcher, B. Zhang, D. J. Parker, J. M. Griffin, T. Hasell, *Nature communications* **2019**, *10*, 647.

[57] R. Steudel, D. Scheschkewitz, *Chemistry of the non-metals*. *Syntheses - structures - bonding - applications*, de Gruyter, Berlin, Boston, **2020**.

[58] L. Crapanzano, W. A. Crichton, G. Monaco, R. Bellissent, M. Mezouar, *Nature materials* **2005**, *4*, 550.

[59] G. K. Ahluwalia, *Applications of Chalcogenides: S, Se, and Te*, Springer International Publishing, Cham, **2017**.

[60] S. Shi, Y. Li, Z. Cui, Y. Yan, X. Zhang, J. Tang, S. Xiao, *Chemical Engineering Journal* **2023**, *470*, 144166.

[61] A. J. Findlay, A. Kamyshny, *Frontiers in microbiology* **2017**, *8*, 2551.

[62] a) A. Garcia-Fuentes, S. Wirtz, E. Vos, H. Verhagen, *EJNFS* **2015**, *5*, 113; b) J. R. Elphick, M. Davies, G. Gilron, E. C. Canaria, B. Lo, H. C. Bailey, *Environmental toxicology and chemistry* **2011**, *30*, 247.

[63] in *The IUPAC Compendium of Chemical Terminology* (Eds.: V. Gold, A. McNaught), International Union of Pure and Applied Chemistry (IUPAC), Research Triangle Park, NC, **2025**.

[64] R. Amna, S. M. Alhassan, *ACS Appl. Polym. Mater.* **2024**, *6*, 4350.

[65] D. Vietti, M. Scherrer in *A John Wiley & Sons, Inc., publication* (Eds.: J. I. Kroschwitz, R. E. Kirk, D. F. Othmer, A. Seidel), Wiley-Interscience, Hoboken, NJ, **2004**.

[66] A. M. Usmani, *Polymer-Plastics Technology and Engineering* **1982**, *19*, 165.

[67] A. Pirayesh, M. Salami-Kalajahi, H. Roghani-Mamaqani, F. Najafi, *Polymer Reviews* **2019**, *59*, 124.

[68] a) R. Martin, A. Rekondo, A. R. de Luzuriaga, P. Casuso, D. Dupin, G. Cabañero, H. J. Grande, I. Odriozola, *Smart Mater. Struct.* **2016**, *25*, 84017; b) J. Canadell, H. Goossens, B. Klumperman, *Macromolecules* **2011**, *44*, 2536; c) D. Y. Wu, S. Meure, D. Solomon, *Progress in Polymer Science* **2008**, *33*, 479.

[69] a) O. Daglar, E. Cakmakci, U. S. Gunay, G. Hizal, U. Tunca, H. Durmaz, *Macromolecules* **2020**, *53*, 2965; b) D. Dong, Y. Zhu, W. Fang, J. Jin, *Macromolecules* **2023**, *56*, 7132; c) Y. Imai, K. Yamanaka, H. Ishikawa, M. Kakimoto, *Macromol. Chem. Phys.* **1999**, *200*, 95.

[70] A. L. Baron, D. R. Blank, *Makromol. Chem.* **1970**, *140*, 83.

[71] a) S. Matsumura, N. Kihara, T. Takata, *J. Appl. Polym. Sci.* **2004**, *92*, 1869; b) S. Seesukphronrarak, S. Kawasaki, K. Kobori, T. Takata, *J. Polym. Sci. A Polym. Chem.* **2007**, *45*, 3073.

[72] L. Infante Teixeira, K. Landfester, H. Thérien-Aubin, *Macromolecules* **2021**, *54*, 3659.

[73] a) E. Klein, P. D. May, J. K. Smith, N. Leger, *Biopolymers* **1971**, *10*, 647; b) K. Imai, T. Shiomi, Y. Tezuka, M. Satoh, *Makromol. Chem., Rapid Commun.* **1985**, *6*, 413.

[74] T. Oyama, J. Ozaki, Y. Chujo, *Polymer Bulletin* **1997**, *38*, 379.

[75] T. Oyama, J. Ozaki, Y. Chujo, *Polymer Bulletin* **1998**, *40*, 503.

[76] T. Oyama, Y. Chujo, *Macromolecules* **1999**, *32*, 7732.

[77] a) H. A. Vogel, *J. Polym. Sci. A-1 Polym. Chem.* **1970**, *8*, 2035; b) M. D. Lechner, *Makromolekulare Chemie*. *Ein Lehrbuch für Chemiker, Physiker, Materialwissenschaftler und Verfahrenstechniker*, Birkhäuser Basel, Basel, **2010**.

[78] J. Black, *Handbook of Biomaterial Properties*, Springer, New York, NY, **1998**.

[79] A. Kausar, S. Zulfiqar, M. I. Sarwar, *Polymer Reviews* **2014**, *54*, 185.

[80] a) Y. Xie, Di Liu, A. Ringuette, J. Pang, H. Mutlu, D. Voll, P. Théato, *ACS Appl. Energy Mater.* **2023**, *6*, 564; b) Y. Xie, Di Liu, A. Ringuette, P. Théato, *ACS Appl. Mater. Interfaces* **2023**, *15*, 24517.

[81] a) L. A. Estrada, J. J. Deininger, G. D. Kamenov, J. R. Reynolds, *ACS Macro Lett.* **2013**, *2*, 869; b) O. Niwa, T. Tamamura, *Synthetic Metals* **1987**, *20*, 235.

[82] K. Ogawa, J. Stafford, S. Rothstein, D. Tallman, S. Rasmussen, *Synthetic Metals* **2005**, *152*, 137.

[83] T. an Chen, R. D. Rieke, *J. Am. Chem. Soc.* **1992**, *114*, 10087.

[84] F. Martínez, J. Retuert, G. Neculqueo, H. Naarmann, *International Journal of Polymeric Materials* **1995**, *28*, 51.

[85] A. Facchetti, *Chem. Mater.* **2011**, *23*, 733.

[86] I. Osaka, R. D. McCullough, *Acc. Chem. Res.* **2008**, *41*, 1202.

[87] T. P. Kaloni, P. K. Giesbrecht, G. Schreckenbach, M. S. Freund, *Chem. Mater.* **2017**, *29*, 10248.

[88] G. Heywang, F. Jonas, *Adv. Mater.* **1992**, *4*, 116.

[89] M. R. Andersson, O. Thomas, W. Mammo, M. Svensson, M. Theander, O. Inganäs, *J. Mater. Chem.* **1999**, *9*, 1933.

[90] D. T. McQuade, A. E. Pullen, T. M. Swager, *Chem. Rev.* **2000**, *100*, 2537.

[91] L. V. Kayser, D. J. Lipomi, *Adv. Mater.* **2019**, *31*, e1806133.

[92] L. Groenendaal, F. Jonas, D. Freitag, H. Pielartzik, J. R. Reynolds, *Adv. Mater.* **2000**, *12*, 481.

[93] R. Gangopadhyay, B. Das, M. R. Molla, *RSC Adv* **2014**, *4*, 43912.

[94] H. R. Kricheldorf, G. Schwarz, *Journal of Macromolecular Science, Part A* **2007**, *44*, 625.

[95] in *The IUPAC Compendium of Chemical Terminology* (Eds.: V. Gold, A. McNaught), International Union of Pure and Applied Chemistry (IUPAC), Research Triangle Park, NC, **2025**.

[96] a) C. G. Overberger, J. K. Weise, *J. Am. Chem. Soc.* **1968**, *90*, 3533; b) H. Kikuchi, N. Tsubokawa, T. Endo, *Chemistry Letters* **2005**, *34*, 376.

[97] M. Kato, K. Toshima, S. Matsumura, *Biomacromolecules* **2005**, *6*, 2275.

[98] a) L. H. Tagle, F. R. Diaz, P. E. Riveros, *Polym J* **1986**, *18*, 501; b) C. Berti, A. Celli, E. Marianucci, *European Polymer Journal* **2002**, *38*, 1281.

[99] a) K. Soga, M. Sato, H. Imamura, S. Ikeda, *J. Polym. Sci. B Polym. Lett. Ed.* **1975**, *13*, 167; b) K. Soga, H. Imamura, M. Sato, S. Ikeda, *J. Polym. Sci. Polym. Chem. Ed.* **1976**, *14*, 677; c) B. OCHIAI, T. ENDO, *Progress in Polymer Science* **2005**, *30*, 183; d) T.-J. Yue, W.-M. Ren, Y. Liu, Z.-Q. Wan, X.-B. Lu, *Macromolecules* **2016**, *49*, 2971; e) W.-M. Ren, T.-J. Yue, M.-R. Li, Z.-Q. Wan, X.-B. Lu, *Macromolecules* **2017**, *50*, 63; f) J.-L. Yang, Y. Wang, X.-H. Cao, C.-J. Zhang, Z. Chen, X.-H. Zhang, *Macromol. Rapid Commun.* **2021**, *42*, e2000472; g) G. A. Bhat, D. J. Darensbourg in *Sulfur-containing polymers*. *From synthesis to functional materials* (Eds.: X.-H. Zhang, P. Théato), Wiley-VCH, Weinheim, **2021**, pp. 39–79.

[100] K. Nakano, G. Tatsumi, K. Nozaki, *J. Am. Chem. Soc.* **2007**, *129*, 15116.

[101] E. A. Castro, *Journal of Sulfur Chemistry* **2007**, *28*, 401.

[102] W. Walter, K.-D. Bode, *Angew. Chem. Int. Ed. Engl.* **1967**, *6*, 281.

[103] E. Dyer, D. W. Osborne, *J. Polym. Sci.* **1960**, *47*, 361.

[104] S. Perveen, A. Yasmin, K. M. Khan, *Natural product research* **2010**, *24*, 18.

[105] a) A. W. Woodhouse, A. Kocaarslan, J. A. Garden, H. Mutlu, *Macromol. Rapid Commun.* **2024**, *45*, e2400260; b) L. V. S. Ceneviva, M. Mierzati, Y. Miyahara, C. T. Nomura, S. Taguchi, H. Abe, T. Tsuge, *Bioengineering (Basel, Switzerland)* **2022**, *9*.

[106] J. A. Calzonetti, C. J. Laursen, *Rubber Chemistry and Technology* **2010**, *83*, 303.

[107] G. B. Kauffman, *Chem. Educator* **2001**, *6*, 50.

[108] S. Trautner, J. Lackner, W. Spendelhofer, N. Huber, J. D. Pedarnig, *Anal. Chem.* **2019**, *91*, 5200.

[109] J. J. Griebel, G. Li, R. S. Glass, K. Char, J. Pyun, *J. Polym. Sci. A Polym. Chem.* **2015**, *53*, 173.

[110] D. A. Boyd, C. C. Baker, J. D. Myers, V. Q. Nguyen, G. A. Drake, C. C. McClain, F. H. Kung, S. R. Bowman, W. Kim, J. S. Sanghera, *Chem. Commun.* **2016**, *53*, 259.

[111] Y. Zhang, K. M. Konopka, R. S. Glass, K. Char, J. Pyun, *Polym. Chem.* **2017**, *8*, 5167.

[112] F. Zhao, Y. Li, W. Feng, *Small Methods* **2018**, *2*, 1800156.

[113] L. J. Dodd, Ö. Omar, X. Wu, T. Hasell, *ACS Catal.* **2021**, *11*, 4441.

[114] I. Gomez, D. Mecerreyes, J. A. Blazquez, O. Leonet, H. Ben Youcef, C. Li, J. L. Gómez-Cámer, O. Bondarchuk, L. Rodriguez-Martinez, *Journal of Power Sources* **2016**, *329*, 72.

[115] E. T. Kim, W. J. Chung, J. Lim, P. Johe, R. S. Glass, J. Pyun, K. Char, *Polym. Chem.* **2014**, *5*, 3617.

[116] a) I. Gomez, O. Leonet, J. A. Blazquez, D. Mecerreyes, *ChemSusChem* **2016**, *9*, 3419; b) D. J. Parker, H. A. Jones, S. Petcher, L. Cervini, J. M. Griffin, R. Akhtar, T. Hasell, *J. Mater. Chem. A* **2017**, *5*, 11682.

[117] N. P. Tarasova, A. A. Zanin, E. G. Krivoborodov, Y. O. Mezhuev, *RSC advances* **2021**, *11*, 9008.

[118] J. M. Chalker, M. Mann, M. J. H. Worthington, L. J. Esdaile, *Organic Materials* **2021**, *03*, 362.

[119] A. P. Grimm, J. M. Scheiger, P. W. Roesky, P. Théato, *Polym. Chem.* **2022**.

[120] J. Jia, J. Liu, Z.-Q. Wang, T. Liu, P. Yan, X.-Q. Gong, C. Zhao, L. Chen, C. Miao, W. Zhao et al., *Nat. Chem.* **2022**.

[121] P. Yan, W. Zhao, F. McBride, D. Cai, J. Dale, V. Hanna, T. Hasell, *Nat Commun* **2022**, *13*.

[122] a) J. Rydz, W. Sikorska, M. Musioł, B. Zawidlak-Węgrzyńska, K. Duale in *Encyclopedia of Renewable and Sustainable Materials* (Ed.: I. A. Choudhury), Elsevier, San Diego, **2020**, pp. 274–284; b) P. B. V. Scholten, J. Cai, R. T. Mathers, *Macromol. Rapid Commun.* **2021**, *42*, e2000745; c) E. F. Fiandra, L. Shaw, M. Starck, C. J. McGurk, C. S. Mahon, *Chemical Society reviews* **2023**, *52*, 8085; d) N. T. Dintcheva, *Polymer* **2024**, *306*, 127136; e) A. Abbasi, M. M. Nasef, W. Z. N. Yahya, *Green Materials* **2020**, *8*, 172.

[123] Y. Deng, Z. Huang, B. L. Feringa, H. Tian, Q. Zhang, D.-H. Qu, *Nat Commun* **2024**, *15*.

[124] a) J. B. Huang, G. S. Zeng, X. S. Li, X. C. Cheng, H. Tong, *IOP Conf. Ser.: Earth Environ. Sci.* **2018**, *167*, 12029; b) R. Steudel, *Angew. Chem. Int. Ed. Engl.* **1975**, *14*, 655.

[125] Y. Xin, H. Peng, J. Xu, J. Zhang, *Adv Funct Materials* **2019**, *29*, 1808989.

[126] N. A. Lundquist, A. D. Tikoalu, M. J. H. Worthington, R. Shapter, S. J. Tonkin, F. Stojcevski, M. Mann, C. T. Gibson, J. R. Gascooke, A. Karton et al., *Chemistry (Weinheim an der Bergstrasse, Germany)* **2020**, *26*, 10035.

[127] a) Z. Sun, M. Xiao, S. Wang, D. Han, S. Song, G. Chen, Y. Meng, *J. Mater. Chem. A* **2014**, *2*, 9280; b) A. G. Simmonds, J. J. Griebel, J. Park, K. R. Kim, W. J. Chung, V. P. Oleshko, J. Kim, E. T. Kim, R. S. Glass, C. L. Soles et al., *ACS Macro Lett.* **2014**, *3*, 229; c) P. T. Dirlam, A. G. Simmonds, R. C. Shallcross, K. J. Arrington, W. J. Chung, J. J. Griebel, L. J. Hill, R. S. Glass, K. Char, J. Pyun, *ACS Macro Lett.* **2015**, *4*, 111; d) A. Hoefling, Y. J. Lee, P. Theato, *Macromol. Chem. Phys.* **2017**, *218*, 1600303; e) S. Diez, A. Hoefling, P. Theato, W. Pauer, *Polymers* **2017**, *9*; f) B. Deng, F. Scheiba, A. Zuo, S. Indris, H. Li, H. Radinger, A. Grimm, C. Njel, *Advanced Energy Materials* **2024**; g) S. Ren, P. Sang, W. Guo, Y. Fu, *Polym. Chem.* **2022**.

[128] A. Hoefling, D. T. Nguyen, Y. J. Lee, S.-W. Song, P. Theato, *Mater. Chem. Front.* **2017**, *1*, 1818.

[129] M. W. Thielke, L. A. Bultema, D. D. Brauer, B. Richter, M. Fischer, P. Theato, *Polymers* **2016**, *8*.

[130] a) L.-A. Ko, Y.-S. Huang, Y. A. Lin, *ACS Appl. Polym. Mater.* **2021**, *3*, 3363; b) N. A. Lundquist, M. J. H. Worthington, N. Adamson, C. T. Gibson, M. R. Johnston, A. V. Ellis, J. M. Chalker, *RSC advances* **2018**, *8*, 1232.

[131] J. M. Scheiger, C. Direksilp, P. Falkenstein, A. Welle, M. Koenig, S. Heissler, J. Matysik, P. A. Levkin, P. Theato, *Angewandte Chemie (International ed. in English)* **2020**, *59*, 18639.

[132] a) C. Herrera, K. J. Ysinga, C. L. Jenkins, *ACS Appl. Mater. Interfaces* **2019**, *11*, 35312; b) S.-J. Lee, G.-Y. Han, M.-B. Yi, J.-H. Back, H.-J. Kim, *Journal of Materials Research and Technology* **2024**, *29*, 1798; c) J. Fan, C. Ju, S. Fan, X. Li, Z. Zhang, N. Hadjichristidis, *Angew. Chem.* **2024**; d) Q. Chen, L. Xu, L. Zhu, L. Gao, J. Luo, X. Yang, Y. Fang, Z. Zhang, J. Dong, *ACS Appl. Polym. Mater.* **2024**.

[133] a) L. E. Anderson, T. S. Kleine, Y. Zhang, D. D. Phan, S. Namnabat, E. A. LaVilla, K. M. Konopka, L. Ruiz Diaz, M. S. Manchester, J. Schwiegerling et al., *ACS Macro Lett.* **2017**, *6*, 500; b) T. S. Kleine, T. Lee, K. J. Carothers, M. O. Hamilton, L. E. Anderson, L. Ruiz Diaz, N. P. Lyons, K. R. Coasey, W. O. Parker, L. Borghi et al., *Angewandte Chemie International Edition* **2019**, *58*, 17656; c) D. A. Boyd, V. Q. Nguyen, D. L. Rhonehouse, G. D. Chin, F. H. Kung, D. J. Gibson, R. R. Nicol, K. J. Ewing, W. Kim, J. S. Sanghera, *ACS Appl. Polym. Mater.* **2024**; d) J. M. Scheiger, P. Theato in *Sulfur-containing polymers*. *From synthesis to functional materials* (Eds.: X.-H. Zhang, P. Théato), Wiley-VCH, Weinheim, **2021**, pp. 305–338; e) S. J. Tonkin, N. Le Pham, J. R. Gascooke, M. R. Johnston, M. L. Coote, C. T. Gibson, J. M. Chalker, *Advanced Optical Materials* **2023**, *11*; f) J. Molineux, T. Lee, K. J. Kim, K.-S. Kang, N. P. Lyons, A. Nishant, T. S. Kleine, S. W. Durfee, J. Pyun, R. A. Norwood, *Advanced Optical Materials* **2024**, *12*.

[134] a) Z. Deng, A. Hoefling, P. Théato, K. Lienkamp, *Macromol. Chem. Phys.* **2018**, *219*, 1700497; b) J. A. Smith, R. Mulhall, S. Goodman, G. Fleming, H. Allison, R. Raval, T. Hasell, *ACS omega* **2020**, *5*, 5229; c) H. Shen, X. Chen, B. Zheng, H. Zhang, *ACS Appl. Polym. Mater.* **2024**, *6*, 14351.

[135] T. R. Martin, K. A. Mazzio, H. W. Hillhouse, C. K. Luscombe, *Chem. Commun.* **2015**, *51*, 11244.

[136] a) V. S. Wadi, K. K. Jena, S. Z. Khawaja, V. M. Ranagraj, S. M. Alhassan, *RSC advances* **2019**, *9*, 4397; b) A. M. Abraham, S. V. Kumar, S. M. Alhassan, *Chemical Engineering Journal* **2018**, *332*, 1; c) I. Bu Najmah, N. A. Lundquist, M. K. Stanfield, F. Stojcevski, J. A. Campbell, L. J. Esdaile, C. T. Gibson, D. A. Lewis, L. C. Henderson, T. Hasell et al., *ChemSusChem* **2021**, *14*, 2352.

[137] a) S. F. Valle, A. S. Giroto, R. Klaic, G. G. Guimarães, C. Ribeiro, *Polymer Degradation and Stability* **2019**, *162*, 102; b) M. Mann, J. E. Kruger, F. Andari, J. McErlean, J. R. Gascooke, J. A. Smith, M. J. H. Worthington, C. C. C. McKinley, J. A. Campbell, D. A. Lewis et al., *Organic & biomolecular chemistry* **2019**, *17*, 1929; c) A. S. M. Ghumman, R. Shamsuddin, R. Sabir, A. Waheed, A. Sami, H. Almohamadi, *RSC advances* **2023**, *13*, 7867.

[138] a) S. Penczek, M. Cypryk, J. Pretula, K. Kaluzynski, P. Lewinski, *Progress in Polymer Science* **2024**, *152*, 101818; b) J. Pyun, C. F. Carrozza, S. Silvano, L. Boggioni, S. Losio, A. R. de Angelis, W. O'Neil Parker Jr, *Journal of Polymer Science* **2022**.

[139] J. A. Smith, S. J. Green, S. Petcher, D. J. Parker, B. Zhang, M. J. H. Worthington, X. Wu, C. A. Kelly, T. Baker, C. T. Gibson et al., *Chemistry (Weinheim an der Bergstrasse, Germany)* **2019**, *25*, 10433.

[140] J. A. Smith, X. Wu, N. G. Berry, T. Hasell, *J. Polym. Sci. A Polym. Chem.* **2018**, *56*, 1777.

[141] K.-S. Kang, K. Iyer, J. Pyun, *Chemistry (Weinheim an der Bergstrasse, Germany)* **2022**.

[142] a) G. Moad, E. Rizzardo, S. H. Thang, *Acc. Chem. Res.* **2008**, *41*, 1133; b) P. Nesvadba, *Chimia* **2018**, *72*, 456.

[143] A. H. E. Müller, K. Matyjaszewski, *Controlled and living polymerizations*. *Methods and materials*, Wiley-VCH-Verl., Weinheim, **2009**.

[144] D.-Y. Yan, G.-F. Cai, *Journal of Macromolecular Science: Part A - Chemistry* **1986**, *23*, 37.

[145] B. Klumperman in *Encyclopedia of polymer science and technology* (Eds.: A. Seidel, M. Peterca, H. F. Mark), Wiley, Hoboken, NJ, **2014**, pp. 1–27.

[146] D. A. Shipp, *Polymer Reviews* **2011**, *51*, 99.

[147] N. Corrigan, K. Jung, G. Moad, C. J. Hawker, K. Matyjaszewski, C. Boyer, *Progress in Polymer Science* **2020**, *111*, 101311.

[148] a) S. Pearson, C. St Thomas, R. Guerrero-Santos, F. D'Agosto, *Polym. Chem.* **2017**, *8*, 4916; b) J. Kreutzer, Y. Yagci, *Polymers* **2017**, *10*.

[149] M. H. Stenzel, C. Barner-Kowollik, *Mater. Horiz.* **2016**, *3*, 471.

[150] S. Aoshima, S. Kanaoka, *Chem. Rev.* **2009**, *109*, 5245.

[151] B. Iván, *Macromolecular Symposia* **1994**, *88*, 201.

[152] G. Moad, E. Rizzardo in *ISSN*, *v.19* (Eds.: A. Abd-El-Aziz, S. Craig, D. Gigmes, B. Z. Tang), Royal Society of Chemistry, Cambridge, **2015**, pp. 1–44.

[153] in *The IUPAC Compendium of Chemical Terminology* (Eds.: V. Gold, A. McNaught), International Union of Pure and Applied Chemistry (IUPAC), Research Triangle Park, NC, **2025**.

[154] a) J. Nicolas, Y. Guillaneuf, C. Lefay, D. Bertin, D. Gigmes, B. Charleux, *Progress in Polymer Science* **2013**, *38*, 63; b) C. J. Hawker, A. W. Bosman, E. Harth, *Chem. Rev.* **2001**, *101*, 3661.

[155] a) J.-S. Wang, K. Matyjaszewski, *J. Am. Chem. Soc.* **1995**, *117*, 5614; b) M. Kato, M. Kamigaito, M. Sawamoto, T. Higashimura, *Macromolecules* **1995**, *28*, 1721.

[156] K. Matyjaszewski, J. Xia, *Chem. Rev.* **2001**, *101*, 2921.

[157] T. Ando, M. Kamigaito, M. Sawamoto, *Macromolecules* **1997**, *30*, 4507.

[158] C. Granel, P. Dubois, R. Jérôme, P. Teyssié, *Macromolecules* **1996**, *29*, 8576.

[159] J. A. Brandts, P. van de Geijn, E. E. van Faassen, J. Boersma, G. van Koten, *Journal of Organometallic Chemistry* **1999**, *584*, 246.

[160] F. Simal, A. Demonceau, A. F. Noels, *Angewandte Chemie International Edition* **1999**, *38*, 538.

[161] G. Moineau, C. Granel, P. Dubois, R. Jérôme, P. Teyssié, *Macromolecules* **1998**, *31*, 542.

[162] P. Lecomte, I. Drapier, P. Dubois, P. Teyssié, R. Jérôme, *Macromolecules* **1997**, *30*, 7631.

[163] Y. Kotani, M. Kamigaito, M. Sawamoto, *Macromolecules* **1999**, *32*, 2420.

[164] K. Matyjaszewski, *Adv. Mater.* **2018**, *30*, e1706441.

[165] a) G. Szczepaniak, L. Fu, H. Jafari, K. Kapil, K. Matyjaszewski, *Acc. Chem. Res.* **2021**, *54*, 1779; b) M. Ding, X. Jiang, L. Zhang, Z. Cheng, X. Zhu, *Macromol. Rapid Commun.* **2015**, *36*, 1702.

[166] J. Chiefari, Y. K. Chong, F. Ercole, J. Krstina, J. Jeffery, T. P. T. Le, R. T. A. Mayadunne, G. F. Meijs, C. L. Moad, G. Moad et al., *Macromolecules* **1998**, *31*, 5559.

[167] G. Moad, E. Rizzardo, S. H. Thang, *Aust. J. Chem.* **2012**, *65*, 985.

[168] G. Moad, E. Rizzardo, S. H. Thang, *Chemistry, an Asian journal* **2013**, *8*, 1634.

[169] A. Favier, M.-T. Charreyre, *Macromol. Rapid Commun.* **2006**, *27*, 653.

[170] C. Barner‐Kowollik, *Handbook of RAFT polymerization*, Wiley-VCH, Weinheim, **2008**.

[171] A. V. Fuchs, K. J. Thurecht, *ACS Macro Lett.* **2017**, *6*, 287.

[172] Z. Zhang, N. Vanparijs, S. Vandewalle, F. E. Du Prez, L. Nuhn, B. G. de Geest, *Polym. Chem.* **2016**, *7*, 7242.

[173] a) T. R. Barlow, J. C. Brendel, S. Perrier, *Macromolecules* **2016**, *49*, 6203; b) A. Vanderkooy, P. Pfefferkorn, M. S. Taylor, *Macromolecules* **2017**, *50*, 3807.

[174] Y. Kodama, M. Barsbay, O. Güven, *Radiation Physics and Chemistry* **2014**, *94*, 98.

[175] P. J. Roth, M. Haase, T. Basché, P. Theato, R. Zentel, *Macromolecules* **2010**, *43*, 895.

[176] R. E. Oesper, *J. Chem. Educ.* **1929**, *6*, 677.

[177] P. Rustemeyer, *Macromolecular Symposia* **2004**, *208*, 1.

[178] a) H. Staudinger, *Angew. Chem.* **1936**, *49*, 801; b) R. Mülhaupt, *Angewandte Chemie Intl Edit* **2004**, *43*, 1054.

[179] H.-A. Klok, P. Theato (Eds.) *Functional polymers by post-polymerization modification*. *Concepts, guidelines, and applications*, Wiley-VCH, Weinheim, **2013**.

[180] a) P. Théato, *Functional Polymers by Post-Polymerization Modification*. *Concepts, Practical Guidelines, and Applications*, John Wiley & Sons Incorporated, Weinheim, **2012**; b) W. Xi, T. F. Scott, C. J. Kloxin, C. N. Bowman, *Adv Funct Materials* **2014**, *24*, 2572.

[181] P. Ferruti, A. Bettelli, A. Feré, *Polymer* **1972**, *13*, 462.

[182] H. G. Batz, G. Franzmann, H. Ringsdorf, *Makromol. Chem.* **1973**, *172*, 27.

[183] J. Yang, H. Huang, J. Zhao, *Org. Chem. Front.* **2023**, *10*, 1817.

[184] M. A. Gauthier, M. I. Gibson, H.-A. Klok, *Angewandte Chemie Intl Edit* **2009**, *48*, 48.

[185] A. Das, P. Theato, *Chemical reviews* **2016**, *116*, 1434.

[186] A. M. Alb, P. Enohnyaket, M. F. Drenski, R. Shunmugam, G. N. Tew, W. F. Reed, *Macromolecules* **2006**, *39*, 8283.

[187] M. Eberhardt, R. Mruk, R. Zentel, P. Théato, *European Polymer Journal* **2005**, *41*, 1569.

[188] A. Das, P. Theato, *Macromolecules* **2015**, *48*, 8695.

[189] H. G. Batz, G. Franzmann, H. Ringsdorf, *Angewandte Chemie Intl Edit* **1972**, *11*, 1103.

[190] P. Rejmanová, J. Labský, J. Kopeček, *Makromol. Chem.* **1977**, *178*, 2159.

[191] V. Šubr, K. Ulbrich, *Reactive and Functional Polymers* **2006**, *66*, 1525.

[192] N. Metz, P. Theato, *European Polymer Journal* **2007**, *43*, 1202.

[193] M. Tesch, J. A. M. Hepperle, H. Klaasen, M. Letzel, A. Studer, *Angewandte Chemie International Edition* **2015**, *54*, 5054.

[194] L. He, K. Szameit, H. Zhao, U. Hahn, P. Theato, *Biomacromolecules* **2014**, *15*, 3197.

[195] A. Mueller, T. Kowalewski, K. L. Wooley, *Macromolecules* **1998**, *31*, 776.

[196] C. Ott, R. Hoogenboom, U. S. Schubert, *Chem. Commun.* **2008**, 3516.

[197] V. Atanasov, J. Kerres, *Macromolecules* **2011**, *44*, 6416.

[198] J.-M. Noy, Y. Li, W. Smolan, P. J. Roth, *Macromolecules* **2019**, *52*, 3083.

[199] J.-M. Noy, M. Koldevitz, P. J. Roth, *Polym. Chem.* **2015**, *6*, 436.

[200] S. Agar, E. Baysak, G. Hizal, U. Tunca, H. Durmaz, *J. Polym. Sci. A Polym. Chem.* **2018**, *56*, 1181.

[201] G. Delaittre, L. Barner, *Polym. Chem.* **2018**, *9*, 2679.

[202] Y. Du, Q. Zeng, L. Yuan, L. He, *Journal of Macromolecular Science, Part A* **2021**, *58*, 521.

[203] J. Chen, L. Dumas, J. Duchet‐Rumeau, E. Fleury, A. Charlot, D. Portinha, *J. Polym. Sci. A Polym. Chem.* **2012**, *50*, 3452.

[204] a) Y. Pei, J.-M. Noy, P. J. Roth, A. B. Lowe, *Polym. Chem.* **2015**, *6*, 1928; b) H. Turgut, A. C. Schmidt, P. Wadhwani, A. Welle, R. Müller, G. Delaittre, *Polym. Chem.* **2017**, *8*, 1288.

[205] D. Varadharajan, G. Delaittre, *Polym. Chem.* **2016**, *7*, 7488.

[206] B. Mekonnen, D. Flahaut, A. Khoukh, L. Perrier, C. Miqueu, A. Bousquet, J. Allouche, D. Grégoire, *Chem. Mater.* **2024**.

[207] J. Wegner, S. Ceylan, A. Kirschning, *Adv. Synth. Catal.* **2012**, *354*, 17.

[208] M. B. Plutschack, B. Pieber, K. Gilmore, P. H. Seeberger, *Chemical reviews* **2017**, *117*, 11796.

[209] J. Wegner, S. Ceylan, A. Kirschning, *Chem. Commun.* **2011**, *47*, 4583.

[210] S. J. Russell, P. Norvig, *Artificial intelligence*. *A modern approach*, Pearson, Boston, **2022**.

[211] J. A. HICKS, H. W. MELVILLE, *Nature* **1953**, *171*, 300.

[212] a) C. W. Coley, D. A. Thomas, J. A. M. Lummiss, J. N. Jaworski, C. P. Breen, V. Schultz, T. Hart, J. S. Fishman, L. Rogers, H. Gao et al., *Science (New York, N.Y.)* **2019**, *365*; b) I. W. Davies, *Nature* **2019**, *570*, 175.

[213] R. F. Service, *Science (New York, N.Y.)* **2023**, *382*, 987.

[214] L. Zhichao, M. Dong, L. Xiongjun, Z. Lu, *Commun Mater* **2024**, *5*.

[215] D. Paul, G. Sanap, S. Shenoy, D. Kalyane, K. Kalia, R. K. Tekade, *Drug discovery today* **2021**, *26*, 80.

[216] a) M. Fichtner, K. Edström, E. Ayerbe, M. Berecibar, A. Bhowmik, I. E. Castelli, S. Clark, R. Dominko, M. Erakca, A. A. Franco et al., *Advanced Energy Materials* **2022**, *12*; b) E. S. Muckley, R. Vasudevan, B. G. Sumpter, R. C. Advincula, I. N. Ivanov, *ACS Appl. Mater. Interfaces* **2023**, *15*, 2329.

[217] G. P. Rangaiah, Z. Feng, A. F. Hoadley, *Processes* **2020**, *8*, 508.

[218] G. P. Rangaiah, A. Bonilla‐Petriciolet, *Multi-objective optimization in chemical engineering*. *Developments and applications*, Wiley, Chichester, **2013**.

[219] a) B. Shahriari, K. Swersky, Z. Wang, R. P. Adams, N. de Freitas, *Proc. IEEE* **2016**, *104*, 148; b) P. I. Frazier, *A Tutorial on Bayesian Optimization*, **2018**.

[220] C. E. Rasmussen, *Gaussian processes for machine learning*, MIT Press, Cambridge, Mass., **2006**.

[221] a) M. J. Asher, B. F. W. Croke, A. J. Jakeman, L. J. M. Peeters, *Water Resources Research* **2015**, *51*, 5957; b) R. Alizadeh, J. K. Allen, F. Mistree, *Res Eng Design* **2020**, *31*, 275.

[222] L. Lu, C. M. Anderson-Cook, T. J. Robinson, *Technometrics* **2011**, *53*, 353.

[223] S. Mozharov, A. Nordon, D. Littlejohn, C. Wiles, P. Watts, P. Dallin, J. M. Girkin, *J. Am. Chem. Soc.* **2011**, *133*, 3601.

[224] J. J. Haven, N. Zaquen, M. Rubens, T. Junkers, *Macromol. React. Eng.* **2017**, *11*.

[225] M. A. Beres, B. Zhang, T. Junkers, S. Perrier, *Polym. Chem.* **2024**.

[226] O. Shyshov, K. A. Siewerth, M. von Delius, *Chemical communications (Cambridge, England)* **2018**, *54*, 4353.

[227] R. Bou Zerdan, Z. Geng, B. Narupai, Y. J. Diaz, M. W. Bates, D. S. Laitar, B. Souvagya, A. K. van Dyk, C. J. Hawker, *Journal of Polymer Science* **2020**, *58*, 1989.

[228] Y. Zhang, N. G. Pavlopoulos, T. S. Kleine, M. Karayilan, R. S. Glass, K. Char, J. Pyun, *J. Polym. Sci. A Polym. Chem.* **2019**, *57*, 7.

[229] M. Rémy, I. Nierengarten, B. Park, M. Holler, U. Hahn, J.-F. Nierengarten, *Chemistry (Weinheim an der Bergstrasse, Germany)* **2021**, *27*, 8492.

[230] J. J. Dale, S. Petcher, T. Hasell, *ACS Appl. Polym. Mater.* **2022**.

[231] A. P. Grimm, B. Deng, S. V. Haridas, D. Voll, C. W. Schmitt, M. von Delius, F. Scheiba, P. Théato, *European Polymer Journal* **2025**, 113815.

[232] O. Shyshov, S. V. Haridas, L. Pesce, H. Qi, A. Gardin, D. Bochicchio, U. Kaiser, G. M. Pavan, M. von Delius, *Nat Commun* **2021**, *12*, 3134.

[233] N. S. Keddie, A. M. Z. Slawin, T. Lebl, D. Philp, D. O'Hagan, *Nat. Chem.* **2015**, *7*, 483.

[234] B. E. Ziegler, M. Lecours, R. A. Marta, J. Featherstone, E. Fillion, W. S. Hopkins, V. Steinmetz, N. S. Keddie, D. O'Hagan, T. B. McMahon, *J. Am. Chem. Soc.* **2016**, *138*, 7460.

[235] S. M. Pratik, A. Nijamudheen, A. Datta, *Chemphyschem : a European journal of chemical physics and physical chemistry* **2016**, *17*, 2373.

[236] M. A. Pope, I. A. Aksay, *Advanced Energy Materials* **2015**, *5*.

[237] F. Yan, J. Jiang, X. Chen, S. Tian, K. Li, *Ind. Eng. Chem. Res.* **2014**, *53*, 11884.

[238] H. Zhang, C. Li, J. Guo, L. Zang, J. Luo, *Journal of Nanomaterials* **2012**, *2012*.

[239] S. S. Zhang, *Journal of Power Sources* **2013**, *231*, 153.

[240] H.-L. Wu, L. A. Huff, A. A. Gewirth, *ACS Appl. Mater. Interfaces* **2015**, *7*, 1709.

[241] M. Liu, Z. Wu, S. Liu, T. Guo, P. Chen, X. Cao, S. Pan, T. Zhou, L. Pompizii, M. Najafov et al., *Angewandte Chemie International Edition* **2024**, e202417624.

[242] Y.-F. Wang, J. Li, J. Huang, T. Qin, Y.-M. Liu, F. Zhong, W. Zhang, Z.-R. Li, *The journal of physical chemistry. C, Nanomaterials and interfaces* **2019**, *123*, 23610.

[243] L. Li, J. S. Nam, M. S. Kim, Y. Wang, S. Jiang, H. Hou, I.-D. Kim, *Advanced Energy Materials* **2023**, *13*.

[244] R. Tatara, P. Karayaylali, Y. Yu, Y. Zhang, L. Giordano, F. Maglia, R. Jung, J. P. Schmidt, I. Lund, Y. Shao-Horn, *J. Electrochem. Soc.* **2019**, *166*, A5090-A5098.

[245] A. Theodoridis, G. Papamokos, M. P. Wiesenfeldt, M. Wollenburg, K. Müllen, F. Glorius, G. Floudas, *The journal of physical chemistry. B* **2021**, *125*, 3700.

[246] C. Shen, J. Xie, M. Zhang, P. Andrei, M. Hendrickson, E. J. Plichta, J. P. Zheng, *J. Electrochem. Soc.* **2019**, *166*, A5287-A5294.

[247] Z. Zeng, X. Liu, *Adv Materials Inter* **2018**, *5*.

[248] K. Zhang, M. A. Lackey, Y. Wu, G. N. Tew, *J. Am. Chem. Soc.* **2011**, *133*, 6906.

[249] S. H. Je, H. J. Kim, J. Kim, J. W. Choi, A. Coskun, *Adv Funct Materials* **2017**, *27*, 1703947.

[250] J. M. M. Pople, T. P. Nicholls, N. Le Pham, W. M. Bloch, L. S. Lisboa, M. V. Perkins, C. T. Gibson, M. L. Coote, Z. Jia, J. M. Chalker, *J. Am. Chem. Soc.* **2023**.

[251] T. Baran, A. DUDA, S. PENCZEK, *J. Polym. Sci. Polym. Chem. Ed.* **1984**, *22*, 1085.

[252] Y. A. Wickramasingha, F. Stojcevski, D. J. Eyckens, D. J. Hayne, J. M. Chalker, L. C. Henderson, *Macro Materials & Eng* **2024**, *309*.

[253] P. Yan, H. Wang, L. J. Dodd, T. Hasell, *Commun Mater* **2023**, *4*.

[254] Y. Zhang, R. S. Glass, K. Char, J. Pyun, *Polym. Chem.* **2019**, *10*, 4078.

[255] J. M. Dust, Z. H. Fang, J. M. Harris, *Macromolecules* **1990**, *23*, 3742.

[256] M. Rozenberg, A. Loewenschuss, Y. Marcus, *Spectrochimica Acta Part A: Molecular and Biomolecular Spectroscopy* **1998**, *54*, 1819.

[257] X. Y. D. Soo, Z. M. Png, X. Wang, M. H. Chua, P. J. Ong, S. Wang, Z. Li, D. Chi, J. Xu, X. J. Loh et al., *ACS Appl. Polym. Mater.* **2022**, *4*, 2747.

[258] D. Craig, J. M. Newton, *International Journal of Pharmaceutics* **1991**, *74*, 33.

[259] G. W. Ehrenstein, G. Riedel, P. Trawiel, *Praxis der thermischen Analyse von Kunststoffen*, Hanser, München, **2003**.

[260] H. Shin, J. Kim, D. Kim, V. H. Nguyen, S. Lee, S. Han, J. Lim, K. Char, *J. Mater. Chem. A* **2018**, *6*, 23542.

[261] M. Brehm, J. M. Scheiger, A. Welle, P. A. Levkin, *Adv Materials Inter* **2020**, *7*.

[262] C. Xia, Y. Peng, Y. Yi, H. Deng, Y. Zhu, G. Hu, *Journal of Magnetism and Magnetic Materials* **2019**, *474*, 424.

[263] Y. Bai, Q. Dong, Y. Shao, Y. Deng, Q. Wang, L. Shen, D. Wang, W. Wei, J. Huang, *Nat Commun* **2016**, *7*, 12806.

[264] Z. Sasan Narkesabad, R. Rafiee, E. Jalilnejad, *Scientific reports* **2023**, *13*, 3670.

[265] S. M. Mobin, V. Mishra, D. K. Rai, K. Dota, A. K. Dharmadhikari, J. A. Dharmadhikari, D. Mathur, P. Mathur, *Dalton transactions (Cambridge, England : 2003)* **2015**, *44*, 1933.

[266] M. K. Denk, *Eur J Inorg Chem* **2009**, *2009*, 1358.

[267] E. Reinhard, E. A. Khan, A. Oguz Akyuz, G. Johnson, *Color Imaging*, A K Peters/CRC Press, **2008**.

[268] C. Copeland, R. J. Conway, J. J. Patroni, R. V. Stick, *Aust. J. Chem.* **1981**, *34*, 555.

[269] N. K. Singha, M. I. Gibson, B. P. Koiry, M. Danial, H.-A. Klok, *Biomacromolecules* **2011**, *12*, 2908.

[270] L. Phillips, A. R. Lacey, M. K. Cooper, *J. Chem. Soc., Dalton Trans.* **1988**, 1383.

[271] C. G. Hardy, L. Ren, T. C. Tamboue, C. Tang, *J. Polym. Sci. A Polym. Chem.* **2011**, *49*, 1409.

[272] a) E. Levillain, F. Gaillard, J. P. Lelieur, *Journal of Electroanalytical Chemistry* **1997**, *440*, 243; b) G. Bieker, D. Diddens, M. Kolek, O. Borodin, M. Winter, P. Bieker, K. Jalkanen, *The journal of physical chemistry. C, Nanomaterials and interfaces* **2018**, *122*, 21770.

[273] A. J. Bard, L. R. Faulkner, *Electrochemical methods*. *Fundamentals and applications*, Wiley, New York, Weinheim, **2001**.

[274] A. P. Grimm, S. T. Knox, C. Y. P. Wilding, H. A. Jones, B. Schmidt, O. Piskljonow, D. Voll, C. W. Schmitt, N. J. Warren, P. Théato, *Macromol. Rapid Commun.* **2025**.

[275] J.-M. Lu, J.-Z. Pan, Y.-M. Mo, Q. Fang, *Artificial Intelligence Chemistry* **2024**, *2*, 100057.

[276] a) A. F. de Almeida, R. Moreira, T. Rodrigues, *Nat Rev Chem* **2019**, *3*, 589; b) C. J. Taylor, K. C. Felton, D. Wigh, M. I. Jeraal, R. Grainger, G. Chessari, C. N. Johnson, A. A. Lapkin, *ACS Cent. Sci.* **2023**, *9*, 957.

[277] B. G. Sumpter, K. Hong, R. K. Vasudevan, I. Ivanov, R. Advincula, *Carbon Trends* **2023**, *10*, 100234.

[278] D. Cambié, C. Bottecchia, N. J. W. Straathof, V. Hessel, T. Noël, *Chemical reviews* **2016**, *116*, 10276.

[279] F. Parveen, N. Watson, A. M. Scholes, A. G. Slater, *Current Opinion in Green and Sustainable Chemistry* **2024**, *48*, 100935.

[280] L. Yu, B. Chen, Z. Li, Y. Su, X. Jiang, Z. Han, Y. Zhou, D. Yan, X. Zhu, R. Dong, *Giant* **2024**, *18*, 100252.

[281] S. Perrier, *Macromolecules* **2017**, *50*, 7433.

[282] Y.-N. Zhou, J.-J. Li, Y.-Y. Wu, Z.-H. Luo, *Chemical reviews* **2020**, *120*, 2950.

[283] M. Hartlieb, *Macromol. Rapid Commun.* **2022**, *43*, e2100514.

[284] a) Y. Wang, M. Fantin, S. Park, E. Gottlieb, L. Fu, K. Matyjaszewski, *Macromolecules* **2017**, *50*, 7872; b) F. Lorandi, M. Fantin, S. Shanmugam, Y. Wang, A. A. Isse, A. Gennaro, K. Matyjaszewski, *Macromolecules* **2019**, *52*, 1479.

[285] a) H. Mohapatra, M. Kleiman, A. P. Esser-Kahn, *Nat. Chem.* **2017**, *9*, 135; b) T. G. McKenzie, E. Colombo, Q. Fu, M. Ashokkumar, G. G. Qiao, *Angewandte Chemie International Edition* **2017**, *56*, 12302.

[286] a) G. Delaittre, C. Dire, J. Rieger, J.-L. Putaux, B. Charleux, *Chem. Commun.* **2009**, 2887; b) W.-M. Wan, C.-Y. Hong, C.-Y. Pan, *Chem. Commun.* **2009**, 5883.

[287] J. Xu, C. Fu, S. Shanmugam, C. J. Hawker, G. Moad, C. Boyer, *Angewandte Chemie International Edition* **2017**, *56*, 8376.

[288] M. Rubens, J. H. Vrijsen, J. Laun, T. Junkers, *Angewandte Chemie (International ed. in English)* **2019**, *58*, 3183.

[289] J. F. R. van Guyse, Y. Bernhard, A. Podevyn, R. Hoogenboom, *Angewandte Chemie Intl Edit* **2023**, *62*, e202303841.

[290] K. Kuroda, M. Ouchi, *Angewandte Chemie International Edition* **2024**, *63*, e202316875.

[291] Q. Zhuo, J. Yang, X. Zhou, T. Shima, Y. Luo, Z. Hou, *J. Am. Chem. Soc.* **2023**, *145*, 22803.

[292] Y. Ling, J. Liu, Y. Dong, Y. Chen, J. Chen, X. Yu, B. Liang, X. Zhang, W. An, D. Wang et al., *Adv. Mater.* **2023**, *35*, e2303641.

[293] M. Reis, F. Gusev, N. G. Taylor, S. H. Chung, M. D. Verber, Y. Z. Lee, O. Isayev, F. A. Leibfarth, *J. Am. Chem. Soc.* **2021**, *143*, 17677.

[294] A. I. Silva Terra, M. Rossetto, C. L. Dickson, G. Peat, D. Uhrín, M. E. Halse, *ACS measurement science au* **2023**, *3*, 73.

[295] S. T. Knox, S. Parkinson, R. Stone, N. J. Warren, *Polym. Chem.* **2019**, *10*, 4774.

[296] A. D. Clayton, A. M. Schweidtmann, G. Clemens, J. A. Manson, C. J. Taylor, C. G. Niño, T. W. Chamberlain, N. Kapur, A. J. Blacker, A. A. Lapkin et al., *Chemical Engineering Journal* **2020**, *384*, 123340.

[297] S. T. Knox, S. J. Parkinson, C. Y. P. Wilding, R. A. Bourne, N. J. Warren, *Polym. Chem.* **2022**, *13*, 1576.

[298] Y. Cao, B. J. Smucker, T. J. Robinson, *Journal of Statistical Planning and Inference* **2015**, *160*, 60.

[299] D. D. Bly, H. J. Stoklosa, J. J. Kirkland, W. W. Yau, *Anal. Chem.* **1975**, *47*, 1810.

[300] a) Y. Qamsane, J. Moyne, M. Toothman, I. Kovalenko, E. C. Balta, J. Faris, D. M. Tilbury, K. Barton, *IEEE Access* **2021**, *9*, 44247; b) C. Ghnatios, P. Gérard, A. Barasinski, *Int J Mater Form* **2023**, *16*.

[301] M. H. Reis, F. A. Leibfarth, L. M. Pitet, *ACS Macro Lett.* **2020**, *9*, 123.

[302] J. Clayden, N. Greeves, S. G. Warren, *Organic chemistry*, Oxford University Press, Oxford, New York, Auckland, **2012**.

[303] P. Brown, E. F. Mooney, *Spectrochimica Acta Part A: Molecular Spectroscopy* **1968**, *24*, 1317.

[304] D. H. Lemmon, *Journal of Molecular Structure* **1978**, *49*, 71.

[305] R. A. Yadav, I. S. Singh, *Proc. Indian Acad. Sci. (Chem. Sci.)* **1985**, *95*, 471.

[306] G. R. Fulmer, A. J. M. Miller, N. H. Sherden, H. E. Gottlieb, A. Nudelman, B. M. Stoltz, J. E. Bercaw, K. I. Goldberg, *Organometallics* **2010**, *29*, 2176.

[307] F. Brotzel, Y. C. Chu, H. Mayr, *The Journal of organic chemistry* **2007**, *72*, 3679.

[308] V. R. Flid, M. L. Gringolts, R. S. Shamsiev, E. S. Finkelshtein, *Russ. Chem. Rev.* **2018**, *87*, 1169.

[309] H. G. Brittain, *Crystal Growth & Design* **2009**, *9*, 3497.

[310] S. F. Parker, K. P. J. Williams, D. Steele, H. Herman, *Phys. Chem. Chem. Phys.* **2003**, *5*, 1508.

[311] O. Herbinet, B. Sirjean, F. Battin-Leclerc, R. Fournet, P.-M. Marquaire, *Energy Fuels* **2007**, *21*, 1406.

[312] M. Hirooka, T. Kato, *J. Polym. Sci. B Polym. Lett. Ed.* **1974**, *12*, 31.

[313] C.-C. Huang, M.-X. Du, B.-Q. Zhang, C.-Y. Liu, *Macromolecules* **2022**, *55*, 3189.

[314] S. Zhang, T. Junkers, S. Kuhn, *Chemical science* **2022**.

[315] F. Lauterbach, M. Rubens, V. Abetz, T. Junkers, *Angewandte Chemie International Edition* **2018**, *57*, 14260.

[316] M. Teodorescu, K. Matyjaszewski*, *Macromol. Rapid Commun.* **2000**, *21*, 190.

[317] G. G. Odian, *Principles of polymerization*, Wiley-Interscience, Hoboken, NJ, **2004**.

[318] a) A. Enten, Y. Yang, Z. Ye, R. Chu, T. Van, B. Rothschild, F. Gonzalez, T. Sulchek, *Journal of laboratory automation* **2016**, *21*, 526; b) D. C. Florian, M. Odziomek, C. L. Ock, H. Chen, S. A. Guelcher, *Scientific reports* **2020**, *10*, 13663.

[319] R. Gruetter, S. A. Weisdorf, V. Rajanayagan, M. Terpstra, H. Merkle, C. L. Truwit, M. Garwood, S. L. Nyberg, K. Uğurbil, *Journal of magnetic resonance (San Diego, Calif. : 1997)* **1998**, *135*, 260.

[320] H. Willcock, R. K. O'Reilly, *Polym. Chem.* **2010**, *1*, 149.

[321] R. Xie, A. R. Weisen, Y. Lee, M. A. Aplan, A. M. Fenton, A. E. Masucci, F. Kempe, M. Sommer, C. W. Pester, R. H. Colby et al., *Nat Commun* **2020**, *11*, 893.

[322] Y. Ren, H. Shui, C. Peng, H. Liu, Y. Hu, *Fluid Phase Equilibria* **2011**, *312*, 31.

[323] M. P. Wiesenfeldt, Z. Nairoukh, W. Li, F. Glorius, *Science (New York, N.Y.)* **2017**, *357*, 908.

Appendix

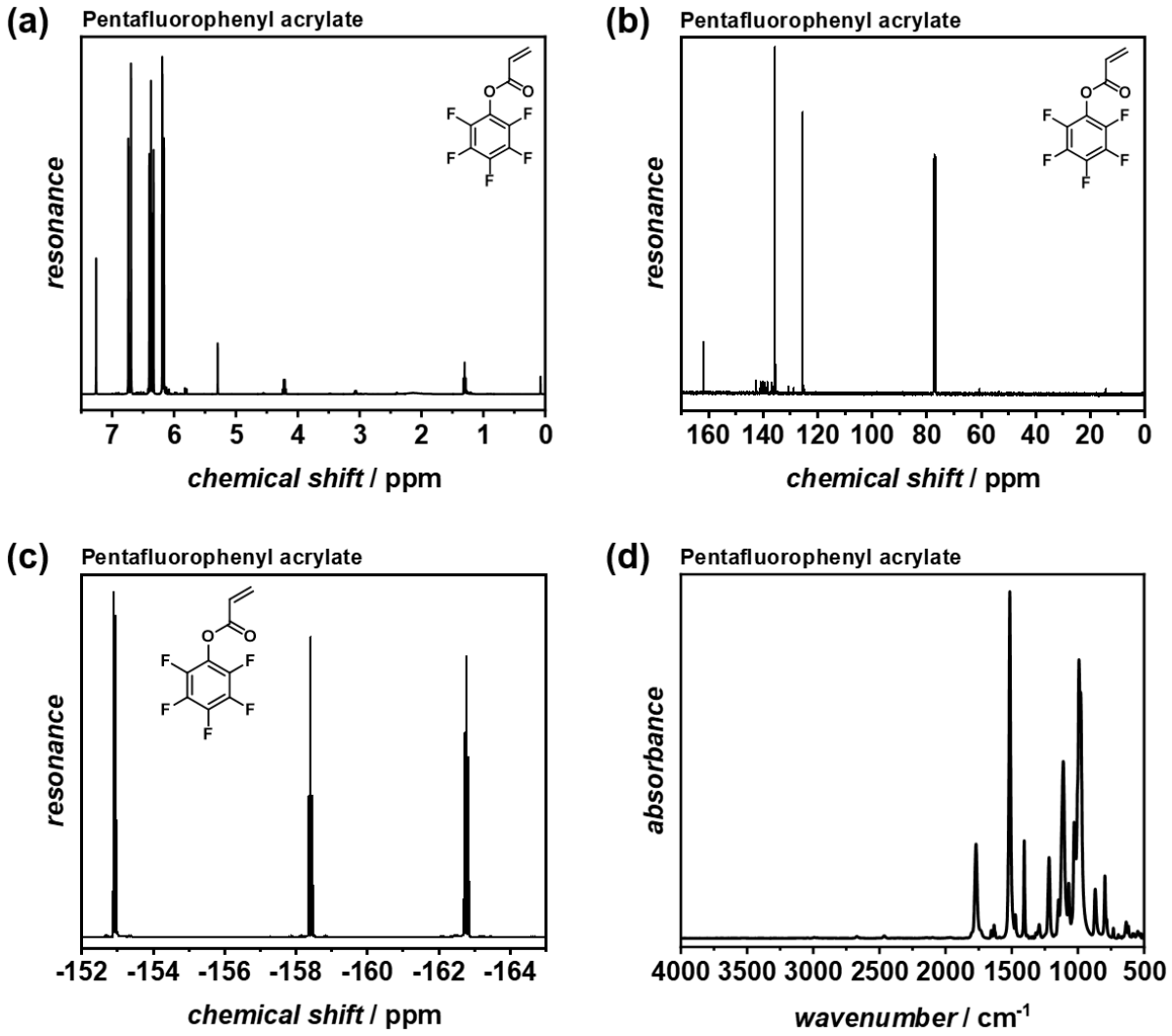

Appendix 1. Characterization of PFPA by ^{1}H NMR (a), ^{13}C NMR (b), ^{19}F NMR (c), and IR (d) spectroscopy. NMR spectra were recorded using $CDCl_3$ as solvent. IR resolution: 2 cm^{-1}.

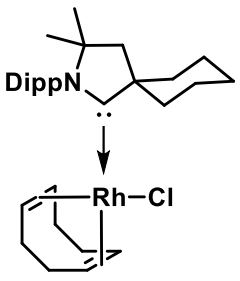

Appendix 2. Complex structure of [Rh(CAAC)(COD)Cl] used for the regioselective hydrogenation of fluorinated arenes for synthesis of all-*cis*-fluorinated compounds.[323]

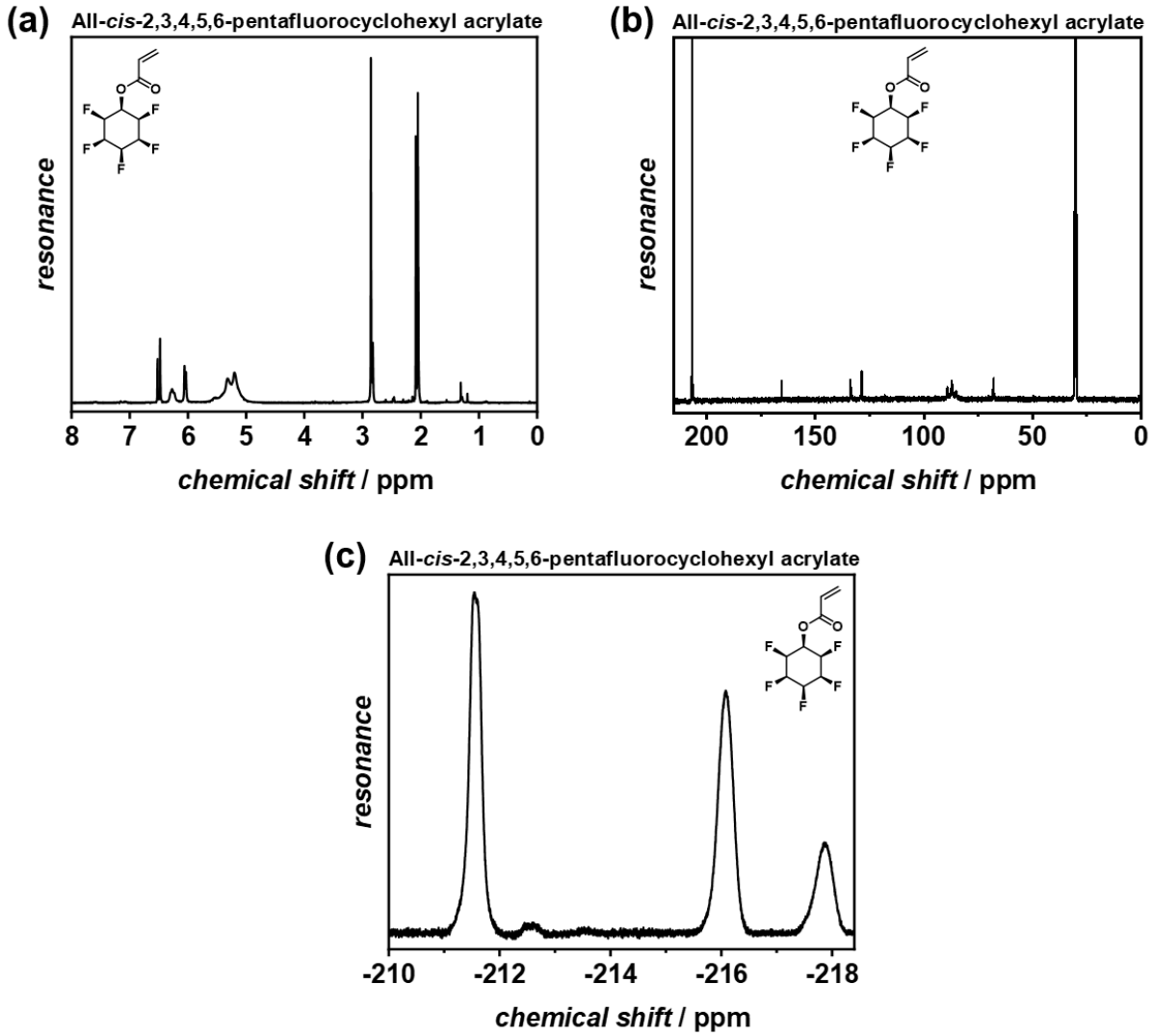

Appendix 3. ^{1}H NMR (a), ^{13}C NMR (b), and ^{19}F NMR (c) spectra of PFCHA recorded in Acetone-d_6.

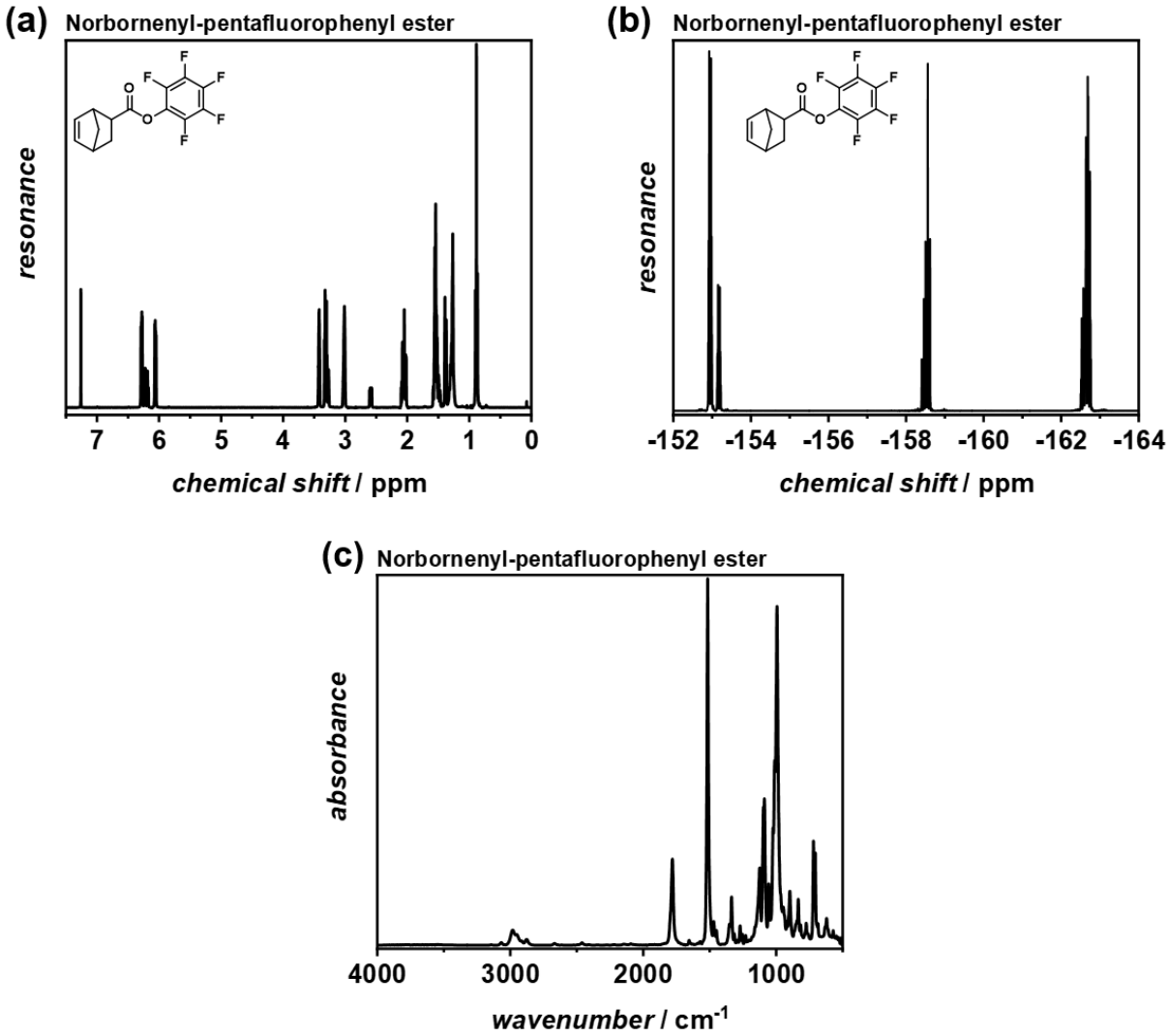

Appendix 4. ^{1}H NMR (a), ^{19}F NMR (b), and ATR FT-IR (c) spectra of NB-PFPE recorded in $CDCl_3$.

conditions	M_n / g mol^{-1}	M_w / g mol^{-1}	*Đ*
150 °C, 4 h	430	710	1.65
150 °C, 24 h	510	1000	1.96
150 °C, 3 d	770	1600	2.08
160 °C, 4 h	460	830	1.80
160 °C, 24 h	510	1000	1.96
160 °C, 3 d	610	3800	6.23
170 °C, 4 h	530	920	1.74
170 °C, 24 h	420	750	1.79
170 °C, 3 d	1000	7200	7.20

Appendix 5. Number average molecular weight (M_n), weight average molecular weight (M_w), and dispersity (*Đ*) of poly(S-*r*-NB-PFPE) after different reaction conditions, determined by SEC. Solvent: THF; calibration: PS.

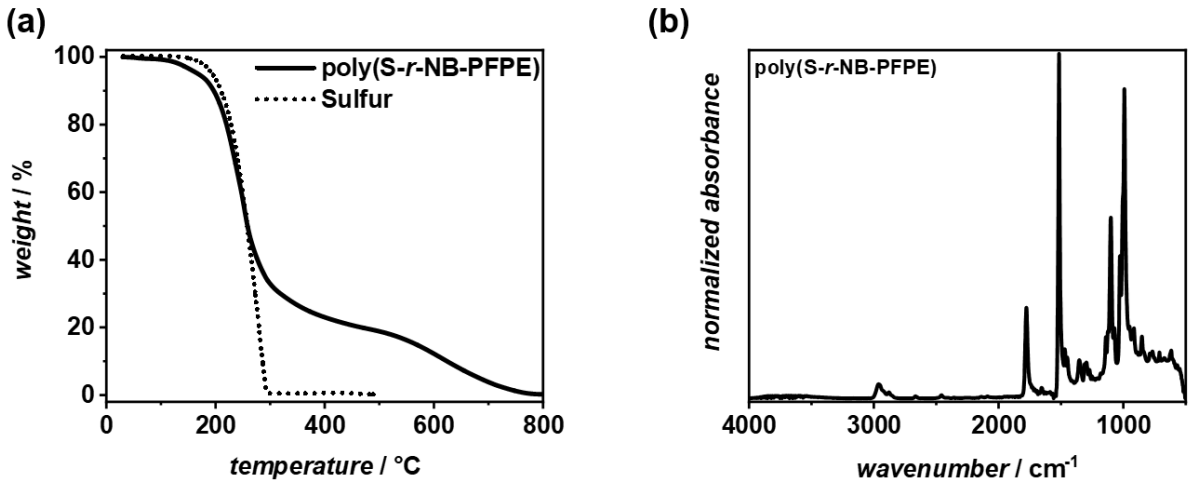

Appendix 6. A) TGA thermogram of poly(S-*r*-NB-PFPE) (solid line) and elemental sulfur (dotted line) in the range of 30 to 800 °C. Poly(S-*r*-NB-PFPE): $T_{5\%}$ = 168 °C; $T_{95\%}$ = 684 °C. Sulfur: $T_{5\%}$ = 194 °C; $T_{95\%}$ = 289 °C. Heating rate: 10 K min-1. B) ATR FT-IR spectrum of poly(S-r-NB-PFPE) in the range of 4000 cm^{-1} to 500 cm^{-1}. Resolution: 2 cm^{-1}; IV conditions: T = 150 °C and t = 3 d.

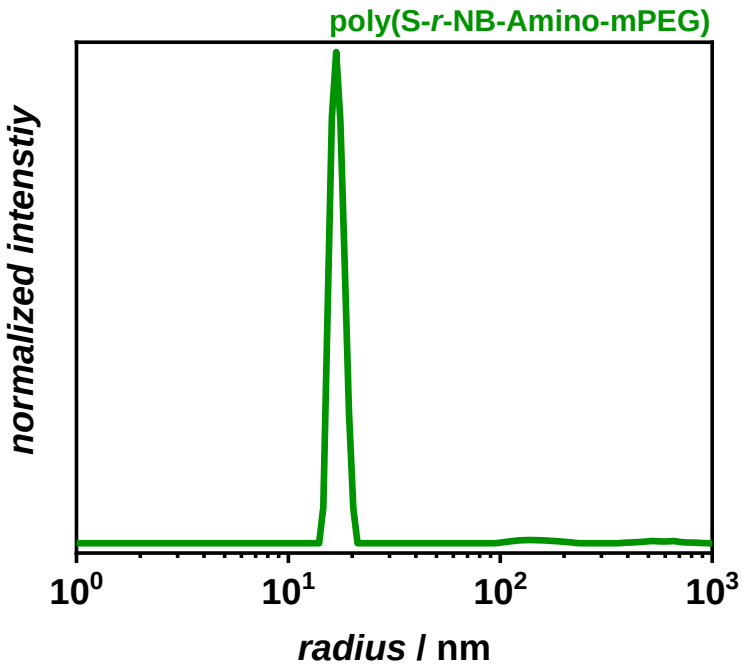

Appendix 7. Dynamic light scattering of poly(S-*r*-NB-Amino-mPEG) nanoparticles in water. The average hydrodynamic radius was 17 nm. Concentration: 3.5 mg mL^{-1}.

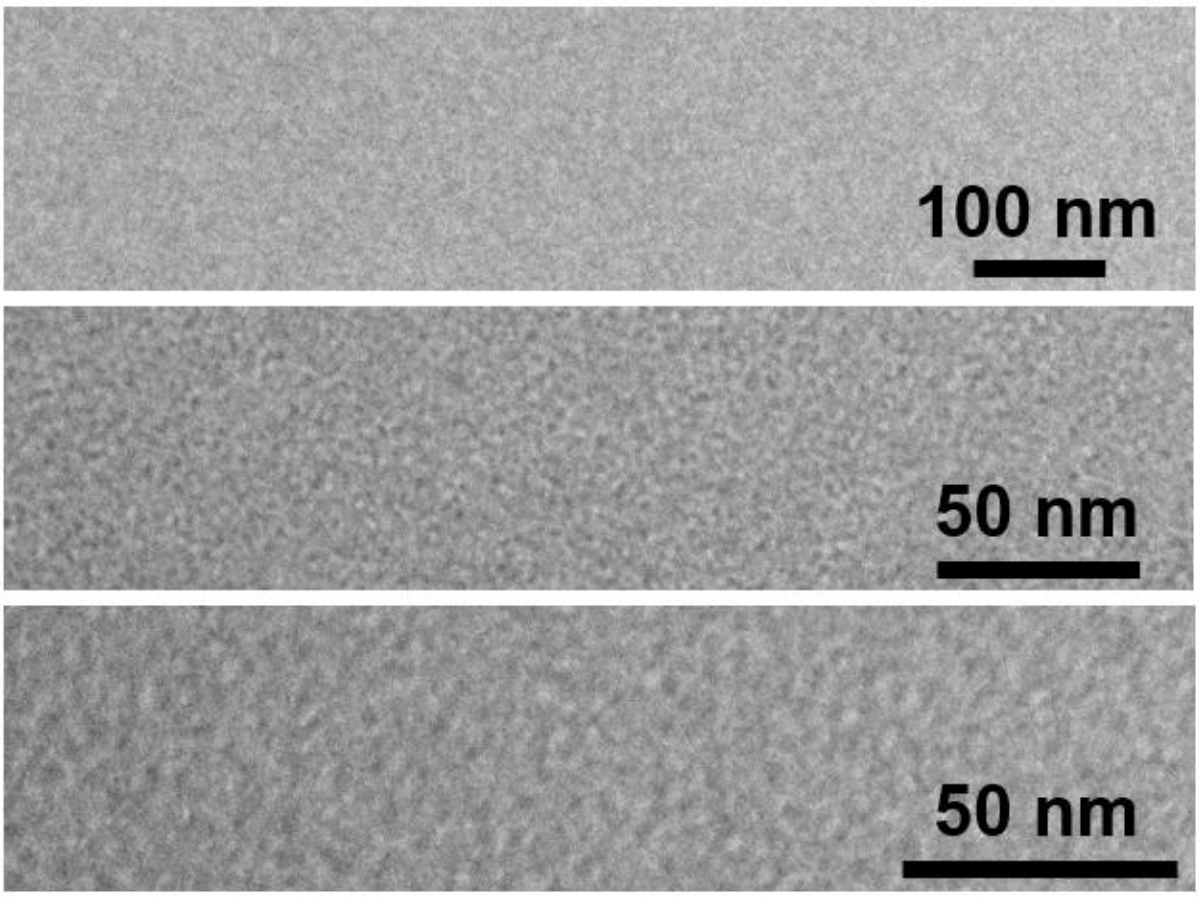

Appendix 8. TEM micrographs of poly(S-*r*-NB-Amino-mPEG) under dry conditions. No defined structures could be observed, indicating that the particle structure of poly(S-*r*-NB-Amino-mPEG) is only persistent in aqueous environments.

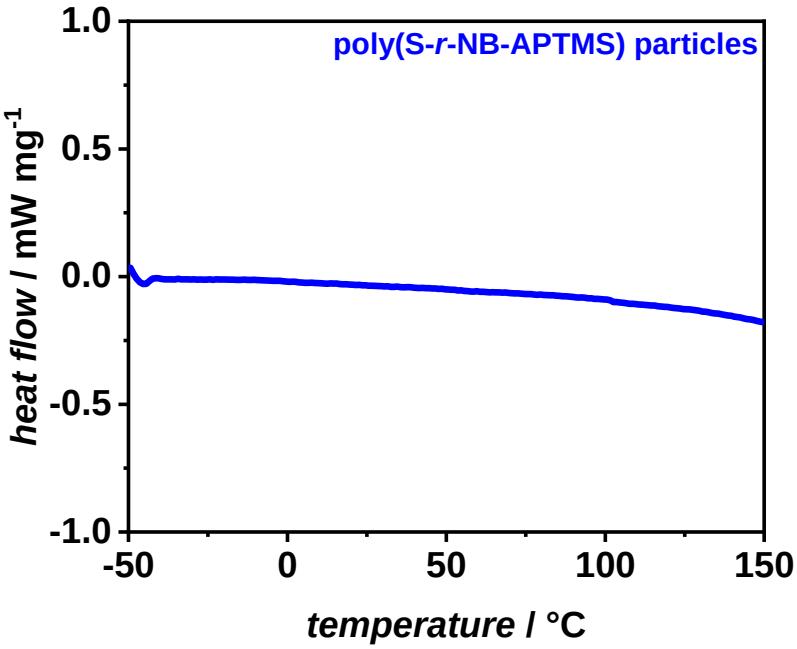

Appendix 9. DSC thermogram of poly(S-*r*-NB-APTMS) particles in the range of -50 to 150 °C at the first heat run. No phase transitions were observed. Heating rate: 10 K min^{-1}.

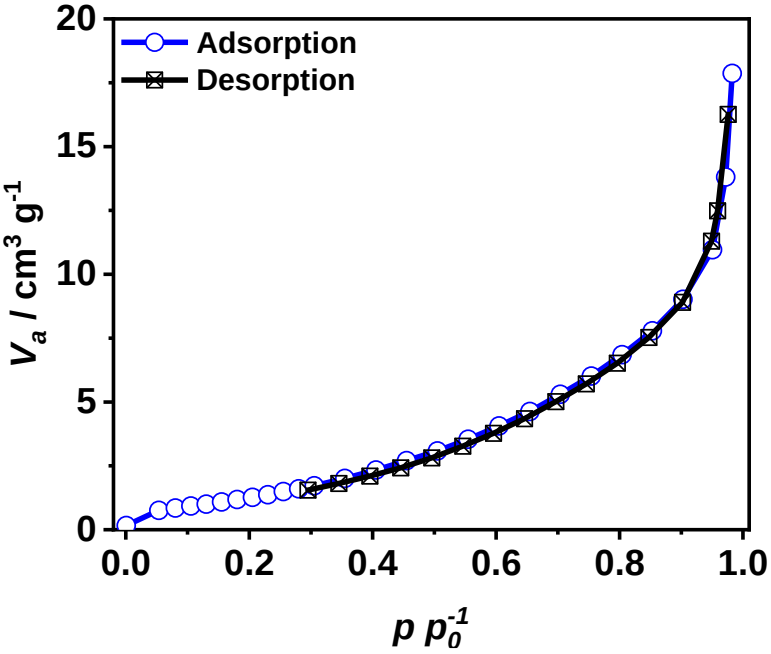

Appendix 10. Adsorption (blue) and desorption (black) isotherms of N_2 of poly(S-*r*-NB-APTMS) particles determined by BRUNAUER-EMMETT-TELLER measurements. Particles were pretreated in vacuum at 100 °C for 2 h prior to N_2 dosing.

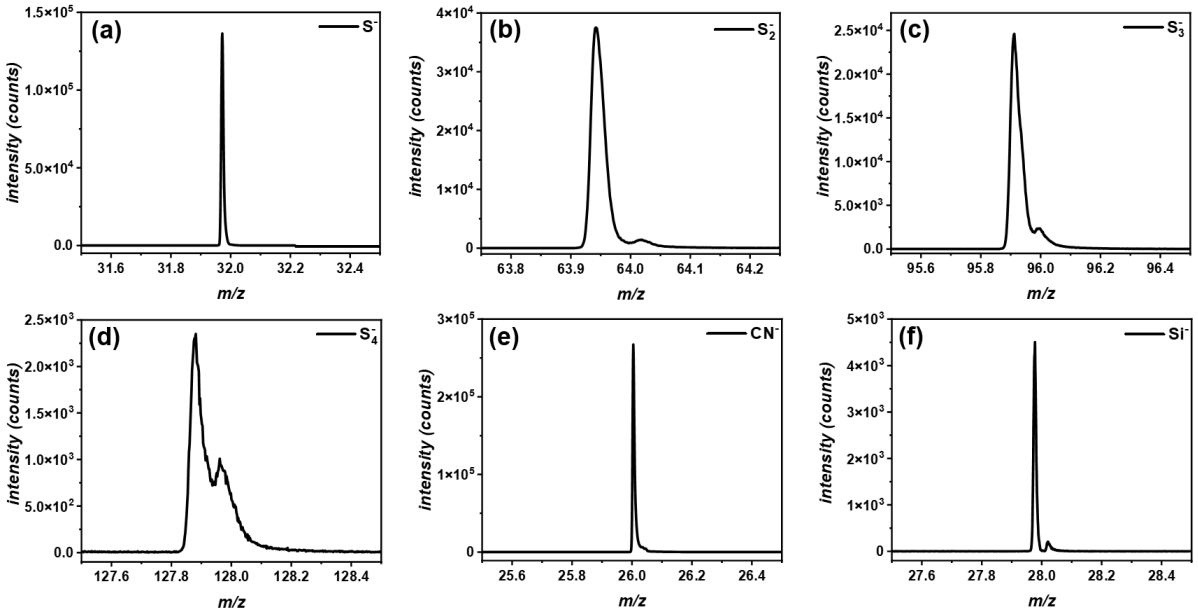

Appendix 11. ToF-SIMS mass spectra of for S^- (a), S_2^- (b), S_3^- (c), S_4^- (d), CN^- (e), and Si^- (f) fragments found on silicon wafers spin-coated with poly(S-*r*-NB-APTMS) solution one time with 1500 rpm for 15 seconds.

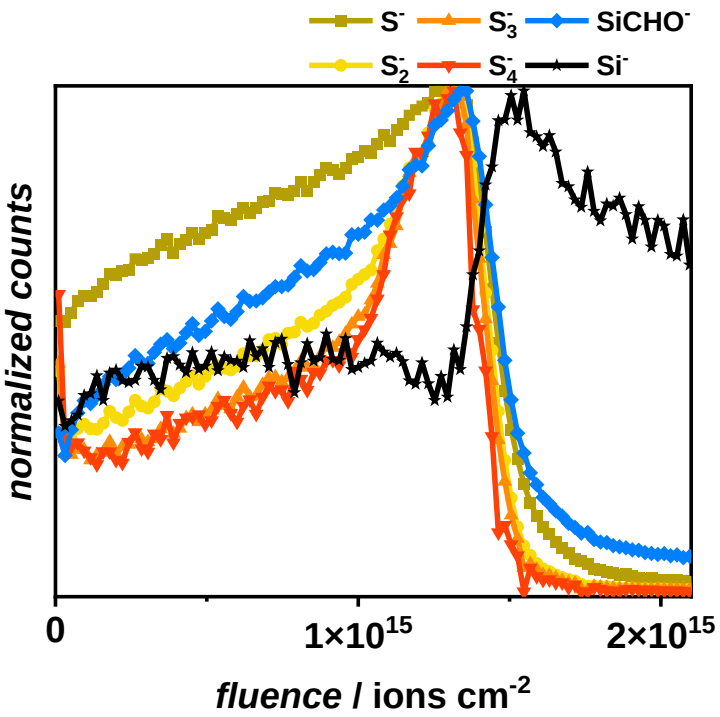

Appendix 12. Normalized fluence spectrum of S_n^- (n = 1 – 4) as well as $SiCHO^-$ and Si^- fragments on a silicon wafer spin-coated with poly(S-*r*-NB-APTMS) solution found by ToF-SIMS. The coating layer can be distinguished from the silicon substrate by a rapid decrease of organic and sulfur fragment counts with an increase of Si^- fragment counts. Additional fragments were omitted for clarity.

added sulfur / wt%	*N* / wt%	*C* / wt%	*H* / wt%	*S* / wt%
-	4.6 ± 0.3	51.7 ± 2.6	5.4 ± 0.4	36.5 ± 3.1
20	3.7 ± 0.0	39.6 ± 0.3	4.1 ± 0.0	47.4 ± 0.4
40	3.2 ± 0.1	34.6 ± 0.4	3.6 ± 0.0	57.0 ± 1.4
60	2.8 ± 0.0	29.9 ± 0.1	3.2 ± 0.0	66.7 ± 0.1
80	2.5 ± 0.1	27.9 ± 1.0	2.9 ± 0.0	72.2 ± 2.0
100	2.2 ± 0.1	25.8 ± 0.2	2.7 ± 0.1	76.1 ± 0.2

Appendix 13. Elemental composition of poly(S-*net*-NB-AA) after the second cross-linking step with different amounts of sulfur. Uncertainty given from standard deviation of 2 measurements.

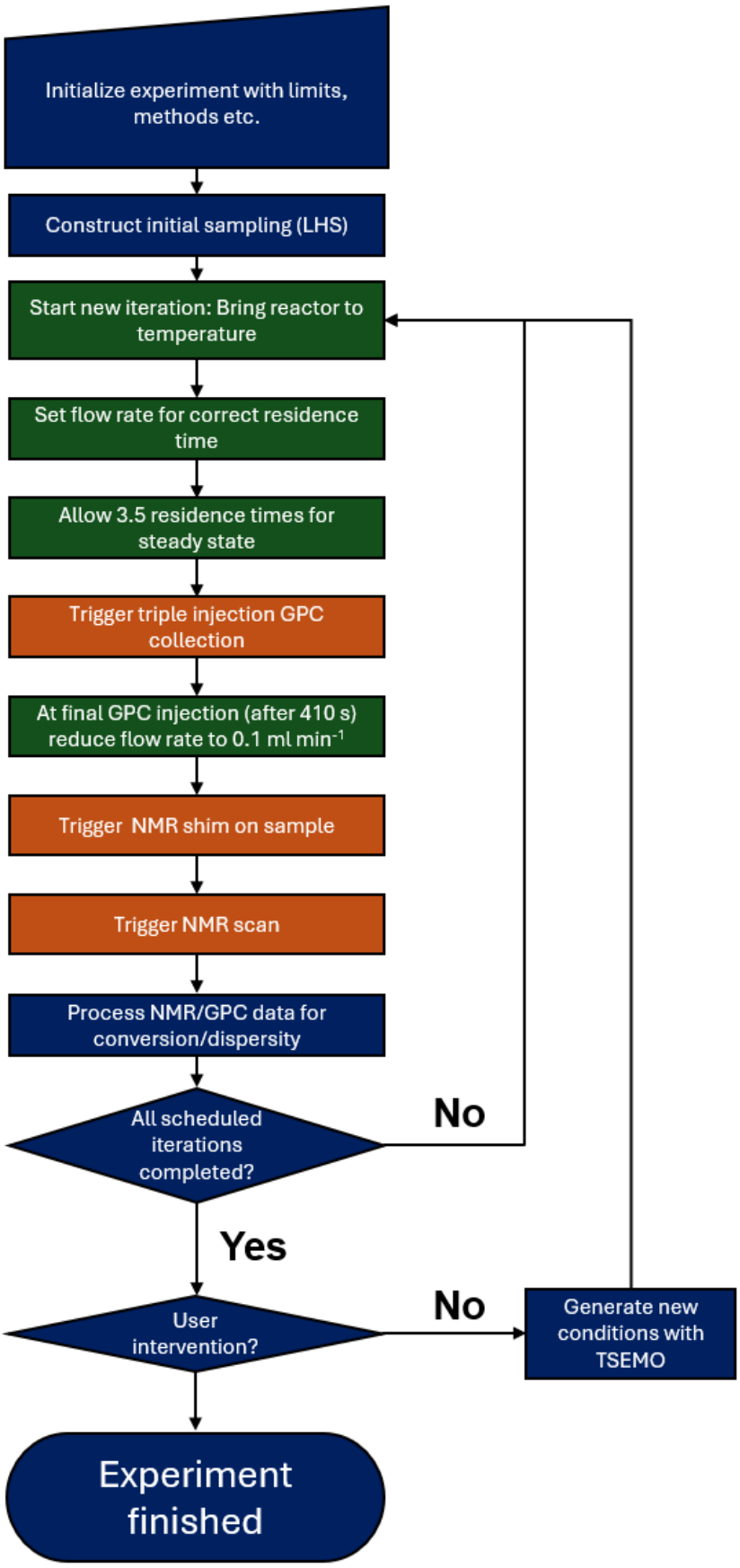

Appendix 14. Workflow visualization of an automated optimization experiment carried-out at the University of Leeds. Key steps or the process are laid out. Blue: computational processes; green: reactor processes; orange: analytical processes. The analytical element of the loop takes approximately 15 minutes, consuming 1.5 mL of reaction solution.

experiment number	*temperature* / °C	*residence time* / min	*monomer conversion* / %	M_n / g mol^{-1}	*Đ*	*hypervolume*
1	70	10	0.6	0	2.00	0
2	78	56	5.9	0	2.00	0
3	82	48	12.0	0	2.00	0
4	86	22	0.5	0	2.00	0
5	94	40	17.1	3690	1.12	0.149
6	98	30	31.9	3570	1.09	0.292
7	102	44	46.3	4600	1.15	0.391
8	106	52	53.6	4740	1.18	0.441
9	114	18	42.9	4130	1.19	0.347
10	120	28	46.9	4020	1.13	0.407
11	118	60	50.4	4320	1.15	0.430
12	94	56	66.4	6230	1.16	0.557
13	104	22	45.4	4450	1.13	0.395
14	108	58	43.0	5000	1.20	0.343
15	110	20	52.1	4610	1.16	0.436
16	118	42	53.7	4470	1.15	0.455
17	108	36	50.4	5050	1.16	0.422
18	100	32	59.9	5760	1.18	0.491
19	96	54	62.2	6180	1.16	0.525
20	108	22	56.9	5140	1.17	0.473
21	98	60	59.3	5820	1.16	0.500
22	102	10	21.4	4300	2.00	0

Appendix 15. Monomer conversion, number average molecular weight, dispersity, and hypervolume of the automation results from the polymerization of PFPA. The first ten experiments (highlighted in gray) were the training experiments, chosen by LHC sampling. Experiment number twelve (red) was found to be the most desirable experiment.

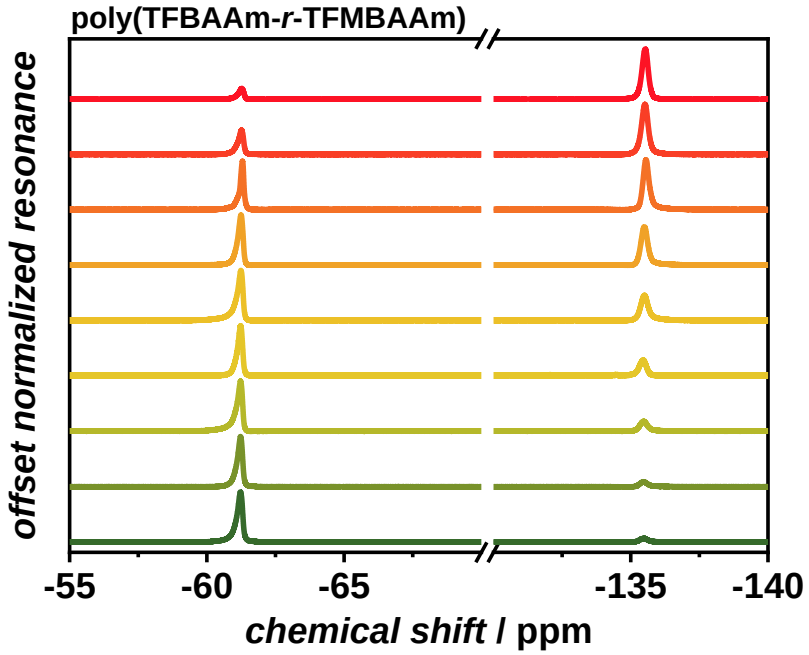

Appendix 16. Offset normalized ^{19}F NMR spectra of poly(TFBAAm-*r*-TFMBAAm) in the region between -55 and -140 ppm. The left peaks at -61 ppm are attributed to the CF_3 group of TFMBAAm while the right peaks at -135 ppm are attributed to the meta-fluorine atoms of TFBA. The amount of TFBA increased from green to red (10 – 90 mol%) while the amount of TFMBA increased from red to green (10 – 90 mol%), respectively.

polymer	M_n / g mol^{-1}	*Đ*
poly(TFBAAm$_{10}$-r-TFMBAAm$_{90}$)	38100	1.11
poly(TFBAAm$_{20}$-r-TFMBAAm$_{80}$)	38300	1.10
poly(TFBAAm$_{30}$-r-TFMBAAm$_{70}$)	39400	1.09
poly(TFBAAm$_{40}$-r-TFMBAAm$_{60}$)	39500	1.09
poly(TFBAAm$_{50}$-r-TFMBAAm$_{50}$)	38600	1.12
poly(TFBAAm$_{60}$-r-TFMBAAm$_{40}$)	39200	1.11
poly(TFBAAm$_{70}$-r-TFMBAAm$_{30}$)	39300	1.11
poly(TFBAAm$_{80}$-r-TFMBAAm$_{20}$)	39900	1.10
poly(TFBAAm$_{90}$-r-TFMBAAm$_{10}$)	40400	1.09

Appendix 17. M_n and *Đ* of poly(TFBAAm-*r*-TFMBAAm). Calibration: PMMA.

polymer	M_n / g mol^{-1}	*Đ*
poly(NBMAAm$_{10}$-*r*-BAAm$_{90}$)	3950	1.34
poly(NBMAAm$_{20}$-*r*-BAAm$_{80}$)	4010	1.33
poly(NBMAAm$_{30}$-*r*-BAAm$_{70}$)	4030	1.33
poly(NBMAAm$_{40}$-*r*-BAAm$_{60}$)	4020	1.33
poly(NBMAAm$_{50}$-*r*-BAAm$_{50}$)	4030	1.34
poly(NBMAAm$_{60}$-*r*-BAAm$_{40}$)	4060	1.34
poly(NBMAAm$_{70}$-*r*-BAAm$_{30}$)	4150	1.33
poly(NBMAAm$_{80}$-*r*-BAAm$_{20}$)	4130	1.33
poly(NBMAAm$_{90}$-*r*-BAAm$_{10}$)	4290	1.33

Appendix 18. M_n and *Đ* of poly(NBMAAm-*r*-BAAm). Calibration: PMMA.

ratio NBMA/BA / mol%	$T_{5\%}$ / °C	$T_{95\%}$ / °C
10/90	151	432
20/80	161	430
30/70	132	495
40/60	120	445
50/50	137	451
60/40	119	475
70/30	112	492
80/20	117	460
90/10	107	466

Appendix 19. $T_{5\%}$ and $T_{95\%}$ temperatures of the thermal decomposition of poly(NBMAAm-*r*-BAAm) with different modification ratios.

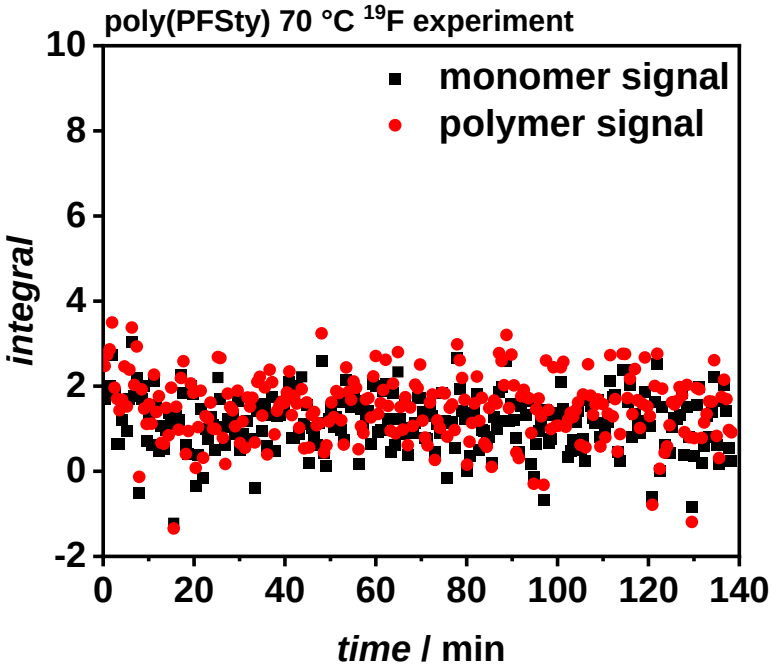

Appendix 20. Integrals of the monomer (black) and polymer (red) regions in a ^{19}F NMR spectrum of during polymerization. No distinction can be made between during the course of the experiment which prevents usage of ^{19}F NMR for the calculation of the monomer conversion.

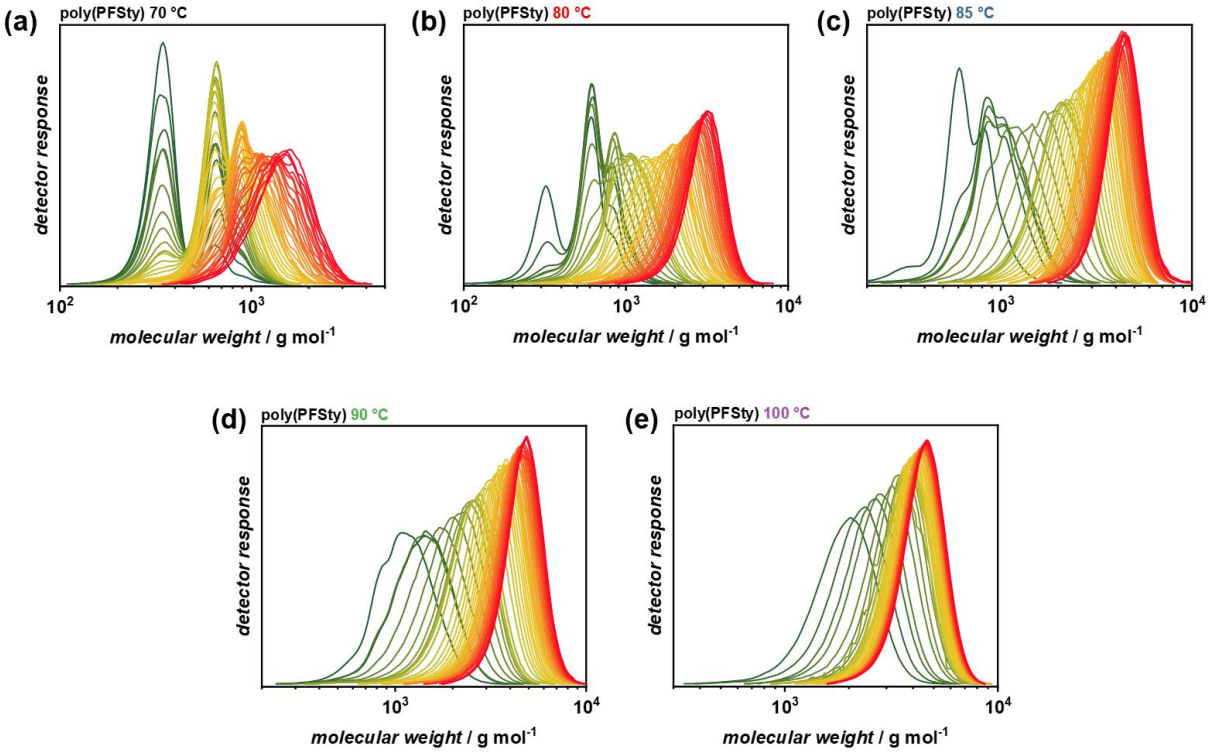

Appendix 21. SEC traces of poly(PFSty) during TT experiments at 70 °C (a), 80 °C (b), 85 °C (c), 90 °C (d), and 100 °C (e). The shift from green to red resembles the increasing residence time from 4 to 60 minutes. Calibration: PS.

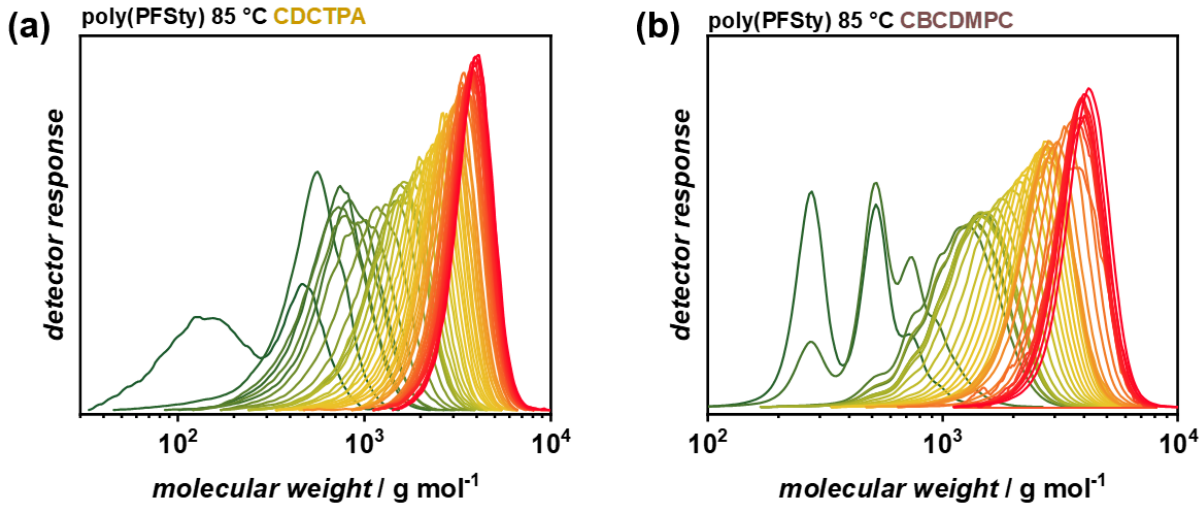

Appendix 22. SEC traces of poly(PFSty) synthesized at 85 °C using CDCTPA (a) and CBCDMPC (b) as RAFT-agents. The shift from green to red resembles the increasing residence time from 4 to 60 minutes. Calibration: PS.

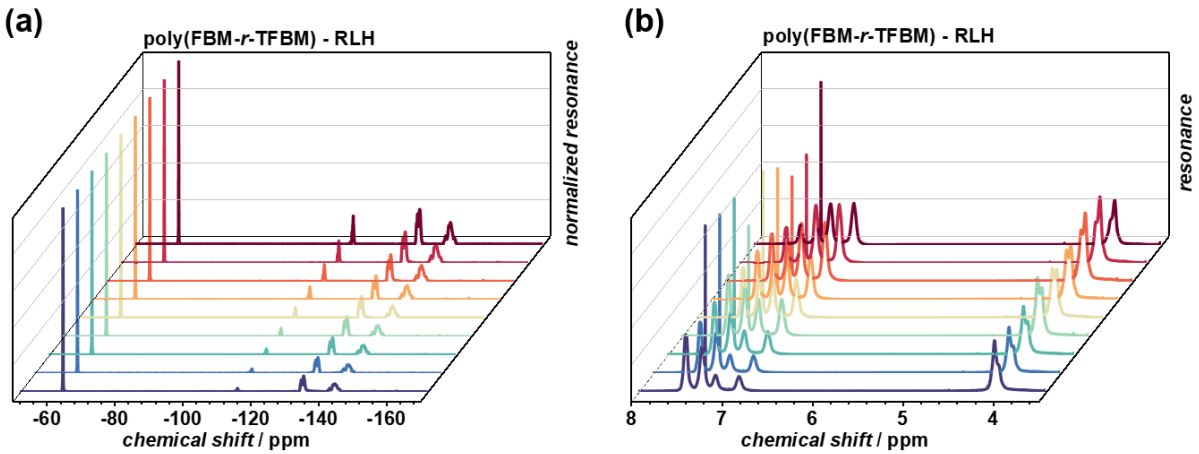

Appendix 23. a) ^{19}F NMR and b) ^{1}H NMR spectra of poly(FBM-*r*-TFBM) with different ratios of FBM and TFBM made by PPM using an RLH. The amount of FBM increased from blue to red (10 – 90 mol%) while the amount of TFBM increased from red to blue (10 – 90 mol%), respectively.

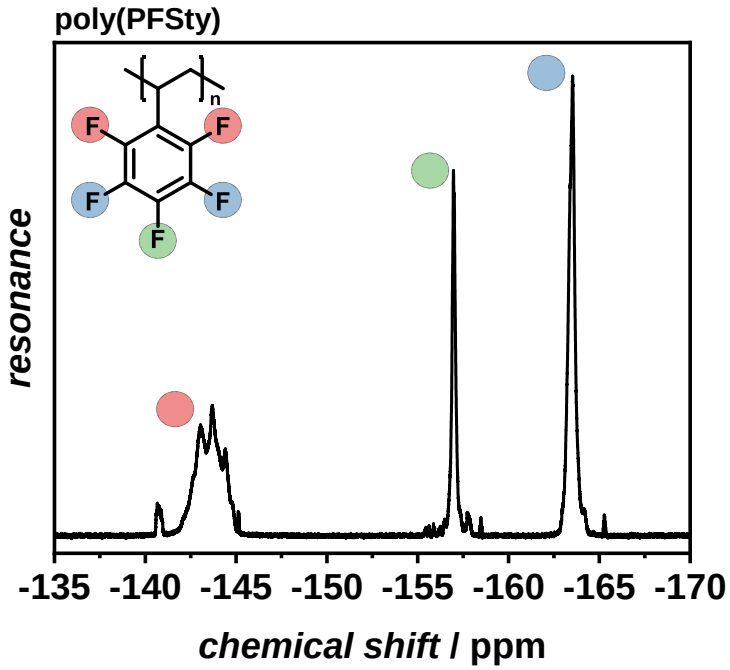

Appendix 24. ^{19}F NMR spectrum of poly(PFSty) in $CDCl_3$. The *ortho*, *meta*, and *para* fluorine atoms are assigned to validate the complete substitution of *para* fluorine atoms by disappearance of the respective resonance at -157 ppm.

polymer	M_n / g mol^{-1}	$Đ$	$M_{p,1}$ / g mol^{-1}	$M_{p,2}$ / g mol^{-1}
poly(PFSty)	8130	1.04	-	-
poly(FBM$_{10}$-r-TFBM$_{90}$)	15200	1.30	12000	21600
poly(FBM$_{20}$-r-TFBM$_{80}$)	16500	1.32	12100	22100
poly(FBM$_{30}$-r-TFBM$_{70}$)	16100	1.31	12100	22000
poly(FBM$_{40}$-r-TFBM$_{60}$)	16800	1.30	12100	21900
poly(FBM$_{50}$-r-TFBM$_{50}$)	16300	1.32	12100	21900
poly(FBM$_{60}$-r-TFBM$_{40}$)	16900	1.31	11900	22100
poly(FBM$_{70}$-r-TFBM$_{30}$)	16400	1.32	12000	21900
poly(FBM$_{80}$-r-TFBM$_{20}$)	16300	1.32	11800	21700
poly(FBM$_{90}$-r-TFBM$_{10}$)	16100	1.32	11600	21700

Appendix 25. M_n, $Đ$, $M_{p,1}$, and $M_{p,2}$ of poly(FBM-*r*-TFBM) made by PPM in continuous flow.

polymer	M_n / g mol^{-1}	$Đ$	$M_{p,1}$ / g mol^{-1}	$M_{p,2}$ / g mol^{-1}
poly(PFSty)	8130	1.04	-	-
poly(FBM$_{10}$-r-TFBM$_{90}$)	17100	1.21	13400	23600
poly(FBM$_{20}$-r-TFBM$_{80}$)	17000	1.22	13400	23600
poly(FBM$_{30}$-r-TFBM$_{70}$)	16500	1.23	13200	23400
poly(FBM$_{40}$-r-TFBM$_{60}$)	16500	1.24	13000	23100
poly(FBM$_{50}$-r-TFBM$_{50}$)	16700	1.24	13100	23400
poly(FBM$_{60}$-r-TFBM$_{40}$)	16500	1.25	12900	23200
poly(FBM$_{70}$-r-TFBM$_{30}$)	16000	1.26	12600	22800
poly(FBM$_{80}$-r-TFBM$_{20}$)	15700	1.27	12500	22600
poly(FBM$_{90}$-r-TFBM$_{10}$)	15400	1.26	11800	21400

Appendix 26. M_n, $Đ$, $M_{p,1}$, and $M_{p,2}$ of poly(FBM-*r*-TFBM) made by PPM using an RLH.

polymer	T_g *flow* / °C	T_g *RLH* / °C
poly(FBM$_{10}$-r-TFBM$_{90}$)	46.0	51.0
poly(FBM$_{20}$-r-TFBM$_{80}$)	47.0	58.5
poly(FBM$_{30}$-r-TFBM$_{70}$)	48.5	59.0
poly(FBM$_{40}$-r-TFBM$_{60}$)	49.5	59.5
poly(FBM$_{50}$-r-TFBM$_{50}$)	51.0	58.5
poly(FBM$_{60}$-r-TFBM$_{40}$)	51.5	58.5
poly(FBM$_{70}$-r-TFBM$_{30}$)	51.5	59.0
poly(FBM$_{80}$-r-TFBM$_{20}$)	52.5	59.0
poly(FBM$_{90}$-r-TFBM$_{10}$)	53.0	58.5

Appendix 27. T_gs of poly(FBM-*r*-TFBM) made by PPM in continuous flow and in small batches using an RLH.

FBA input ratio / mol%	*FBA ratio in polymer* / mol%	*TFMBA input ratio* / mol%	*TFMBA ratio in polymer* / mol%
10	0.7	90	99.3
20	1.3	80	98.7
30	2.9	70	97.1
40	3.2	60	96.8
50	5.1	50	94.9
60	7.1	40	92.9
70	11.0	30	89.0
80	16.9	20	83.1
90	32.0	10	68.0

Appendix 28. Input ratios of FBA and TFMBA and final ratios of FBAm and TFMBAm found in the resulting poly(S-*r*-NB-FBAm-*r*-TFMBAm) polymers. Resulting ratios differ dramatically from the expected input ratios.

polymer	M_n / g mol^{-1}	*Đ*
poly(S-*r*-NB-PFPE)	930	1.34
poly(S-*r*-NB-FBAm$_{10}$-*r*-TFMBAm$_{90}$)	890	1.09
poly(S-*r*-NB-FBAm$_{20}$-*r*-TFMBAm$_{80}$)	900	1.11
poly(S-*r*-NB-FBAm$_{30}$-*r*-TFMBAm$_{70}$)	860	1.10
poly(S-*r*-NB-FBAm$_{40}$-*r*-TFMBAm$_{60}$)	830	1.11
poly(S-*r*-NB-FBAm$_{50}$-*r*-TFMBAm$_{50}$)	820	1.11
poly(S-*r*-NB-FBAm$_{60}$-*r*-TFMBAm$_{40}$)	770	1.10
poly(S-*r*-NB-FBAm$_{70}$-*r*-TFMBAm$_{30}$)	760	1.11
poly(S-*r*-NB-FBAm$_{80}$-*r*-TFMBAm$_{20}$)	740	1.11
poly(S-*r*-NB-FBAm$_{90}$-*r*-TFMBAm$_{10}$)	710	1.10

Appendix 29. M_n and *Đ* of poly(S-*r*-NB-PFPE) and poly(S-*r*-NB-FBAm-*r*-TFMBAm). Calibration: PS.

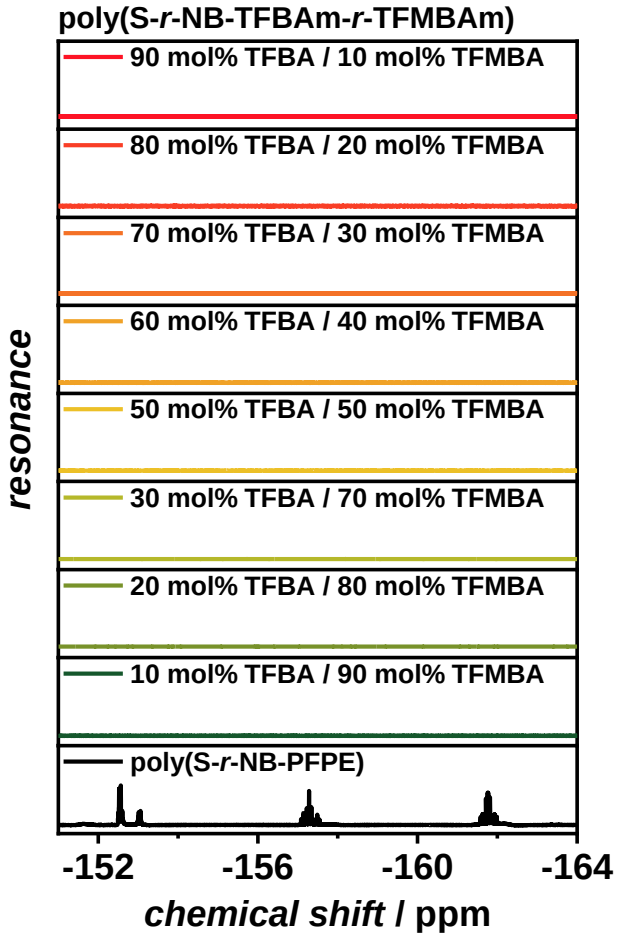

Appendix 30. Stacked ^{19}F NMR spectra of poly(S-*r*-NB-PFPE) (black) and poly(S-*r*-NB-TFBAm-*r*-TFMBAm) (colored) modified with different rations of TFBA and TFMBA. The synthesis was conducted in continuous flow at 50 °C with a residence time of 5 min prior to polymer isolation. No more signals in the region of aromatic poly(S-*r*-NB-PFPE) resonances were found which confirms the quantitative conversion of PFP-ester groups. The amount of TFBA increased from green to red (10 – 90 mol%) while the amount of TFMBA increased from red to green (10 – 90 mol%), respectively. The sample with 40 mol% TFBA / 60 mol% TFMBA modification ratio was lost during polymer workup.

polymer	M_n / g mol^{-1}	*Đ*
poly(S-*r*-NB-PFPE)	930	1.34
poly(S-*r*-NB-NBMAm$_{10}$-*r*-BAm$_{90}$)	820	1.10
poly(S-*r*-NB-NBMAm$_{20}$-*r*-BAm$_{80}$)	820	1.09
poly(S-*r*-NB-NBMAm$_{30}$-*r*-BAm$_{70}$)	810	1.09
poly(S-*r*-NB-NBMAm$_{40}$-*r*-BAm$_{60}$)	800	1.09
poly(S-*r*-NB-NBMAm$_{50}$-*r*-BAm$_{50}$)	800	1.09
poly(S-*r*-NB-NBMAm$_{60}$-*r*-BAm$_{40}$)	800	1.09
poly(S-*r*-NB-NBMAm$_{70}$-*r*-BAm$_{30}$)	800	1.10
poly(S-*r*-NB-NBMAm$_{80}$-*r*-BAm$_{20}$)	800	1.09
poly(S-*r*-NB-NBMAm$_{90}$-*r*-BAm$_{10}$)	800	1.10

Appendix 31. M_n and *Đ* of poly(S-*r*-NB-PFPE) and poly(S-*r*-NB-NBMAm-*r*-BAm). Calibration: PS.